Spring 2023

Microscale Chemical Manipulation and Imaging Using Photoactive Molecules and Light

Uroob Haris
Southern Methodist University, uroob.333@gmail.com

MICROSCALE CHEMICAL MANIPULATION AND IMAGING

USING PHOTOACTIVE MOLECULES

AND LIGHT

Approved by:

_____
Prof. Alexander R. Lippert
Associate Professor of Chemistry

_____
Prof. John D. Buynak
Professor of Chemistry

_____
Prof. Tomce Runčevski
Assistant Professor of Chemistry

_____
Prof. David Y. Son
Professor of Chemistry

_____
Prof. Stephen Sekula
Professor of Physics

MICROSCALE CHEMICAL MANIPULATION AND IMAGING USING PHOTOACTIVE MOLECULES AND LIGHT

A Dissertation Presented to the Graduate Faculty of the

Dedman College

Southern Methodist University

in

Partial Fulfillment of the Requirements

for the degree of

Doctor of Philosophy

with a

Major in Chemistry

by

Uroob Haris

B.A., Chemistry, Southern Methodist University
B.B.A., Management, Southern Methodist University

May 13, 2023

ACKNOWLEDGMENTS

This thesis and the five-year long journey inside it would not have been possible without some very key people. I would like to express my sincere gratitude to my advisor Prof. Alex Lippert, who nurtured the curiosity and passion of a green undergraduate researcher and helped funnel them into critical thinking and science. With your guidance, instruction, and encouragement I have grown into a confident and independent scientist who is not just enthusiastic but now also prepared to dissect the world. I am a better investigator, writer, presenter, thinker, mentor, and scientist after 5+ years of learning from you. An advisor knows better than anyone else about their students' science – the good (the clean NMRs, the colorful columns, the grants and awards) and the not-so-good (the failed syntheses, the weeks of repetitive data collection, the hard work that never made it to publication.) Through it all, I've felt supported by you – thank you!

I would also like to thank my thesis committee members Dr. John Buynak, Dr. David Son, Dr. Stephen Sekula, and Dr. Tom Runcevski for their time, feedback, and expertise. Learning from all of you (since I was an undergrad in some cases!) has helped me evolve into the scientist I am today. Your dedication to seeing students succeed and your enthusiasm for science and research inspires me to always push myself towards success as well as do my part in the success of others. Your insightful comments and suggestions have been valuable and have encouraged me to become a better researcher. I want to acknowledge the members of the Department of Chemistry at SMU as well, for making our department an easygoing and collaborative place to work in. Special thanks

to Mandy Graham, Dr. Humason, Dr. Lattman, Dr. O'Brien and Mrs. Adams for always looking out for the graduate students and for fostering a community spirit through departmental events.

A big thanks to all my lab mates over the years: Maha, Weiwei and Briley – the best experiments in the lab and the best conversations in the office were with the three of you. Tate, Lisa, Chancellor and Husain – thank you for the fun, the camaraderie and the humor. Hours can go by in seconds if you all are around. Bo, Luke, and Jian – thank you for the tips, techniques, and knowledge. Made, Josh, Gen Chen, Rokia, and Caleb – thank you for keeping a friendly, organized, and collaborative environment in the group. Sometimes these things can hold us together when the experiments are falling apart!

Lastly, a heartfelt thank you to my family. My academic journey has been a breeze (and sometimes a mildly strong gust) thanks to the love and support I receive from them. To my parents who were always ready with prayers and wishes for my success, who gave me everything I needed to reach where I am, and who offered me comfort (mom) and advice (dad) when I needed: Thank you. Words are not enough to express how thankful and blessed I am to have you. To my siblings who (sometimes) made an effort to read my papers and understand my research, and who (always) hyped me up and made me feel confident in my work: Thank you. You remind me to feel proud and thankful for where I am. To my husband, who joined the PhD journey late but has stood by me and chosen me every day since we met, and celebrated me more than anyone else: thank you. My life is richer now, thanks to you. To my grandparents, my extended family, and my friends: your constant support and unwavering faith in me drives me forward – thank you!

Haris, Uroob B.A., Chemistry, Southern Methodist University, Dallas
B.B.A., Management, Southern Methodist University, Dallas

Microscale Chemical Manipulation and Imaging
Using Photoactive Molecules
And Light

Advisor: Dr. Alexander Lippert
Doctor of Philosophy conferred May 13, 2023
Dissertation completed May 5, 2023

Chemical manipulation with light has been an active and growing area of research with important implications in materials science, biotechnology, and environmental science. From early investigations of light sensitive materials for photography in the 19th century, to printing billions of transistors on a semiconductor chip in present day, scientists have gained a deep understanding of photochemistry and the processes that allow us to harness light for everyday applications. In this work, we explore microscale fabrication and molecular imaging using light and photoactive molecules as foundational tools. We develop a visible-light mediated technique for high resolution microscale chemical lithography comprising of a home-built digital light processing fluorescence microscope, optimized photochemical reactions, and light responsive molecules. We leverage the ability to control, structure, and build with visible light at a microscale to fabricate self-propelling catalytic micromotors based on existing and novel catalytic systems, and characterize their performance. To further the horizons of light-mediated chemistries to cutting-edge single molecular resolutions, we introduce chemical systems with paired fluorescence and reactivity, which in conjunction with super resolution imaging will allow for chemical lithography with unprecedented specificity. Finally, we design and apply near-infrared light emitting molecular

systems for chemiluminescent imaging from within biological tissue, furthering advancement of non-invasive methods for molecular biosensing and quantification. Altogether, these works demonstrate the versatility and growing applications of visible light for microscopic chemical manipulation and imaging when combined with tailored photoactive molecules.

TABLE OF CONTENTS

LIST OF FIGURES

LIST OF SCHEMES

LIST OF TABLES

LIST OF PUBLICATIONS

1. Haris, U.; Osman, R.; Cabello, M. C.; Lippert, A. R. A Silicon Rhodamine 1,2-Dioxetane Chemiluminophore for *In-Vivo* Near Infrared Imaging. *In preparation*.

2. Haris, U.; Lippert, A. R. Exploring the Structural Space of Chemiluminescent 1,2-Dioxetanes. *ACS Sens.* **2022**, *8*, 3–11.

3. Haris, U.; Plank, J. T.; Li, B.; Page, Z. A.; Lippert, A. R. Visible Light Chemical Micropatterning Using a Digital Light Processing Fluorescence Microscope. *ACS Cent. Sci.* **2022,** *8,* 67–76.

4. Haris, U.; Kagalwala, N. H.; Kim, Y.; Lippert, A. R. Seeking Illumination: The Path to Chemiluminescent 1,2-Dioxetanes for Quantitative Measurements and In Vivo Imaging. *Acc. Chem. Res.* **2021**, *54*, 2844–2857.

5. Li, B.; Haris, U.; Aljowni, M.; Nakatsuka, A.; Patel, S. K.; Lippert, A. R. Tuning the Photophysical Properties of Spirolactam Rhodamine Photoswitches. *Isr. J. Chem.* **2021**, *61*, 244-252.

6. Lefton, J. B.; Pekar, K. B.; Haris, U.; Zick, M. E.; Milner, P. J.; Lippert, A.; Pejov, L.; Runcevski, T. Defects Formation and Amorphization of Zn-MOF-74 Crystals by Post-Synthetic Interactions with Bidentate Adsorbates. *J. Mat. Chem. A.* **2021**, *9*, 19698-19704

7. Ryan, L. S.; Gerberich, J.; Haris, U.; Nguyen, D.; Mason, R. P.; Lippert, A. R. Ratiometric pH Imaging Using a 1,2-Dioxetane Chemiluminescence Resonance Energy Transfer Sensor in Live Animals. *ACS Sens*. **2020**, *5,* 2925-2932.

8. Lippert, A. R.; Aljowni, M.; Li, B.; Haris, U.; O'Brien, C.; Clark, D. S. System and Method for A Three-Dimensional Optical Switch Display (OSD) Device, US10843410B2, November 24, **2020**.

In the name of God, the Entirely Merciful, the Especially Merciful.

Chapter 1

INTRODUCTION

1.1. Light and chemical manipulation

Chemical manipulation with light has been an active and growing area of research for several decades, encompassing various techniques to initiate chemical reactions or to control the behavior of molecules in chemical systems with light. While photochemistry and the use of light in chemical reactions has a long history dating back to the 19th century, it made up only a small facet of the fast-growing field of chemistry at the time.[1] With the development of lasers, flash photolysis, and laser spectroscopy in the in the 20th century, a more detailed understanding of the mechanisms behind photochemical reactions was possible, and the potential of light for chemical manipulation was realized, ushering in an era of rapid development in the field of photochemistry.[2,3,4] Now, the ability to understand, control, and harness light has demonstrated applications in a wide range of exciting fields, from jaundice therapy for infants[5] to the printing of billions of transistors on a semiconductor chip.[6]

In this chapter, we first discuss the fundamentals of photochemistry and the behavior of photoactive molecules when they interact with light. Next, we look at the variety of applications of light for studying and manipulating chemical systems, and place the work presented in this thesis in the context of these applications.

1.2. Luminescence and the Jablonski diagram

Photoactive molecules are molecules that exhibit a chemical or physical change when they absorb light energy. One way to visually represent the electronic behavior of photoactive molecules is the Jablonski diagram. This graphical representation of molecular electronics consists of different energy levels of a molecule. The lowest energy level, S_0, is the singlet ground state. Higher levels than this are singlet excited states (S_1, S_2...), and within different electronic states are multiple vibrational states (V_0, V_1, V_2…). According to the Grotthuss-Draper law, for any photochemical reaction to take place, light must first be absorbed by a compound. Reflection or transmittance of light does not result in photochemistry. When a molecule absorbs a photon of light, it gets excited to a higher energy level (Figure 1-1 A). Once in its excited state, the molecule first relaxes to the lowest vibrational level of the excited state in a process called vibrational relaxation (1-1 B). From here, the molecule may relax back to the ground state through one of several different pathways. It can release the energy as heat, in a non-radiative process known as internal conversion (1-1 C), it can participate in energy transfer to another molecule, or it can release the energy as light in radiative decay phenomena known as luminescence. Three types of luminescence will be discussed: fluorescence, phosphorescence, and chemiluminescence.

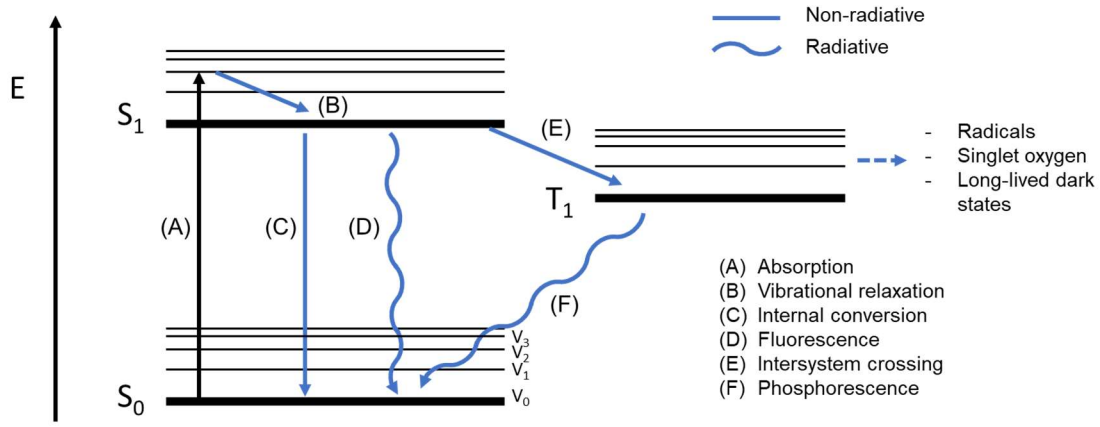

Figure 1-1. Jablonski diagram illustrating photochemical processes.

Fluorescence occurs when the excited molecule relaxes from the singlet excited state to the ground state by releasing a photon of light (1-1 D). Since the molecule first relaxes to the lowest vibrational state of the excited state by releasing energy as heat (vibrational relaxation 1-1 B) and then relaxes to S_0 via photon emission, the energy of the photon emitted is generally lower than the energy of the photon that was absorbed. Because of this, the wavelength of the emitted light of a fluorescent molecule is red-shifted as compared to the wavelength of the absorbed light. This difference in energy (and wavelength) is known as the Stokes shift, and forms the basis of fluorescence imaging, where light emission from a fluorescent sample can be observed without interference from the excitation light, which is filtered by wavelength selective filters. Owing to the higher resolution, contrast, and versatility of fluorescence imaging as compared to conventional light microscopy, over the past century this technique has evolved into a keystone of biological imaging.[7,8,9] The quantum yield of fluorescence (Φ_{fl}) of a fluorophore is a measure of how efficiently it converts absorbed photons into emitted photons as described by equation 1-1.

$$\Phi_{fl} = \frac{n\ photons\ emitted}{n\ photons\ absorbed} \qquad (Eq\ 1-1)$$

High quantum yields indicate that a fluorescent molecule is a good emitter, and useful for various applications such as fluorescence microscopy, sensing, and imaging.

A second type of luminescence is phosphorescence. In this case, the molecule releases energy as light, but from a long-lived triplet excited state (T_1) instead of the singlet excited state. This process of changing spin multiplicity is known as intersystem crossing (1-1 E), and phosphorescence is the slow radiative decay from the T_1 state (1-1 F). Aside from phosphorescence, other notable photochemical processes also occur from the triplet excited state.[10] In chapter 2, we use photoinitiators to mediate chemical reactions with light. When irradiated with

light, molecules such as these undergo intersystem crossing to the long-lived triplet excited state where they have unpaired electrons with parallel spins that make them more reactive and more prone to reactions generating free radicals. In chapter 4, we discuss mechanisms of toggling fluorescent molecules between being fluorescent and being non-fluorescent for super resolution imaging. Many of these super resolution imaging dyes undergo intersystem crossing. From the S_1 state, fluorescent molecules can relax by emitting light, but from a T_1 state molecules can access long-lived dark states and decay non-radiatively.[11] In chapter 5, we use methylene blue as a photosensitizer to generate singlet oxygen. When irradiated with light, the photosensitizer accesses its triplet excited state and transfers energy to molecular oxygen to generate singlet oxygen. Overall, while phosphorescence is not a subject of this work, other processes occurring from the triplet state are referenced.

Chemiluminescence is a type of luminescence which does not require absorption of light to access the singlet excited state and emit light, unlike fluorescence and phosphorescence. Instead, the singlet excited state is accessed via a chemical reaction where a high energy excited state intermediate is generated, and a photon is emitted as the intermediate relaxes to ground state. The quantum yield of chemiluminescence (Φ_{CL}) is a measure of the efficiency of a chemical reaction at converting chemical energy into light energy, as described by equation 1-2.

$$\Phi_{fl} = \frac{n\ photons\ emitted}{n\ limiting\ reactant} \qquad (Eq\ 1-2)$$

While chemiluminescence is not strictly a photochemical process in that it is not a response to light absorption, it is strongly associated with the interaction of matter and light and the principles of photochemistry. The lack of requirement for light excitation to generate emission has enabled chemiluminescence to bypass many of the limitations that fluorescence entails. The high signal to

noise ratio, the lack of light scattering, and the low phototoxicity as compared to fluorescence make this technique optimal for biological imaging, and numerous developments have been made in the field over the past few decades.[12]

1.3. Chemistry applications of visible light

From early investigations of light sensitive materials for photography in the 19th century,[13] to photodynamic therapy for cancers in the present day,[14] scientists have gained a deep understanding of photochemistry and furthered light-based chemistries for everyday applications. While ultraviolet light and high energy wavelengths have been a key player in driving many of these processes for a long time, new advances are enabling a trend towards the visible and redder region of the spectrum, where there is better chemical and biocompatibility, lower associated costs, and higher selectivity. Three broad categories of how light can be used for chemistry are discussed below.

Light for driving chemistry. Light can be used to drive chemical transformations that may be complex, resource-intensive, or even impossible to achieve by other means. Organic photocatalysis,[15,16] for example, has become a powerful tool in synthetic chemistry, enabling a wide range of transformations that are difficult to achieve using traditional methods. Chemical reactions such as C-H functionalization, cross-couplings, bioconjugations and radical reactions have been accomplished through use of visible-light-absorbing organic dyes and photoredox catalysts via energy transfer or electron transfer mechanisms.[15,16,17] These reactions are more environmentally friendly and a sustainable alternative to traditional synthetic methods. The thiol-ene photoclick reaction is one example.[18] This photoinitiated ligation reaction between thiols and alkenes can be driven by visible light in the presence of a photoinitiator such as eosin y. Because of its high yield and simplicity, the reaction has seen applications in materials science, polymer

chemistry, and molecular synthesis, including for surface functionalization,[19] photolithography,[20] and bioorganic functionalization.[21] The light-driven Wolff rearrangement reaction of α-diazoketones has also found many applications in organic synthesis, for example in the Arndt-Eistart homologation reaction.[22] A common industrial application of the Wolff rearrangement is in Novolac-based positive photoresists for photolithography, which upon UV exposure become water soluble.[22] Recently, a photocaged fluorophore Rhodamine BNN, activated by visible light was reported, with uncaging mechanism based on the Wolff rearrangement reaction for applications in microscopy.[23] In our work, we utilize visible light-driven reactions such as the thiol-ene reaction and Wolff rearrangement reaction which have been used for synthetic transformations in bulk, to achieve patterned chemical manipulation on a microscopic scale with visible light.

Light for chemical imaging. The interaction of visible light with photoresponsive molecules enables visualization of molecules and microenvironments with high resolutions, minimal invasiveness, and low side reactions. While X-rays, PET scans and electron microscopes, can provide vital information for material characterization or clinical diagnoses, sample preparation, cost, and radiative damage are considerations that make visible light-based methods more attractive. More importantly, the ability to synthetically tailor these photoactive molecules allows specifically targeting and studying areas or species of interest. For example, fluorescent molecules, which emit light in response to light excitation have been customized for application in immunoassays,[24] DNA sequencing,[25] subcellular imaging,[26] molecular imaging,[27] and imaging of microscale materials.[28] Advancements in lasers, optics and high-performance organic fluorescent agents have recently enabled imaging at resolutions beyond the diffraction limit of light, allowing study of processes and pathways that were inaccessible previously.[29] Chemiluminescent molecules, which bypass the need for light excitation altogether, have also been similarly crafted for

generating light response to analytes of interest. This visible light emitting technology has applications in clinical lab research,[30] forensics,[30] environmental monitoring,[31],[32] bioimaging,[33],[34] and photodynamic therapy.[34] For applications *in-vivo,* there is a shift in efforts towards lower energy NIR imaging agents due to superior penetration of these wavelengths through tissue. Research on NIR fluorescent and chemiluminescent bioreporters which emit at 600+ nm in aqueous systems with high quantum yield continues to grow.[35] In our work, we develop and apply specialized molecules for fluorescence microscopy of new chemical micropatterning techniques, for novel super resolution imaging systems, and for chemiluminescent imaging with energy transfer based NIR light emission.

Light for targeting chemistry. Because light can be controlled in space and time, a profound implication of carrying out chemistry with light is the spatiotemporal control granted over light-mediated processes. By selectively illuminating certain areas of a sample or material, we can control where and when chemical reactions occur. Numerous exciting advancements have been made with light for targeted reactions. Optogenetics involves activating or deactivating certain cells, most notably in the brain, by targeting them with light.[36] This has been key in neurobiology, for elucidating how brain circuits work and understanding how behaviors are controlled by the brain, as well as in other fields such as cardiology,[37] cell biology,[38] and plant sciences.[39] Light-sensitive drug delivery systems,[40] photopharmacology,[41] and photodynamic therapy[42] are also emerging light-based technologies. Because these are light controlled, the time and location of their activation can be non-invasively controlled for maximum efficacy and minimal off-target effects. In nanofabrication as well, the ability to target chemistry by controlling light plays a crucial role. In two-photon polymerization (also known as direct laser writing), ultrafast laser pulses initiate chemical reactions in a non-linear absorption process, allowing for the fabrication of

complex three-dimensional structures with nanoscale resolution.[43] In stimulated emission depletion (STED) lithography, one wavelength of light is used for activating a chemical reaction, while a second wavelength in a surrounding donut shaped beam is used for deactivating chemical reactions, effectively minimizing the area of exposure to sub-Abbe resolution.[44] In our work, we spatially structure light on the microscale for targeted chemistry, chemical manipulation, and micropatterning.

The work in this thesis focuses on the development and application of chemistries that are driven, targeted, and imaged with light. We explore microscale fabrication and molecular imaging using light and photoactive molecules as foundational tools. We develop a visible-light mediated technique for high resolution microscale chemical lithography comprising of a home-built digital light processing fluorescence microscope, optimized photochemical reactions, and light responsive molecules. We leverage the ability to control, structure, and build with visible light at a microscale to fabricate self-propelling catalytic micromotors based on existing and novel catalytic systems, and characterize their performance. To further the horizons of light mediated chemistries to cutting-edge single molecular resolutions, we introduce chemical systems with paired fluorescence and reactivity, which in conjunction with super resolution imaging will allow for chemical lithography with unprecedented specificity. Finally, we design and apply near-infrared light emitting molecular systems for chemiluminescent imaging from within biological tissue, furthering advancement of non-invasive methods for molecular biosensing and quantification. Altogether, these works demonstrate the versatility and growing applications of visible light for microscopic chemical manipulation and imaging when combined with tailored photoactive molecules.

1.4. References

1. Roth, H. D. The Beginnings of Organic Photochemistry. *Ange. Chem. Int. Edit.* **1989**, *28* (9), 1193–1207.
2. Laser Photolysis and Spectroscopy: A New Technique for the Study of Rapid Reactions in the Nanosecond Time Range. *Proceedings of the Royal Society of London. Series A. Mathematical and Physical Sciences* **1968**, *308* (1492), 95–110.
3. George, T. F.; Beri, A. C.; Lam, K.-S.; Lin, J.-T.; Rochester Univ Ny Dept Of Chemistry. Laser Photochemistry. **1981**. https://apps.dtic.mil/sti/pdfs/ADA101432.pdf (accessed Mar 13, 2023).
4. Verdieck, J. F. Chemical Reactions Induced by Laser Radiation. *Nuclear Applications* **1969**, *6* (5), 474–482.
5. Branisteanu, D.; Dirzu, D.; Toader, M.; Branisteanu, D.; Nicolescu, A.; Brihan, I.; Bogdanici, C.; Branisteanu, G.; Dimitriu, A.; Anton, N.; Porumb, E. Phototherapy in Dermatological Maladies (Review). *Experimental and Therapeutic Medicine* **2022**, *23* (4).
6. Apple unveils M1 Ultra, the world's most powerful chip for a personal computer. https://www.apple.com/newsroom/2022/03/apple-unveils-m1-ultra-the-worlds-most-powerful-chip-for-a-personal-computer/ (accessed Mar 21, 2023).
7. Combs, C. A. Fluorescence Microscopy: A Concise Guide to Current Imaging Methods. *Current Protocols in Neuroscience* **2010**, *50* (1).
8. Renz, M. Fluorescence Microscopy-A Historical and Technical Perspective. *Cytometry Part A* **2013**, *83* (9), 767–779.
9. Specht, E. A.; Braselmann, E.; Palmer, A. E. A Critical and Comparative Review of Fluorescent Tools for Live-Cell Imaging. *Annual Review of Physiology* **2017**, *79* (1), 93–117.
10. Zhao, J.; Wu, W.; Sun, J.; Guo, S. Triplet Photosensitizers: From Molecular Design to Applications. *Chemical Society Reviews* **2013**, *42* (12), 5323.
11. Nahidiazar, L.; Agronskaia, A. V.; Broertjes, J.; van den Broek, B.; Jalink, K. Optimizing Imaging Conditions for Demanding Multi-Color Super Resolution Localization Microscopy. *PLOS ONE* **2016**, *11* (7).
12. Yang, M.; Huang, J.; Fan, J.; Du, J.; Pu, K.; Peng, X. Chemiluminescence for Bioimaging and Therapeutics: Recent Advances and Challenges. Chemical Society Reviews 2020, 49 (19), 6800–6815.
13. Sheppard, S. E. The Chemistry of Photography. I. Historical Considerations. *Journal of Chemical Education* **1927**, *4* (3), 298.

14. Li, X.; Lovell, J. F.; Yoon, J.; Chen, X. Clinical Development and Potential of Photothermal and Photodynamic Therapies for Cancer. *Nature Reviews Clinical Oncology* **2020**, *17* (11), 657–674.

15. Romero, N. A.; Nicewicz, D. A. Organic Photoredox Catalysis. *Chemical Reviews* **2016**, *116* (17), 10075–10166.

16. Zhou, Q. Q.; Zou, Y. Q.; Lu, L. Q.; Xiao, W. J. Visible-Light-Induced Organic Photochemical Reactions through Energy-Transfer Pathways. *Angewandte Chemie International Edition* **2018**, *58* (6), 1586–1604.

17. Srivastava, V.; Singh, P. K.; Singh, P. P. Recent Advances of Visible-Light Photocatalysis in the Functionalization of Organic Compounds. *Journal of Photochemistry and Photobiology C: Photochemistry Reviews* **2022**, *50*, 100488.

18. Hoyle, C. E.; Bowman, C. N. Thiol-Ene Click Chemistry. *Angewandte Chemie International Edition* **2010**, *49* (9), 1540–1573.

19. Liu, B.; Deng, X.; Xie, Z.; Cheng, Z.; Yang, P.; Lin, J. Thiol-Ene Click Reaction as a Facile and General Approach for Surface Functionalization of Colloidal Nanocrystals. *Advanced Materials* **2017**, *29* (36), 1604878.

20. Wang, Q.; Cui, H.; Wang, X.; Hu, Z.; Tao, P.; Li, M.; Wang, J.; Tang, Y.; Xu, H.; He, X. Exceptional Light Sensitivity by Thiol–Ene Click Lithography. *Journal of the American Chemical Society* **2023**, *145* (5), 3064–3074.

21. Grim, J. C.; Brown, T. E.; Aguado, B. A.; Chapnick, D. A.; Viert, A. L.; Liu, X.; Anseth, K. S. A Reversible and Repeatable Thiol–Ene Bioconjugation for Dynamic Patterning of Signaling Proteins in Hydrogels. *ACS Central Science* **2018**, *4* (7), 909–916.

22. Kirmse, W. 100 Years of the Wolff Rearrangement. *European Journal of Organic Chemistry* **2002**, *2002* (14), 2193.

23. Belov, V. N.; Wurm, C. A.; Boyarskiy, V. P.; Jakobs, S.; Hell, S. W. Rhodamines NN: A Novel Class of Caged Fluorescent Dyes. *Angewandte Chemie International Edition* **2010**, *49* (20), 3520–3523.

24. Gosling, J. P. A Decade of Development in Immunoassay Methodology. *Clinical Chemistry* **1990**, *36* (8), 1408–1427.

25. Smith, L. M.; Sanders, J. Z.; Kaiser, R. J.; Hughes, P.; Dodd, C.; Connell, C. R.; Heiner, C.; Kent, S. B.; Hood, L. E. Fluorescence Detection in Automated DNA Sequence Analysis. *Nature* **1986**, *321* (6071), 674–679.

26. Specht, E. A.; Braselmann, E.; Palmer, A. E. A Critical and Comparative Review of Fluorescent Tools for Live-Cell Imaging. *Annual Review of Physiology* **2017**, *79* (1), 93–117.

27. Ntziachristos, V. Fluorescence Molecular Imaging. *Annual Review of Biomedical Engineering* **2006**, *8* (1), 1–33.

28. Wöll, D.; Flors, C. Super-Resolution Fluorescence Imaging for Materials Science. *Small Methods* **2017**, *1* (10), 1700191.

29. Prakash, K.; Diederich, B.; Heintzmann, R.; Schermelleh, L. Super-Resolution Microscopy: A Brief History and New Avenues. *Philosophical Transactions of the Royal Society A: Mathematical, Physical and Engineering Sciences* **2022**, *380* (2220).

30. Khan, P.; Idrees, D.; Moxley, M. A.; Corbett, J. A.; Ahmad, F.; von Figura, G.; Sly, W. S.; Waheed, A.; Hassan, M. I. Luminol-Based Chemiluminescent Signals: Clinical and Non-Clinical Application and Future Uses. *Applied Biochemistry and Biotechnology* **2014**, *173* (2), 333–355.

31. Ocaña-González, J. A.; Ramos-Payán, M.; Fernández-Torres, R.; Villar Navarro, M.; Bello-López, M. Á. Application of Chemiluminescence in the Analysis of Wastewaters – A Review. *Talanta* **2014**, *122*, 214–222.

32. Al Yahyai, I.; Al-Lawati, H. A. J. A Review of Recent Developments Based on Chemiluminescence Detection Systems for Pesticides Analysis. *Luminescence* **2020**, *36* (2), 266–277.

33. Haris, U.; Kagalwala, H. N.; Kim, Y. L.; Lippert, A. R. Seeking Illumination: The Path to Chemiluminescent 1,2-Dioxetanes for Quantitative Measurements and *in Vivo* Imaging. *Accounts of Chemical Research* **2021**, *54* (13), 2844–2857.

34. Wang, Z.; Huang, J.; Huang, J.; Yu, B.; Pu, K.; Xu, F. J. Chemiluminescence: From Mechanism to Applications in Biological Imaging and Therapy. *Aggregate* **2021**, *2* (6).

35. Haris, U.; Lippert, A. R. Exploring the Structural Space of Chemiluminescent 1,2-Dioxetanes. *ACS Sensors* **2022**, *8* (1), 3–11.

36. Chen, W.; Li, C.; Liang, W.; Li, Y.; Zou, Z.; Xie, Y.; Liao, Y.; Yu, L.; Lin, Q.; Huang, M.; Li, Z.; Zhu, X. The Roles of Optogenetics and Technology in Neurobiology: A Review. *Frontiers in Aging Neuroscience* **2022**, *14*.

37. Entcheva, E.; Kay, M. W. Cardiac Optogenetics: A Decade of Enlightenment. *Nature Reviews Cardiology* **2020**, *18* (5), 349–367.

38. Emiliani, V.; Entcheva, E.; Hedrich, R.; Hegemann, P.; Konrad, K. R.; Lüscher, C.; Mahn, M.; Pan, Z.-H.; Sims, R. R.; Vierock, J.; Yizhar, O. Optogenetics for Light Control of Biological Systems. *Nature Reviews Methods Primers* **2022**, *2* (1).

39. Shikata, H.; Denninger, P. Plant Optogenetics: Applications and Perspectives. *Current Opinion in Plant Biology* **2022**, *68*, 102256.

40. Tao, Y.; Chan, H. F.; Shi, B.; Li, M.; Leong, K. W. Light: A Magical Tool for Controlled Drug Delivery. *Advanced Functional Materials* **2020**, *30* (49), 2005029.

41. Hüll, K.; Morstein, J.; Trauner, D. *In Vivo* Photopharmacology. *Chemical Reviews* **2018**, *118* (21), 10710–10747.

42. Correia, J. H.; Rodrigues, J. A.; Pimenta, S.; Dong, T.; Yang, Z. Photodynamic Therapy Review: Principles, Photosensitizers, Applications, and Future Directions. *Pharmaceutics* **2021**, *13* (9), 1332.

43. Harinarayana, V.; Shin, Y. C. Two-Photon Lithography for Three-Dimensional Fabrication in Micro/Nanoscale Regime: A Comprehensive Review. *Optics & Laser Technology* **2021**, *142*, 107180.

44. Klar, T. A.; Wollhofen, R.; Jacak, J. Sub-Abbe Resolution: From Sted Microscopy to Sted Lithography. *Physica Scripta* **2014**, *T162*, 014049.

Chapter 2

CHEMICAL MICROPATTERNING WITH VISIBLE LIGHT USING A DIGITAL LIGHT PROCESSING FLUORESCENCE MICROSCOPE

2.1. Introduction

Patterning chemical reactivity with high spatiotemporal resolution and chemical versatility is fundamentally important in advancing emergent technologies, including nanorobotics,[1] bioprinting,[2] photopharmacology,[3,4] and additive manufacturing.[5] While high-resolution nanofabrication techniques like electron beam lithography,[6] dip-pen nanolithography,[7] and direct laser writing/two photon polymerization[1] can provide exceptional precision, they come at a significant cost, with low throughput and limited chemical versatility. In contrast, optical methods such as stereolithography and digital light processing (DLP) offer a relatively inexpensive and high-throughput alternative, providing access to a wide range of light-mediated chemical reactions.[1,8]

DLP methods, which use digital micromirror devices (DMD) to structure light with pixel specificity,[9] offer the advantages of high fabrication speeds, scalability, and high resolution. These methods are often referred to as projection micro-stereolithography (PμSL)[10] or microscale continuous optical printing (μCOP),[11] and typically use UV light (364–405 nm) to induce polymerization with micrometer scale resolution. UV light, however, limits the scope of compatible materials, increases the cost of optics, and can interfere with certain chemistries. For

these reasons, blue light (450–485 nm) DLP systems are beginning to be explored for hydrogels and bioprinting.[12,13] Despite these promising advances, microprinting using lower energy green or red light remains rare, particularly with DLP systems, which have largely been limited to use with polymerization chemistry. Moreover, multiplexing DLP with fluorescence microscopy is underexplored.

Advancements in photoclick and photopolymerization chemistries make them ideally poised for integration with micropatterning.[14] One attractive photochemical system for micropatterning is the thiol-ene photoligation.[15,16] Visible light thiol-ene reactions can be conducted with eosin y as a photoinitiator,[17] and this chemistry has been used in a versatile molecular patterning technique for printing biocompatible hydrogels.[18,19] The photochemistry of diazoacetates and diazonium-photocaged compounds has also been exploited, particularly for photoactivatable single molecule localization experiments [20,21] and photochemical synthetic transformations, [22] but there are very limited examples of photochemical patterning with this motif.[23] Recently, photopolymerization resins for visible light 3D-printing have also been developed for use with DLP technology and multi-color photoinitiation, and efforts to improve printing resolution with these are ongoing.[24]

Here,[25] we report the development of a DLP fluorescence microscope and associated photochemistry capable of performing photochemical reactions using blue (465 nm), green (520 nm), and red (624 nm) light with high spatiotemporal precision. Molecular micropatterning of silicon rhodamine dyes onto solid polymer beads is carried out and tracked using the built-in fluorescence microscope, and high-resolution 2D and 3D polymerizations are achieved using recently disclosed visible light formulations.[24] Using a photoactivatable diazoketone caged rhodamine dye, we demonstrate that this apparatus and chemistry can be used to perform spatial

patterning of molecules inside of living cells with single cell resolution, as well as printing of fluorescence images onto polymer films with photographic quality and resolution as high as 2.1 μm.

2.2. Results and Discussion

2.2.1. DLP Microscope Construction and Characterization

To achieve highly resolved and spatially precise chemistry, we designed and constructed a DLP fluorescence microscope capable of projecting patterned visible light onto microscale substrates with simultaneous fluorescence imaging (Figure 2-1A, B). Digital light processing was accomplished using the digital micromirror device and projection engine in a LightCrafter 4500 projector (Texas Instruments, USA). Previously, we have employed the LightCrafter and similar projectors in fabrication of a volumetric 3D digital light photoactivatable dye display (3D Light PAD) for patterned activation and excitation of photoswitchable fluorophores with ultraviolet and visible light.[26,27] For the DLP microscope, the LightCrafter was used with its projection optics removed. The setup includes a DLP4500FQE DMD chip and an IPD 1231 light engine containing collimated red, green, and blue LEDs.[9] Light from the LEDs is projected towards the DMD chip and the reflected light from the DMD mirrors is directed through an adjustable diaphragm aperture, followed by collimation using a 100 mm achromatic doublet collimation lens. The collimated patterned light is then directed through a dichroic mirror to reflect short wavelength excitation light and transmit long wavelength light, and an emission bandpass filter to transmit light from 672–712 nm or 583–603 nm, regions that correspond with the fluorescence emission of the red fluorescent dyes used in this study. For non-fluorescent samples, the filter cube could be easily replaced with one fitted with a 90:10 optical beamsplitter for reflected light microscopy. A 4x (NA = 0.10), a 40x (NA = 0.60), and a 100x (oil, NA = 1.30) objective were used to focus light onto a

sample slide that could be moved using an XY translational stage. Fluorescence emission from the sample was collimated through the objective and directed back through the filter cube, followed by focusing through a tube lens (100 mm achromatic doublet) onto the sensor of a Chameleon®3 Monochrome sCMOS Camera. A photograph of the DLP microscope is shown in Figure 2-1B, and vendors and part numbers are included in Table 2-1 (Section 2.4.2.1). Two zoom housings were included for (1) focusing the projected light onto the sample and (2) focusing the light from the sample onto the camera. The modular design of the DLP microscope enabled easy incorporation of supplemental elements; with the addition of a single-axis motorized translational stage to the existing setup, a stereolithography-capable microscope was achieved as described below.

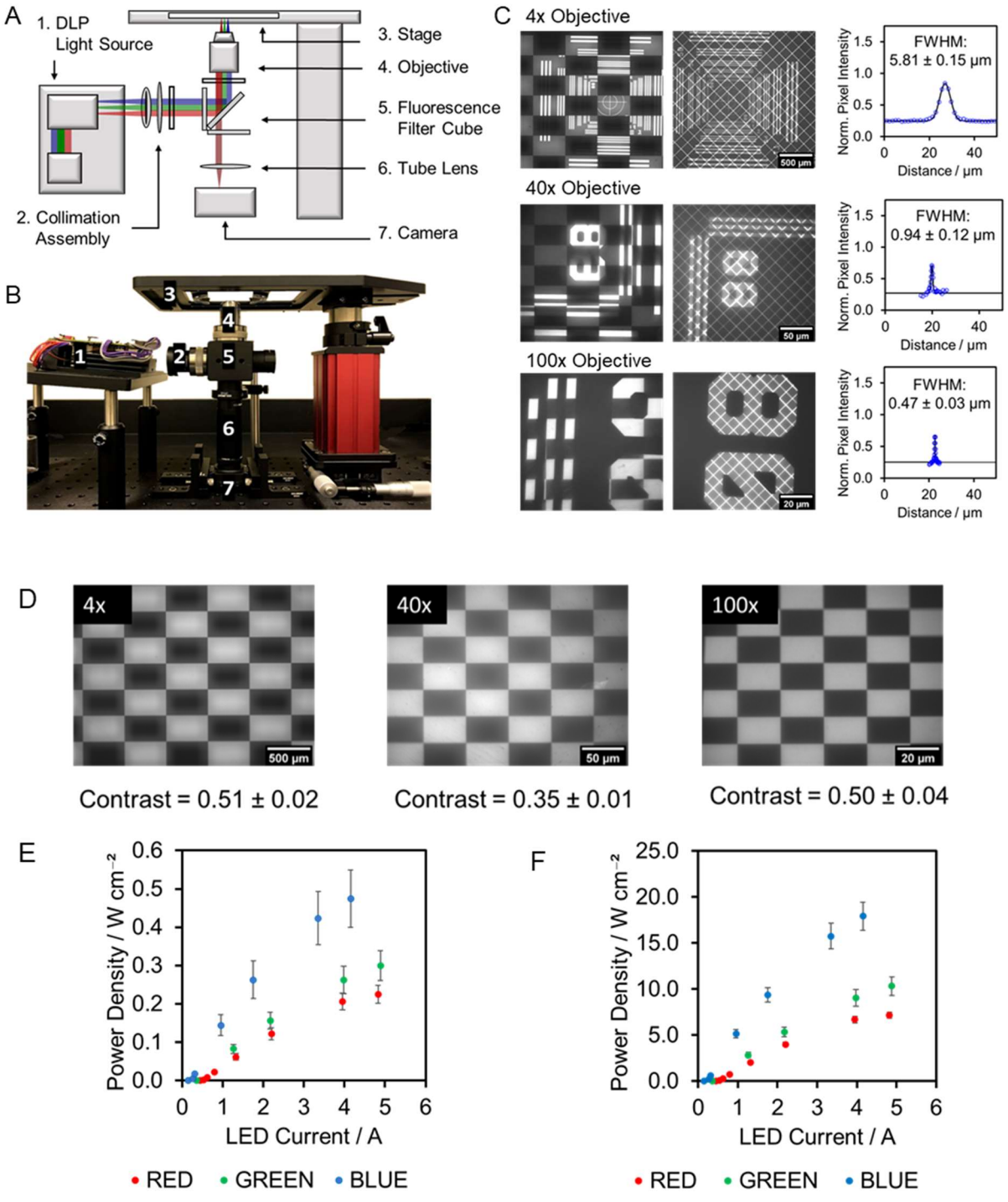

Figure 2-1 (A) Design scheme and (B) photograph of the DLP microscope setup. Part details are provided in Table 2-1 in section 2.4.2.1. (C) Checkerboard pattern and one-pixel width diagonal lines projected onto a target resolution slide using 4x, 40x, and 100x objectives. Projection resolution with each objective was determined as the FWHM of the Gaussian fit (black line) to

imaged pixel intensities (blue circles) across projected one-pixel wide lines. Error on FWHM is ± S.D. with n = 3 different lines measured. (D) Determination of projection contrast between light and dark areas of a checkerboard pattern with 4x, 40x, and 100x objectives. Error on contrast values is ± S.D. with n = 3 different light and dark areas measured. (E) Irradiation power density of the DLP microscope with increasing LED current for 4x and (F) 40x objectives for blue, green and red LEDs. Error bars are ± S.D, n = 3 independent measurements. Figures with permission from reference 25.

Following construction of the DLP microscope, we evaluated the light patterning capability of the system using the checkerboard and diagonal lines internal test patterns of the LightCrafter 4500 (Figure 2-1C). Patterned light using the red LED was projected through a 90:10 beamsplitter onto a microscope resolution target slide (Thorlabs, #R1L3S10P) using 4x, 40x, and 100x objectives. With each objective, sharp patterns were achieved with good light/dark contrast that could be tuned using the adjustable diaphragm aperture (Figure 2-1D). The resolution of projection was evaluated using the single pixel width diagonal lines internal test pattern. An intensity profile across the projected diagonal lines was generated in ImageJ, and the resolution was determined as the full width at half maximum (FWHM) of the resultant Gaussian profiles (Figure 2-1C). Using this method, we determined projection resolution to be 5.81 ± 0.15 μm using the 4x objective, 0.94 ± 0.12 μm with the 40x objective, and 0.47 ± 0.03 μm with the 100x objective. The irradiation capability of the DLP microscope was also characterized (Figure 2-1E, F). Using a Si photodiode sensor and a digital optical power meter (ThorLabs, #S120VC, #PM100D), we measured the power density while irradiating with each LED of the LightCrafter using the different objectives and varying LED current settings. The maximum power density achieved with a 4x objective was 0.22 ± 0.02 W cm^{-2} with the red LED, 0.30 ± 0.04 W cm^{-2} with the green LED, and 0.48 ± 0.07 W cm^{-2} with the blue LED. With the 40x objective, the maximum power densities achieved were 7.17 ± 0.35 W cm^{-2}, 10.33 ± 1.02 W cm^{-2}, and 17.93 ± 1.53 W cm^{-2} for the red, green, and blue LEDs respectively. Owing to the short focal length and working distance of the 100x objective,

power density measurements under this objective using the standard photodiode sensor, which is concave could not be obtained. Use of a microscope slide power sensor (ThorLabs #S175C) may allow determination of these values.

2.2.2. Visible Light-Based Reaction Systems

We next turned our attention to photoinitiated chemical reactions that we could employ for chemical microprinting using the DLP microscope. We investigated the thiol-ene photoclick reaction between thiols and alkenes, initiated by a visible light photoinitiator, and the light-mediated insertion of diazo compounds into nucleophilic functionalities such as O–H and N–H bonds via direct carbene insertion or ketene trapping of their Wolff rearrangement products (Scheme 2-1).

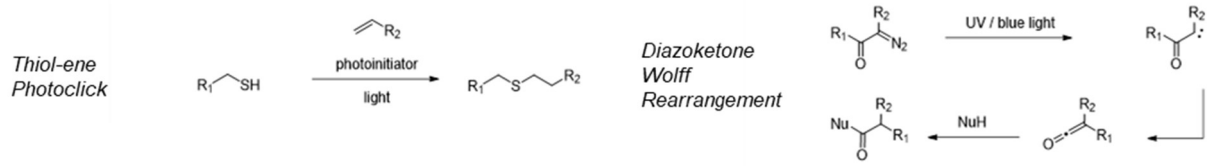

Scheme 2-1. Light based thiol-ene photoclicking and Wolff rearrangement of diazoketones.

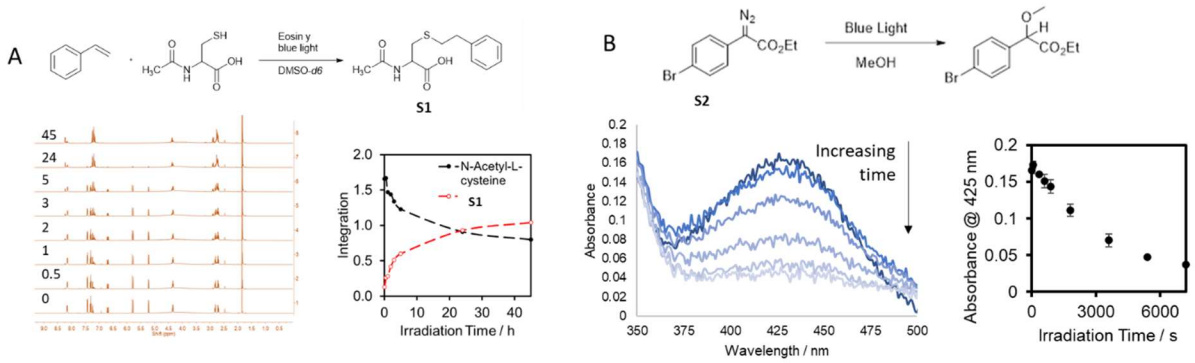

Figure 2-2. (A) Reaction scheme and ^{1}H NMR kinetics of thiol-ene reaction between model compounds styrene and N-acetyl cysteine with eosin y and blue light irradiation at 0, 0.5, 1, 2, 3, 5, 24, and 45 h durations. Integrals of peaks between 2.93–2.78 ppm of starting material (black) and sulfide product S1 (red) are plotted against irradiation time. (B) Reaction scheme and absorbance decay kinetics for diazonium photolysis of model compound S2 with blue light irradiation for 0, 1, 6, 10, 15, 30, 60, 90, and 120 min. Absorbance at 425 nm is plotted against irradiation time. Error bars are ± S.D. with n = 3 independent replicates.

These chemistries interested us because of the fast kinetics and high yields in response to visible light in model systems (Figure 2-2A, B), and so we leveraged them for observable covalent modification of thiol-, amine- or alcohol- containing polymer constructs with fluorescent rhodamine molecules. We immobilized free thiols on commercially available NovaSyn-TG amino resin, which are 90 μm diameter polymer beads used in peptide synthesis; amide coupling with fmoc- and mmt- protected cysteine, and subsequent cleavage of the mmt group with 1% trifluoroacetic acid (TFA), yielded the thiol-modified SH-resin as a platform for thiol-ene chemistry (Figure 2-3A). Reactions on solid resin cannot be easily monitored using conventional techniques like NMR, mass spectrometry, or IR spectroscopy. In order to observe the thiol-ene photoconjugation, we developed a system of fluorescent tagging and imaging. The alkene reaction partner is covalently tagged with a fluorescent dye, so that when the tagged alkene molecules react with thiols on the resin surface, the resin becomes covalently linked to the fluorescent dye and can be imaged with fluorescence microscopy. A near-IR emitting silicon rhodamine dye, **SiR** was synthesized for this purpose, [28] designed to result in increased fluorescence at the sites of thiol-ene ligation on the SH-resin beads. **SiR** was synthesized from the silicon anthrone **1** and *tert*-butyl protected 3-iodo-4-methylbenzoate in a modified procedure.[29] We encountered side reactions and almost no reaction yield when following literature protocols which use the bromo benzoate for lithium halogen exchange, and for safety reasons we did not explore pathways incorporating *tert*-butyllithium. Previous work has shown that lithium iodine exchange occurs faster as compared to lithium bromine exchanges,[30] and so we used *n*-butyllithium as the lithiating agent, postulating that the fast lithium-iodine exchange outcompetes the nucleophilic addition of *n*-BuLi to the anthrone. A standard amide coupling of **SiR** with 4-amino styrene provided the thiol-ene partner **SiR-sty** in high yield (Figure 2-3B). λ_{max} for **SiR-sty** was found to be 685 nm in DMSO (Figure 2-12B). We

reacted the thiol-modified SH-resin with **SiR-sty** and eosin y in DMSO under blue light irradiation for 22 hours and observed strong fluorescence emission from beads when the reaction was irradiated, as compared to almost no emission observed when the reaction was conducted in the dark, confirming that on-bead reaction progress could be monitored via fluorescence emission of the **SiR-sty** (Figure 2-3C). Ellman's reagent was used to further verify that irradiation with blue light led to depletion of free thiols and that the reaction with **SiR-sty** resulted in a 79 ± 13% conversion (Figure 2-15, Table 2-2 in section 2.4.4.4).

For photochemical patterning with diazo compounds, we envisioned using a fluorescent turn-on approach employing Wolff rearrangement of the Rhodamine B based diazonium photocaged dye Rhodamine BNN (**RhBNN**).[20] Upon photolysis of **RhBNN**'s diazoketone caging group with blue light, a carbene is generated, which rapidly undergoes a Wolff rearrangement to a ketene intermediate. The ketene can be subsequently trapped by nucleophilic species such as alcohols and amines to uncage the bright fluorescence emission characteristic of rhodamine B (Figure 2-12 C, D). Though we found that Wolff rearrangement products of **RhBNN** undergo photobluing with long exposure to high intensity light like other similar organic fluorophores,[31] the relatively short irradiation durations and low light intensities in our studies did not cause photobluing (Figure 2-12 E–H). We used polyvinylalcohol (PVA) to prepare films doped with **RhBNN**, theorizing that the solid PVA could also serve as the source of nucleophilic hydroxyl groups required for trapping the uncaged **RhBNN**. This was confirmed when we irradiated 50 μm thick films of PVA containing Rhodamine BNN (**RhBNN**-PVA) coated onto glass microscope slides with blue light; the films displayed strong red fluorescence when irradiated with blue light for 22 hours as compared to those that were kept in the dark (Figure 2-3D).

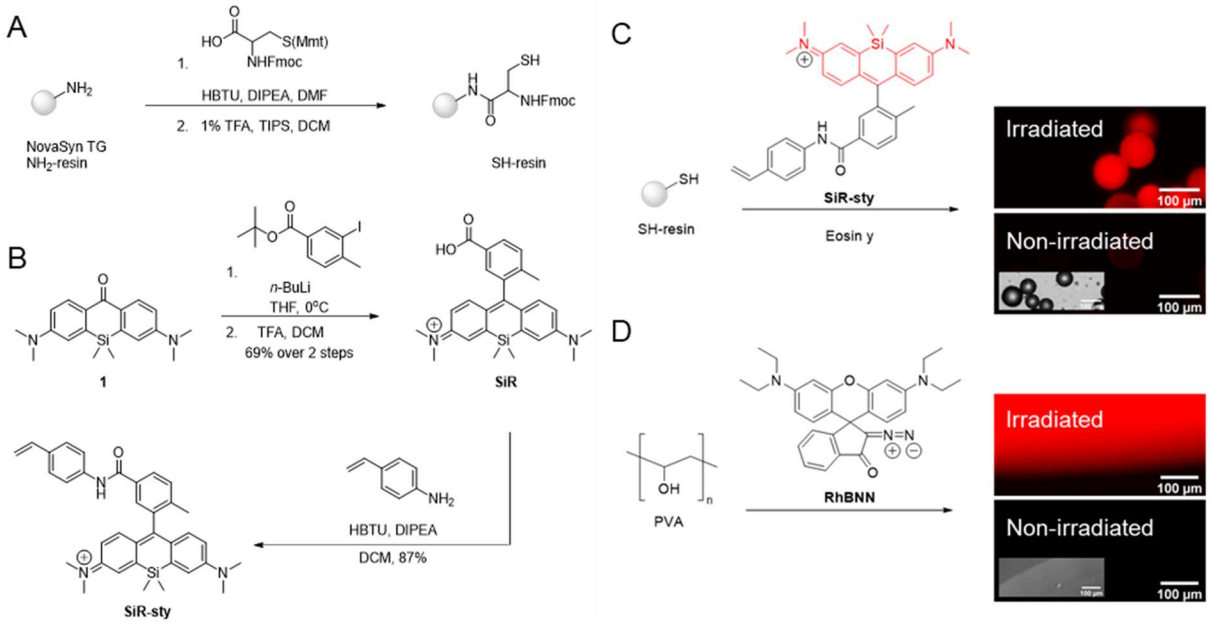

Figure 2-3. Visible light mediated reaction systems for solid microprinting. (A) Synthesis of thiol-functionalized SH-resin. (B) Synthesis of fluorophore-tagged alkene, SiR-sty. (C) Reaction scheme and EVOS-fl fluorescence images (Ex: 635/18 Em: 692/40) of washed SH-resin beads after reacting in a solution of 3 mM SiR-sty and 70 µM eosin y in DMSO for 22 h with and without blue light irradiation from a 100 W LED lamp at 0.04 W cm^{-2}. (D) Reaction scheme and EVOS-fl fluorescence images (Ex: 542/20 Em: 593/40) of PVA films doped with 20 µM RhBNN with and without 22 h blue light irradiation from a 100 W LED lamp at 0.04 W cm^{-2}. Inset: brightfield images. Figures with permission from reference 25.

2.2.3. Chemical Micropatterning

We proceeded to apply the thiol-ene and Wolff rearrangement chemistries for surface micropatterning using the newly developed DLP microscope for patterned visible light irradiation and fluorescence imaging. We first attempted micropatterning using a 4x objective. SH-resin beads were added onto a glass microscope slide with 20 µL of a **SiR-sty** and eosin y solution in DMSO. Patterned light in a grid pattern from the LightCrafter was focused onto a field of the beads through the fluorescence filter cube and 4x objective (Figure 2-4A). After 15 minutes of patterned illumination with high intensity blue light (0.5 W cm^{-2}), red fluorescence emission of the sample was imaged using a uniform field of weak excitation light (0.02 W cm^{-2}) and the filter cube optimized for silicon rhodamine fluorescence. Clear patterns were observed on the beads,

indicating successful 3D microprinting of silicon rhodamine dye on the solid bead surface (Figure 2-4B). The covalent attachment of the dye was further confirmed by washing the beads thoroughly with DMSO and imaging them on an EVOS-*fl* fluorescence microscope through an Invitrogen Cy5-optimized filter cube (Ex: 635/18 Em: 692/40, ThermoFisher #AMEP4956) (Figure 2-4C). Micropatterning experiments with **RhBNN**-PVA films also displayed successful patterning under a 4x objective. Patterned blue light irradiation of the 20 µM **RhBNN**-PVA coated glass slides at 0.5 W cm^{-2} resulted in clear patterning within 10 minutes, which could be observed on the DLP microscope and an EVOS-*fl* microscope using an RFP filter cube (Ex: 542/20 Em: 593/40, ThermoFisher #AMEP4952) (Figure 2-4 D–F).

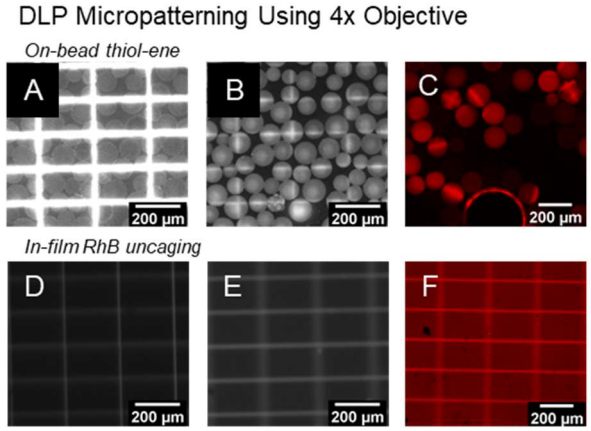

Figure 2-4. DLP micropatterning characterization. For micropatterning with a 4x objective: (A) Fluorescence DLP microscope image of SH-resin in **SiR-sty** during irradiation with 0.5 W cm^{-2} blue light in a grid pattern for 15 min using a 4x objective and (B) after irradiation, imaged under uniform excitation through a 692/40 nm emission filter. (C) EVOS-*fl* microscope image of resin from B after washing with DMSO (Ex: 635/18 nm, em: 692/40 nm). (D) DLP fluorescence images of 20 µM **RhBNN**-PVA film during irradiation with 0.5 W cm^{-2} blue light in a grid pattern for 10 min through a 4x objective and (E) after irradiation, imaged under uniform green light excitation through a 692/40 nm emission filter. (F) EVOS-*fl* fluorescence image of the PVA film from E (Ex: 542/20 nm, em: 593/40 nm). Figures with permission from reference 25.

We then moved to patterning with a 40x objective for further characterization and optimization of the visible light microprinting chemistries. The stronger objective allowed us to focus patterns onto fields measuring 287 µm x 215 µm (2048 x 1536 px, with 1 µm = 7.14 px determined using ThorLabs resolution target slide

#R1L3S10P) that contained single beads, as well as to achieve higher intensities of irradiation light.

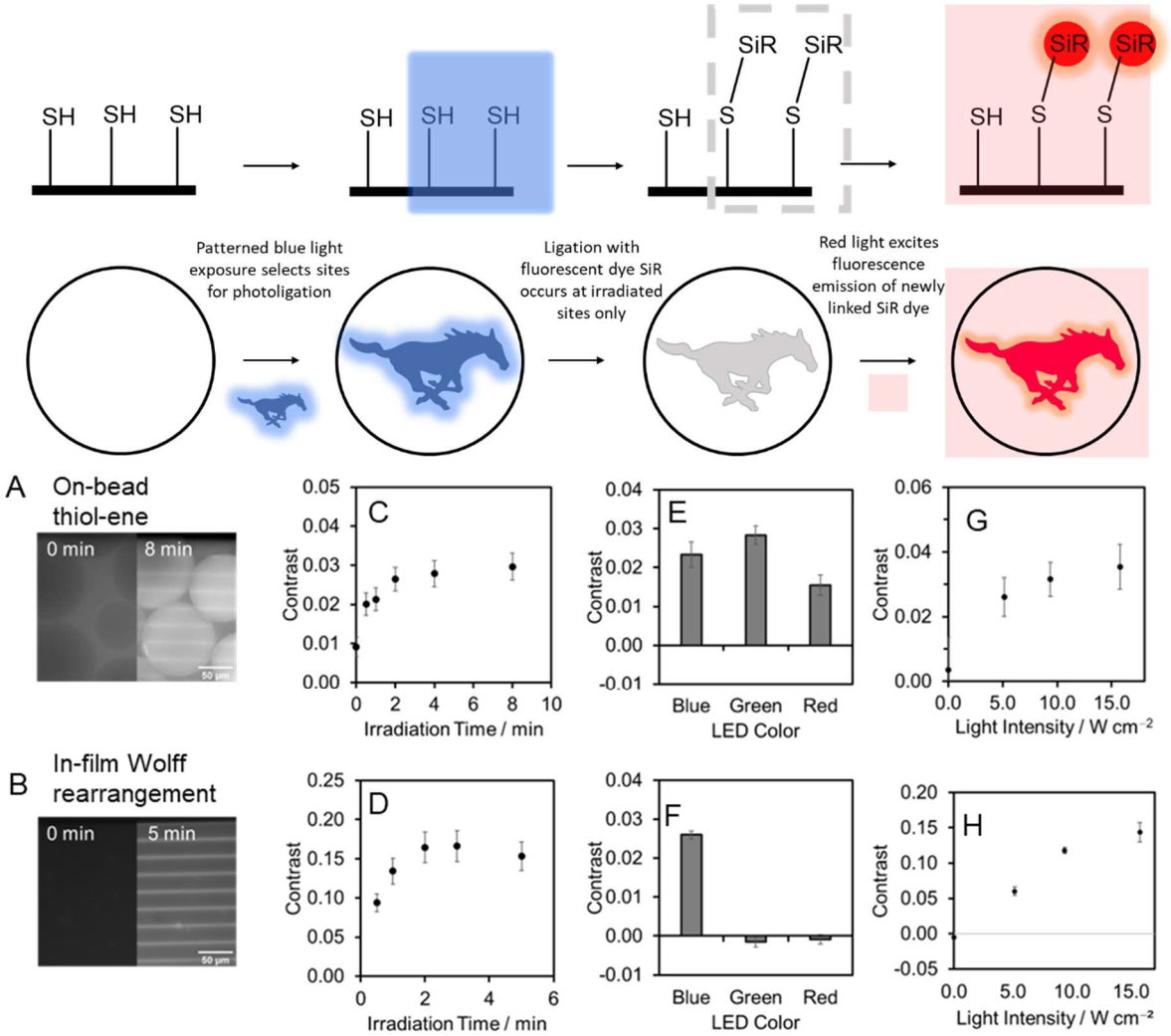

Figure 2-5. DLP micropatterning with a 40x objective. Top: design schematic for single bead thiol-ene patterning. (A) DLP microscope images of thiol-resin beads in 3 mM SiR-sty and eosin y solution before and after 8 min of horizontal lines patterned blue light irradiation at 17.9 W cm^{-2} imaged using uniform excitation and 692/40 nm emission filter. (B) DLP fluorescence images of RhBNN-PVA film-cast glass slides before and after 5 min of horizontal lines patterned blue light irradiation at 17.9 W cm^{-2} imaged under uniform green light excitation through a 692/40 nm emission filter. (C) Contrast between light and dark areas of patterned beads or (D) films with increasing blue light irradiation time at 17.9 Wcm^{-2}. (E) Patterning contrast with varying LED color for thiol-ene bead micropatterning after 10 min of irradiation or (F) RhBNN-PVA film micropatterning after 2 min of irradiation with 8.5 W cm^{-2} blue, green, or red light. (G) Patterning contrast with varying irradiation light intensity for thiol-ene bead micropatterning and (H) RhBNN-PVA patterning with 8 min of blue light irradiation. Errors for are ± S.E. with n = 9–19 lines across 3–6 independent replicates. Figures with permission from reference 25.

We projected a horizontal lines pattern onto individual SH-resin beads in a solution of **SiR-sty** and eosin y using high intensity blue light (17.9 W cm^{-2}) through the 40x objective. Before irradiation, the beads appeared as featureless circles during fluorescence imaging, but after patterned blue light irradiation, clear horizontal lines were observed under a uniform field of fluorescence excitation, indicating covalent linkage of the **SiR-sty** dye at the targeted sites (Figure 2-5A).

Similarly, clear patterning was observed on the **RhBNN**-PVA coated glass slides when irradiated with blue light in a horizontal lines pattern at this magnification (Figure 2-5B). Notably, in addition to successful patterning in PVA films, the **RhBNN** Wolff rearrangement chemistry also worked for surface functionalization of amine and thiol labelled resin beads, displaying high precision and contrast micropatterning with blue light (Figure 2-17), which we later exploit for orthogonal patterning with thiol-ene and Wolff reaction chemistries in the same system (Figure 2-11N).

Progress of the reactions was assessed by measuring the mean pixel intensities of SH-resin beads or **RhBNN**-PVA films at irradiated and non-irradiated areas as a measure of contrast as it correlated with blue light irradiation times (Figure 2-5C, D). From these experiments, an optimal irradiation time using the 40x objective with high intensity blue light was determined to be 5 minutes for the thiol-ene patterning, and 2 minutes for the rhodamine B uncaging. The contrast achieved with **RhBNN** micropatterning was substantially higher than for the thiol-ene chemistry, which may be due to the high background fluorescence emission of the **SiR-sty** solution in the thiol-ene system. In comparison, **RhBNN** is non-fluorescent prior to reacting with the polymer hydroxyl groups, and thus results in high contrast upon photo-uncaging. Through studies varying irradiation light color, we found that patterning with the **RhBNN** Wolff rearrangement chemistry occurred only under blue light irradiation, while the thiol-ene micropatterning proceeded under

blue, green and red light irradiation (Figure 2-5 E, F). Contrast data showed that blue and green light resulted in more effective thiol-ene ligation than red light did, which matches with the spectral absorbance of eosin y, supporting its role as a photoinitiator in this reaction. Since the patterning using Wolff rearrangement chemistry of RhBNN was found to occur significantly faster than the with thiol-ene reaction and was mediated by blue light activation only, we leveraged the differences between this reaction and the thiol-ene reaction, which was found to be slower, but occurred under red and green light, to achieve both chemistries orthogonally. This is demonstrated later in Figure 2-11N.

We also studied the effect of light intensity on the patterning contrast for on-bead thiol-ene micropatterning and **RhBNN**-PVA film micropatterning and found that increasing LED intensity generally gave higher contrast under controlled conditions, but the contrast approached a plateau at higher intensities (Figure 2-5G, H).

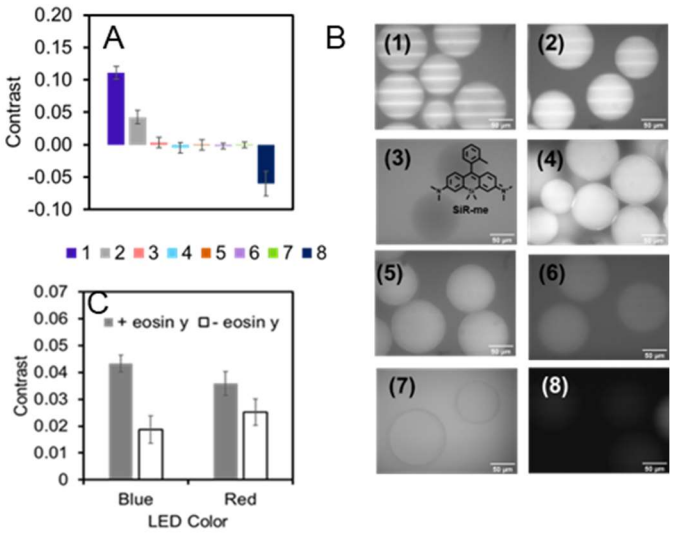

Figure 2-6. Thiol-ene control experiments. (A) Pattern contrast and (B) DLP images achieved with 10 min blue light irradiation under varying conditions: (1) SH-resin, 3 mM SiR-sty, 70 µM eosin y, blue light (2) SH resin, SiR-sty, no eosin y, blue light (3) SH resin, SiR-me, eosin y, blue light (4) S(Mmt) resin, SiR-sty, eosin y, blue light (5) NH_2 resin, SiR-sty, eosin y, blue light (6) SH resin, SiR-sty, eosin y, 0.3 mM TEMPO, blue light (7) SH resin, SiR-sty, eosin y, blue light, brightfield image (8) SH resin, eosin y only. Error bars are ± S.E, n = 11–19 lines across 3 replicates. (C) Pattern contrast achieved with 5 min of blue or red light irradiation at 8.5 W cm^{-2} in a stripes pattern with and without eosin y present. Error bars are ± S.E., n = 9 lines across 3 replicates.

Extensive control experiments allowed us to confirm that the mechanism of the **SiR-sty** patterning was indeed radical thiol-ene photoclick chemistry (Figure 2-6). Absence of thiol functionality from the beads, alkene functionality from the fluorophore, or addition of free-radical inhibitor TEMPO, led to no observed patterning. Interestingly, experiments lacking eosin y did result in some patterning, indicating that the reaction can take place without this photoinitiator, perhaps mediated by the silicon rhodamine itself, [32] though not as efficiently (Figure 2-6 C).

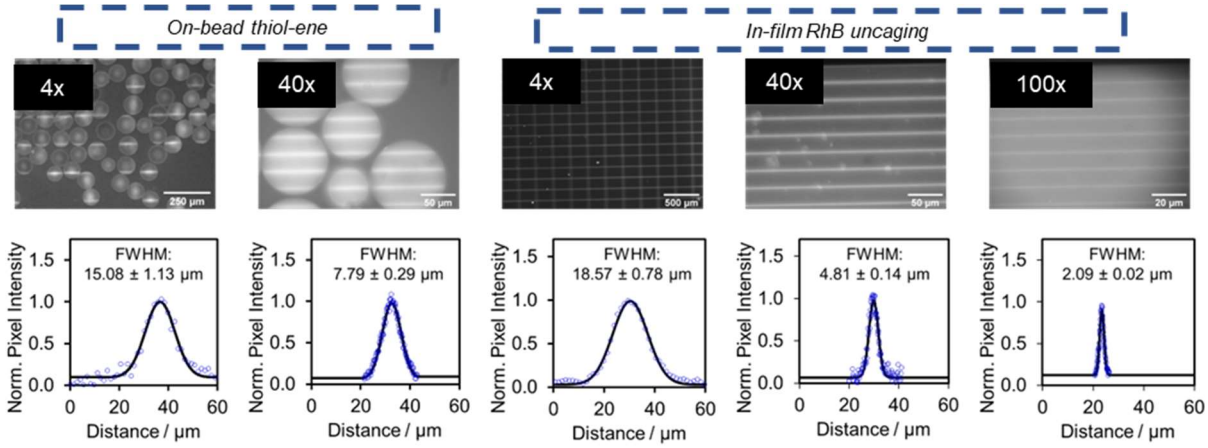

Figure 2-7. Patterning resolution determination. DLP fluorescence images and representative Gaussian fits (black line) to pixel intensity data (blue circles) for on-resin thiol-ene and in-film rhodamine B uncaging in horizontal line or grid pattern using 4x, 40x, and 100x objectives. Errors are ± S.E. with n = 9–19 different patterned lines across 3–6 independent replicates. Figures with permission from reference 25.

We determined the resolution of patterning with different objectives using a similar method as for determining the projection resolution of the DLP microscope. SH-resin beads or **RhBNN**-PVA films were irradiated with blue light in a grid pattern or horizontal line pattern at different magnifications and fluorescence images were then acquired under uniform excitation (Figure 2-7). Intensity profiles across the patterned lines were fit to a Gaussian function and resolution was determined as the FWHM of the Gaussian fit in ImageJ. For the thiol-ene patterning system, on-bead patterning resolution using a 4x objective was found to be 15.08 ± 1.13 µm, and 7.79 ± 0.29 µm using a 40x objective. For the Wolff rearrangement photochemical patterning in **RhBNN**-PVA

films, the resolution achieved with a 4x objective was 18.57 ± 0.78, and 4.81 ± 0.14 μm with a 40x objective. Resolutions achieved on beads using the thiol-ene system at 40x are lower than those on **RhBNN**-PVA films, possibly because of the curvature of the beads and the presence of a light-scattering solution surrounding the beads. Photopatterning was also achieved using a 100x objective on the **RhBNN**-PVA films with a patterning resolution of 2.09 ± 0.02 μm. For the thiol-ene on-bead patterning, although horizontal line, grid, and checkerboard patterns were observed on the beads, due to low contrast between irradiated and non-irradiated areas, pixel intensities did not fit a Gaussian distribution. A conservative estimate of this patterning resolution is approximated as 3.5–5.0 μm by visual inspection of the patterned bead images (Figure 2-16). Combined, these results indicate that precise chemical functionalization and highly resolved micropatterning can be achieved with multicolor visible light using the DLP microscope.

2.2.4. Patterned Labelling of Live Cells

We next leveraged the DLP microscope and **RhBNN** Wolff rearrangement chemistry for visible light driven targeted labelling of live cells with fluorescent molecules. We incubated A549 lung epithelial cells grown in T25 cell culture flasks with 20 μM **RhBNN** in PBS and 2% DMSO for 30 mins to allow for uptake. After rinsing with PBS, the cells were imaged on the DLP microscope and irradiated with patterned blue light at 9.4 W cm^{-2} in a split field pattern that irradiated only the left half of the field. The blue light was removed and fluorescence emission of cells was imaged using a uniform field of green light at timepoints from 0–30 seconds (Figure 2-8 A, B). With increasing irradiation time, cells on the irradiated side of the field displayed increased fluorescence emission whereas cells on the non-irradiated side of the field remained non-fluorescent throughout (Figure 2-8 C), demonstrating that living cells can be targeted and

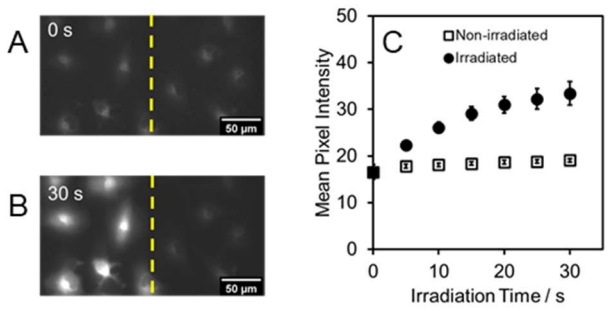

Figure 2-8. DLP Micropatterning of live A549 cells using visible light. (A) DLP fluorescence image of cells incubated for 30 mins with 20 µM **RhBNN** under a 40x objective before blue light irradiation and (B) after 30 s of blue light irradiation at 9.4 W cm^{-2} with a split field pattern which irradiates the left half of the field. (C) Plot of average pixel intensities of all cells in irradiated (left of dotted line in B) and non-irradiated (right of dotted line in B) half of field with increasing irradiation times. Error bars are ± S.D. with n = 3 independent replicates. Figure from reference 25. Experiment conducted by Joshua Plank and Bo Li, SMU.

selectively functionalized with fluorescent dye using visible light mediated chemistry and the DLP microscope.

2.2.5. Microscale Photocuring

We further explored the utility of DLP patterning by employing it for visible-light photocuring of liquid resin to achieve solid microprints, vetting it for 3D printing applications. A three-component polymerization system consisting of dimethylacrylamide (DMA) monomer, trimethylpropane triacrylate (TMPTA) crosslinker, and visible light photoredox catalysts H-Nu 470, Rose Bengal, or zinc tetraphenyl porphyrin (ZnTPP) with donor and acceptor co-initiators was used. [24] Experiments were carried out on glass microscope slides with a 260 µm deep layer of liquid resin (Figure 2-18 A). First, we conducted experiments to characterize the relationship between print width, light intensity, and irradiation time to optimize microscale photocuring conditions. Vertical lines of 74 µm width were printed from a 4:1 mixture of DMA:TMPTA, 2 wt% iodonium acceptor, 0.2 wt% borate donor, and 0.1 wt% Rose Bengal initiator with 1, 2, 3 and 4 seconds of irradiation time using 48 mW cm^{-2}, 83 mW cm^{-2}, and 160 mW cm^{-2} intensities of green light through a 4x objective (Figure 2-9A). After washing with isopropyl alcohol, the solid prints were imaged using reflected light microscopy on the DLP microscope, and the print widths were measured in ImageJ. With increasing irradiation time and

irradiation intensity, the print width was found to increase (Figure 2-9 A). Too low or too high of an irradiation time or irradiation intensity led to prints with widths deviating from the width of the projected pattern. A close match between the print width and the projected pattern was achieved at the optimal set of photocuring conditions, which was found to be 1–2 seconds of irradiation at 160 or 83 mW cm^{-2}. Microprints such as the checkerboard internal test pattern of the LightCrafter

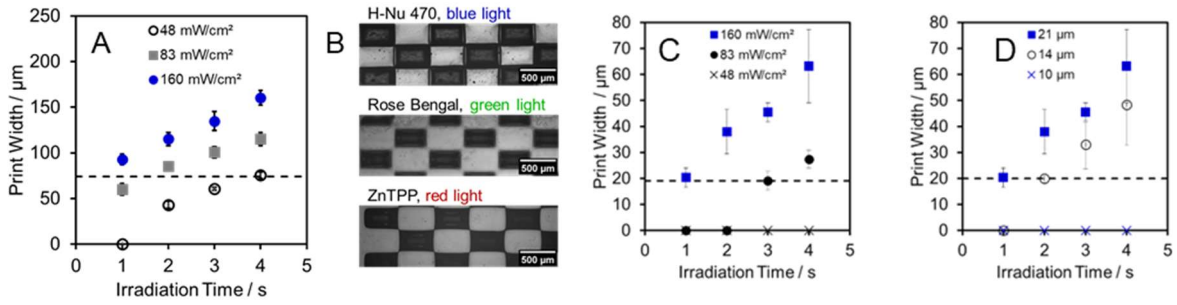

Figure 2-9. Optimization of DLP microscale photocuring and print resolution determination. (A) Plot of cured print width against irradiation time at 48, 83, and 160 mW cm^{-2} green light irradiation intensity. The projected pattern width was 74 µm (dotted line). (B) Light microscopy images of washed prints formed on glass slides after photocuring using 83 mW cm^{-2} blue (H-Nu 470 initiator), green (Rose Bengal initiator), or red (ZnTPP initiator) irradiation light for 2 seconds in a checkerboard pattern. (C) Plot of cured print width against irradiation time at 48, 83, and 160 mW cm^{-2} irradiation intensity. The projected pattern width was 21 µm. Dotted line represents the highest average print resolution achieved. Error bars are ± S.D. with n = 3 independent replicates. (D) Plot of cured print width against irradiation time with varying projected pattern widths at 160 mW cm^{-2} green light intensity. Dotted line represents highest average print resolution achieved. Error bars are ± S.D. with n = 3 independent replicates. Figures from reference 25.

were successfully achieved with blue, green, and red light initiated photocurable resins under these conditions (Figure 2-9B).

The photocuring resolution was characterized by projecting lines of progressively smaller widths onto sample slides containing the green light-initiated resin mixture for durations of 1–4 seconds and at intensities of 48–160 mW cm^{-2}, with pattern widths ranging from 9.8 µm to 300 µm (Figure 2-18B). The prints were washed and imaged, and widths were measured in ImageJ to

determine the smallest print width that could be obtained with the microscale DLP photocuring technique. We found that prints of 40 µm width and above were easily achievable at all three light intensities that were studied. Finer resolution, as low as 20 µm width prints, could be attained using 80 mW cm^{-2} or 163 mW cm^{-2} blue light irradiation for 3 or 1 seconds respectively (Figure 2-9C). Attempts to improve this resolution further by reducing the projected width to 14 µm or 10 µm and irradiating at high intensity resulted in no print development even at long irradiation durations until timepoints where the printed line width surpassed 20 µm (Figure 2-9D). This lack of intermediate print widths between zero and 20 µm suggests a limitation of 20 µm resolution that may perhaps be overcome by use of inert atmosphere or oxygen scavengers.

With demonstrated capability of the DLP microscope to photocure resin on the microscale with high resolution, we next outfitted it for 3D microprinting applications (Figure 2-10A). Addition of a motorized stage for z translation onto the existing xy stage of the DLP microscope evolved an inverted 3D printing setup with which 3D prints such as pyramids of 1.2 mm height and 100 µm resolution in the z axis were generated (Figure 2-10B).

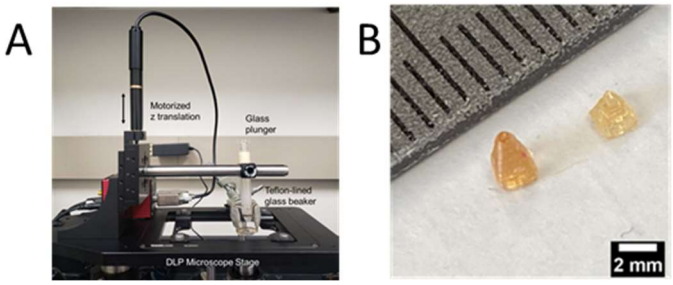

Figure 2-10. (A) Photograph of 3D printing set up affixed onto DLP microscope stage. (B) Photograph of 3D printed pyramids printed using the DLP microscope and blue-light-initiated polymer resin. Patterned light at 140 mW cm^{-2} was projected for 2 s per layer onto the bottom of a fluorinated film-lined beaker containing liquid resin, and prints were built onto a glass print bed affixed to a motorized stage for z-translation. Figure with permission from reference 25. Experiment conducted by Joshua Plank, SMU.

2.2.6. Demonstrations of Microscale Chemistry

Finally, we demonstrate the versatility and ease-of-use of the DLP microscope for microprinting of varied chemical functionalities and constructs (Figure 2-11). The top row of Figure 2-11 shows photocured solid 2D prints prepared from blue light-initiated polymerization of liquid resin on a glass microscope slides using a 4x objective. Highly precise prints such as a maze pattern, a microfluidics pattern, and a printed circuit board (PCB) pattern were achieved by projecting light from a PowerPoint slide in the Parallel RGB mode of the LightCrafter (Figure 2-11A–C). Clipart and icons including the SMU Mustang mascot and science cartoons, as well as text were printed on the microscale with high detail and resolution (Figure 2-11D–F). Well-resolved 3D microprints such as the chess piece and pyramids in Figure 2-11G were achieved via photopolymerization in a bottom-up 3D printing setup. Patterned surface functionalization of solid resin beads with fluorescent silicon rhodamine and rhodamine B dyes using thiol-ene chemistry and diazonium insertion chemistry is shown in the second and third row of Figure 2-11. Structured light was precisely targeted on samples to achieve micropatterning on individual beads using a 40x objective in shapes, text, and patterns such as the yin-yang symbol, a checkerboard pattern, and a star, among others (Figure 2-11H–M). The two chemistries could also be carried out orthogonally on SH-resin beads with prolonged red light irradiation mediating the thiol-ene photoclicking with **SiR-sty**, and quick flashes of patterned blue light uncaging and trapping **RhBNN** on beads. Fluorescence emission from the distinct fluorophores in distinct patterns was individually imaged through the appropriate emission filters (Figure 2-11 N). Live cells were easily labelled with rhodamine B using diazoketone Wolff rearrangement chemistry; highly confluent fields of cells were labelled in a split field pattern and a checkerboard pattern under a 4x objective (Figure 2-11 O,P), and desired individual cells could be targeted for single-cell activation using a 40x objective (Figure 2-11 Q). Detailed photographs which maintained their contrast and resolution over

prolonged periods were printed onto PVA films using photo-uncaging of **RhBNN**. A photograph of the Dallas Hall building was printed on a 2.5 mm x 1.7 mm area of film (1840 x 1268 px, with 1 μm = 0.73 px) using the 4x objective (Figure 2-11 R). Photographs of the DLP microscope and a closeup of a cat were printed with a 40x objective (Figure 2-11 S,T) on areas as small as 170 μm x 210 μm (1246 x 1506 px, 1 μm = 7.14 px). Intricate patterning was also achieved under a 100x objective on the **RhBNN**-PVA films; a QR code measuring 48 μm x 48 μm (850 x 850 px, with 1 μm = 17.8 px), a printed circuit board pattern with feature sizes of 2 microns, resolution charts, as well as legible text, icons, and chemical structures were generated with only seconds of light irradiation and no wash steps required (Figure 2-11 U–Z). These demonstrations showcase the range of applications and chemical versatility of DLP chemical micropatterning.

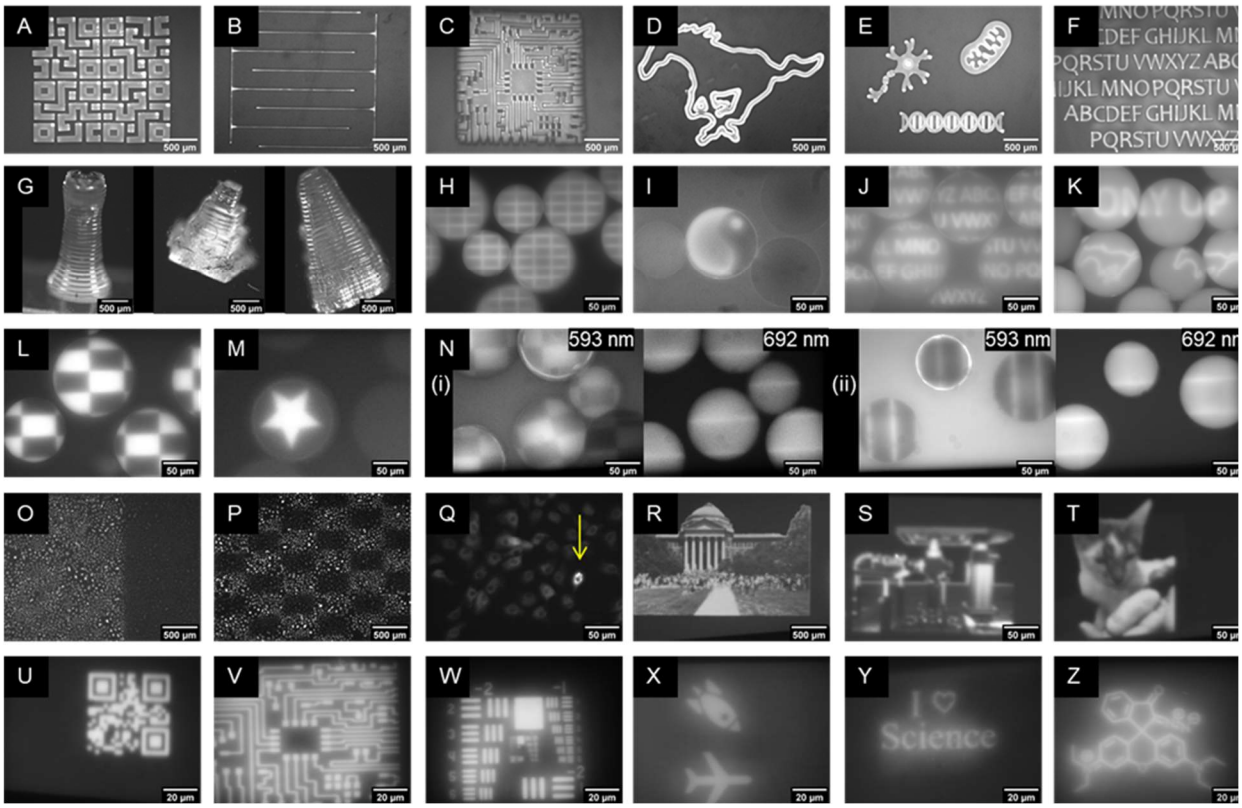

Figure 2-11. Demonstration of DLP microscale photocuring, 3D printing, on-bead micropatterning, live-cell labelling and film patterning. A–F: Fluorescence DLP images of microscale photocured solid resin. (A) Maze pattern, (B) microfluidics pattern, (C) printed circuit board pattern, (D) SMU mustang mascot, (E) neuron, mitochondria, and DNA clipart, and (F) alphabet text. (G) Fluorescence images of DLP 3D microprinted rook and pyramids. H–K: Thiol-ene patterning of SiR-Sty on SH-resin beads in (H) grid pattern, (I) yin-yang pattern, (J) alphabet text, and (K) SMU mustang mascot and "PONY UP" slogan. L–M: Rhodamine B modification of NH2-resin beads in (L) checkerboard pattern and (M) star pattern. (N) Dual patterning of RhBNN (fluorescence imaged through 593/20 nm filter) and SiR-sty (fluorescence imaged through 692/40 nm filter) on SH-resin beads in (i) checkerboard and horizontal lines pattern, and (ii) vertical lines and horizontal lines pattern. O–Q: Fluorescence images of live A549 cells labelled with rhodamine B in (O) split field pattern, (P) checkerboard pattern, and (O) a desired single cell labelled in a confluent field of cells. R–Z: Fluorescence DLP images of microprinting in RhBNN-PVA films. (R) Dallas Hall building, (S) DLP microscope, (T) pet cat, (U) QR code, (V) printed circuit board pattern, (W) United States Air Force resolution test pattern, (X) rocket and airplane clipart, (Y) text, and (Z) Rhodamine BNN structure. Scale bars correspond to the magnifying objective used for patterning and imaging; scale bar represents 500 µm with 4x objective, 50 µm with 40x objective, and 20 µm with 100x objective. Figures with permission from reference 25.

2.3. Summary and Conclusions

In summary, we present a visible light based chemical micropatterning technique comprising a home-built digital light processing (DLP) fluorescence microscope and photochemical reaction systems. The DLP microscope is capable of spatially structuring blue, green, and red visible light for targeted excitation and photoinitiation of microscale samples via focusing lenses, reaching projection resolutions finer than half a micron. Interchangeable light filters and a CMOS camera enable fluorescence imaging and light microscopy in this modular system. We optimized and leveraged visible-light based thiol-ene photoclicking and diazoketone Wolff rearrangements for real time-observable printing of silicon rhodamine and rhodamine B molecules onto solid resin beads with resolutions better than 10 μm using red, green, and blue light. Microprints approaching 2 μm resolution were achieved through photo-uncaging of **RhBNN** in PVA films with structured blue light without the need for washing steps, providing stunning examples of photograph quality microscopic prints. DLP micropatterning was also employed in targeted fluorescent-labelling of selected single live cells from confluent fields. Resin photocuring ability of the DLP microscope and stereolithography 3D printing applications were also examined, and we showed that solid 2D polymer prints with 20 μm xy resolution, and 3D prints with 100 μm z resolution could be generated without specialty equipment.

Owing to the versatility and ease-of-use of DLP chemical microprinting, we envision a wide range of ground-breaking applications for this technique, spanning across fields such as 3D printing, nanorobotics, and metamaterials. Compatibility with living cells offers a potentially transformative technology to target molecules to specific cells and subcellular structures with a high level of control and throughput. To manifest these possibilities and unlock doors to more emerging areas, we continue to explore advanced optical setups and chemistry that will elevate the

resolution, contrast, throughput, and chemical compatibility of visible light DLP chemical microprinting to new heights.

2.4. Experimental Methods

2.4.1. General Methods and Materials

^{1}H NMR and ^{13}C NMR for characterization of compounds and monitoring reactions were acquired on a JEOL 500 MHz spectrometer in the Department of Chemistry at Southern Methodist University in $CDCl_3$ or DMSO-d6 (Cambridge Isotope Laboratories, Cambridge, MA). Absorbance spectra were collected using either a DU 800 or a HORIBA QM-8075-11 spectrophotometer. Fluorescence spectra were acquired using either a Hitachi F-7000 fluorescence spectrophotometer or a HORIBA QM-8075-11 spectrophotometer. H-Nu 470 and 2-(butyryloxy)-*N*,*N*,*N*-trimethylethan-1-aminium butyltriphenylborate, (Borate V) were purchased from Spectra Group Limited. All other reagents were purchased through Sigma-Aldrich (St. Louis, MO), Alfa Aesar (Ward Hill, MA), ThermoFisher Scientific (Waltham, MA), or Tokyo Chemical Industry (Tokyo Japan). High resolution mass spectroscopy was performed on a Shimadzu IT-TOF (ESI source) at the Shimadzu Center for Advanced Analytical Chemistry at the University of Texas, Arlington.

2.4.2. DLP Microscope

- <u>Microscope Parts</u>

Table 2-1. List of microscope parts.

Part Description	Manufacturer	Part #
DLP LightCrafter 4500	Texas Instruments	DLPLCR4500EVM
Lever-Actuated Iris Diaphragm (Ø1 – Ø25 mm)	ThorLabs	SM1D25
Ø1" Mounted Achromatic Doublet Lens, f= 100 mm, ARC: 400-1100 nm	ThorLabs	AC254-100-AB-ML
Zoom Housing for Ø1" Optics, 4.1 mm Travel	ThorLabs	SM1ZM

Kinematic 30 mm Cage Cube Insert for Fluorescence Filter Sets	ThorLabs	DFM1
Ø25.0 mm Premium Shortpass Filter, Cut-Off Wavelength: 650 nm	ThorLabs	FESH0650
660 nm edge BrightLine® epi-fluorescence dichroic beamsplitter	Semrock	FF660-Di02-25x36
692/40 nm BrightLine® single-band bandpass filter	Semrock	FF01-692/40-25
tdTomato Excitation (531/20 nm), Emission (531/20 nm), and Dichroic (562 nm) Filter set	ThorLabs	MDF-TOM
Ø1" 90:10 (R:T) UVFS Plate Beamsplitter, Coating: 400–700 nm	ThorLabs	BSX10
Rigid Stand with Large Insert Holder, Adj. Height: 198.1 –309.3 mm	ThorLabs	MP150-MLSH
Slide/Petri Dish Holder for Inverted Microscopes	ThorLabs	MLS203P2
Rigid Stand Adapter Plate, 1/4"-20 Taps	ThorLabs	MPA1
Self-Contained XY 25 mm Translation Stage, 1/4"-20 Taps	ThorLabs	LX20
Ø1" Mounted Achromatic Doublet Lens, f= 100 mm, ARC: 400-700 nm	ThorLabs	AC254-100-A-ML
SM1 Lens Tube, 2.50" Thread Depth	ThorLabs	SM1L25
SM1 Lens Tube Spacer, 1" Long	ThorLabs	SM1S10
FLIR/Point Grey Chameleon®3 Monochrome Camera	Teledyne FLIR	CM3-U3-31S4M-CS
Olympus PLN 4X Objective	Olympus	1-U2B222
Optika M-773 40x/0.60 IOS LWD W-PLAN Objective	Optika	OPM-773
Optika Objective M-1064, IOS W-PLAN F 100x/1.30 (oil)	Optika	OPM-1064
****3D Printing parts****		
12 mm (0.47") One-Axis Motorized Translation Stage, 1/4"-20 Taps	ThorLabs	MT1-Z8
K-Cube Brushed DC Servo Motor Controller (Power Supply Not Included)	ThorLabs	KDC101
15 V, 2.4 A Power Supply Unit with 3.5 mm Jack Connector for One K- or T-Cube	Thorlabs	KPS101
Right-Angle Bracket for MT Series Translation Stages	ThorLabs	MT402
Right-Angle Clamp for Ø1/2" Posts, 3/16" Hex	ThorLabs	RA90

Red, Green, and Blue LEDs are included in the projection engine of the LightCrafter: Green #CGQ9WP, Red #LEAQ9WP, Blue #LEBQ9WP (OSRAM, Germany).

- Projection Resolution

For projection resolution measurements, the DLP microscope was fitted with a filter cube containing a 90:10 beamsplitter and 4x objective for reflected light imaging. A resolution target slide (Thorlabs, #R1L3S10P) was placed on the stage and diagonal lines were focused onto the target slide using red light. Images were collected and analyzed in ImageJ. A line selection was drawn across a single projected diagonal line and the intensity profile of pixels along the selection was generated. The intensity data was fit to a Gaussian distribution and FWHM was determined as FWHM = $2\sqrt{2ln2}\sigma$ using the standard deviation from the Gaussian distribution fit. The process

was repeated for determination of projection resolutions with 40x and 100x objectives. Immersion oil was used between the 100x objective and the target slide, and the target slide was placed with the patterned side facing down (facing the objective) due to the short focal length of the higher magnification lens.

- Projection Contrast

Contrast was determined by projecting a checkerboard pattern onto the target slide through a 90:10 beamsplitter as above using red light through a 4x objective (Figure S1B). Contrast between the light and dark squares of the checkerboard was determined by getting a mean pixel intensity in each region and using the formula for contrast: $\frac{(Light-Dar\ )}{(Light+Dark)}$. The procedure was repeated with the 40x objective and 100x objective for contrast under these objectives.

- Magnification Scale

The scale for imaging with the 4x, 40x, and 100x objectives was determined using a ThorLabs resolution target slide. Lines on the target slide with known widths in micrometers were imaged under each objective through the 90:10 beamsplitter, and the width of the lines in pixels was then measured in ImageJ to determine the scale for each objective.

4x objective: 1 μm = 0.73 px
40x objective: 1 μm = 7.14 px
100x objective: 1 μm = 17.8 px

- Power Density

The power densities of the DLP microscope irradiation were measured at different LED current settings using a Thorlabs Digital light meter and photodiode sensor (ThorLabs, #S120VC, #PM100D). A solid field of light was projected from the LightCrafter through a 4x objective onto

a resolution target slide to correctly focus the objective. Then the slide was replaced with the Si photodiode power sensor. The LED current and LED color was varied using the DLP LightCrafter graphical user interface (GUI) and the total wattage readings were recorded at each setting. The GUI current settings were converted to current in Amperes using the provided conversions in the LightCrafter specifications.[9] Wavelength settings for the light meter were set to 450 nm for the blue LED measurements, 530 nm for the green LED measurements, and 630 nm for the red LED measurements. Power density was calculated as the Watts per cm^2, with the illuminated area measured as 1.22 x 10^{-1} cm^2 under the 4x objective. A similar procedure was used to measure the power density using the 40x objective. The illuminated area was measured to be 1.22 x 10^{-3} cm^2 with this objective. The measurements were collected in triplicate and averaged. Power densities with the 100x objective were not measured due to the photodiode being incompatible with the short focal length of the objective; LED current values in Amperes and GUI projector settings are provided instead of power densities in experimental methods for these experiments.

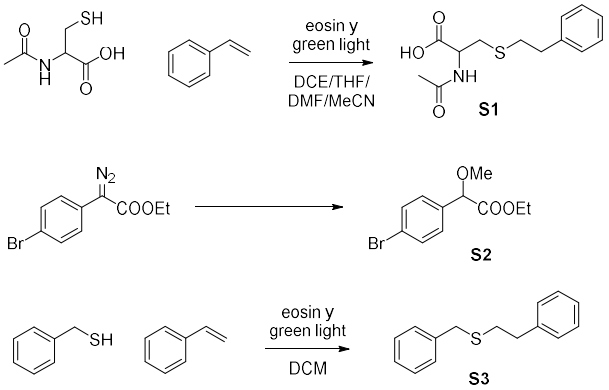

Scheme 2-2. Model thiol-ene and Wolff rearrangement reactions

2.4.3. Thiol-ene and Diazonium Photolysis Model Reactions

- Thiol-ene studies

N-acetyl-S-phenethylcysteine (S1). Eosin y (0.016 g, 0.0025 mmol, 0.025 equiv) and N-acetyl L-cysteine (0.212 g, 1.3 mmol, 1.3 equiv) were dissolved in dry THF (4 mL) in a round bottom flask, to which styrene (0.115 mL, 1.0 mmol, 1 equiv) was then added. The flask was illuminated

with green light from a 100W lamp, and the reaction was allowed to stir for 20 h at rt. A mass spectrum peak at 268 m/z was observed. The THF was rotavapped off, and the product was isolated via column chromatography with 20:1 DCM:MeOH to afford the product as an orange solid (0.224 g, 83%). The reaction was repeated in different solvents (dry MeCN, dry DMF, dry THF, and DCE) and crude proton NMR were obtained in $CDCl_3$ to assess conversion.

For **NMR kinetics of S1 formation**, styrene (11.0 μL, 0.096 mmol, 1.0 equiv), *N*-acetyl-L-cysteine (18.9 mg, 0.12 mmol, 1.3 equiv), and eosin y (1.7 mg, 0.026 mmol, 0.03 equiv) were combined with 0.6 mL DMSO-*d6* and transferred to an NMR tube and an ^{1}H NMR spectrum was acquired for 0 hours of irradiation time point. The NMR tube was then irradiated using a 100 W blue LED (Westinghouse, PA) from a distance of 14 cm. The power density at this distance was measured to be 0.02 W cm^{-2}. ^{1}H NMR spectra were acquired after 0.5 h, 1 h, 2 h, 3 h, 5 h, 24 h, and 45 h of irradiation. Combined aromatic peaks (δ 7.46 – 7.11) were calibrated to 5 units and the integrals of the CH_2 peak of *N*-acetyl-L-cysteine (δ 2.84 – 2.78, black dotted trace) and sulfide **S1** (δ 2.92 – 2.85, red dotted trace) were plotted against irradiation time.

Benzyl(phenethyl)sulfane (S3).[33] Eosin y (0.0162 g, 0.025 mmol, 0.025 equiv) was added to a 2-neck flask, which was then flushed with nitrogen. DCM (4 mL) was added to the flask, followed by styrene (0.115 mL, 1.00 mmol, 1 equiv) and benzyl mercaptan (0.352 mL, 3.00 mmol, 3 equiv). The reaction flask was illuminated with green light from a 100W lamp, and stirred at rt for 24 h, at which point TLC indicated no more styrene starting material and mass spectrum showed product peak at 267 ($M+K^+$). The DCM was rotavapped off, and the proton NMR spectrum of the crude showed almost complete conversion of the styrene to the sulfide product **S3**.

- <u>Diazonium Photolysis UV/Vis Studies</u>

Compound **S2** was prepared via a previously established method using tosyl azide.[34] A 2 mM solution of **S2** was prepared in methanol in a quartz cuvette, which was then irradiated with blue light using a 100 W blue LED (Westinghouse, PA) from a distance of 14 cm. The power density at this distance was measured to be 0.02 W cm^{-2}. Absorbance spectra were collected from 300–600 nm after 0, 1, 6, 10, 15, 30, 60, 90, and 120 min of irradiation time (3 nm excitation slit, 1 nm emission slit, 1 nm step sizes, 0.01 s nm^{-1} scan rate). Peak absorbance was observed at 425 nm and decreased over time with photolysis. The experiment was repeated three times, with reaction progress monitored by absorbance at 425 nm.

2.4.4. Synthesis and Characterization of Dyes

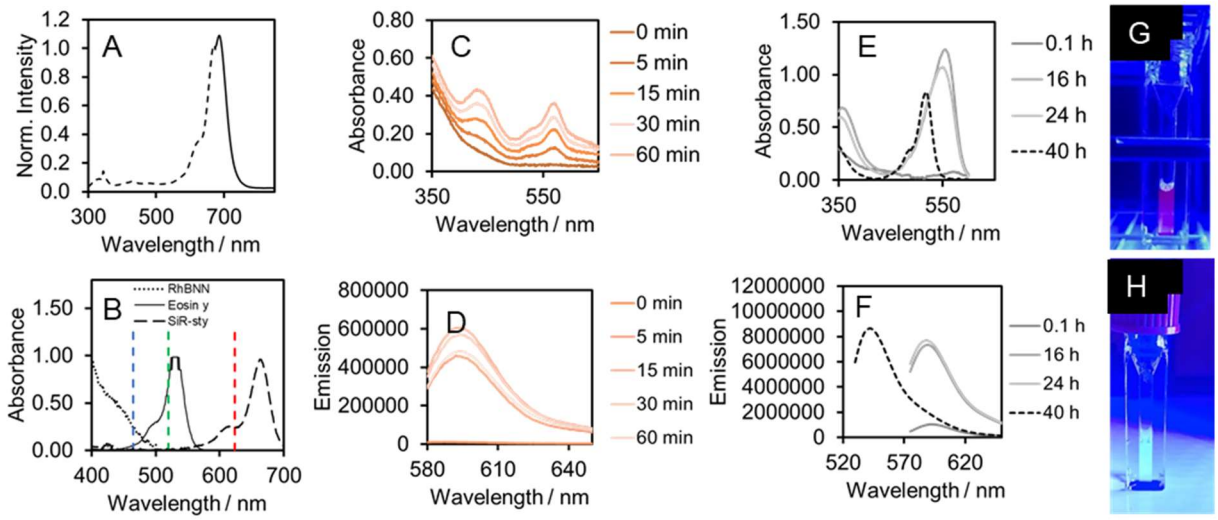

Figure 2-12. (A) Fluorescence excitation and emission profile of **SiR-sty** in DMSO. λ_{em} = 685 nm, λ_{ex} = 665 nm. (B) Normalized absorbance spectra of **RhBNN** (400–500 nm), eosin y (400–700 nm), and **SiR-sty** (400–700 nm) in DMSO with vertical lines indicating peak emission wavelengths of the blue (465 nm), green (520 nm), and red (624 nm) LightCrafter LEDs. (C) Absorbance and (D) fluorescence emission spectra of 0.1 mM **RhBNN** after irradiation with 0.05 W cm^{-2} blue light for 0–60 min in DMSO. (E) Absorbance and (F) fluorescence emission traces of 0.1 mM **RhBNN** after prolonged irradiation with 0.05 W cm^{-2} blue light for 0–40 hours. Photobluing was observed between 24 h and 40 h of irradiation. (G) Photograph of 0.1 mM **RhBNN** in DMSO after 24 hours of blue light irradiation and (H) after 40 hours of blue light irradiation.

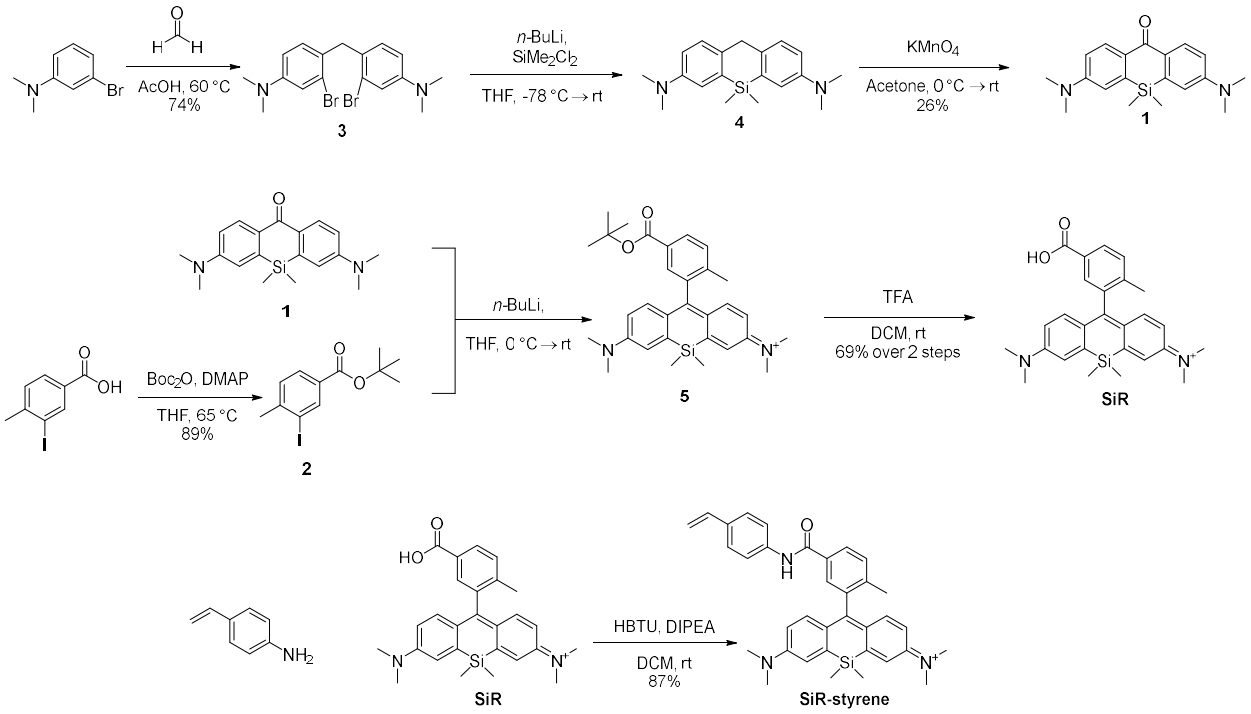

Scheme 2-3. Synthesis of fluorescent dyes **SiR and SiR-styrene**

4,4'-methylenebis(3-bromo-N,N-dimethylaniline) (3). 3-Bromo-N,N-dimethylaniline (2.10 mL, 14.7 mmol, 2 equiv) was combined with 3 mL of 37% formaldehyde and dissolved in 24 mL acetic acid. The reaction was heated to 60 °C and stirred for 1.5 h, after which TLC showed that the starting material was used up. The volatiles were rotavapped off and Saturated $NaHCO_3$ was added carefully to the reaction until pH = 8. A white precipitate formed, which was extracted with EtOAc several times. The combined organic layers were washed with H_2O and brine, dried over Na_2SO_4 and concentrated to obtain the crude product as a pink solid, which was then purified using column chromatography with 20:1 hexanes:EtOAc as the solvent system. The off-white solid can be further recrystallized using hot hexanes (2.27 g, 74%). ^{1}H NMR (500 MHz, $CDCl_3$): δ 6.96 (d, J = 2.9 Hz, 2H), 6.87 (d, J = 8.6, 2H), 6.59 (dd, J = 2.9, 8.6 Hz, 2H), 4.02 (s, 2H), 2.92 (s, 12H); ^{13}C NMR (125 MHz, $CDCl_3$) δ 150.14, 130.89, 127.17, 125.73, 116.35, 111.97, 40.65, 40.00.

N3,N3,N7,N7,5,5-hexamethyl-5,10-dihydrodibenzo[b,e]siline-3,7-diamine (4). Compound **3** (1.97 g, 4.78 mmol, 1 equiv) was added into an oven-dried 3-neck flask fitted with an additional funnel and flushed with N_2. Anhydrous THF (30 mL) was added to dissolve the starting material. The reaction was cooled to –78 °C, and 1.6M *n*-BuLi in hexanes (8.00 mL, 12.8 mmol, 2.7 equiv) was added to the flask dropwise over 30 mins via addition funnel while stirring. The reaction changed from colorless to yellow. The reaction was allowed to stir at –78 °C for an additional 20 mins, at which point, the TLC indicated no more staring material present and the appearance of a new spot that turned blue on exposure to air. Dichlorodimethylsilane (0.80 mL, 6.63 mmol, 1.4 equiv) was then added to the flask dropwise. The reaction was allowed to stir for 28 hours, with the temperature rising from –78 °C to rt. The reaction was then quenched with 8 mL of 1M HCl to give a blue solution and was then basified to pH 8 with sat. $NaHCO_3$. The whole was extracted with DCM thrice, and the combined organic layers were concentrated to obtain a gray oil, which was used crude immediately for the next step.

3,7-bis(dimethylamino)-5,5-dimethyldibenzo[b,e]silin-10(5H)-one (1). Crude compound **4** was dissolved in 70 mL acetone and cooled to 0 °C. $KMnO_4$ (2.30 g, 14.6 mmol, 3 equiv) was added portionwise every 15 mins over the next 2 hours, and then stirred at rt for 17 hours, while monitoring disappearance of starting material via TLC. The product appeared as a yellow fluorescent spot on TLC. The reaction was filtered over Celite to afford a clear green solution, which was concentrated to obtain the crude product as a green solid. Purification via column chromatography with 5:1:1 hexanes: EtOAc: $CHCl_3$ solvent system and then recrystallization with hot 5:2:1 hexanes: EtOAc: $CHCl_3$ solvent afforded the product as yellow crystals (399 mg, 26%). ^{1}H NMR (500 MHz, $CDCl_3$): δ 8.40 (d, J = 9.2 Hz, 2H), 6.83 (dd, J = 2.9, 9.2 Hz, 2H), 6.79 (d,

J = 2.9 Hz, 2H), 3.09 (s, 12H), 0.47 (s, 6H); ^{13}C NMR (125 MHz, $CDCl_3$) δ 185.36, 151.25, 140.57, 131.70, 129.72, 114.32, 113.22, 40.13, –0.89.

tert-butyl 3-iodo-4-methylbenzoate (2). 3-Iodo-4-methylbenzoic acid (2.00 g, 7.63 mmol, 1 equiv), di-*tert*-butyl dicarbonate (4.10 g, 19.0 mmol, 2.5 equiv), and DMAP (0.19 g, 1.53 mmol, 0.2 equiv) were combined in a flask and dissolved in 20 mL anhydrous THF. The reaction was heated to 60 °C and stirred under reflux for 20 hours. After cooling the reaction to rt, the THF was rotavaped off and the residue was dissolved in Et_2O, which was then washed with sat. aq. $NaHCO_3$ (x3), H_2O, and brine. The organic layer was dried over Na_2SO_4 and concentrated to a golden oil. Purification via column chromatography with 9:1 hexanes:EtOAc yielded the product as a golden oil (2.17 g, 89%). ^{1}H NMR (500 MHz, $CDCl_3$): δ 8.36 (d, J = 1.7 Hz, 1H), 7.81 (dd, J = 1.7, 8.0 Hz, 1H), 7.22 (d, J = 8.0 Hz, 1H), 2.42 (s, 3H), 1.55 (s, 9H); ^{13}C NMR (125 MHz, $CDCl_3$): δ 164.23, 146.18, 139.90, 131.25, 129.40, 129.23, 100.51, 81.41, 81.02, 28.40, 28.24, 27.97.

N-(10-(5-carboxy-2-methylphenyl)-7-(dimethylamino)-5,5-dimethyldibenzo[b,e]silin-3(5H)-ylidene)-N-methylmethanaminium (SiR). [29] Compound **2** (1.57 g, 4.93 mmol, 4 equiv) and silicon anthrone **1** (0.400 g, 1.23 mmol, 1 equiv) were added to an oven dried flask, which was evacuated and flushed with N_2 (x3). Dry THF (25 mL) was added and the reaction was stirred until starting materials dissolved. The reaction was then cooled to 0 °C, and 1.5M *n*-BuLi in hexanes (3.5 mL, 5.25 mmol, 4.2 equiv) was added dropwise. The reaction was stirred for an additional 3 hours at rt. 1M HCl was added to quench the reaction, resulting is an intense blue solution of pH = 1. Saturated $NaHCO_3$ was added to neutralize the reaction, which was then extracted with DCM several times. The blue organic layer was washed with brine and dried over Na_2SO_4 and concentrated to a blue solid. This crude *t*-butyl ester product **5** was dissolved in DCM (15 mL) and trifluoroacetic acid (3 mL) was added. The reaction was stirred at rt for 3.5 h, while monitoring

product formation via mass spectroscopy. The volatiles were then evaporated under reduced pressure. The reaction was purified using column chromatography with 10% MeOH in DCM to obtain **SiR** as a blue solid (0.377 g, 69%). ^{1}H NMR (500 MHz, CD_3OD): δ 8.10 (dd, J = 2.3, 8.0 Hz, 1H), 7.72 (d, J = 1.7 Hz, 1H), 7.53 (d, J = 8.0 Hz, 1H), 7.37 (d, J = 2.3 Hz, 2H), 7.02 (d, J = 9.7 Hz, 2H), 6.77 (dd, J = 2.9, 9.7 Hz, 2H), 3.34 (s, 12H), 2.10 (s, 3H), 0.62 (s, 3H), 0.60 (s, 3H); ^{13}C NMR (125 MHz, CD_3OD): δ 169.05, 168.86, 155.78, 149.51, 142.60, 141.93, 140.34, 131.72, 131.23, 131.14, 129.78, 128.28, 122.35, 115.41, 40.94, 19.65, –1.10, –1.31.

N-(7-(dimethylamino)-5,5-dimethyl-10-(2-methyl-5-((4-vinylphenyl)carbamoyl) phenyl)dibenzo[b,e]silin-3(5H)-ylidene)-N-methylmethanaminium (**SiR-sty**). In a round-bottom flask, silicon rhodamine (**SiR**) (0.020 g, 0.045 mmol, 1 equiv) was dissolved in 2 mL DCM. DIPEA (0.02 mL, 0.14 mmol, 3.0 equiv) was added, followed by HBTU (0.020 g, 0.053 mmol, 1.2 equiv). The reaction was stirred for 10 min at rt, after which 4-vinylaniline (0.01 mL, 0.085 mmol, 2.0 equiv) was added. The reaction was tightly capped and allowed to stir at rt overnight. After 18 hours, the reaction was washed with H_2O and brine, dried over Na_2SO_4, and concentrated to obtain the crude product, which was purified via column chromatography, first using DCM as the eluent followed by 1% methanol in DCM. The product was obtained as a blue solid (21 mg, 87%). ^{1}H NMR (500 MHz, $CDCl_3$): δ 8.69 (s, 1H), 7.89 (dd, J = 2.3, 8.0 Hz, 1H), 7.62 (d, J = 8.6 Hz, 2H), 7.56 (d, J = 1.7 Hz 1H), 7.37 (d, J = 8.0 Hz, 1H), 7.26 (d, J = 8.6 Hz, 2H), 7.24 (s, 1H) 7.08 (d, J = 2.9 Hz, 2H), 6.95 (d, J = 9.7 Hz, 1H), 6.58 (m, J = 7.2 Hz, 1H), 6.49 (d, J = 9.8 Hz, 1H), 5.59 (d, J = 18.3 Hz, 1H), 5.11 (d, J = 11.5 Hz, 1H), 3.26 (s, 12H), 2.77 (s, 3H), 0.57 (s, 3H), 0.52 (s, 3H); ^{13}C NMR (125 MHz, $CDCl_3$): δ 168.24, 165.43, 154.02, 148.30, 141.26, 139.56, 138.68, 137.88, 136.17, 132.57, 132.38 130.73, 127.68, 127.26, 126.55, 120.65, 120.28, 114.09, 112.77, 55.47, 40.72, 38.56, 19.37, –0.86, –1.52. HRMS; calculated for $C_{35}H_{37}N_3OSi$ $[M+H]^+$ 544.2779,

found 544.2773. Fluorescence spectra of SiR-sty in DMSO is included in Figure 2-12A. Absorbance of **SiR-sty** in relation to peak emission wavelengths of the LightCrafter LEDs is shown in Figure 2-12B.

2-diazo-3',6'-bis(diethylamino)spiro[indene-1,9'-xanthen]-3(2H)-one (RhBNN). Rhodamine BNN was prepared using a modified literature procedure.[35] In a round-bottom flask, Rhodamine B (939 mg, 2.0 mmol, 1.0 equiv) was placed under a nitrogen atmosphere and dissolved with 20 mL anhydrous dichloromethane. Oxalyl Chloride (1.0 mL, 12 mmol, 6.0 equiv) was added dropwise at room temperature, and allowed to stir at room temperature for 4 hours. The reaction mixture was added into 10 mL deionized water, then quickly extracted into dichloromethane, dried with anhydrous sodium sulfate, and concentrated in vacuo. The resulting residue was placed into a round-bottom flask under nitrogen atmosphere and dissolved into 20 mL anhydrous dichloromethane. The flask was cooled to 0 °C via an ice bath. (Trimethylsilyl)diazomethane solution in hexanes (2.0 mL of 2 M solution, 4.0 mmol, 2.0 equiv) and triethylamine (0.25 mL) were added. Reaction mixture was allowed to warm to room temperature and stir for 18h. Solvent and excess reagents were removed in vacuo to yield crude product, which was then purified via silica gel column chromatography (100:0 to 90:10 gradient of dichloromethane to isopropyl alcohol). The product was obtained as a brown solid (500 mg, 55%). Absorbance of **RhBNN** after uncaging in relation to peak emission wavelengths of the LightCrafter LEDs is shown in Figure 2-12B. Increase in absorbance and emission of 0.1 mM RhBNN in DMSO upon blue light irradiation over 1 hour at 0.05 W cm^{-2} is shown in Figure 2-12C, D. Change in emission and absorbance of **RhBNN** with prolonged blue light irradiation for 0–40 hours at 0.05 W cm^{-2} in DMSO is presented in Figures 2-12E, F. At 40 hours of irradiation, significant photobluing of the uncaged RhBNN is observed as compared to at 24 h (Figure 2-12G, H).

2.4.5. Thiol-ene Bead Chemistry Methods

- SH-resin Synthesis

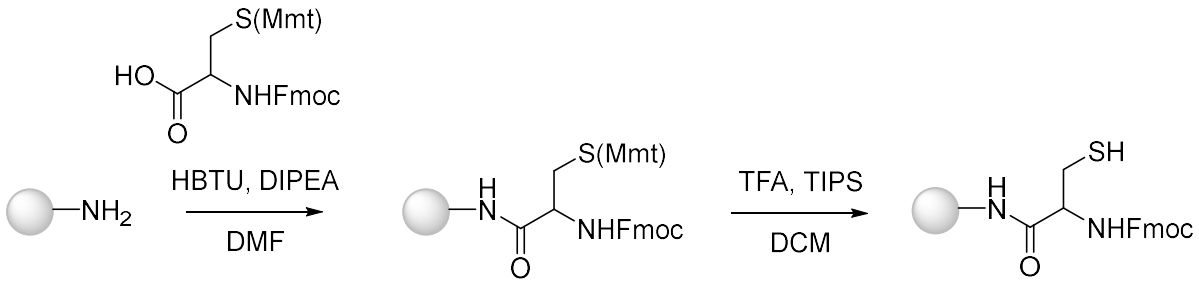

Amine-functionalized NovaSyn®TG amino resin (90 μm) polymer resin beads (Novabiochem #855007, 310 mg, 0.078 mmol, 1.0 equiv) were swollen in DMF for 30 mins in a 10 mL fritted reaction syringe. Separately, a solution of pre-activated carboxylic acid was prepared using Fmoc-cys(Mmt)-OH (143, mg 0.232 mmol, 3.0 equiv), DIPEA (41 μL, 0.231 mmol, 3.0 equiv), and HBTU (87 mg, 0.229 mmol, 3.0 equiv) in 2.5 mL DMF, and was allowed to react for 10 mins. The activated solution was then pulled into the fritted syringe containing swollen resin with additional 2 mL DMF, and then allowed to react overnight without stirring. After 24 h, the resin was washed with DMF (4 mL x 5), and cycles of isopropanol and DCM (4 mL x 3), and lastly DCM (4 mL x 2). The resin was then allowed to dry under a stream of air.

In a 2 mL fritted syringe, the Fmoc-cys(Mmt) functionalized resin (100 mg) was swollen in DCM for 30 mins, and then washed with a cleaving cocktail consisting of DCM, 1–2% trifluoroacetic acid, and 1% triisopropylsilane until the wash solutions no longer turned yellow (5 x 5 min x 1 mL). The Mmt-cleaved resin was then washed with DCM and isopropanol in cycles (5 mL x 3) and allowed to dry under a stream of air after a final wash with DCM.

- On-bead Thiol-ene Sample Preparation

Thiol functionalized resin beads soaked in DMSO were added onto glass microscope slides or #1.5 coverslips. A solution of 3 mM **SiR-sty** and 70 μM eosin y was prepared in DMSO. 20 μL of this solution was added onto the resin and a glass coverslip was placed on top. This process was carried out with room lights turned off. The stock solution of 3 mM **SiR-sty** and 70 μM eosin y was stored in a vial covered with tin foil in a dark cabinet at room temperature and kept well for up to several months. Thiol-functionalized resin was stored in a fritted syringe in a minimal volume of DMSO and kept well for up to several weeks.

- Bulk on-bead thiol-ene

A sample slide with thiol resin and **SiR-sty** stock was prepared as described above and irradiated using a 100 W blue LED (Westinghouse, PA) from a distance of 6 cm for 22 hours (0.04 W cm^{-2}). After 22 h, the resin beads were washed into a beaker using DMSO and transferred into a fritted syringe using a needleless 3 mL syringe. The resin was washed using cycles of iPrOH and DCM (1 mL x 3 x 5 min), after which the beads were dried under a stream of air for 5 mins and then added onto a glass microscope slide for imaging. The beads were imaged on an EVOS Fl fluorescence microscope installed with a Cy5 filter cube (628/40 nm excitation and 685/40 nm emission) with a 20x objective at 1% LED intensity and 15 ms integration time through a neutral density filter to attenuate the fluorescence response. Brightfield images were acquired using the transmitted light mode of the EVOS microscope. A control experiment was similarly carried out but was kept in a dark cabinet for 22h.

- Thiol Quantification with Ellman's Reagent

Calibration curve. Thiol content on resin was determined using a procedure based on a previously reported method.[36] To generate an absorbance versus [SH] calibration curve, an

Ellman's Reagent stock solution (solution A) containing Ellman's Reagent (2.5 mM) and DIPEA (14 mM) was freshly prepared in methanol, and a 0.5 mM stock solution of *N*-acetyl-L-cysteine (solution B) was prepared in methanol. Solution A was then diluted in solution B to yield 1.0 mL solutions of 0 μM, 5 μM, 10 μM, 25 μM, 50 μM, and 100 μM *N*-acetyl-L-cysteine. The solutions were allowed to sit for 1 h, after which absorbance scans were obtained. Absorbances at 412 nm were plotted against *N*-acetyl-L-cysteine concentrations to generate a calibration curve (Figure 2-13A).

Resin thiol content. A sample slide with thiol resin and **SiR-sty** stock was prepared as described above and irradiated using a 100 W blue LED (Westinghouse, PA) from a distance of 6 cm for 2 hours (0.04 W cm^{-2}). The resin was then washed into a beaker using DMSO and transferred into a pre-weighed fritted syringe using a needleless 3 mL syringe. The resin was washed with cycles of iPrOH and DCM (1 mL x 3 x 5 min), after which the beads were dried thoroughly under a stream of air for 15 mins. The syringe was weighed again, and the mass of the resin was recorded. 1 mL of solution A was pulled into the fritted syringe and allowed to react with the resin for 1 hour, after which the absorbance of the solution at 412 nm was collected. The concentration was determined based on the *N*-acetyl-L-cysteine calibration, and thiol loading of the resin was determined using the mass of the resin. A similar procedure was used to determine thiol content of samples without light irradiation and resin for which the thiols were Mmt-protected (Figure 2-13B). Absorbance data for thiol-ene yield determination is provided in Table 2-2 below.

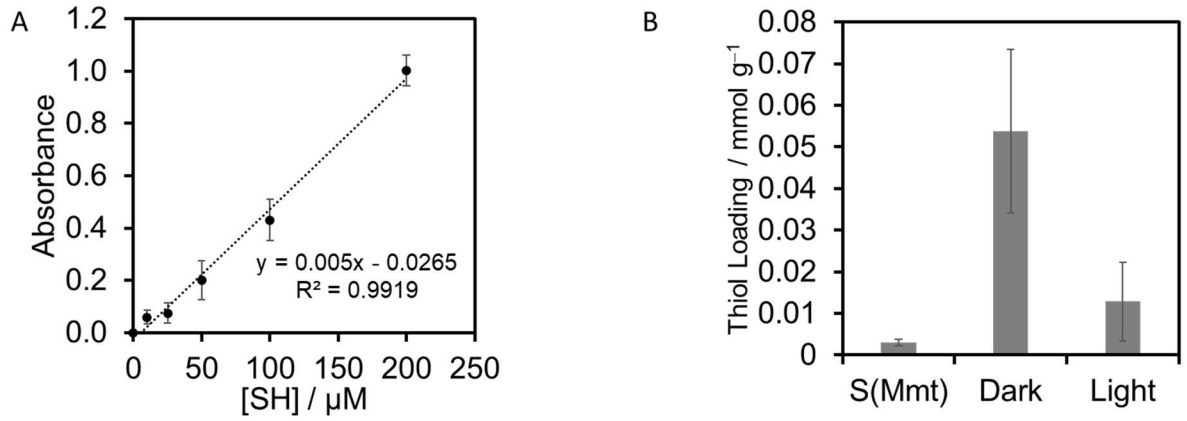

Figure 2-13. (A) Thiol calibration curve for absorbance with Ellman's reagent. (B) Thiol loading determined using Ellman's reagent of Fmoc-cysteine(Mmt)-OH functionalized resin before deprotection of the thiol "S(Mmt)", after deprotection of the thiol using TFA and then reacting in **SiR-sty** and eosin y in DMSO without any light irradiation "dark", and after 20 hours of irradiation of the SH-resin with blue light in a solution of **SiR-sty** and eosin y in DMSO "light".

Table 2-2. Thiol loading of resin with Mmt-protected thiol resin, SH-resin before thiol-ene reaction and SH-resin after thiol-ene reaction.

		Abs	Conc / µM	µmol	mmol	Mass / g	SH loading mmol/g	Conversion / %
Trial 1	0h	1.48E-01	3.49E+01	3.49E-02	3.49E-05	1.10E-03	3.17E-02	
	20h	1.66E-03	5.63E+00	5.63E-03	5.63E-06	3.00E-03	1.88E-03	94.09
	S(Mmt)	7.57E-03	6.81E+00	6.81E-03	6.81E-06	2.80E-03	2.43E-03	
Trial 2	0h	6.30E-01	1.31E+02	1.31E-01	1.31E-04	1.90E-03	6.91E-02	
	20h	2.10E-01	4.74E+01	4.74E-02	4.74E-05	2.50E-03	1.89E-02	72.57
	S(Mmt)	8.29E-03	6.96E+00	6.96E-03	6.96E-06	2.50E-03	2.78E-03	
Trial 3	0h	4.58E-01	9.69E+01	1.94E-01	1.94E-04	3.20E-03	6.05E-02	
	20h	7.98E-02	2.13E+01	2.13E-02	2.13E-05	1.20E-03	1.77E-02	70.74
	S(Mmt)	3.32E-03	5.96E+00	5.96E-03	5.96E-06	1.50E-03	3.98E-03	

- On-bead thiol-ene micropatterning

General methods. For micropatterning experiments, the DLP microscope was fitted with a 650 nm shortpass excitation filter, 660 nm dichroic beamsplitter, 692/40 nm bandpass emission filter, and 40x or 4x objective (Olympus 1-U2B222, Optika M-773). Camera settings were fixed using FlyCapture camera GUI at brightness = 5.859%, exposure = –3.00 EV, sharpness = 1024, gamma = 1.00, shutter = 17.887 ms, gain = 37.395 dB, and frame rate = 55.516 fps. All images

were captured in bursts of 20–25 frames that were averaged in ImageJ before analysis. To image the beads, weak blue light (measured as 0.02 W cm^{-2} under the 4x objective, and 0.20 W cm^{-2} with 40x objective) in the pre-set "solid field" internal test pattern was used and emission was observed through a 692/40 nm filter for red fluorescence. To pattern the beads, patterns from pre-set LightCrafter internal test patterns or PowerPoint slides in parallel RGB mode were used. Sample slides with thiol resin and **SiR-sty** stock were prepared as described above and experiments were carried out in a dark room.

Patterning using a 4x objective. A sample slide was prepared with SH-resin and **SiR-sty** stock as described above. A field of densely packed beads was imaged on the DLP microscope through a 4x objective and irradiated with a grid internal test pattern for 15 mins using high intensity blue light (0.48 W cm^{-2}). The patterned beads were imaged with weak blue LED excitation and then carefully washed by blotting off the solution with a Kimwipe, adding a few drops of DMSO and repeating this procedure five times. The slide containing washed beads in DMSO was then imaged on an EVOS Fl microscope with 628/40 nm excitation and 685/40 nm emission filters and a 20x objective at 1% LED intensity and 15 ms integration time through a neutral density filter.

Patterning using a 40x objective. 1. Irradiation Time Dependence. A sample slide was prepared above and imaged on the DLP microscope through a 40x objective. Beads were irradiated for 0, 1, 2, 4, and 8 min with the horizontal line internal test pattern under a 40x objective using high intensity blue light (17.9 W cm^{-2}). Images were captured at each time point using a uniform field of weak blue excitation (0.20 W cm^{-2}). The average intensity projections of the frames at each time point were analyzed in ImageJ. The mean pixel intensities across areas that were patterned by horizontal lines ("light" areas) and areas that were not patterned under the horizontal

lines ("dark" areas) were measured, and pattern contrast was determined as $\frac{(Light-Dark)}{(Light+Dar\ )}$. Three independent experiments were performed, and n = 12 different light and dark areas were sampled. 2. LED Color Dependence. Studies were carried out similar to the above procedure. Beads were irradiated using blue, green, or red light for 10 min with horizontal lines internal test pattern using a 40x objective with light intensity of 8.5 W cm^{-2}. Images were captured after 10 min of irradiation using weak uniform blue excitation and pattern contrast was determined as above. Three independent experiments were performed, and n = 14–16 different light and dark areas were sampled. 3. Control experiments. Slides were irradiated with a horizontal lines pattern using a 40x objective, with light intensity = 9.38 W cm^{-2} and irradiation time = 10 min under the following reaction conditions. (1) SH-resin, 3 mM **SiR-sty**, 70 μM eosin y, blue light (2) SH-resin, 3 mM **SiR-sty**, no eosin y, blue light (3) SH resin, 3 mM SiR-me, 70 μM eosin y, blue light (4) S(Mmt) resin, 3 mM **SiR-sty**, 70 μM eosin y, blue light (5) NH_2 resin, 3 mM **SiR-sty**, 70 μM eosin y, blue light (6) SH resin, 3 mM **SiR-sty**, 70 μM eosin y, 0.3 mM TEMPO, blue light (7) SH resin, 3 mM **SiR-sty**, 70 μM eosin y, blue light, brightfield image (8) SH resin, 70 μM eosin y only. Contrast was determined as above. **SiR-me** was synthesized from iodobenzene and silicon anthrone **1** using the procedure used for preparing **SiR**. Fluorescence images and contrast data for control experiments are in Figure S6B and C. Experiments were also carried out with 5 minutes of red and blue irradiation (8.5 W cm^{-2}) in a stripes pattern with and without eosin y to investigate the role of **SiR-sty** as a photoinitiator. Under red light irradiation, contrast was achieved with and without eosin y. Better contrast was achieved when eosin y is present. In the absence of eosin y, the reaction does proceed under blue light, but is more efficient under red light, as would be expected if SiR is contributing to initiating the reaction. 4. Irradiation Intensity Dependence. Beads were irradiated using blue light for 8 min with horizontal lines internal test pattern under a 40x objective with

irradiation intensities of 0.00, 5.14, 9.38, and 15.75 W cm^{-2}. Images were captured after 8 mins under weak uniform blue excitation and pattern contrast was determined as above. Three independent experiments were performed, and n = 14–15 different light and dark areas were sampled.

On-bead patterning resolution. Thiol functionalized beads were patterned with horizontal lines for 8–10 mins using a 40x objective with green or blue light (irradiation intensity = 8.50–9.38 W cm^{-2}). After this time, fluorescence images were captured under uniform weak blue light excitation, and the average projection of 25 frames was analysed in ImageJ. The intensity profile of pixels across a patterned line was plotted and a Gaussian fit was generated. Resolution is reported as full width at half maximum (FWHM) of this Gaussian distribution, with FWHM = $2\sqrt{2ln2}\sigma$. Datasets which fit a gaussian model with R^2 greater than 0.80 were used for resolution determination. A similar procedure was used for determining patterning resolution with a 4x objective. A grid pattern was used, irradiation time was 15 min, and irradiation intensity was 0.48 W cm^{-2}. Thiol-ene on-bead patterning resolution using a 4x objective was found to be 15.08 ± 1.13 µm, and 7.79 ± 0.29 µm using a 40x objective. Patterning with a 100x objective was achieved using an Optika M-1064 oil immersion objective. Resolution for 100x objective on-bead patterning was determined by visual inspection of collected images. Selections were created across visibly patterned lines and measured (Figure 2-14).

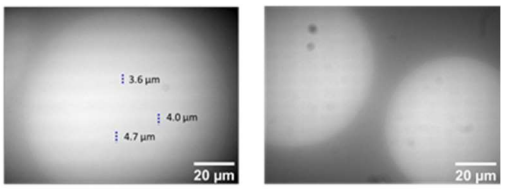

Figure 2-14. Thiol-ene on-bead patterning with a 100x objective in horizontal line and grid patterns. Printing resolution was approximated to be between 3.5 and 5.0 µm.

2.4.6. RhBNN Wolff Rearrangement Chemistry

- RhBNN-PVA film sample preparation

A stock solution of 1 wt% 72,000 MW PV was prepared in deionized water by adding 1.00 g PVA to 70.0 mL H_2O and heating carefully to a boil. After all solids dissolved, an additional 30.0 mL aliquot of water was added and stirred in. This solution was cooled and stored in a tightly capped container to be used over several months. From this PVA solution stock, **RhBNN** doped PVA solutions were produced as needed. In a 2 mL centrifuge tube, a total of 980 μL PVA stock and 20 μL **RhBNN** solution were combined to minimize frothing as follows: 490 μL of PVA stock solution was transferred, followed by 20 μL of 1 mM **RhBNN** in DMSO, and finally another 490 μL of PVA stock. Solution was gently mixed via syringe pumping before storing in a dark box wrapped in aluminum foil for up to 1 week. Films were fabricated via drop casting of 75 μL of doped PVA onto glass microscope slides or #1.5 coverslips and allowed to dry overnight.

- Bulk in-film RhBNN Wolff Rearrangement

A **RhBNN**-PVA sample slide was irradiated using a 100 W blue LED (Westinghouse, PA) from a distance of 6 cm for 21 hours (0.04 W cm^{-2}). The film was then imaged on an EVOS Fl fluorescence microscope installed with an Invitrogen RFP filter cube (542/20 nm excitation and 593/40 nm emission) with a 20x objective at 60% LED intensity and 120 ms integration time. A control experiment was conducted and imaged similarly but was kept in a dark cabinet for 22 h. Locating the edges of the film was accomplished using brightfield or phase contrast microscopy which was possible in the transmitted light mode of the EVOS microscope.

- In-film RhBNN Wolff Rearrangement DLP Micropatterning

General methods. For micropatterning experiments, the DLP microscope was fitted with a 650 nm shortpass excitation filter, 660 nm dichroic beamsplitter, 692/40 nm bandpass emission

filter, and a 4x, 40x, or 100x objective (Olympus 1-U2B222, Optika M-773, Optika M-1064). Camera settings were fixed using FlyCapture camera GUI at brightness = 5.859%, exposure = −3.00 EV, sharpness = 1024, gamma = 1.00, shutter = 17.887 ms, gain = 37.395 dB, and frame rate = 55.516 fps. All images were captured in bursts of 25−50 frames that were averaged in ImageJ before analysis. To image the films, weak green light (measured as 0.083 W cm^{-2} under the 4x objective and 1.132 W cm^{-2} under the 40x objective) in the pre-set "solid field" internal test pattern was used. To pattern the beads, high intensity blue light (measured as 0.48 W cm^{-2} with 4x and 17.9 W cm^{-2} with 40x objective) was used with patterns from pre-set LightCrafter internal test patterns or PowerPoint slides in parallel RGB mode. Sample films were prepared as above.

Micropatterning using a 4x objective. **RhBNN**-PVA sample was prepared on a microscope slide as described above. A field of the film was focused on using a 4x objective and irradiated with a grid internal test pattern for 10 min using high intensity blue light (0.48 W cm^{-2}). The blue light was then removed, and the patterned film was imaged via weak green LED excitation (0.02 W cm^{-2}). Films were additionally imaged on an EVOS Fl microscope with an RFP filter cube (542/20 nm excitation and 593/40 nm emission) and a 4x objective at 60% LED intensity and 250 ms integration time.

Micropatterning using a 40x objective. 1. Kinetics. Films were irradiated for 0 s, 30 s, 60 s, 90 s, 2 min, 3 min, 4 min, and 5 min with horizontal lines internal test pattern under a 40x objective using high intensity blue light (17.93 W cm^{-2}). Images were captured at each time point under weak uniform green excitation (1.13 W cm^{-2}). The average intensity projections of the frames at each time point were generated and analyzed in ImageJ. Mean pixel intensities across areas that were patterned by horizontal lines ("light" areas) and areas that were not patterned under the horizontal lines ("dark" areas) were measured, and pattern contrast was determined as

$\frac{(Light-Dar\ )}{(Light+Dark)}$. Three independent experiments were performed, and n = 9 different light and dark areas were sampled. 2. LED Color Dependence. Studies were carried out similar to the above procedure. Films were irradiated using blue, green, or red light for 2 min with horizontal lines internal test pattern with a 40x objective at 8.0 W cm^{-2}. Images were captured under weak uniform green excitation (2.83 W cm^{-2}) and pattern contrast was determined as above. Three independent experiments were performed, and n = 9 different light and dark areas were sampled. 3. Light intensity dependence. Studies were carried out similar to the above procedure. Films were irradiated using blue light for 5 min with horizontal lines internal test pattern with a 40x objective at intensities of 0.000 W cm^{-2}, 5.14 W cm^{-2}, 9.38 W cm^{-2}, and 15.75 W cm^{-2}. Images were captured under weak uniform green excitation (2.83 W cm^{-2}) and pattern contrast was determined as above. Three independent experiments were performed, and n = 9 different light and dark areas were sampled.

Micropatterning using a 100x objective. **RhBNN**-PVA sample was prepared on a #1.5 coverslip as described above. The film was focused on using the 100x objective under oil immersion and then irradiated with a horizontal lines test pattern for 10s using blue light (GUI current setting = 50, corresponding to LED current = 0.95 A). The patterned film was imaged with uniform green LED excitation (GUI current setting = 10, corresponding to green LED current 0.54 A).

In-film patterning resolution. **RhBNN**-PVA sample was prepared on a #1.5 coverslip as described above. The film was focused on using the 100x objective under oil immersion and then irradiated with a horizontal lines test pattern for 10s using high intensity blue light (GUI current setting = 50, corresponding to LED current = 0.95 A). After this time, fluorescence images were

captured via uniform green excitation (GUI current setting = 10, corresponding to green LED current 0.54 A), and the average projection of 25 frames was analyzed in ImageJ. The intensity profile of pixels across a patterned line was plotted and a Gaussian fit was generated. Resolution is reported as full width at half maximum (FWHM) of this Gaussian distribution, with FWHM = $2\sqrt{2ln2}\sigma$. Datasets which fit a gaussian model with R^2 greater than 0.80 were used for resolution determination. A similar method was used for 4x and 40x objective patterning resolution determination. For the 4x objective, a grid internal test pattern was projected for 10 min using high intensity blue light (0.48 W cm^{-2}) and imaged via green LED excitation (0.02 W cm^{-2}). For the 40x objective, films were irradiated for 60 s with horizontal lines internal test pattern using blue light (17.93 W cm^{-2}) and images were captured under uniform green excitation (1.13 W cm^{-2}). In-film printing resolution was found to be 18.57 ± 0.78 μm with the 4x objective, 4.81 ± 0.14 μm with the 40x objective, and 2.09 ± 0.02 μm with the 100x objective.

*Evaluation of image persistence and diffusion of photoactivated **RhBNN** in PVA films.* Studies were carried out similar to the above procedure. Films were irradiated using blue light for 1 min with grid internal test pattern using a 40x objective at intensity 15.75 W cm^{-2}. A sequence of images was captured under weak uniform green excitation (2.83 W cm^{-2}) every 1 s for 10 s, and then every 10 s for 360 s, turning off the excitation light in between photographs to prevent photobleaching. Three independent experiments were performed, with no significant diffusion observed in any of the experiments. The printed film was left on the microscope stage undisturbed overnight, and an additional image was then acquired after 18 h under weak uniform green excitation (2.83 W cm^{-2}). No significant band widening was observed between the 0 h time point and 18 h time point images, indicating little to no diffusion over the time frame.

- On-bead RhBNN Wolff Rearrangement DLP Micropatterning

RhBNN uncaging and Wolff rearrangement chemistry was also achieved on amine-functionalized resin beads. Similar procedures were used as for doing on-bead thiol-ene chemistry. NovaSyn®TG amino resin (90 μm) polymer resin beads (Novabiochem #855007) were swollen in DMSO for 30 mins in a 10 mL fritted reaction syringe. Beads were added onto microscope slides and submersed in a solution of 1.0 mM **RhBNN** in DMSO. The slide was then irradiated with patterned blue light in horizontal line pattern or checkerboard pattern from the DLP microscope from a 4x or 40x objective (Figure 2-15A, B) Irradiation time dependence and LED color dependence experiments were conducted (Figure 2-15C, D). Resolution of RhBNN Wolff rearrangement patterning on NH2-resin beads was found to be 9.84 ± 1.61 μm using the 40x objective and irradiating with 17.9 W cm^{-2} blue light for 30 s in horizontal lines pattern.

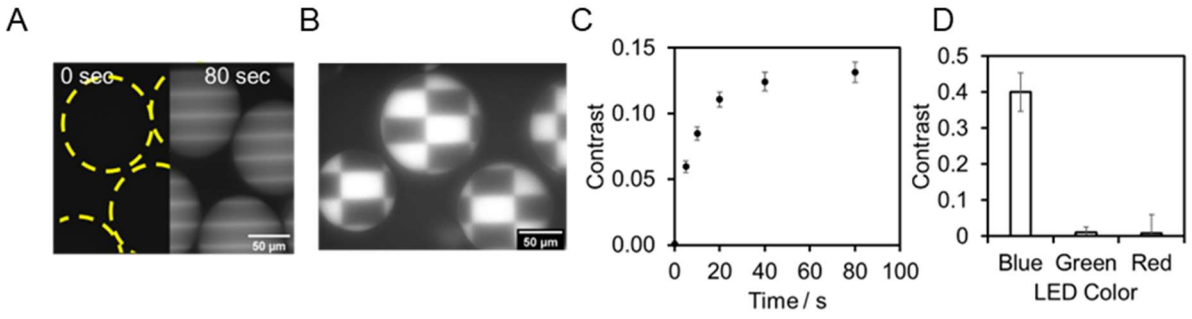

Figure 2-15. (A) NH_2-resin beads in 1 mM **RhBNN** solution in DMSO before and after 80 s of blue light irradiation in horizontal line pattern. (B) NH_2-resin beads in 1 mM **RhBNN** solution in DMSO patterned with checkerboard pattern through a 40x objective for 10 s using 17.9 W cm^{-2} blue light. (C) Contrast dependence on irradiation time for NH_2-resin in 1 mM **RhBNN** irradiated with horizontal lines for 0–100 s using 17.9 W cm^{-2} blue light. (D) Contrast versus LED color for NH_2-resin in 1 mM **RhBNN** irradiated with checkerboard pattern for 30 s using 17.9 W cm^{-2} blue light.

- RhBNN Wolff Rearrangement for Cell Labeling

Preparation of cell samples. Human lung adenocarcinoma epithelial cells (A549) cells were purchased from ATCC (CCL-185) and cultured in Ham's F-12K media supplemented with 10% Fetal Bovine Serum (FBS) and 1% antibiotics (penicillin/streptomycin, 100 mg/mL). Cell lines were cultured and maintained in 175 mL cell culture flasks (Falcon, BD353136) in a humidified incubator at 37 °C with 5% CO2. For each experiment, cells were passaged by seeding in T25 cell culture flasks (Falcon, 29185-298) and covering with 5.0 mL of media. These experimental flasks were allowed to grow for 2 to 3 days, or until they had reached between 70% and 90% confluence. A 1 mM RhBNN stock solution in DMSO was prepared and stored in dark for use over several weeks. To each flask of confluent cells, 50 μL of this RhBNN stock solution was directly added to the T25 flask without replacement or removal of media (final concentration: 10 μM RhBNN, 1% DMSO). The flasks were gently agitated, and then allowed to incubate for 30 min to uptake the RhBNN. Medium was then removed, and cells were washed with 2 x 5 mL PBS buffer to remove any RhBNN not uptaken by the live cells. The cells were submersed in PBS for micropatterning experiments.

Confluent field cell patterning using a 4x objective. 90% confluent A549 cells in a T25 flask were incubated with RhBNN and prepared for imaging as described above. A field densely packed with cells was focused on using the 4x objective on the DLP microscope. Cells were irradiated with the preset checkerboard pattern for 0 min, 5 min, and 10 min with high intensity blue light (0.48 W cm^{-2}) and imaged under weak green light (0.16 W cm^{-2}).

Irradiation time dependence using a 40x objective. 90% confluent A549 cells in a T25 flask were incubated with RhBNN and prepared for imaging as described above. A field of cells was focused on under a 40x objective. Using the Parallel RGB input of the LightCrafter 4500 to mirror a PowerPoint slide, a split field pattern was projected onto the field of cells with high

intensity blue light (9.4 W cm^{-2}) for 0 s, 30 s, 60 s, and 90 s and then imaged under uniform weak green light (2.8 W cm^{-2}).

Single cell selection using a 40x objective. A549 cells were incubated with RhBNN and prepared for imaging as described above. A field of cells was focused under a 40x objective and imaged under uniform green light (2.8 W cm^{-2}) prior to patterning. Using MS Powerpoint, a pattern that would irradiate only a single selected cell was generated and projected using the Parallel RGB input of the LightCrafter 4500. The cells were irradiated for 0 s, 30 s, 60 s, and 90 s with high intensity blue light (9.4 W cm^{-2}) and imaged under weak green light (2.8 W cm^{-2}). The selected cell that was irradiated showed a significant increase in fluorescent intensity, whereas cells not irradiated showed no significant increase in fluorescent intensity.

2.4.7. Resin Photocuring

- Photocuring Sample Preparation

Liquid resin mixtures were prepared according to published procedure.[24] A 4:1 mixture of *N*,*N*-Dimethylacrylamide (DMA) to trimethylolpropane triacrylate (TMPTA) was prepared containing 2 wt% H-Nu254 acceptor ([4-(octyloxy)phenyl](phenyl)iodonium hexafluoroantimonate diphenyliodonium) and 0.2 wt% Borate V donor (2-(butyryloxy)-*N*,*N*,*N*-trimethylethan-1-aminium butyltriphenylborate). 0.1 wt% Rose Bengal photoinitiator was used for green light irradiation, 0.1 wt% H-Nu 470 was used for blue light irradiation and 0.3 wt% Zinc tetraphenylporphyrin (ZnTPP) for red light irradiation. No opaquing agents were used. 100 µL of the mixture was pipetted onto a glass microscope slide bordered with a double layer of vinyl-coated adhesive tape. A #1.5 glass coverslip was placed on the tape to sandwich the solution (Figure 2-16A). The depth of the solution measured to be 0.26 ± 0.03 mm by using digital

microcalipers (Fisher #14-648-17): depth of solution = (height of slide + tape + coverslip) – (height of slide + coverslip).

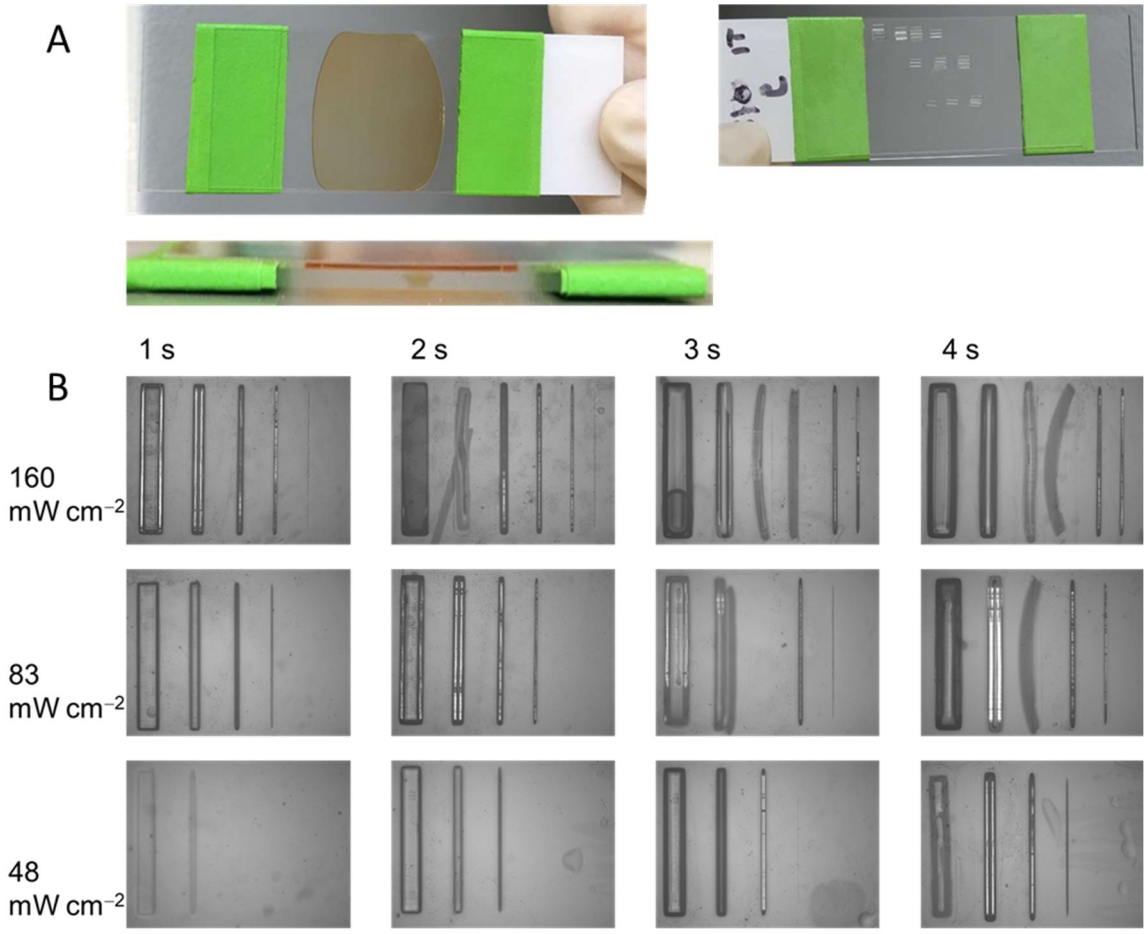

Figure 2-16. (A) Photographs of glass slides with sandwiched liquid resin before photocuring (top view and side view), and after photocuring and washing the solid prints (top view). (B) DLP reflected light microscopy images of a representative trial for line width prints for optimizing photocuring conditions and determining print resolution. Lines of widths from 9–300 µm were projected onto green light-initiated mix using 48–160 mW cm^{-2} green light for 1–4 s.

- DLP Photocuring Methods

A sample slide containing the green photoinitator mixture was placed on the DLP microscope stage. The LightCrafter was set to Parallel RGB mode to mirror a PowerPoint slide and weak red light (2 mW cm^{-2}) was projected through a 90:10 beamsplitter and 4x objective to

focus the patterned light onto the coverslip of the sample. The sample was then irradiated with 48, 83, or 160 mW cm^{-2} green light for 1, 2, 3, or 4 seconds with desired patterns. For optimization of conditions and photocuring resolutions, lines of 9 μm to 300 μm width were projected onto the sample under the varying irradiation intensities and irradiation durations. Figure 2-16B shows appearance of prints after photocuring and wash. Multiple experiments were carried out on each prepared slide by shifting the stage in xy between experiments for a fresh field. After photocuring, the excess liquid resin was washed off by flowing isopropanol between the slide and coverslip. The washed photocured solid print on the glass slide was then imaged on the DLP microscope using red light through a 90:10 beamsplitter for brightfield imaging. Width of the washed solid prints was measured using line selection tool in ImageJ to determine the printing resolution. Fluorescence images of prints were obtained by exciting the photosensitizer contained in the solid resin with a uniform field of blue light at high enough intensity that emission could be observed through a 692/40 nm emission filter. Similar methods were used for photocuring blue and red light irradiated mixtures different patterns.

2.4.8. Conditions for prints in Figure 2-11

A–F. Prints were photocured from blue light initiated liquid resin by irradiating through a 4x objective using blue light at 140 mW cm^{-2} for 2 s. Patterns were mirrored from PowerPoint slides using the Parallel RGB mode of the LightCrafter. Prints were washed with isopropyl alcohol and then imaged using uniform blue light to excite fluorescence which was imaged through a 692/40 nm filter.

G. 3D Prints were photocured from blue light initiated liquid resin by irradiating through a 4x objective using blue light at 140 mW cm^{-2} for 2 s per 100 μm layer. Models were sliced in

ChiTuBox to generate the pattern projected for each layer. Patterns were imported into and mirrored from PowerPoint slides using the Parallel RGB mode of the LightCrafter. Prints were washed with ethyl acetate and then imaged at uniform green light illumination of 83 mW cm^{-2}, imaged through a 692/40 nm filter

H–K. Micropatterning was carried out on SH-resin submerged in 3 mM **SiR-sty** and 70 μm eosin y solution in DMSO. Patterns from a Powerpoint slide or from the test patterns of the Lightcrafter were projected through a 40x objective onto the beads using blue light at 9.4 W cm^{-2} for 5–10 min. Uniform blue light (0.2 W cm^{-2}) was then used to excite fluorescence, which was imaged through a 692/40 nm filter.

L–M. Micropatterning was carried out on NH_2-resin submerged in 1 mM **RhBNN** solution in DMSO. Patterns from a PowerPoint slide or from the test patterns of the LightCrafter were projected through a 40x objective onto the beads using blue light at 17.9 W cm^{-2} for 5–15 s. Uniform green light (9.042 W cm^{-2}) was then used to excite fluorescence, which was imaged through a 692/40 nm filter.

N. Dual chemistry micropatterning was carried out on SH-resin submerged in a solution of 1.5 mM **SiR-sty**, 35 μm eosin y, and 0.5 mM **RhBNN** in DMSO on a microscope slide with a coverslip on top. (i) The checkerboard internal test pattern of the DLP microscope was projected through a 40x objective for 5 s using blue light at 9.4 W cm^{-2} to achieve patterned **RhBNN** functionalization. Then horizontal stripes from a Powerpoint slide were projected on the same field of beads using red light for 5 min at 8.5 W cm^{-2} to achieve patterned SiR-sty functionalization. Uniform green light was used to excite uncaged RhBNN fluorescence which was imaged through a 593/20 nm emission filter, and weak uniform blue light was used to excite SiR-sty fluorescence, which was

imaged using a 692/40 nm emission filter. (ii) A similar procedure as above was used. Vertical stripes from a Powerpoint slide were projected onto a field of resin using blue light (9.4 W cm^{-2}) for 10 s, after which horizontal stripes were projected using green light for 3 min at 10.3 W cm^{-2}. Imaging was performed as above.

O–P. Micropatterning was carried out on A549 cells incubated with 20 μM **RhBNN**. Patterns from a PowerPoint slide or from the test patterns of the LightCrafter were projected through a 4x objective onto a highly confluent field of cells using blue light at 0.48 W cm^{-2} for 10 min. Uniform green light (0.16 W cm^{-2}) was then used to excite fluorescence in the cells, which was imaged through a 692/40 nm filter.

Q. Micropatterning was carried out on A549 cells incubated with 20 μM **RhBNN**. A PowerPoint slide containing a small white area on a black background was prepared to map onto a field of cells through a 40x objective such that only a desired single cell would be under the white area. The pattern was projected using blue light at 9.4 W cm^{-2} for 30 sec. Uniform green light (4.8 W cm^{-2}) was then used to excite fluorescence in the cells, which was imaged through a 692/40 nm filter.

R. Micropatterning was carried out on **RhBNN**-PVA films on glass microscope slides. The monochrome Dallas Hall photograph from a PowerPoint slide was projected through a 4x objective onto the film using blue light at 0.48 W cm^{-2} for 5 min. Uniform green light (0.26 W cm^{-2}) was then used to excite fluorescence of the film, which was imaged through a 692/40 nm filter.

S–T. Micropatterning was carried out on **RhBNN**-PVA films on glass microscope slides. The monochrome photographs from a PowerPoint slide were projected through a 40x objective onto the film using blue light at 17.930 W cm^{-2} for 10 s. Uniform green light (2.83 W cm^{-2}) was then used to excite fluorescence of the film, which was imaged through a 692/40 nm filter.

U–Z. Micropatterning was carried out on **RhBNN**-PVA films on glass #1.5 coverslips. Images from a PowerPoint slide were projected through a 100x oil objective onto the film using blue light at GUI current = 100 for 2–5 s. Uniform green light at GUI current = 10–15 was then used to excite fluorescence of the film, which was imaged through a 692/40 nm filter.

2.5. References

1. J. Li and M. Pumera. 3D printing of functional microrobots. *Chem. Soc. Rev.,* 2021, **50**, 2794-2838.
2. M. Lee, R. Rizzo, F. Surman and M. Zenobi-Wang. Guiding Lights: Tissue Bioprinting Using Photoactivated Materials. *Chem. Rev.,* 2020, **120**, 10950-11027.
3. K. Hüll, J. Morstein and D. Trauner. In Vivo Photopharmacology. *Chem. Rev.,* 2018, **118**, 10710-10747.
4. W. A. Velema, W. Symanski and B. L. Feringa, Photopharmacology: Beyond Proof of Principle. *J. Am. Chem. Soc.,* 2014, **136**, 2178-2191.
5. M. Mao, J. He, X. Li, B. Zhang, Q. Lei, Y. Liu and D. Li. The Emerging Frontiers and Applications of High-Resolution 3D Printing. *Micromachines,* 2017, **8**, 113.
6. M. Altissimo. E-beam lithography for micro-/nanofabrication. *Biomicrofluidics,* 2010, **4**, 0265043.
7. G. Liu, S. H. Petrosko, Z. Zheng and C. A. Mirkin. Evolution of Dip-Pen Nanolithography (DPN): From Molecular Patterning to Materials Discovery. *Chem. Rev.,* 2020, **120**, 6009-6047.
8. B. D. Fairbanks, L. J. Macdougall, S. Mavila, J. Sinha, B. E. Kirkpatrick, K. S. Anseth and C. N. Bowman. Photoclick Chemistry: A Bright Idea. *Chem. Rev.,* 2021, advanced online publication, DOI: 10.1021/acs.chemrev.0c01212.
9. TI DLP LightCrafter 4500 Evaluation Module User's Guide. https://www.ti.com/lit/ug/dlpu011f/dlpu011f.pdf, accessed on May 18, 2021.
10. Sun, C.; Fang, N.; Wu, D. M.; Zhang, X. Projection micro-stereolithography using digital micro-mirror dynamic mask. *Sens. Actuators A Phys.* **2005**, *121* (1), 113−120.

11. Zhu, W.; Li, J.; Leong, Y. J.; Rozen, I.; Qin, X.; Dong, R.; Wu, Z.; Gao, W.; Chung, P. H.; Wang, J.; Chen, S. 3D-Printed Artificial Microfish. *Adv. Mater.* **2015**, *27* (30), 4411–4417.

12. Dorsey, P. J.; Rubanov, M.; Wang, W.; Schulman, R. Digital Maskless Photolithographic Patterning of DNA-Functionalized Poly(ethylene glycol) Diacrylate Hydrogels with Visible Light Enabling Photodirected Release of Oligonucleotides. *ACS Macro. Lett.* **2019**, *8* (9), 1133−1140.

13. Li, D.; Miao, A.; Jin, X.; Shang, X.; Liang, H.; Yang, R. An automated 3D visible light stereolithography platform for hydrogel-based micron-sized structures. *AIP Adv.* **2019**, *9*, 065204.

14. Lu, P.; Ahn, D.; Delafresnaye, L.; Yunis, R.; Corrigan, N.; Boyer, C.; Barner-Kowollik, C.; Page, Z. A. Wavelength-selective light-matter interactions in polymer science. *Matter* **2021**, *4* (7), 2172–2229.

15. Hoyle, C. E.; Bowman, C. N. Thiol–Ene Click Chemistry. *Angew. Chem. Int. Edit.* **2010**, *49* (9), 1540−1573.

16. Lowe, A. B. Thiol–ene "click" reactions and recent applications in polymer and materials synthesis: a first update. *Polym. Chem.* **2014**, *5*, 4820–4870.

17. Shih, H.; Lin, C. C. Visible-Light-Mediated Thiol-Ene Hydrogelation Using Eosin-Y as the Only Photoinitiator. *Macromol. Rapid Commun.* **2013**, *34* (3), 269−273.

18. DeForest, C. A.; Anseth, K. S. Cytocompatible Click-based Hydrogels with Dynamically-Tunable Properties Through Orthogonal Photoconjugation and Photocleavage Reactions. *Nat. Chem.* **2011**, *3*, 925−931.

19. Dobos, A.; Van Hoorick, J.; Steiger, W.; Gruber, P.; Markovic, M.; Andriotis, O. G.; Rohatscehek, A.; Dubruel, P.; Thurner, P. J.; Van Vlierberghe, S.; Baudis, S.; Ovsianikov, A. Thiol–Gelatin–Norbornene Bioink for Laser-Based High-Definition Bioprinting. *Adv. Healthc. Mater.* **2020**, *9* (15), 1900752.

20. Belov, V. N.; Wurm, C. A.; Boyarskiy, V. P.; Jakobs, S.; Hell, S. W. Rhodamines NN: A Novel Class of Caged Fluorescent Dyes. *Angew. Chem. Int. Edit.* **2010**, *49* (20), 3520–3523.

21. Thiel, Z.; Rivera-Fuentes, P. Single-Molecule Imaging of Active Mitochondrial Nitroreductases Using a Photo-Crosslinking Fluorescent Sensor. *Angew. Chem. Int. Ed.* **2019**, *58*, 11474−11478.

22. Ciszewski, Ł. W.; Rybicka-Jasińska, K.; Gryko, D. Recent developments in photochemical reactions of diazo compounds. *Org. Biomol. Chem*. **2019**, *17*, 432–448.

23. Hu, J.; Liu, Y.; Khemtong, C.; El Khoury, J. M.; McAfoos, T. J.; Taschner, I. S. Photochemical Patterning of a Self-Assembled Monolayer of 7-Diazomethylcarbonyl-2,4,9-trithiaadmantane on Gold Films via Wolff Rearrangement. *Langmuir* **2004**, *20* (12), 4933–4938.

24. Ahn, D.; Stevens, L. M.; Zhou, K.; Page, Z. A. Rapid High-Resolution Visible Light 3D Printing. *ACS Cent. Sci.* **2020**, *6* (9), 1555−1563

25. Haris, U.; Plank, J. T.; Li, B.; Page, Z. A.; Lippert, A. R. "Visible Light Chemical Micropatterning Using a Digital Light Processing Fluorescence Microscope." *ACS Cent. Sci.* **2021**, *8*, 67-76.

26. Patel, S. K.; Cao, J.; Lippert, A. R. A Volumetric Digital Light 3D Photoactivatable Dye Display. *Nat. Commun.* **2017**, *8*, 15239.

27. Li, B.; Haris, U.; Aljowni, M.; Nakatsuka, A.; Patel, S. K.; Lippert, A. R. Tuning the Photophysical Properties of Spirolactam Rhodamine Photoswitches. *Isr. J. Chem.* **2021**, *61*, 242-252.

28. Lukinavičius, G.; Umezawa, K.; Olivier, N.; Honigmann, A.; Yang, G.; Plass, T.; Mueller, V.; Reymond, L.; Jr, I. R. C.; Luo, Z.-G.; Schultz, C.; Lemke, E. A.; Heppenstall, P.; Eggeling, C.; Manley, S.; Johnsson, K. A Near-Infrared Fluorophore for Live-Cell Super-Resolution Microscopy of Cellular Proteins. *Nature Chemistry* **2013**, *5* (2), 132.

29. Ryan, L. S.; Gerberich, J.; Haris, U.; Nguyen, D.; Mason, R. P.; Lippert, A. R. Ratiometric pH Imaging Using a 1,2-Dioxetane Chemiluminescence Resonance Energy Transfer Sensor in Live Animals. *ACS Sens.* **2020**, *5,* 2925-2932.

30. Lumpi, D.; Wagner, C.; Schöpf, M.; Horkel, E.; Ramer, G.; Lendl, B.; Fröhlich, J. Fibre Optic ATR-IR Spectroscopy at Cryogenic Temperatures: In-Line Reaction Monitoring on Organolithium Compounds. *Chem. Commun*. **2012**, *48*, 2451– 2453

31. Butkevich, A. N.; Bossi, M. L.; Lukinavičius, G.; Hell, S. W. Triarylmethane Fluorophores Resistant to Oxidative Photobluing. *J. Am. Chem. Soc*. **2019**, *141* (2), 981–989.

32. Wang, C.; Zhang, H.; Zhang, T.; Zou, X.; Wang, H.; Rosenberger, J. E.; Vannam, R.; Trout, W. S.; Grimm, J. B.; Lavis, L. D.; Thorpe, C.; Jia, X; Fox, J. M. Enabling in vivo Photocatalytic Activation of Rapid Bioorthogonal Chemistry by Repurposing Si-Rhodamine Fluorophores as Cytocompatible Far-Red Photocatalysts. *J. Am. Chem. Soc.* **2021**, *143* (28), 10793−10803.

33. Limnios, D.; Kokotos, C. G. Photoinitiated Thiol-Ene "Click" Reaction: An Organocatalytic Alternative. *Advanced Synthesis & Catalysis* **2017**, *359* (2), 323–328.

34. Z. Song, Y. Wu, T. Xin, C. Jin, X. Wen, H. Sun and Qing-Long Xu. The Rh(ii)-catalyzed formal N-S bond insertion reaction of aryldiazoacetates into N-phenyl-sulfenyl phthalimide, *Chem. Commun.* **2016**, ***52***, 6079−6082.

35. V. Belov, C. Wurm, V. Boyarskiy, S. Jakobs, and S. Hell, S. Rhodamines NN: a novel class of caged fluorescent dyes, *Angew. Chem. Int. Ed.* **2010**, *49*, 3520−3523.

36. J. P. Badyal, A. M. Cameron, N. R. Cameron, D. M. Coe, R. Cox, B. G. Davis, L. J. Oates, G. Oye and P. G. Steel. A simple method for the quantitative analysis of resin bound thiol groups, *Tetrahedron Lett.* 2001, **42**, 8531−8533.

Chapter 3

CATALYTIC SELF-PROPELLING CHEMICAL MICROMOTORS FABRICATED WITH VISIBLE LIGHT

3.1. Introduction

Chemical micromotors[1] are microscale devices that are capable of self-propulsion through fluids due to the chemical reactions that occur on their surface in response to external physical or chemical stimuli such as electromagnetic fields, thermal gradients, and catalytic substrates. From the first instances of work on artificial, self-propelled microswimmers which focused on demonstrating motion fueled by chemical stimuli to replicate nature,[2,3] the field now encompasses tailoring these agents for varied purposes[4] including degradation of chemical/biological warfare agents,[5,6] environmental remediation,[7,8,9] and enhancement of biomolecule sensing, transport, and delivery.[10,11,12] The motion of chemical micromotors is driven by the conversion of chemical energy into mechanical motion, usually achieved by loading the device with a catalyst that causes a chemical reaction to occur when the device is exposed to its substrate. Mechanisms of propulsion for motors that do not have mechanically moving parts[13,1] include self-diffusiophoresis wherein a chemical concentration gradient is generated that propels the device,[14] self-electrophoresis wherein an electric field is generated to propel the device,[3] self-thermophoresis wherein a thermal gradient is created to propel the device,[15] Marangoni effects, wherein surface tension gradients propel the device,[16] and gas generation wherein bubble recoil propels the device.[17,18]

Many techniques have been developed for fabricating these self-propelled microscale and nanoscale motors, including template-assisted manufacture,[3,19] physical vapor deposition,[20] rolled up technology,[21] and assembly of molecules or nanoparticles.[22] While these conventional methods can be used for synthesizing large quantities of regularly shaped motors such as nanowires, helices, and Janus particles, they are limited in their ability to fabricate micromotors of arbitrary shapes with high resolution. Additive manufacturing i.e., 3D printing, is a newer technique which can allow bypassing these limitations in shape and complexity.[23,24] Among additive manufacturing / 3D printing techniques that have been used for fabricating micromotors are direct laser writing (DLW) also known as two photon polymerization (TPP),[25] wherein laser beams are scanned to alter a resist under two photon absorption, stereolithography (SLA),[26] wherein a print is photocured layer by layer, and microscale continuous optical printing (μCOP) or digital light processing (DLP) printing,[27] wherein light patterned by a digital micromirror device (DMD) is used to build a print layer-wise. These techniques have expanded the scope of micromotor fabrication and enabled manufacture of specialized and biomimetic structures. DMD based methods in particular are attractive because of their faster speed and higher throughput as compared to direct laser writing and stereolithography. The use of UV curable resin, however, has limited the technique to UV light, which raises the cost of optics, and specialized components as compared to visible light.

In this chapter, we demonstrate DMD-based additive manufacturing for fabricating microscale polymer propulsion motors using visible light. We investigate performance of these motors with MnO_2 catalyzed decomposition of hydrogen peroxide, and a novel propulsion system, the Rh_2OAc_4 catalyzed decomposition of ethyl diazoacetate.

3.2. Results and Discussion

Our work in developing chemical micromotors branched from our earlier demonstrations of carrying out patterned and targeted chemical functionalization of substrates with light.[28] Using a custom-built digital light processing fluorescence microscope, which has the ability to pattern and image light microscopically, we carried out photo-mediated thiol-ene photoclick, Wolff rearrangement, and polymerization reactions on the microscale on polymer substrates to introduce fluorescent molecules of interest at target sites (Chapter 2). In this chapter we investigate how we can harness the same principles and methods for incorporating fluorescent dyes and photocuring resin for fabricating catalytic micromotors. We develop microscale polymer devices with embedded catalyst using visible light. Of the catalytic systems we explore is the catalytic decomposition of hydrogen peroxide which is well-known and vastly applied for micromotor propulsion, using manganese oxide (MnO_2) catalyst. We also investigate a catalytic system that is yet to be applied for micromotor propulsion in the literature to the best of our knowledge, which is the decomposition of diazo compounds using a rhodium acetate catalyst (Rh_2OAc_4).

3.2.1. Optimized Methods for Fabrication of Motors

We printed micromotors from visible light photocuring of acrylamide polymer. In chapter 2, we demonstrated microscale 2D and 3D printing with 20 μm lateral resolution using a recently published visible-light photocurable resin and DLP micropatterning.[28,29] A similar technique was used for printing micromotors, with some modifications to the setup that enabled incorporation of catalyst and isolation and recovery of prints.

Resin formulation: The photocurable resin mix consists of dimethylacrylamide (DMA) monomer, trimethylpropane triacrylate (TMPTA) crosslinker, a visible light activated photoredox catalyst, and donor and acceptor co-initiators for enhanced efficiency of photoredox. For printing micromotors, we selected Rose Bengal as the photocatalyst based on its easy availability, low cost,

and green light activation. Typical formulation for photocuring is 4 parts monomer to 1 part crosslinker. For fabricating micromotors, we found that increasing the crosslinker density led to improved results in generating prints, so a 2:1 monomer to crosslinker ratio was used. This allowed for (1) more uniform suspension of the MnO_2 and Rh_2OAc_4 catalyst particles in the resin mixture due to the higher viscosity of the crosslinker and (2) fast polymerization of the resin mixture despite inhibitory effects of the added metal catalysts.

FEP film: Fluorinated ethylene propylene is a common material used as a release layer or non-stick surface in 3D printing, particularly in resin-based printing processes. In chapter 2, in demonstrations of microscale 3D printing with the DLP microscope and the photocurable resin, we used FEP film to ensure release of each subsequent layer of the print from the resin vat before the next layer could be printed on it. For demonstration of 2D prints on microscope slides, FEP film was not used since releasing these prints from the glass was not required. In the case of micromotor prints, while they are printed as 2D prints (single layer only), after photocuring is complete, they need to be released from the glass slide surface for recovery and use as micromotors. To enable this, glass slides were layered with FEP film before addition of resin and photocuring. After washing, cured prints could be easily transferred to a fresh slide for characterising and testing. Without FEP film, it is not possible to transfer cured microscale prints without damaging them.

Glass coverslip with spacer: For photocuring using the DLP microscope as described in chapter 2, liquid resin solution was added onto a FEP coated microscope slide. The glass slide was bordered with 2 layers of vinyl tape (to ensure space between the microscope slide and a glass coverslip that was placed on top. Having a space between the two surfaces allowed for (1) incorporating height into the print, (2) controlling the height of the print (depth of the solution was

around 0.2 mm with two layers of tape) and (3) preventing the slide and the coverslip from sticking to each other. While prints can be generated without a coverslip on top, we found that placement of a coverslip helped with (1) preventing spilling of the liquid resin, (2) limiting inhalation of fumes from the solution, and (3) focusing light from the DLP microscope for photocuring.

Incorporation of catalyst: We identified two methods of incorporating catalyst into the prints which reproducibly produced good results. The catalyst could be pre-mixed into the liquid resin before addition to the microscope slide (Figure 3-1 A). While this strategy worked well for MnO_2 which is unreactive towards the components of the resin (the pre-mixed solution can be stored and used for several experiments), for Rh_2OAc_4, reaction with the acrylamide monomer over time deactivates the catalyst and good results are obtained only with immediate use. A second strategy we devised was firmly spreading a thin layer of the solid catalyst onto the FEP film, followed by addition of the liquid resin mixture (Figure 3-1 B, C). This proved effective for both catalysts and enabled more uniform loading and consistency across prints.

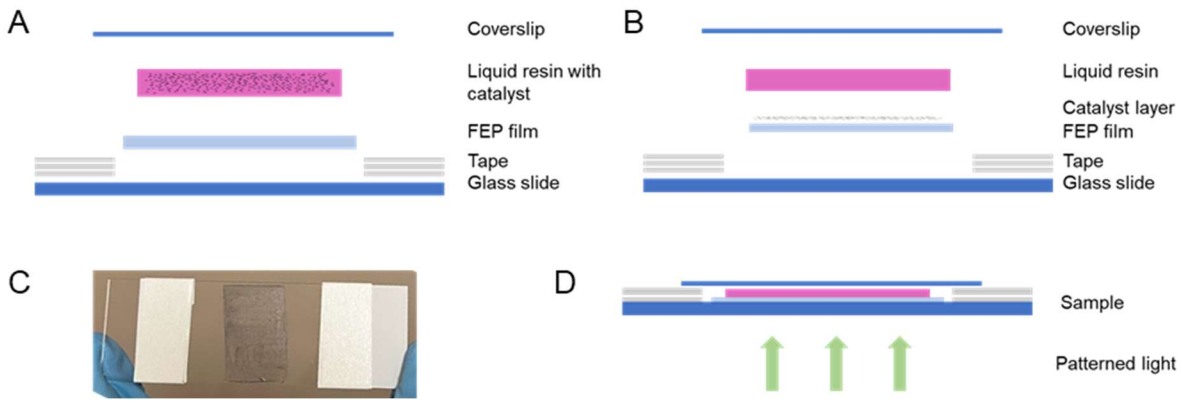

Figure 3-1. Strategies for incorporating catalyst into resin sample for photocuring. (A) Mixing the catalyst into the liquid resin before or after addition to the microscope slide. (B) Spreading a layer of catalyst onto FEP film on the microscope slide before addition of liquid resin. (C) Photograph of a microscope slide with tape spacers, FEP film, and layer of MnO_2 spread onto the FEP film. (D) Photocuring resin on the prepared sample slide using patterned light from the DLP microscope.

Table 3-1. Photocuring success with irradiation time for 25 μm prints with green light irradiation at 0.3 W cm^{-2}

	10 s	17 s	18 s	19 s	20 s
0.3 W cm^{-2} irradiation for 25 μm prints	Unsuccessful	Mostly unsuccessful	Mostly unsuccessful	Mostly unsuccessful	Mostly successful

Photocuring conditions: The prepared sample slides were irradiated with patterned green light using the DLP microscope (Figure 3-1 D). Higher intensities of light and longer durations of irradiation were generally required for photocuring with the added catalysts as compared to when printing without the MnO_2 or Rh_2OAc_4. This may be due to (1) light scattering by the non-transparent layer of catalyst spread on the FEP film or (2) inhibition of the radical reaction by the metal catalysts. For small prints (~25 μm), more than 20 seconds of green light irradiation at 0.3 W cm^{-2} (highest power setting) were required for print development. For prints of 60 μm in diameter, 5+ seconds of irradiation were required. With larger prints than this, the light intensity or irradiation time was reduced significantly.

Micromotor shape and size: With the light patterning capability of the DLP microscope, micromotors of different shapes and sizes were generated using structured light. We found that at small sizes (25–60 μm), circles printed best. Larger sized motors could be printed in a variety of shapes such as square, triangle, rectangle, and fish (Figure 3-2). By controlling the depth of the resin solution, interesting 3D structures could be obtained due to the shape of the light beam, for example, while printing 2D squares, 3D square-based pyramids were generated as light penetrated past the surface of the solution (Figure 3-2 E).

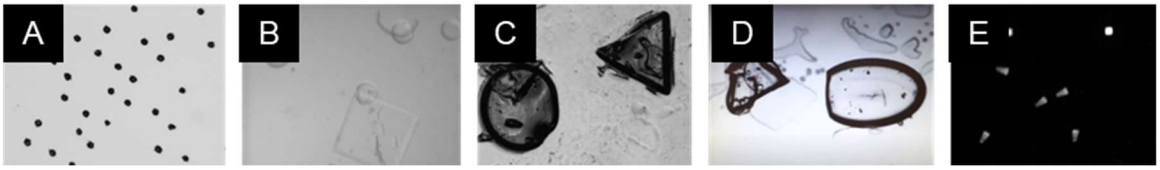

Figure 3-2. Micromotor shapes and sizes. (A) 40 µm circle motors. (B) 250+ µm circle and square prints. (C) 250+ µm circle and triangle prints. (D) Fish shaped print. Tail loaded with catalyst broke off from body. (E) 150 µm pyramid shaped prints.

Washing: After photocuring, prints were washed very carefully to remove the liquid resin since the presence of the FEP film could lead to the prints being washed away as well. This was not a problem in chapter 2 since the resin was directly on glass and prints remained stuck to the slide through the wash steps. For washing micromotor prints, first the resin solution was soaked off using paper towel without disturbing any cured prints. Isopropanol was added to the slide using a pipet and then soaked with a paper towel. This was repeated multiple times until no more of the pink resin solution remained.

Post-curing and transferring: For clean recovery of the printed micromotors, we found that a long post-cure (10+ min) with UV light after washing was a key step. Without curing with UV light, the prints are fragile semi-solids and may get damaged in the process of transferring to a fresh slide, may not get transferred at all, or may form aggregates with each other. This was the case in many trials with Rh_2OAc_4 motors, where lack of post-curing resulted in large aggregates of smaller prints during the washing and transferring steps. For most MnO_2 prints, a post-cure was carried out. To transfer the UV cured prints to a clean slide for testing or characterization, the slide with the prints was gently pressed against a clean slide. Because of the FEP film on the original slide, the prints are released easily and transfer to the new slide. Since the prints were cured into hard solids during the UV post cure, they do not stick too tightly to the fresh slide and propulsion experiments can be carried out.

Characterization: The micromotor prints were characterized using an EVOS-*fl* microscope under brightfield illumination with a 4x objective. The built-in recording feature of the EVOS microscope captures videos at a rate of 1 frame every 10 sec, which is not fast enough to capture useful data. Because of this, propulsion experiments were recorded using an iPhone camera in video mode.

3.2.2. Manganese (II) oxide / hydrogen peroxide micromotors

Hydrogen peroxide (H_2O_2) is a powerful oxidizing agent that can decompose into water and oxygen gas.

$$2\ H_2O_{2\ (aq)} \rightarrow 2\ H_2O_{\ (l)} + O_{2\ (g)}$$

This decomposition reaction can be catalyzed by various substances, including transition metal ions, metal oxides, and enzymes.[30] Manganese (II) oxide (MnO_2) is one commonly used catalyst for this decomposition, owing to its ability to act as an electron transfer mediator and provide a surface for adsorption in the breakdown process. Manganese oxide has several properties that make it suitable for use in micromotors. It has high catalytic activity and stability, which allows it to efficiently catalyze reactions under harsh conditions.[31] Additionally, it has a relatively low toxicity compared to other metal catalysts, making it a safer option for use in biomedical and environmental applications.[32,33] Numerous micromotors have been developed which use MnO_2 to catalyze H_2O_2 decomposition, including those coating it onto the surface of particles, such as silica or polystyrene.[34,35] In this work, we develop motors with embedded MnO_2 using visible light photocuring for propulsion via decomposition of hydrogen peroxide.

First, we verified that the MnO_2 catalyst is stable in the polymer resin that the micromotors will be fabricated with, and that photocured polymer containing the MnO_2 is able to generate

oxygen gas when treated with H_2O_2. On a glass microscope slide, we prepared a suspension of the liquid resin mixed with powdered MnO_2 and irradiated it with green light in a pattern of circles under the DLP microscope through a 4x objective. The excess solution was then rinsed off with isopropanol, leaving the MnO_2 doped prints stuck to the slide. The prints were imaged under brightfield illumination and showed that catalyst particles were incorporated and addition of H_2O_2 (30% in water) led to vigorous bubble production (Figure 3-3 A). Removal of the peroxide solution led to cessation of bubbling (Figure 3-3 B).

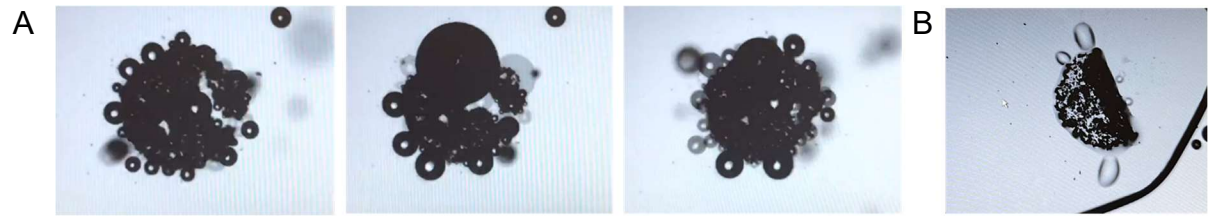

Figure 3-3. (A) Frames from a video showing generation of bubbles by MnO_2 loaded photocured polymer prints in 30% H_2O_2. (B) Prints from A after removal of H_2O_2 solution from the sample. (Table 3-2 entry 82 in experimental methods section).

3.2.2.1. Optimizing MnO_2 micromotor performance

After verifying the performance of the catalyst in photocured resin, we next conducted a series of experiments to optimize conditions for performance of the micromotors. Behavior of the motors was divided into three categories: (1) generation of bubbles observed and (2) motion of the microdevice observed and (3) self-propelled motion of the device observed. These were assessed in studies varying several parameters as discussed below.

Substrate solvent system: MnO_2 loaded prints were treated with the H_2O_2 substrate in a variety of solvent systems. In 30% H_2O_2 in water, good bubble generation from the motors was observed. Motion was also observed, though while some wriggling motions were generated by bubble recoil, they were superseded by displacement of the prints floating to the surface and center

of the water due to effects of buoyant force and surface tension. To counteract the effects of these forces, we tried mixtures of water with different organic solvents. We explored DMF, isopropanol, and ethanol since these would lower the surface tension of the water as well as lower the density of the solution. In a 1:2 mixture of DMF and water, similar results were obtained as with only water. In a 1:2 mixture of ethanol and water, large bubbles were formed, and propulsive motion was observed, but was limited to wriggling motions in a small area. In a 1:2 mixture of isopropanol and water, bubbling and significant displacement was observed.

H_2O_2 concentration and surfactant: In 3% and 30% H_2O_2 in water bubbles were generated reproducibly. For mixture systems such as with isopropanol, 10% H_2O_2 provided the best results generally. Higher H_2O_2 resulted in greater production of gas and faster motion. Addition of surfactant such as SDS or soap led to no change in propulsive activity, however, the size of the bubbles was smaller and accumulation of bubbles increased drastically (Figure 3-4). A thick foam developed in the substrate solution on addition of 1% SDS in water with 3% H_2O_2.

Figure 3-4. Motors in water with soap, 1% SDS and 3% H_2O_2. (Table 3-2 entry 62 in experimental methods section).

Slide setup: Use of FEP film and coverslip for propulsion experiments were parameters we investigated. With FEP films, bubbles tended to accumulate and grow on the film instead of being expelled through the solution. With use of FEP film, the solvent also developed a much larger contact angle and domed shape. Coverslips helped to prevent doming at the surface of liquids (especially water) and reduced the effects of surface tension. However, coverslips also led to accumulation of gas bubbles in the sample, leading to drying out of the motors.

Solvent volume: We observed many effects on micromotor behavior that were a direct result of the solvent such as buoyancy, surface tension, and currents in volumes of solvent sufficient to submerge the prints. To counteract this, we absorbed the solvent gently from the slide using a kimwipe so that only a minimal volume (could not be observed by eye) remained on the slide. This led to enough substrate on the slide to result in gas generation but not enough that solvent effects would interfere with motion of the motors, and highly motile motors walking on the glass unhindered by solvent effects were reproducibly observed.

Micromotor size and shape: we found that the size of the micromotor was directly relevant to its motion. While large prints were effective at generating bubbles, they generally did not exhibit motion driven by gas propulsion. Larger prints were also more resistant to currents in the solvent. Smaller prints showed movement in response to the gas generation, but also tended to be easy targets of surface tension and solvent currents. Several shapes were explored. For the smallest prints, only circles could be generated. However, for larger prints, we generated circles, rectangles, cones, and other multiplexed shapes. Because these were larger in size, they did not exhibit efficient self-propulsion, but did generate bubbles as expected.

Asymmetric catalyst loading: Catalyst was loaded asymmetrically into prints using a stepwise scheme. First, catalyst loaded prints were generated. These were then transferred to a clean slide and resin without any catalyst was added. The second, unloaded part of the micromotor was then printed aligned with the loaded part. Large asymmetric prints were generated with relative ease and asymmetric gas generation from these hybrids was observed (Figure 3-5 B). However, no directional motion was observed. This is likely due to the large size of the motors. Smaller asymmetric prints were more challenging to fabricate due to requirement of precise alignment between the loaded and unloaded components of the motor. We generated 50 – 100 μm

sized hybrids composed of one circle with catalyst and an appended circle without catalyst (Figure 3-5 A). These also produced asymmetric bubble generation and demonstrate potential for directional motion. Another technique for asymmetric catalyst loading was generating "single layer 3D" prints by increasing the depth of the resin solution when photocuring and focusing light at the farther surface of the solution (Figure 3-5 D). While the height of the print was tall (~150 µm), only the base surface which is in contact with the catalyst-lined FEP is loaded with catalyst. We generated cones and square-based pyramids using this method, as well as complexes from these shapes (3-5 C,D).

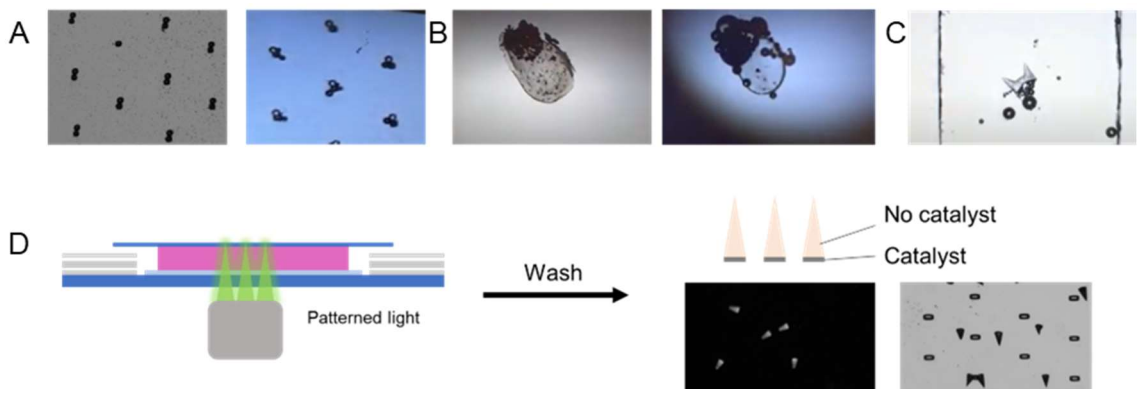

Figure 3-5. (A) 50 µm asymmetrically loaded hybrid prints. Asymmetric bubble generation can be observed with addition of 10% H_2O_2 in 60% iProH (table 3-2 entry 1 in experimental methods section). (B) 600 µm asymmetrically loaded hybrid print. Asymmetric bubble generation can be observed with addition of 3% H_2O_2 (table 3-2 entry 81). (C) Asymmetrically loaded hybrid print fabricated using a "single layer 3D printing" method. Asymmetric bubble generation can be observed with addition of 10% H_2O_2 in 30% iPrOH. (table 3-2 entry 26) (D) Schematic for "single layer 3D printing" method which combines larger depth of solution with distant focal point and MnO_2 lined FEP for asymmetric catalyst loading.

3.2.2.2. Propulsive motion in MnO_2 motors

With variations in the conditions described above, different types of motion were observed from the MnO_2 micromotor prints. These have been categorized as below:

Propulsion along currents: In solvent mixtures such as 30% iPrOH or EtOH in water, or mixtures of ethanol and isopropanol, convection currents were generated in the solvent due to (1) mixing different density and viscosity solvents and (2) bubble generation cumulatively displacing the low-density solvent. In these cases, the prints demonstrated significant motion due to the solvent currents (Figure 3-6 A, B). We can identify that the motion is due to currents because bubbles and foreign objects in the sample also exhibit similar patterns of motion (i.e., following the currents). Motion due to currents is fast and covers large areas.

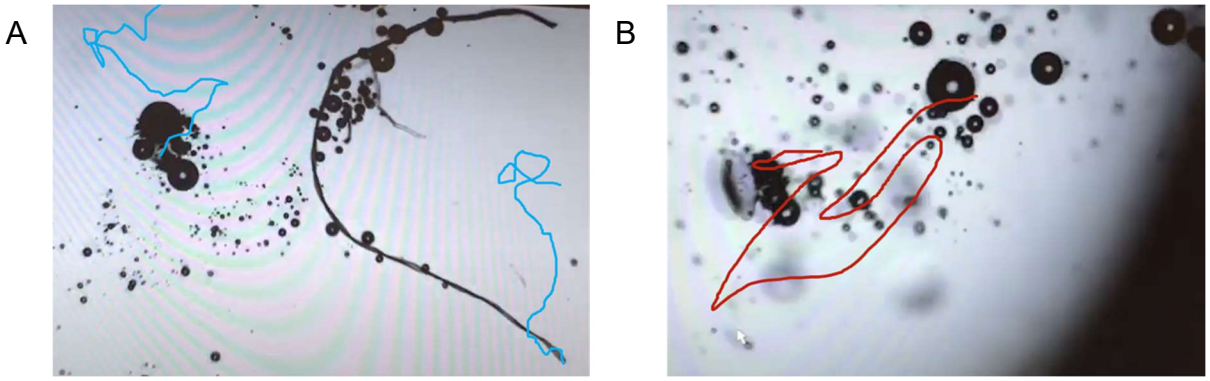

Figure 3-6. (A) Solvent currents cause motion of ~100 µm MnO_2 loaded circular print and a dust strand in a mixture of water, isopropanol and ethanol with 10% H_2O_2. (table 3-2 entry 39) (B) Solvent currents cause motion of a ~200 µm asymmetrically MnO_2 loaded print in a 30% isopropanol mixture with water and 10% H_2O_2. (table 3-2 entry 18).

Propulsion along air-solvent interfaces: An interesting behavior linked to prints floating at the surface of the liquid was their "skating" movement at air-solvent interfaces (Figure 3-7 A, B, C). We found that micromotor prints in a large volume of solvent (observable by eye) on a microscope slide often accumulated at air-solvent interfaces for example at the boundaries of the solvent, on air bubbles generated by the motors. A system containing water or other liquids tends to minimize its interfacial free energy by minimizing the area of the interface with the highest energy.[36] In this case, the interface between the solvent (polar) and air (less polar) is high in free energy, and presence of the micromotors at this surface minimize it. In combination with

propulsion of the motors due to currents or bubble generation, motion along these interfaces was generated and motors were observed to skate in smooth motions on the surface of air bubbles (Figure 3-7 A) and "hopped" between bubbles (Figure 3-7 B), as well as skated at the boundary of the solvent (Figure 3-7 C).

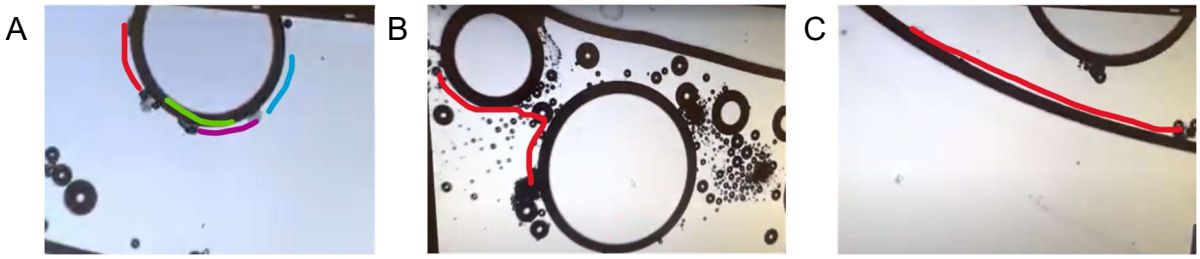

Figure 3-7. Micromotor propulsion at air-liquid interfaces. (A) Several 25 µm MnO_2 circular prints skating along the surface of an air bubble in 10% H_2O_2 and 60% EtOH in water (table 3-2 entry 54). (B) Motor skating along a bubble and then hopping to a neighboring bubble in 10% H_2O_2 and 30% EtOH in water (table 3-2 entry 52). (C) Motor skating along the boundary of the solvent in 10% H_2O_2 and 30% EtOH in water (table 3-2 entry 49). Motion over time is tracked using colored lines.

Self-assembly: Micromotors regardless of shape and size demonstrated self-assembly behavior. Similar behavior has been studied in the literature and has been attributed to capillary effects, surface tension, and minimization of interfacial free energy (also described as the Cheerios effect, owing to the breakfast cereal exhibiting this behavior).[36,2] We found small motors to aggregate together over short periods of time (Figure 3-8 A). More notable than the self-assembly, which has been studied and implemented for different purposes in the literature, was that in most instances, after assembly, bubble recoil caused disassembly and then reassembly repetitively (Figure 3-8 B). This led to many different configurations and combinations of motor assemblies over a span of seconds. Interestingly, non-loaded prints did not exhibit assembly behavior, perhaps due to affinity for the glass slide surface and their lack of bubble production.

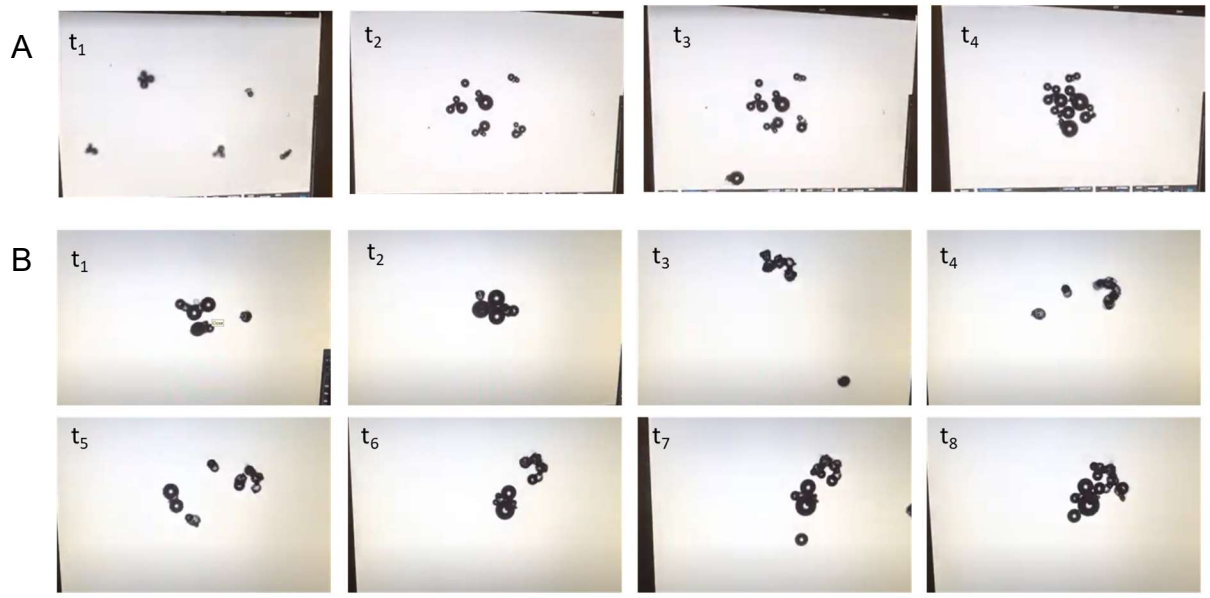

Figure 3-8. Self-assembly of micromotors. (A) Micromotors drifting towards each other and self-assembling in 3% H_2O_2 (table 3-2 entry 71). (B) At t_1 25 µm MnO_2 circular motors in 3% H_2O_2 start collecting and then assemble together at t_2. An incoming motor at t_3 joins the assembly and then bubble generation leads to dissembly and formation of small structures at t_5. At t_6 the smaller structures regroup into larger ones. At t_7 more microbots join the assembly. At t_8, all micromotors are part of a single assembly, which continues to undergo the process of dissembly and assembly with time (table 3-2 entry 68, 65, 57).

Wriggling in place: Some motors demonstrated wriggling behavior caused by generation of bubbles instead of propulsion over area (Figure 3-9 A, B, C). This was usually observed with larger prints (100+ µm), likely because the force generated by the gas bubbles is not sufficient for overcoming inertia and propelling the large motor. Asymmetrically loaded cone print dimers that generated bubbles from one side also showed wriggling behavior (Figure 3-9 C).

Figure 3-9. Wriggling motion of (A) ~100 µm motor in 3% H_2O_2 in ethanol (table 3-2 entry 43) and (B) ~100 µm motor in 3% H_2O_2 in water (table 3-2 entry 77). (C) ~150 µm cone shaped asymmetrically loaded motor in 10% H_2O_2 with 30% isopropanol in water (table 3-2 entry 31). Motion over time is tracked in red or green.

Displacement by bubble growth in channels: In experiments where we used glass cover slides to restrict the motors, the solvent and the gas bubbles to microchannels, effectively limiting the outlets for the gas, we observed bubble growth and displacement of the motors by these bubbles (Figure 3-10). Despite being uniformly loaded motors, these exhibited directionality towards the side of the channel that was less hindered: bubbles tended to grow large on the hindered side of the channel instead of being expelled, thus propelling the motor towards the opposite direction. Hinderance in the channels was a combination of narrower channel width and presence of other motors that provided a surface for bubbles to exert force on.

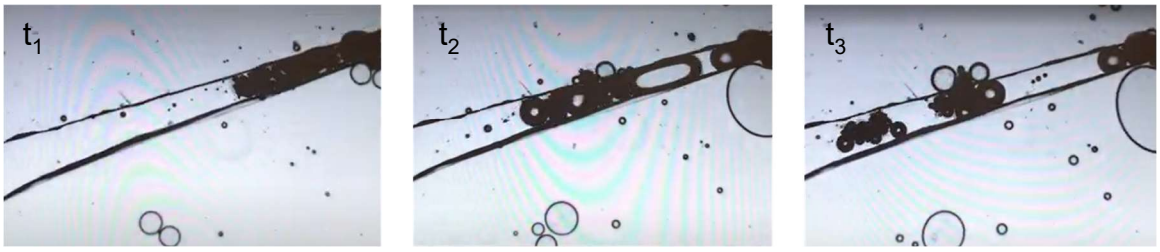

Figure 3-10. 25 µm micromotors accumulated at the narrow end of a channel at t_1 generate bubbles in the H_2O_2 substrate in a mixture of H_2O, iPrOH, and EtOH . Outlets for gas expulsion are limited especially at the narrow end of the channel where an obstructing motor is trapped (t_2). Growing bubbles propel the motors towards the wider end of the channel (t_3) (table 3-2 entry 41).

Jet-like propulsion: In one case, a large print (70 x 150 µm) with a high density of catalyst in large volume of solvent (enough to submerge the motor) produced strong jets of bubbles (Figure 3-11). The motor was a hybrid of a circular catalyst-loaded print and a circular non-loaded print and was treated with 10% H_2O_2 and 30% iPrOH in water. The rapid streams of bubbles generated thrust force and the print was observed to spiral around its non-loaded center. The direction of the jet of bubbles was directly opposite the direction of motion and the heading of the non-loaded component, indicating intrinsic directionality of the motor relative to itself caused by the asymmetry in the catalytic activity of the motor (Figure 3-11, red and green arrows). Additional experiments under similar conditions resulted in motion but such jet-like propulsion was not observed perhaps due to orientation of the motors, as discussed in section 3.2.2.2 (table 3-2 entry 38).

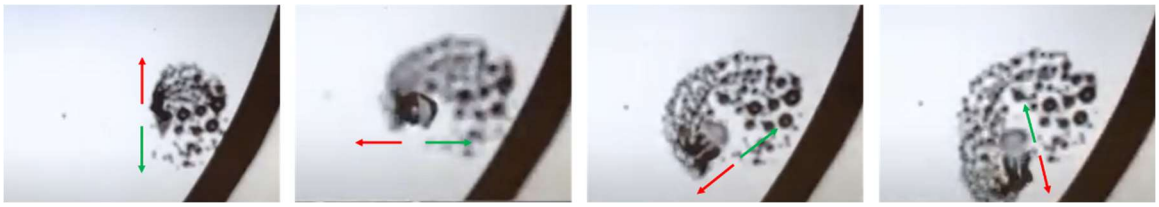

Figure 3-11. Asymmetrically loaded MnO_2 hybrid motor rapidly expelling bubbles (red arrow), propelling the motor in the opposite direction (green arrow) of bubble expulsion in 10% H_2O_2 and 30% iPrOH in water (table 3-2 entry 37).

Whizzing on glass: when the smallest circular motors (25 µm) were treated with a minimal volume of solvent, just enough to be present on the glass but not enough to submerge the prints, the effects of solvent currents, density, and surface tension were largely bypassed. The prints were observed to bounce and whizz around on the glass slide, covering large area in singular motions in 10% H_2O_2 and 30% iPrOH in water (Figure 3-12 A). The glass surface likely provides a better

surface for bubble recoil then liquid, leading to the bouncing behavior. Because the motors are not asymmetric, the direction of motion was generally random. However, we did notice that over time, the motors tended to self-assemble or congregate together (Figure 3-12 B). While this may suggest diffusiophoresis as H_2O_2 is depleted over time and motors assemble at areas of higher H_2O_2, it is more likely that the assembly is an effect of capillary action and surface tension as discussed above. Observing the process over a long time via time lapse imaging reveals that the substrate solution evaporates last at the point of aggregation.

The rapid movement of the motors and their tendency to self-assemble resulted in their noteworthy ability to carry, push, or swarm around foreign objects in a manner that is reminiscent of antibodies or ants. In Figure 3-12 C, motors gather around a dust strand (area of high surface tension). In Figure 3-12 D, two motors push and pull a dust strand towards the center of aggregation, however, ultimately are unsuccessful in transporting it to the center. With smaller sized objects or an object which the motor has greater affinity, this type of cargo delivery may be possible.

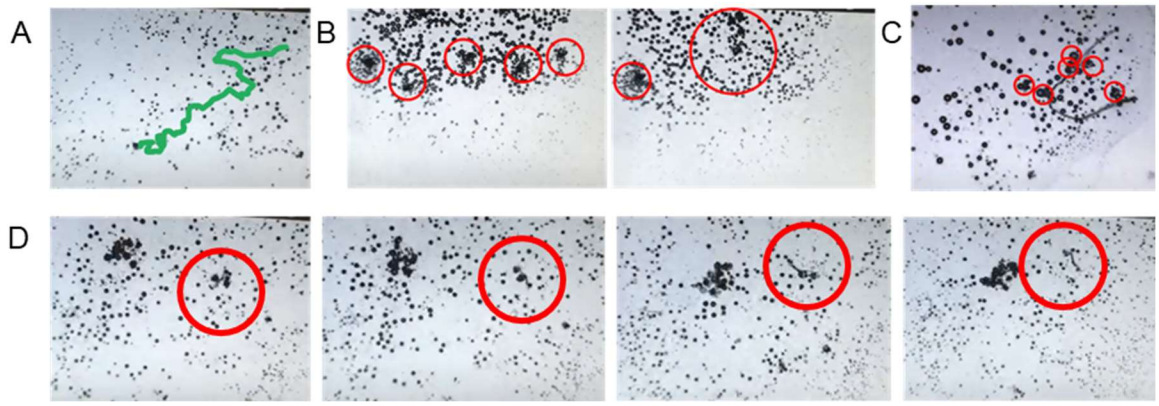

Figure 3-12. (A) Tracked motion of a motor whizzing in minimal volume of 10% H_2O_2 and 30% iPrOH in water (table 3-2 entry 4). (B) Motors spread out over an area (left image) self-assemble over time (right image) in minimal volume of 10% H_2O_2 and 30% iPrOH in water (table 3-2 entry 15). (C) Motors swarming around a long dust strand due to surface tension effects in minimal volume of 10% H_2O_2 and 30% iPrOH in water (table 3-2 entry 6). (D) Motors near a dust strand (red) exert force on the strand causing it to shift around and towards the assembly of micromotors in minimal volume of 10% H_2O_2 and 30% iPrOH in water (table 3-2 entry 4).

3.2.3. Rhodium (II) acetate – ethyl diazoacetate motors

Diazoacetates are highly reactive organic molecules containing the diazo functional group (—N=N). Ethyl diazoacetate (EDA) is one common, commercially available diazoacetate which is used widely as a reagent in organic synthesis, particularly in formation of new carbon-carbon or carbon-heteroatom bonds.[37] The key property of ethyl diazoacetate that makes it useful in synthesis is its ability to act as a carbene precursor. Carbenes have a neutral carbon atom containing only 6 valence electrons, two of which are unpaired, making the molecule highly reactive and short-lived. When treated with a transition metal catalyst such as rhodium (II) acetate (Rh_2OAc_4), ethyl diazoacetate undergoes a metal-catalyzed decomposition to form a metal carbene intermediate, which can then react with a variety of nucleophiles to form new bonds.[38] Importantly for us, in generation of the carbene intermediate, nitrogen gas is evolved (Scheme 3-1). While this chemistry has been explored extensively for numerous synthetic reactions including C—H insertions and

enantioselective transformations,[38] application of this catalytic system for propulsion micromotors is not yet reported.

Our strategy for making micromotors based on this catalytic generation of nitrogen gas involves embedding Rh_2OAc_4 catalyst in polymer microstructures and then treating them to ethyl diazoacetate (EDA) substrate solution to result in gas production and bubble recoil propulsion.

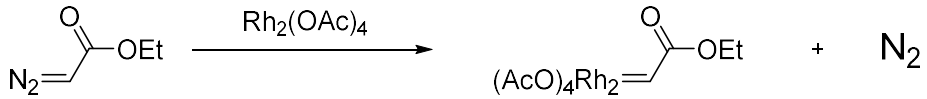

Scheme 3-1. Formation of a metal-carbene intermediate in Rh_2OAc_4 catalyzed decomposition of ethyl diazoacetate generates nitrogen gas.

In dichloromethane (DCM), Rh_2OAc_4 is an insoluble solid. Addition of ethydiazoacetate results in rapid gas generation (Figure 3-13 A, B). We first determined whether the Rh_2OAc_4 catalyst would be compatible with the polymer resin mixture for fabricating micromotors. The photocurable resin consists of dimethylacrylamide and TMPTA triacrylate. Addition of approximately 1 mg of Rh_2OAc_4 in 0.5 mL of TMPTA showed that while the solubility in TMPTA was poor, the catalyst was stable over several hours in this mixture (Figure 3-13 E, F). Addition of 1 mg of rhodium acetate in DMA led to the catalyst dissolving and initially forming a green solution (as is the color of Rh_2OAc_4), which then started turning to a pink color with time (Figure 3-13 C). Treating the solution after it turned pink to ethyl diazoacetate substrate led to no gas generation (Figure 3-13 D). This suggested oxidation of the Rh_2OAc_4 dimer from Rh_2(II, II) to Rh_2(II, III). Previously, it has been documented in the literature that amidate ligands bind strongly to the rhodium dimer core than carboxylate ligands do, and result in higher propensity for oxidation to the pink Rh_2(II, III) variant.[39] For reactions with diazoacetates, Rh_2(II, III) compounds serve as inefficient catalysts.[40] It may be that dimethylacrylamide ligands behaves similarly, i.e., bind strongly with rhodium and lower the oxidation potential. While oxidation of the catalyst and the

color change was not observed in the TMPTA mixture, gas generation was still minor due to poor mixing of EDA substrate with viscous TMPTA. Based on these experiments we determined that the life of rhodium acetate in the liquid resin mixture is short, and photocuring experiments were thus carried out by spreading catalyst on the FEP film on a glass slide or adding the catalyst to the resin mixture right before photocuring, to prevent oxidation before curing.

Catalyst	Solvent	Initial	After 3 hr	+ EDA after 3 hr
Rh_2OAc_4	DCM	Green suspension	Green suspension (Fig A)	Rapid gas generation (B)
Rh_2OAc_4	DMA	Green solution	Pink solution (Fig C)	No gas generation (D)
Rh_2OAc_4	TMPTA	Green suspension	Green suspension (Fig E)	Minor gas generation (F)

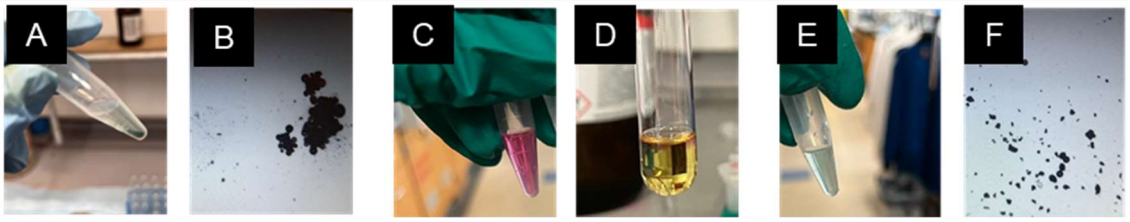

Figure 3-13. Behavior of Rh_2OAc_4 in DCM (A, B), DMA (C, D), and TMPTA (E, F) with time and addition of EDA.

3.2.3.1. Optimization of Rh_2OAc_4 motors

Use of the Rh_2OAc_4–EDA catalytic system for propelling micromotors is novel, and several conditions were studied and optimized to ensure performance. Some parameters remain to be investigated and fine-tuned in future studies.

Catalyst loading: Two strategies for loading micromotor prints with the Rh_2OAc_4 catalyst were explored. One method involved preparing the liquid resin mixture and adding it onto a glass slide with FEP film and tape spacers, and then adding the catalyst powder to the liquid followed by the coverslip and photocuring. While loaded prints could be generated using this method, the powder failed to disperse uniformly through the liquid and tended to collect at edges of the

solution. This led to unevenly loaded prints. Additionally, the larger sized particles or aggregates encapsulated in the print could sometimes tear through the print during the wash and isolation procedure due to the high density and larger particle size of the catalyst. For these reasons, spreading the catalyst on the FEP film and then adding liquid resin and coverslip to the slide was more effective.

Substrate: While ethyl diazoacetate solution (with 13% DCM as sold by the manufacturer) was effective as the substrate solution and bubbles were produced by the motors when treated with this solution, we found that the motion of the motors was enhanced with the addition of styrene to the solution. This may be due to (1) the physical properties of styrene, such as its density and viscosity, and (2) the rhodium catalyzed cyclopropanation reaction of styrene with EDA enhancing nitrogen generation. In most experiments we used 1:2 EDA:styrene as the substrate system. This was also favorable due to safety reasons.

Size and shape: Interestingly, we observed self-propelled motion from micromotors of large and small sizes with the Rh_2OAc_4 – EDA catalytic system. Perhaps this is because of the low viscosity of styrene as compared to water, which would reduce the drag force experienced by the motor. The prints also swelled to a larger size on addition of the organic substrate solution. Large aggregates of circular prints, up to 300 μm in size, exhibited propulsion. We did not yet investigate prints of <100 μm in size. We also observed that motors which were arbitrarily shaped aggregates of circular prints seemed to perform as well, if not better, than motors of defined shape. This may be because the aggregation lends a 3D element to the shape of the motor which improves performance.

Slide set up: With the rhodium acetate motors, we found that using FEP film to line the microscope slide for propulsion experiments led to good self-propulsion of motors. While aqueous

solutions have a large contact angle with the FEP film which interfered with self-propelling motion of the MnO_2 motors, the organic, non-polar solution of EDA in styrene did not show similar doming and interference. Additionally, because the low polarity solution has low surface tension, use of a cover slip on top of the solution to break the effects of surface tension was not required.

Catalyst asymmetry: While generating Rh_2OAc_4 hybrids is still in early stages of investigation, we were able to achieve these asymmetrically loaded motors (Figure 3-14 A). First, catalyst loaded components were printed with the catalyst mixed into the liquid resin. After washing and transferring the prints to a fresh slide, resin without catalyst was added to the prints and the non-loaded component of the motors was printed. This is yet to be attempted on scales of <100 µm. With motors ranging from 200 – 1000+ µm, asymmetric bubbling from the hybrids was observed, however, directional motion or propulsion due to asymmetry in catalyst loading has not yet been reproducibly observed.

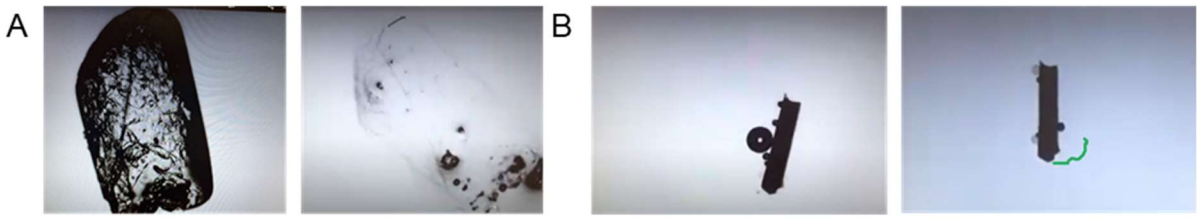

Figure 3-14. (A) Asymmetrically loaded Rh_2OAc_4 hybrid before and after addition of EDA/styrene solution (table 3-3 entry 14). (B) Large crystal of Rh_2OAc_4 in EDA/styrene solution generating bubbles and slight motion tracked in green (table 3-3 entry 17).

Catalyst surface area: We synthesized "microrods" of Rh_2OAc_4 by growing 200-500 µm crystals of rhodium acetate and studying their performance as motors when treated with ethyl diazoacetate (Figure 3-14 B). Interestingly, these crystals exhibited slow bubble generation, likely due to the lower surface area for catalysis as compared to powdered catalyst, and motion was found to be minimal, likely due to the large size and density of the crystals. Small particles of the rhodium

acetate (as received from supplier) generated significantly more bubbles and demonstrated impressive motion. Based on this, we moved forward using small catalyst particle sizes. It is worth investigating the effects of powdering the rhodium acetate obtained from the supplier even further.

Aggregation: Often, Rh_2OAc_4 micromotor prints formed aggregates during the isolation and wash procedure after photocuring, especially when the UV post-cure step was not carried out. These remained as aggregates in the catalyst substrate solutions as well, and led to interesting propulsion behavior, such as jet-like propulsion discussed later.

3.2.3.2. Motion of Rh_2OAc_4 motors

We categorized the motion of the Rh_2OAc_4 motors based on their behavior when treated with the EDA and styrene substrate solution.

Aggregation: Self-assembly and aggregation was observed with Rh_2OAc_4 motors, however, not to the same extent as with MnO_2 motors. While bubbles generated by the Rh_2OAc_4 catalyst propelled the motor in random directions, self-assembly through capillary forces was sometimes found to overpower these smaller self-propelled movements when large prints were in the solution (Figure 3-15).

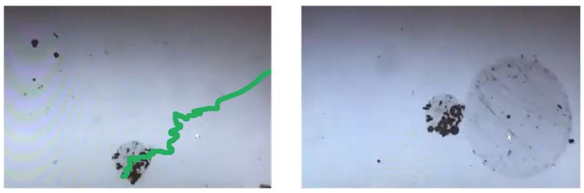

Figure 3-15. Small motor moving toward and assembling with a large print in EDA substrate. Smaller motions due to self-propulsion and bubble recoil are observed but overpowered by capillary interactions (table 3-3 entry 22).

Stepping: From large prints that generated bubbles slowly, stepping behavior was observed (Figure 3-16). As each bubble was extruded, the print took a "step" forward due to the recoil. This movement was observed in EDA (without any styrene) when large bubbles were regularly extruded from a specific site on the print or when smaller bubbles collected and burst consistently

at a specific site. In Figure 3-16 A and B, large motors consistently generate large bubbles at specific sites marked in red. Recoil from expulsion of these results in directional stepping motion along the path tracked in green.

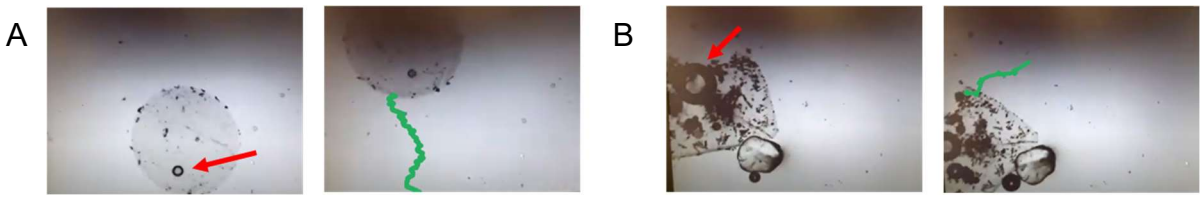

Figure 3-16. Recoil from large bubbles produced at site marked with red arrow results in stepping motion along path marked in green for (A) a 660 µm circular Rh_2OAc_4 motor (table 3-3 entry 25, 26, 27) and (B) a 700 x 550 µm rectangular Rh_2OAc_4 motor in EDA (table 3-3 entry 21).

Figure 3-17. (A) non-directional crawling motion from a 150 µm motor in EDA with fast bubble generation oriented parallel to the slide surface (table 3-3 entry 20). (B) wriggling motion from an aggregate of circular motors oriented parallel to the slide surface with slower bubble generation in 1:2 EDA:styrene (table 3-3 entry 2). (C) Directional crawling motion from an aggregate of two circular motors with asymmetric density of bubble generation across the motor in 1:2 EDA:styrene (table 3-3 entry 32). Paths of the motors are tracked in green.

Crawling/Wriggling: generation of gas throughout the motor relatively uniformly and quickly resulted in crawling motion with no overall directionality (Figure 3-17 A) or wriggling motions with no displacement over area (Figure 3-17 B). If the density of bubbles extruded was significantly asymmetric across the motor, some directionality was observed (Figure 3-17 C). Notably, even if gas generation was vigorous, as long as the motor is oriented horizontally (parallel

to the glass slide surface), with bubbles being extruded above or beneath the print, only small movements were exhibited. This is in contrast to when the print orients vertically (perpendicular relative to the slide surface), as discussed below.

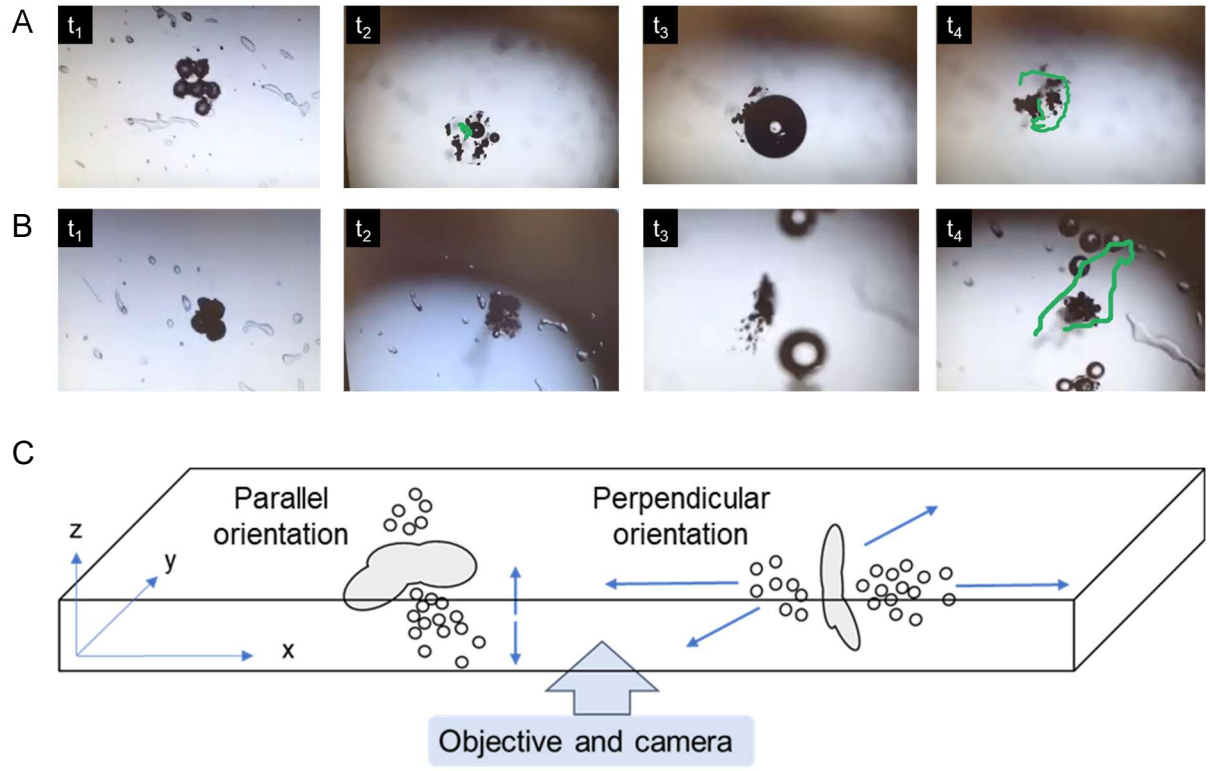

Figure 3-18. (A) Aggregate of dry circular motors on microscope slide (t_1) swells and starts generating gas when EDA is added, with no significant displacement over area while the motor is parallel to the slide (t_2). Rapid growth of a large air bubble (t_3) causes reorientation of the motor to being perpendicular to the slide, in which orientation it covers area in XY axes. Motion of motor is tracked in green (table 3-3 entry 29, 30, 31). (B) Aggregate motor displaying similar behavior as in A except in this case reorientation is caused by rapid bubble jets (t3) instead of by bubble growth. (table 3-3 entry 28). (C) Jet propulsion from motors oriented horizontally (parallel to the slide) are largely restricted to motion in the Z axis (a few hundred microns). Self-propulsion from vertically oriented motors (perpendicular to the slide) can cover large areas in the XY axes and motion is observable with the microscope objective.

Jet-like propulsion: Like with MnO_2 motors, some Rh_2OAc_4 motors released fast jets of bubbles which propelled the motors when in enough solvent to submerge the motor. These were often larger complexes of small circular prints, formed during the wash procedure after

photocuring when UV post-curing was not carried out (Figure 3-18 A, B, t_1). On addition of substrate, the aggregates swell and generate gas (Figure 3-18 A, B, t_2). Thrust from the rapid bubble growth (Figure 3-18 A, t_3) or rapid bubble expulsion (Figure 3-18 B, t_3) cause the motor to reorient itself from being parallel to the slide to being perpendicular to the slide. Importantly, these motors that oriented perpendicular to the slide surface demonstrated the jet-like movement and propelled themselves over large areas (Figure 3-18 A, B, t_4). Prints oriented parallel to the slide are largely restricted to propulsion in the Z axis, which is a few hundred microns deep, from the surface of the liquid to the surface of the slide (Figure 3-18 C). For motors oriented vertically, large areas for displacement in the XY direction are accessible and observable with the microscope objective.

3.3. Summary and conclusions

In summary, we developed methods for fabricating microscale polymer propulsion motors as small as 25 μm with embedded catalyst using visible light initiated photocurable resin and the DLP microscope. We investigated performance of these motors with MnO_2 catalyzed decomposition of hydrogen peroxide, and a novel propulsion system, the Rh_2OAc_4 catalyzed decomposition of ethyl diazoacetate. Methods for fabricating and isolating micromotors were optimized and their performance under varying conditions was characterized. Gas generation and self-propulsion was observed in both systems, as well as interesting behavior such as self-assembly, effects of reorientation, and whizzing on glass in minimal substrate solution. The methods and studies presented in this work provide a foundation for further experiments to systematically investigate and quantify these behaviors. A deep understanding of the behavior of these micromotors will facilitate streamlining of their features and ultimately advance their application in technology and medicine.

3.4. Experimental Methods

3.4.1. Micromotor Fabrication

Resin preparation. Liquid resin mixtures were prepared using published formulations with some modification.[24] A 2:1 mixture of *N*,*N*-Dimethylacrylamide (DMA) to trimethylolpropane triacrylate (TMPTA) was prepared containing 1 wt% H-Nu254 acceptor ([4-(octyloxy)phenyl](phenyl)iodonium hexafluoroantimonate diphenyliodonium) and 0.1 wt% Borate V donor (2-(butyryloxy)-*N*,*N*,*N*-trimethylethan-1-aminium butyltriphenylborate). 0.1 wt% Rose Bengal was used for photoinitiating under green light irradiation. No opaquing agents were added.

Non-loaded sample prep. On a glass microscope slide lined with 2 cm x 2 cm of adhesive FEP film and bordered with a double layer of vinyl-coated adhesive tape, 50 µL of the resin mixture was pipetted on. A #1.5 glass coverslip was placed on the tape to sandwich the solution.

Catalyst loaded sample prep. (1) Catalyst mixed in solution: 600 µL resin solution was prepared as above. MnO_2 or Rh_2OAc_4 (1 mg) was added to the mixture. For MnO_2 catalyst, the mixture was sonicated for 20 s for uniform suspension of the catalyst. This solution could be stored in the dark and used over 2-3 days. 50 µL of the solution was added onto the FEP lined slide and sandwiched with a coverslip as above. For Rh_2OAc_4 catalyst, the resin was not sonicated and had to be used within 1-2 hours of preparation. (2) Catalyst lined on FEP: MnO_2 or Rh_2OAc_4 (1 mg) powder catalyst was added to the FEP film lined slide. Using a polypropylene pipet tip, the catalyst powder was spread firmly and evenly on the FEP film. The excess was then tapped off. This gave an average catalyst loading on the FEP film of 0.18 mg/cm^2.

Photocuring. The prepared sample slide was placed on the stage of the DLP microscope (chapter 2) and imaged using weak red light (PWM = 10). Parallel RGB mode of the DLP projector was

used to mirror a powerpoint slide with patterns for micromotor printing eg a grid of circles. Light from the projector was focused onto the FEP film or coverslip. Then the light irradiation conditions were changed to high intensity green light for photocuring (PWM = 255) for 2 – 30 seconds. Large patterns (~300 μm – 1 mm) were photocured in less than 5 seconds. Small prints (~25 – 50 μm) required 30 or more seconds of light irradiation. To determine whether on not prints hade been generated, the slide was tilted to its side to gently move aside the solution covering the prints. The prints could then be observed by eye. Multiple patterning experiments could be carried out on the same slide by changing the field irradiated or, when needed, gently tilting the resin solution to an unused area of the slide.

Wash, post-cure and transfer. For washing micromotor prints, first the resin solution was soaked off using paper towel without disturbing any cured prints. Isopropanol was added to the slide using a pipet and then soaked with a paper towel. This was repeated multiple times until no more of the pink resin solution remained. The slide was then irradiated with 254 nm UV light from a handheld TLC plate viewing lamp for 10 min. The UV cured prints were transferred to a clean slide for testing or characterization, by gently pressing the slide with the prints against a clean slide.

3.4.2. Compilation of MnO_2 microbot experiment videos

Table 3-2. Compilation of MnO_2 microbot experiment videos

Entry	Link	Solvent	Shape	Bubbles	Propulsion	Notes
Table 3-2: MnO2						
1	https://photos.go	60 ip 10 po	circle+circle	yes, hybrid	aggregation, slow	mno2 in solution
2	https://photos.go	60 ip 10 po	circle+circle	yes, hybrid	no	mno2 in solution
3	https://photos.go	30 ip 30 h2o 3	circle	yes final	agregated already	aggregate of many tinys
4	https://photos.go	1:01:01	circle	yes	yes	propulsion and aggregation, dust strand
5	https://photos.go	1:01:01	circle	yes	yes	propulsion
6	https://photos.go	1:01:01	circle	yes	yes	propulsion and aggregation, dust strand
7	https://photos.go	1:01:01	circle	yes	yes	in solvent
8	https://photos.go	1:01:01	circle	yes initial	yes	timelapse, stuck to glass then carried off
9	https://photos.go	1:01:01	circle	yes	no	stuck to glass, large
10	https://photos.go	1:01:01	circle	yes	no	excessive bubbles
11	https://photos.go	1:01:01	circle	yes	yes	propulsion and aggregation
12	https://photos.go	1:01:01	circle	yes	yes	propulsion and aggregation
13	https://photos.go	1:01:01	circle	yes	no	stuck to glass, large
14	https://photos.go	1:01:01	circle	yes	yes	minimal solvent
15	https://photos.go	1:01:01	circle	yes	yes	minimal solvent, good tracker
16	https://photos.go	1:01:01	circle	yes	no	current. Aggregate
17	https://photos.go	1:01:01	circle	yes	no	
18	https://photos.go	1:01:01	circle+circle	yes	currents	much solvent, huuge aggregates
19	https://photos.go	1:01:01	circle+circle	yes	no	
20	https://photos.go	1:01:01	circle	yes	currents	much solvent
21	https://photos.go	1:01:01	circle	yes	currents	same exp as above
22	https://photos.go	1:01:01	rectangle	no	no	channel cover slip, control only
23	https://photos.go	1:01:01	rectangle, cone	yes	currents	channel cover slip, control and test
24	https://photos.go	1:01:01	cone	yes	no	cone against channe;
25	https://photos.go	1:01:01	cone	yes	slight	movements of cone in channel
26	https://photos.go	1:01:01	cone dimer	yes	slight	movements of cone dimer in channel
27	https://photos.go	1:01:01	cone dimer	yes	currents	cone dimer with much currents
28	https://photos.go	1:01:01	cone dimer	yes	no	no channel
29	https://photos.go	10po 30 ip	catalyst			
30	https://photos.go	10po 30 ip	cone	yes	no	
31	https://photos.go	10po 30 ip	cone	yes	wriggling	
32	https://photos.go	10po 30 ip	cone	yes	wriggling	2 cones large bubbles
33	https://photos.go	10po 30 ip	cone	yes	no	large bubbles that don't burst
34	https://photos.go	10po 30 ip	circle+circle	yes	wriggling	hybrid bubbling
35	https://photos.go	10po 30 ip	circle+circle	yes	wriggling	big hybrid bubbling
36	https://photos.go	10po 30 ip	circle+circle	yes	wriggling	big hybrid bubbling
37	https://photos.go	10po 30 ip	circle+circle	yes	yes much. Rocket	big hybrid bubbling rocket
38	https://photos.go	10po 30 ip	circle+circle	yes much	wriggling	compare to above
39	https://photos.go	ip and et mixe	circle	small bubbles	much curents	mixed solvents
40	https://photos.go	ip and et mixe	circle	small bubbles	no	timelapse in a channel. No propulsion
41	https://photos.go	ip and et mixe	circle	small bubbles	bubble push	movement in channel

42	https://photos.go	10po 60 30ip	circle	yes	skate along surface	coverslip
43	https://photos.go	10po 60 30et	circle	big bubbles	wriggling	big bubbles in etoh. Coverslip
44	https://photos.go	10po 60 30ip		small bubbles	currents	small bubbles in ip isolated prints wo coverslip?
45	https://photos.go	1po: 2wa	circle	yes	no	water. Bubbles don't disperse. Coverslip
46	https://photos.go	1:01:01 etoh	circle	yes	no	catalyst in etoh. Print near end, coverslip
47	https://photos.go	1:01:01 ip	circle	yes	yes	proplsion in ip, coverslip
48	https://photos.go	1:1:1 et	circle	yes	yes	bubbling, skating, coverslide
49	https://photos.go	1:1:1 et				skate on bubble
49	https://photos.go	1:1:1 et				skate on edge bubble
50	https://photos.go	1:1:1 et				good propulsion then skating on bubbles
51	https://photos.go	1:1:1 et				
52	https://photos.go	1:1:1 et				
53	https://photos.go	1:01:02				less peroxide more et, slow bubbling
54	https://photos.go	1:01:02				walking on bubble
55	https://photos.go	1:01:02				no movement in water
56	https://photos.go	3% in water	circle	yes	yes but bouyancy	All aggregate to surface once unstuck. No coverslip
57	https://photos.go	3% 1:1 H2O D	circle	yes	uyancy, aggregation an	All aggregate to surface once unstuck. No coverslip
58	https://photos.go	with 1% SDS	circle	yes, slow	no	no mevement and vvv slow bubbles
59	https://photos.go	30% in water	circle, 3D	yes, slow	no	no mevement and fizzy bubbles
60	https://photos.go	30% in water				no mevement and fizzy bubbles
61	https://photos.go	30% in water				no mevement and fizzy bubbles
62	https://photos.go	foaming soap / 1% SDS				crazy foam and too much fizz
63	https://photos.go	with 1% SDS		yes	no	generation and accumulation of bubbles
64	https://photos.go	30% in water		yes	yes bouyancy	peel off and float to top.
65	https://photos.go	30% in water		yes	yes bouyancy	float and congregate to center. Recoil at center
66	https://photos.go	3% in water with 1mg/mL SDS		yes	yes bouyancy	nice initial. Flow to middle. Dense fizz
67	https://photos.go					size of 0.25' prints
68	https://photos.go	3% in water		yes, slow	yes, bouyancy	accumulate in center. Interesting assembly
69	https://photos.go	3% in water (and dmf?)		yes, slow	yes, bouyancy	accumulate in center. Interesting assembly
70	https://photos.go	3% in water (and dmf?)				near the end of vid, the recoil fights the bouyancy
71	https://photos.go	3% in water (and dmf?)		yes	yes bouyancy	nice tracker. 5 prints come together
72	https://photos.go	3% in water on FEP		yes, big slow	slight	on FEP
73	https://photos.go	30% in water on FEP		yes, big slow	slight	on FEP
74	https://photos.go	3% in DMSO		yes, few	no	DMSO on FEB no bubbles
75	https://photos.go	30% in water on glass		yes		no coverslip, accumulate in middle
76	https://photos.go	3% water on glass		yes slower	no	h202 conc dep
77	https://photos.go	3% h202 in water		yes	wriggling	bubbles generated on fep
78	https://photos.go	3% in water		yes	no, stuck	
79	https://photos.go	3% in water	rect on circl	yes	wriggling	hybrid bubble gen
80	https://photos.go	3% in water	rect on circl	yes	wriggling	
81	https://photos.go	3% in water	rect on circl	yes	wriggling	initial
82	https://photos.go	10-30% po	circle	yes	no	bubbling in peroxide first ever

3.4.3. Compilation of Rh_2OAc_4 microbots experiment videos

Table 3-3. Compilation of Rh_2OAc_4 microbots experiment videos

1	https://photos.go 1:2 eda:sty	rect agg		some twisting	no fep
2	https://photos.go 1:2 eda:sty	circ agg	yes	some breathing	with fep
3	https://photos.go 1:2 eda:sty	circ agg	yes		timelapseaggs generate big bubbles
4	https://photos.go 1:2 eda:sty	circ agg			aggs generate big bubbles
5	https://photos.go 1:2 eda:sty	circ agg	yes	yes	agg with much bubble hobbles around on fep
6	https://photos.go 1:2 eda:sty	circ agg	yes	yes	same exp as above
7	https://photos.go 1:2 eda:sty	circ agg	yes	yes	same exp as above
8	https://photos.go 1:2 eda:sty	circ agg	yes	yes	same exp as above
9	https://photos.go 1:2 eda:sty	circ agg	yes	yes	same exp as above
10	https://photos.go 1:2 eda:sty	circ agg	yes	yes	too much chnages in camera
11	https://photos.go 1:2 eda:sty	2-3 circles	yes	wriggling	with FEP
12	https://photos.go 1:2 eda:sty	2-3 circles	yes	no	time lapse and big bubbles
13	https://photos.go 1:2 eda:sty	ıted over each other like fish and shapes			
14	https://photos.go eda		yes	no	first hybrid bubbling
15	https://photos.go eda				photograph of above
16	https://photos.go eda	crystal	yes	slight	crystals generating bubbles and moving around
17	https://photos.go eda	crystal	yes	slight	crystals generating bubbles and moving around
18	https://photos.go eda	powder	yes	caried by current	small pieces of catalyst
19	https://photos.go eda	circl	yes	no	coverslip means air fast
20	https://photos.go eda	circ	yes	yes	dense loading
21	https://photos.go eda	rect agg	yes	yes	stepping behavior
22	https://photos.go eda	circ	yes	yes	good assymm movement and then agg
23	https://photos.go eda		yes	wriggling	
24	https://photos.go eda		yes	breathing	
25	https://photos.go eda	big circ	yes	yes, stepping	
26	https://photos.go eda				same exp as above
27	https://photos.go eda				same exp as above
28	https://photos.go eda	aggregte	yes	yes	rhodium rocket on FEP , rocket when on its side
29	https://photos.go eda	aggregte	yes	yes	rhodium rocket on FEP , rocket when on its side
30	https://photos.go eda	aggregte			exp above ctd
31	https://photos.go eda	aggregte			exp above ctd
32	https://photos.go 1:2 eda:sty	aggregate	yes	yes	assymetric movement

3.5. References

1. Moran, J.; Posner, J. Microswimmers with No Moving Parts. *Physics Today* **2019**, *72* (5), 44–50.
2. Ismagilov, R. F.; Schwartz, A.; Bowden, N.; Whitesides, G. M. Autonomous Movement and Self-Assembly. *Angewandte Chemie* **2002**, *114* (4), 674–676.
3. Paxton, W. F.; Kistler, K. C.; Olmeda, C. C.; Sen, A.; St. Angelo, S. K.; Cao, Y.; Mallouk, T. E.; Lammert, P. E.; Crespi, V. H. Catalytic Nanomotors: Autonomous Movement of Striped Nanorods. *Journal of the American Chemical Society* **2004**, *126* (41), 13424–13431.

4. Karshalev, E.; Esteban-Fernández de Ávila, B.; Wang, J. Micromotors for "Chemistry-on-the-Fly." *Journal of the American Chemical Society* **2018**, *140* (11), 3810–3820.

5. Li, J.; Singh, V. V.; Sattayasamitsathit, S.; Orozco, J.; Kaufmann, K.; Dong, R.; Gao, W.; Jurado-Sanchez, B.; Fedorak, Y.; Wang, J. Water-Driven Micromotors for Rapid Photocatalytic Degradation of Biological and Chemical Warfare Agents. *ACS Nano* **2014**, *8* (11), 11118–11125.

6. Singh, V. V.; Martin, A.; Kaufmann, K.; D. S. de Oliveira, S.; Wang, J. Zirconia/Graphene Oxide Hybrid Micromotors for Selective Capture of Nerve Agents. *Chemistry of Materials* **2015**, *27* (23), 8162–8169.

7. Soler, L.; Magdanz, V.; Fomin, V. M.; Sanchez, S.; Schmidt, O. G. Self-Propelled Micromotors for Cleaning Polluted Water. *ACS Nano* **2013**, *7* (11), 9611–9620.

8. Uygun, D. A.; Jurado-Sánchez, B.; Uygun, M.; Wang, J. Self-Propelled Chelation Platforms for Efficient Removal of Toxic Metals. *Environmental Science: Nano* **2016**, *3* (3), 559–566.

9. Teo, W. Z.; Zboril, R.; Medrik, I.; Pumera, M. Fe0 Nanomotors in Ton Quantities (1020 Units) for Environmental Remediation. *Chemistry - A European Journal* **2016**, *22* (14), 4789–4793.

10. Díez, P.; Esteban-Fernández de Ávila, B.; Ramírez-Herrera, D. E.; Villalonga, R.; Wang, J. Biomedical Nanomotors: Efficient Glucose-Mediated Insulin Release. *Nanoscale* **2017**, *9* (38), 14307–14311.

11. Kuralay, F.; Sattayasamitsathit, S.; Gao, W.; Uygun, A.; Katzenberg, A.; Wang, J. Self-Propelled Carbohydrate-Sensitive Microtransporters with Built-in Boronic Acid Recognition for Isolating Sugars and Cells. *Journal of the American Chemical Society* **2012**, *134* (37), 15217–15220.

12. Molinero-Fernández, Á.; Moreno-Guzmán, M.; López, M. Á.; Escarpa, A. Biosensing Strategy for Simultaneous and Accurate Quantitative Analysis of Mycotoxins in Food Samples Using Unmodified Graphene Micromotors. *Analytical Chemistry* **2017**, *89* (20), 10850–10857.

13. Moran, J. L.; Posner, J. D. Phoretic Self-Propulsion. *Annual Review of Fluid Mechanics* **2017**, *49* (1), 511–540.

14. Pavlick, R. A.; Sengupta, S.; McFadden, T.; Zhang, H.; Sen, A. A Polymerization-Powered Motor. *Angewandte Chemie International Edition* **2011**, *50* (40), 9374–9377.

15. Jiang, H.-R.; Yoshinaga, N.; Sano, M. Active Motion of a Janus Particle by Self-Thermophoresis in a Defocused Laser Beam. *Physical Review Letters* **2010**, *105* (26).

16. Zhang, H.; Duan, W.; Liu, L.; Sen, A. Depolymerization-Powered Autonomous Motors Using Biocompatible Fuel *J. Am. Chem. Soc.* **2013**, *135*, 15734– 15737

17. Zhou, Y.; Dai, L.; Jiao, N. Review of Bubble Applications in Microrobotics: Propulsion, Manipulation, and Assembly. *Micromachines* **2022**, *13* (7), 1068.

18. Chi, Q.; Wang, Z.; Tian, F.; You, J.; Xu, S. A Review of Fast Bubble-Driven Micromotors Powered by Biocompatible Fuel: Low-Concentration Fuel, Bioactive Fluid and Enzyme. *Micromachines* **2018**, *9* (10), 537.

19. Gao, W.; Sattayasamitsathit, S.; Orozco, J.; Wang, J. Highly Efficient Catalytic Microengines: Template Electrosynthesis of Polyaniline/Platinum Microtubes *J. Am. Chem. Soc.* **2011**, *133*, 11862– 11864

20. Lee, T. C.; Alarcon-Correa, M.; Miksch, C.; Hahn, K.; Gibbs, J. G.; Fischer, P. Self-Propelling Nanomotors in the Presence of Strong Brownian Forces *Nano Lett.* **2014**, *14*, 2407– 2412

21. Solovev, A. A.; Mei, Y.; Bermudez Urena, E.; Huang, G.; Schmidt, O. G. Catalytic Microtubular Jet Engines Self- Propelled by Accumulated Gas Bubbles *Small* **2009**, *5*, 1688– 1692

22. Wilson, D. A.; Nolte, R. J. M.; van Hest, J. C. M. Autonomous Movement of Platinum-Loaded Stomatocytes *Nat. Chem*. **2012**, *4*, 268– 274

23. Ye, J.; Wilson, D. A.; Tu, Y.; Peng, F. 3D-Printed Micromotors for Biomedical Applications. *Advanced Materials Technologies* **2020**, *5* (11), 2000435.

24. Dabbagh, S. R.; Sarabi, M. R.; Birtek, M. T.; Seyfi, S.; Sitti, M.; Tasoglu, S. 3D-Printed Microrobots from Design to Translation. *Nature Communications* **2022**, *13* (1).

25. Malinauskas, M.; Farsari, M.; Piskarskas, A.; Juodkazis, S. Ultrafast Laser Nanostructuring of Photopolymers: A Decade of Advances. *Physics Reports* **2013**, *533* (1), 1–31.

26. Huang, J.; Qin, Q.; Wang, J. A Review of Stereolithography: Processes and Systems. *Processes* **2020**, *8* (9), 1138.

27. Chaudhary, R.; Fabbri, P.; Leoni, E.; Mazzanti, F.; Akbari, R.; Antonini, C. Additive Manufacturing by Digital Light Processing: A Review. *Progress in Additive Manufacturing* **2022**.

28. Haris, U.; Plank, J. T.; Li, B.; Page, Z. A.; Lippert, A. R. Visible Light Chemical Micropatterning Using a Digital Light Processing Fluorescence Microscope. *ACS Cent. Sci.* **2021**, *8*, 67-76

29. Ahn, D.; Stevens, L. M.; Zhou, K.; Page, Z. A. Rapid High-Resolution Visible Light 3D Printing. *ACS Central Science* **2020**, *6* (9), 1555–1563.

30. Naeem, S.; Naeem, F.; Mujtaba, J.; Shukla, A.; Mitra, S.; Huang, G.; Gulina, L.; Rudakovskaya, P.; Cui, J.; Tolstoy, V.; Gorin, D.; Mei, Y.; Solovev, A.; Dey, K. Oxygen Generation Using Catalytic Nano/Micromotors. *Micromachines* **2021**, *12* (10), 1251.

31. Zheng, J. Y.; Zhao, W. K.; Song, L.; Wang, H.; Yan, H.; Chen, G.; Han, C. B.; Zhang, J. Advances of Manganese-Oxides-Based Catalysts for Indoor Formaldehyde Removal. *Green Energy & Environment* **2022**.

32. Xu, H.; Yan, N.; Qu, Z.; Liu, W.; Mei, J.; Huang, W.; Zhao, S. Gaseous Heterogeneous Catalytic Reactions over MN-Based Oxides for Environmental Applications: A Critical Review. *Environmental Science & Technology* **2017**, *51* (16), 8879–8892.

33. Chen, Y.; Cong, H.; Shen, Y.; Yu, B. Biomedical Application of Manganese Dioxide Nanomaterials. *Nanotechnology* **2020**, *31* (20), 202001.

34. Wang, H.; Zhao, G.; Pumera, M. Beyond Platinum: Bubble-Propelled Micromotors Based on Ag and Mno2 Catalysts. *Journal of the American Chemical Society* **2014**, *136* (7), 2719–2722.

35. Safdar, M.; Minh, T. D.; Kinnunen, N.; Jänis, J. Manganese Oxide Based Catalytic Micromotors: Effect of Polymorphism on Motion. *ACS Applied Materials & Interfaces* **2016**, *8* (47), 32624–32629.

36. Bowden, N. B.; Weck, M.; Choi, I. S.; Whitesides, G. M. Molecule-Mimetic Chemistry and Mesoscale Self-Assembly. *Accounts of Chemical Research* **2000**, *34* (3), 231–238.

37. Aquino, G. A.; Silva-Jr, F. P.; Ferreira, S. B. Ethyl Diazoacetate. *SynOpen* **2023**, *07* (01), 110–113.

38. Moss, R. A.; Doyle, M. P.; Davies, H. M. L.; Parr, B. T. In *Contemporary Carbene Chemistry*; Wiley: Hoboken, NJ, **2014**.

39. Varela-Álvarez, A.; Yang, T.; Jennings, H.; Kornecki, K. P.; Macmillan, S. N.; Lancaster, K. M.; Mack, J. B.; Du Bois, J.; Berry, J. F.; Musaev, D. G. Rh2(II,III) Catalysts with Chelating Carboxylate and Carboxamidate Supports: Electronic Structure and Nitrene Transfer Reactivity. *Journal of the American Chemical Society* **2016**, *138* (7), 2327–2341.

40. Doyle, M. P. Perspective on Dirhodium Carboxamidates as Catalysts. *The Journal of Organic Chemistry* **2006**, *71* (25), 9253–9260.

Chapter 4

CHEMICAL SYSTEMS WITH PAIRED REACTIVITY AND FLUORESCENCE FOR SUPER RESOLUTION NANOFABRICATION

4.1. Introduction

Nanofabrication and precise manipulation of materials are increasingly setting the pace for continued improvement in emerging innovations.[1,2] From energy storage[3] to cancer therapeutics,[4] a shift towards miniaturization to dimensions ranging from 1 to 100 nanometers has been the observed trend in numerous fields of research. Though there is unlimited potential for the application of nanorobotics and nanomaterials in medicine[5,6,7,8,9] and technology,[10,11,12,13] limitations of resolution, cost, and scalability in current lithographic nanofabrication methods hinder the large scale realization of these possibilities.[14]

The most widespread lithographic technique, used in mass production of silicon-based integrated circuits, patterns light onto photoresists through masks followed by developing and etching procedures.[15] Despite the high throughput of this method, there is room for improved resolution without the incursion of high costs of photomasks and deep UV-compatible optics. On the opposite end of the spectrum, electron beam lithography, which uses a targeted beam of electrons to alter resists, achieves very high resolutions, but at high costs and with low throughput.[16] Neither photolithography nor e-beam lithography can selectively target desired molecular sites for versatile chemical syntheses, allowing no basis for innovations that stem from chemical alterations

with molecular specificity. The use of UV light and electron beams limits the range of substrates and chemical reactions.

A number of lithography techniques originate from principles of their microscopy counterparts. Dip Pen Nanolithography (DPN) uses scanning probe microscope tips to deposit substrates onto wafers through capillary action of a water meniscus.[17] Larger-area patterning requires arrays of thousands of "pens" which are fragile and expensive. STED (Stimulated Emission Depletion) lithography techniques which branch from STED microscopy,[18] consist of polymerization reactions on a resist that are initiated by excitation pulses of light, and co-irradiation with inhibiting wavelengths of light spatially patterned in a donut shape around the initiating beam of light to minimize the effective area of initiation.[19,20] Though high resolutions can be achieved, the technique is costly and only applicable to a narrow range of photoresists, photoinitiators, and photoinhibitors with specific photophysical properties.

SMLM (single molecule localization microscopy)[21] is another class of microscopy techniques which allow bypassing the diffraction limit of light for imaging. While SMLM now comprises an impressive arsenal of techniques, these are largely all targeted towards and limited to imaging. Unlike STED, DPN, and electron microscopy which have diverged into lithographic methods, the principles of SMLM are just beginning to be explored for nanofabrication. In this chapter, we develop special molecular systems which can be paired with SMLM to achieve nanolithography. Conventional fluorescence microscopy is limited in resolution by the diffraction of light: when a point source of light is imaged through an objective, the smallest size that it can be resolved to is given by

$$\lambda/_{2NA}$$

where λ is the wavelength of light and NA is the numerical aperture of the objective. Instead of a perfectly focused image, a diffraction pattern of the light, described by its point spread function (PSF) is obtained. A single fluorescent molecule, when emitting, appears as a spot with a 200−800 nm diameter. In SMLM, post-imaging analysis of this PSF can determine the molecule's precise location down to a few nanometers (Figure 4-1A).[22] Proximity to other emitters, however, leads to spatial overlap of the point spread functions of multiple emitters and prevents precise localization of these molecules (Figure 4-1B).

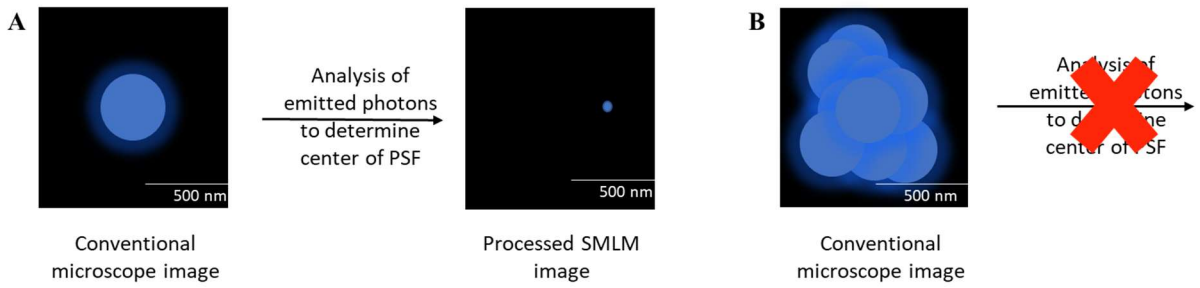

Figure 4-1. (A) Fluorescence images of single emitters can be used to determine their precise location by analysis of their point spread functions. (B) Spatial overlap of PSF of multiple emitters in proximity prevents precise localization

To overcome this limitation, a special class of "blinking" fluorescent molecules are used, which switch between their fluorescent and non-fluorescent states. At any point in time during image acquisition, only a small population of the molecules are in their fluorescent state, after which they revert to the dark state, and a different subset becomes fluorescent (Figure 4-2). Consequently, even if there are molecules in spatial proximity to each other, they are imaged at separate times according to their spontaneous blinking. Every image that is acquired captures the fluorescence emission of a small population of the molecules, and their locations can be precisely determined using localization software. Thousands of these processed images, captured with time, are then reconstructed to give a super-resolution image of all the molecules that emitted within the

captured timeframe. Figure 4-3 shows the difference in resolution between conventional microscopy and SMLM.[22]

Single molecule imaging dyes (blinking dyes) have evolved over time, with early dyes such as rhodamine and fluorescein giving way to newer dyes like Cy3, Cy5, and Alexa Fluor dyes. These newer dyes have higher quantum yields, better photostability, and are more prone to blinking, making them ideal for single molecule imaging experiments.[23] In addition, they have narrower absorption and emission spectra, making it easier to distinguish between different molecules. A variety of mechanisms and strategies have been developed to induce blinking in such molecules, including photo-switchable dyes that can be toggled between bright and dark states by exposing them to specific wavelengths of light,[21,24,25] photoactivatable dyes that can be converted from a dark state to a bright state by exposing them to a high-intensity light pulse,[26] photobleaching and fluorescence recovery of individual dye molecules,[27,28,29] and spontaneously interconverting dyes that interchange between emissive and non-emissive states via intramolecular or intermolecular reactions mediated in special buffer systems.[30,31,34,40] While the mechanism and implications of blinking fluorescence have been widely explored due to the utility in super resolution imaging, blinking *reactivity* and its conjunction with fluorescence has not yet been investigated.

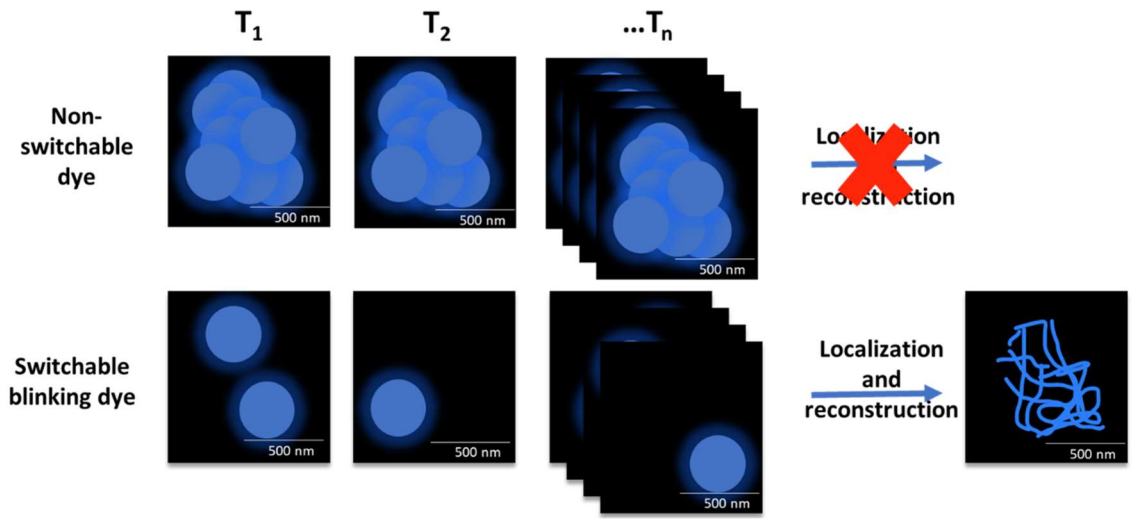

Figure 4-2. Conventional fluorescence microscopy cannot achieve resolutions beyond the diffraction limit. Using SMLM and blinking fluorophores allows super-resolution imaging. At any point in time, a small subset of molecules is in their fluorescent state while others are non-fluorescent. Many images are acquired over a short period of time, with each image having a different subset of molecules that are fluorescent. The fluorescent molecules in each image are localized. Reconstruction of thousands of images with localized molecules results in a super-resolution image of all the molecules that emitted within the captured timeframe.

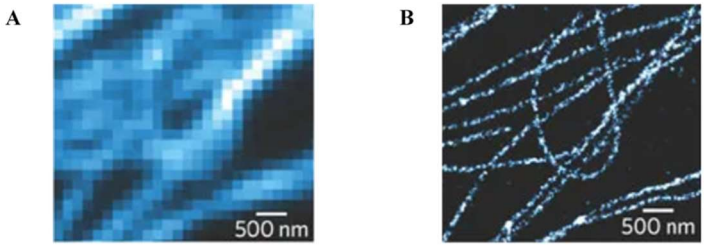

Figure 4-3. (A) Conventional microscopy image and (B) SMLM image of microtubules labeled with blinking dye Alexa Fluor 647. Figures reproduced with permission from reference 22. Copyright Springer Nature.

Previously, we developed a visible light mediated microscopy and lithography system for carrying out targeted chemical reactions on substrates using visible light with resolutions as high as 2.1 µm (Chapter 2).[32] In this chapter, we aim to develop chemical systems that are SMLM compatible and also chemically reactive, in order to push DLP patterning resolution beyond the diffraction limit of light, thus achieving lithography with single molecule specificity. By combining single molecule localization fluorescence microscopy with the light-

mediated reactions explored in Chapter 2, and tailored reactive molecules developed in this chapter, we aim to achieve chemical synthesis with single molecule precision in future studies.

4.2. Results and Discussion

4.2.1. Design principle for thiol-ene reactive blinking systems

In chapter 2, we explored the thiol-ene photoclick reaction between alkenes and thiols for functionalizing polymer resin beads with fluorescent dyes such as silicon rhodamine and rhodamine B. Since the thiol-ene ligation is a light-mediated reaction, targeting light at desired thiol-functionalized sites on a solid surface allows for spatial selectivity. The DLP microscope described in chapter 2 is capable of illuminating surfaces with patterned light with as much as 500 nm resolution. Figure 4-4 shows an illustrative example of a solid surface that is modified with thiols being irradiated with uniform blue light (Figure 4-4 A) and patterned blue light shaped by the digital micromirror device of the DLP projector (Figure 4-4 B). When in media containing a green fluorescent alkene and blue-light initiated photoinitiator eosin y, thiol-ene photoligation will occur at the immobilized thiol-sites on the solid surface that are under the light illumination. After washing, areas that show increased green fluorescence emission in response to fluorescence excitation are areas where thiol-sites have photoconjugated with the green-tagged alkene. Though the initiating blue light can be directed to very small areas, as small as 500 nm x 500 nm using the DLP microscope developed in chapter 2, beam spot sizes can not be resolved past their diffraction limit. As such, though sub-micron resolution is possible by focusing light, it cannot be focused to an extent that it targets only a single molecule. Figure 4-4C shows how even the smallest possible resolved beam of light would cause photoligation to occur at hundreds of thiol molecules in the irradiated area. Targeting single molecules cannot be conducted solely by structuring and focusing light.

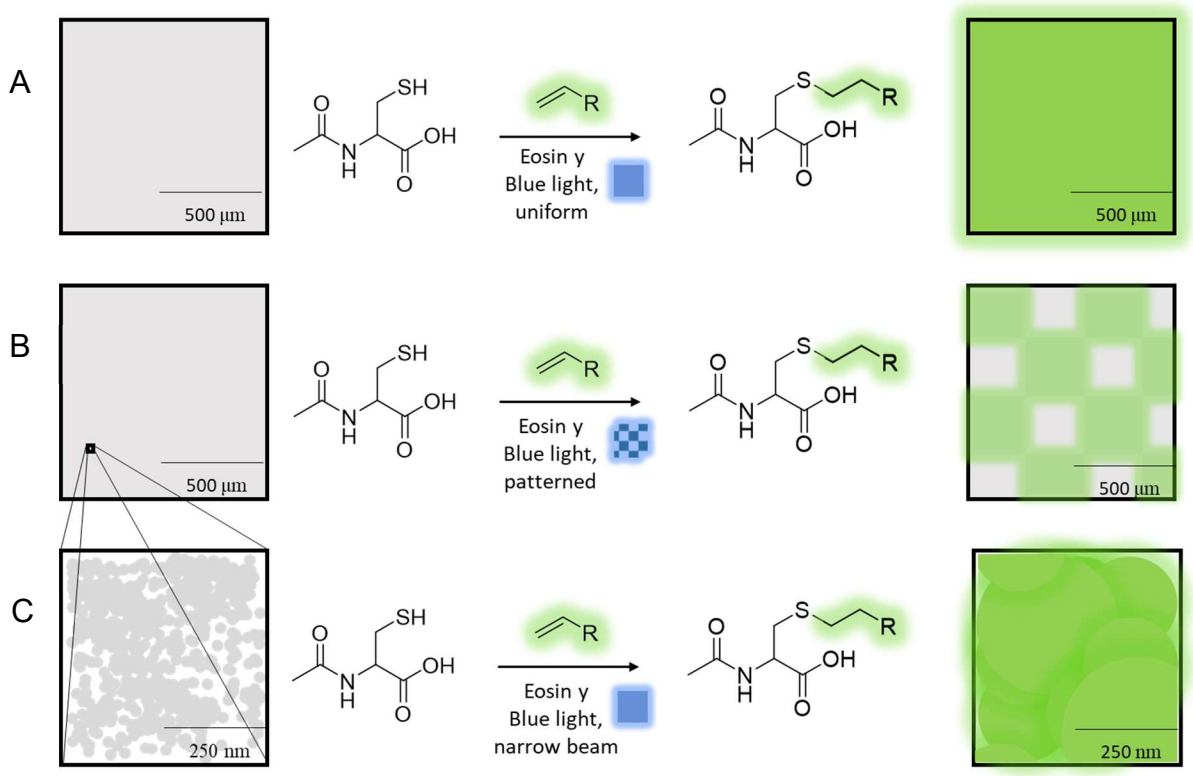

Figure 4-4. Diagram of irradiation of a thiol-modified solid surface (gray) with (A) uniform blue light and (B) patterned blue light in the presence of eosin y and a green fluorescent dye-tagged alkene leads to photoligation at the sites that are under the light illumination. Imaging the fluorescence emission of the tag under excitation light after washing off unreacted alkene shows lithography. (C) Focusing the irradiating blue light beam down to its smallest resolvable area (200–800 nm) leads to all thiol molecules within that area to undergo the ligation.

A combination of light patterning with novel blinking dyes, which not only switch between their fluorescent and non-fluorescent states, but also simultaneously between their reactive and unreactive states, may allow single-molecule precision. Figure 4-5 depicts the behavior of such a proposed dye and how it may be leveraged for chemistry at a single molecular scale. When in its closed form (Figure 4-4A), the dye is non-fluorescent, and its thiol functionality is caged as a sulfide. Spontaneously, the dye blinks into its open form (Figure 4-4 B), uncaging the reactive thiol functionality as well as becoming fluorescent. If this area is now illuminated with blue light,

even though there are many molecules in the field of illumination, only the very small subset that are in the open form at this time will undergo thiol-ene photoligation.

In this section, we explore two ways to of pairing fluorescence and reactivity: ring opening and closing (**TESiR**, **TMSiR**) and dynamic exchange chemistry (thiol-thioester exchange).

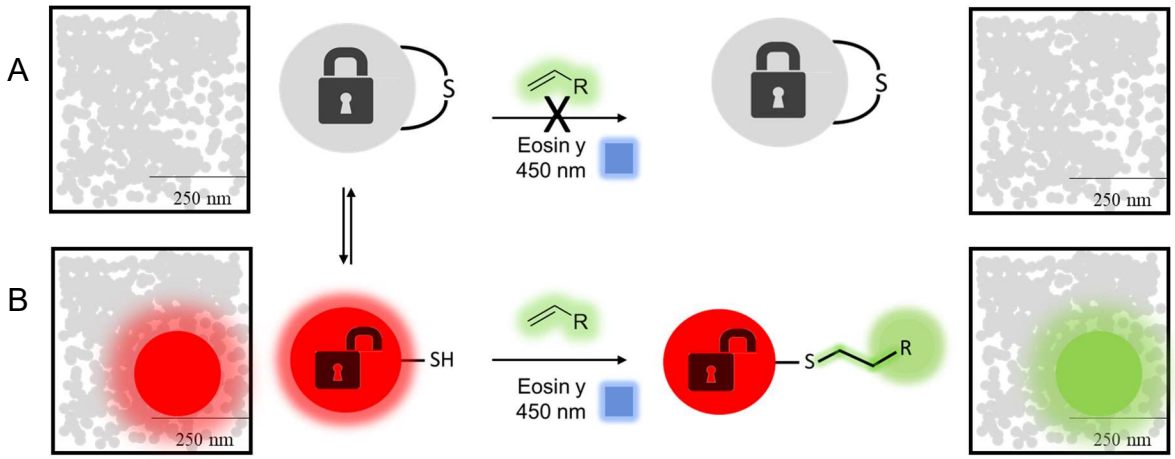

Figure 4-5. Super resolution photolithography using special blinking fluorescent dyes that switch spontaneously from unreactive sulfide to reactive thiol. (A) As sulfides, the dye molecules do not react with the alkene upon blue light irradiation. After wash, no green fluorescence emission is observed. (B) When a dye molecule spontaneously opens and uncages its thiol functionality, it can undergo the thiol-ene reaction when illuminated with blue light. Surrounding molecules that are in their closed forms do not react. After wash, green fluorescence is observed from the single molecule that reacted.

4.2.2. Ring opening systems **TMSiR** and **TESiR** for thiol-ene chemistry

4.2.2.1. Design and synthesis

We first synthesized **TMSiR** (thiomethyl silicon rhodamine), a derivative of a turn-on fluorescent agent 'MMSiR' previously reported in the literature for its use as a fluorescent sensor for hypochlorous acid (HOCl).[33] Upon oxidation of the sulfide by HOCl, and consequent ring opening the compound becomes irreversibly fluorescent. We wondered if instead of oxidation of

the sulfide, we could instead observe reversible interconversion between the sulfide and thiol forms (Scheme 4-1 A).

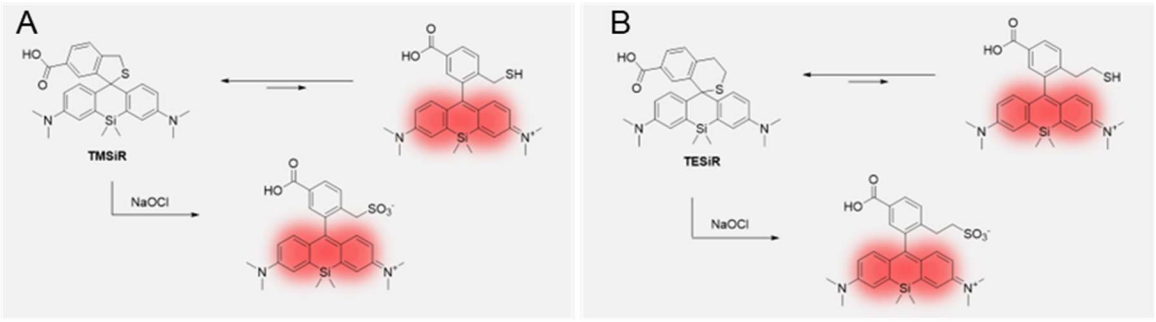

Scheme 4-1. Reversible equilibrium between sulfide and thiol closed and open forms, and irreversible oxidation to the open sulfonate forms of (A) **TMSiR** and (B) **TESiR**.

To synthesize **TMSiR**, 3-iodo-4-methylbenzoic acid was first reacted with 1-boc anhydride to generate the *t*-butyl protected compound **1**, which was then brominated at the methyl position using NBS (Scheme 4-2). A nucleophilic substitution of the bromine with *t*-butyl mercaptan furnished compound **3**, which was then reacted with silicon anthrone (chapter 2 compound **1**) via a lithium halogen exchange and nucleophilic addition reaction. Cleavage of the tert-butyl protecting groups on the thiol and the carboxylic acid generated **TMSiR** as a pale blue, non-fluorescent compound in its closed form.

We also designed **TESiR** (thioethyl silicon rhodamine), which is identical to **TMSiR** except the sulfur herterocycle contains 6 members instead of 5 (Scheme 4-1 B). While Baldwin's rules indicate that ring closure for the 5 membered ring in **TMSiR** (5-exo-trig) and the 6 membered ring in **TESiR** (6-exo-trig) are both favorable, literature suggests that an extension of the ring size in **TESiR** may increase the fluorescence lifetime of the molecule, (and the proportion of these molecules in their open thiol form), with the closed form still dominating, as is ideal for blinking dyes.[34]

For synthesis of the novel compound **TESiR**, 3-iodo-4-methylbenzoic acid was brominated at the methyl position and then subjected to an aqueous Wittig reaction[35] with formaldehyde to form the vinyl benzoic acid **7** (Scheme 4-2). After tert-butyl protection of the carboxylic acid, a hydroboration oxidation was carried out to add a hydroxyl group, which was then substituted by a tosyl group and subjected to nucleophilic substitution by tert-butyl mercaptan. Addition of this compound **10** to the silicon anthrone (chapter 2 compound 1) and subsequent deprotection of tert-butyl groups yielded **TESiR** as a pale blue solid.

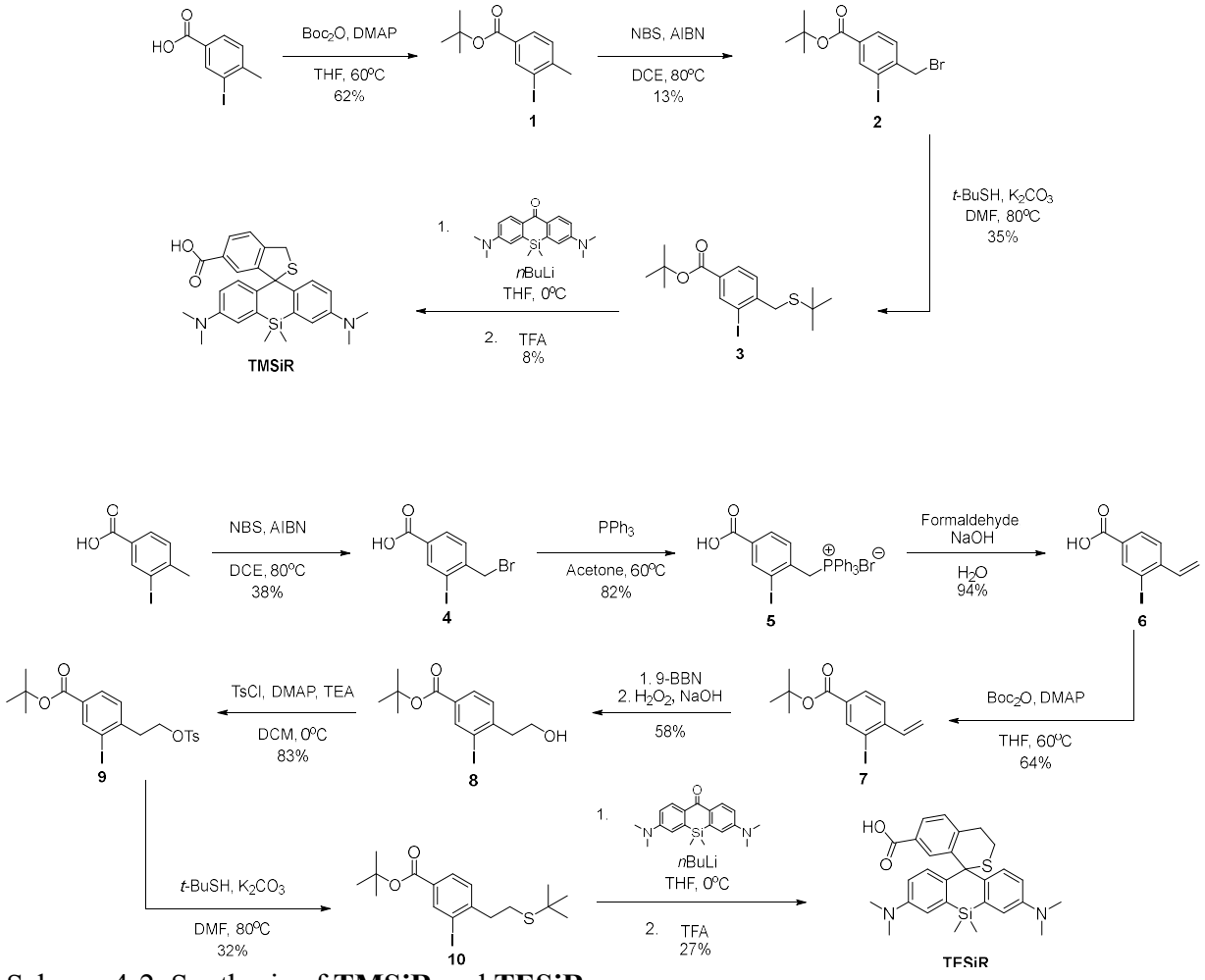

Scheme 4-2. Synthesis of **TMSiR** and **TESiR**.

4.2.2.2. **TMSiR** and **TESiR** spectroscopic characterization

Following synthesis, we characterized the fluorescence properties of **TMSiR** and **TESiR**. In the absence of HOCl, no fluorescence was observed from **TMSiR**. With addition of HOCl, a deep blue color developed, and fluorescent response was observed due to oxidation of the sulfide to the sulfite and opening of the ring, as previously shown in literature (Figure 4-6 A). We investigated if instead of using hypochlorous acid, we could establish a reversible opening and closing of the dye by varying pH to interconvert between the closed ring sulfide form and open thiol form. pH dependence studies of the molecule in buffers ranging from pH 1 to pH 10 indicated no significant pH dependence – the compound remains closed and non-fluorescent independent of pH (Figure 4-6 B). Similar results were obtained for **TESiR**: significant response was observed with NaOCl, but pH dependent emission was not observed (Figure 4-6 C, D).

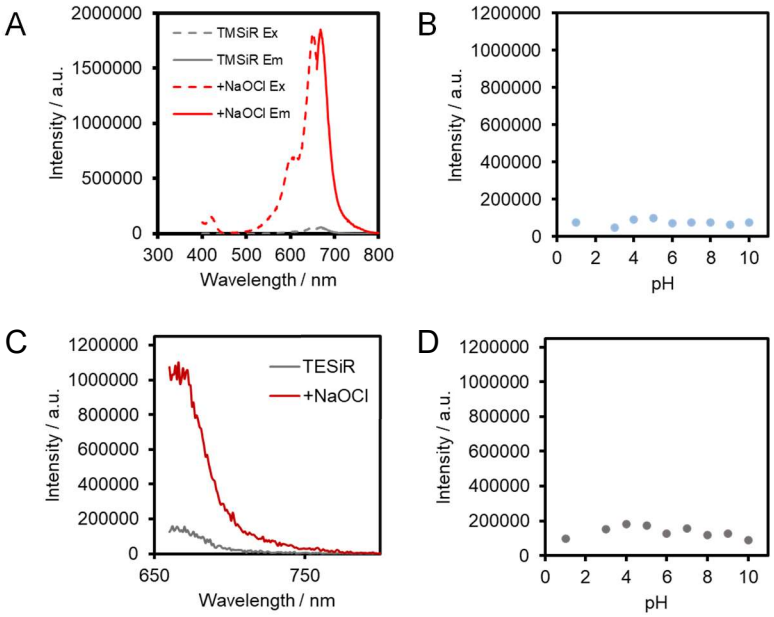

Figure 4-6. (A) Fluorescence excitation and emission spectra of 0.4 µM **TMSiR** in 1% MeOH in PBS pH = 7.4 with (red) and without (gray) 1 mM NaOCl. (B) Emission of 0.4 µM **TMSiR** at 665 nm in varying pH between 1 and 10 with 1% MeOH. (C) Fluorescence excitation and emission spectra of 0.5 µM **TESiR** in 1% MeOH in PBS pH = 7.4 with (red) and without (gray) 1 mM NaOCl. (D) Emission of 0.5 µM **TESiR** at 665 nm in varying pH between 1 and 10 with 1% MeOH.

We also investigated solvent dependence of **TMSiR** fluorescence emission (Figure 4-7). In DMSO, 1 M HCl, and PBS buffer (pH 7.4), the compound displayed minimal fluorescence. In DCM, MeOH, and MeCN some fluorescence emission was observed, while in $CHCl_3$ and EtOH acidified with 0.1% TFA, fluorescence emission signal indicated a 1:1 distribution of **TMSiR** in the open and closed forms. These studies are promising and suggest that the ratio of open to closed form of the dye can be tuned by varying the solvent.

We next explored if the reactive thiol handle on **TMSiR** could be used in chemical reactions to trap the dye in its open form (Figure 4-7 C). Disulfide exchange is an exchange reaction between thiols and disulfides where a thiol attacks the disulfide to break its S—S bond and form a new mixed disulfide comprising partly of the thiol and partly of the original disulfide. We treated **TMSiR** in aqueous solution with the disulfide Ellman's reagent (5,5′-dithiobis-(2-nitrobenzoic acid or DTNB) and monitored changes in fluorescence emission (Figure 4-7 B). Over a period of 3 hours, the fluorescence emission increased, indicating disulfide exchange of **TMSiR** with DTNB and formation of the disulfide with **TMSiR** in its open form. Reaction with N-ethylmaleimide (NEM), which irreversibly traps thiols by reaction with the maleimide also showed similar increased fluorescence, however the increase in intensity was not as high as with DTNB (Figure 4-7 B, C).

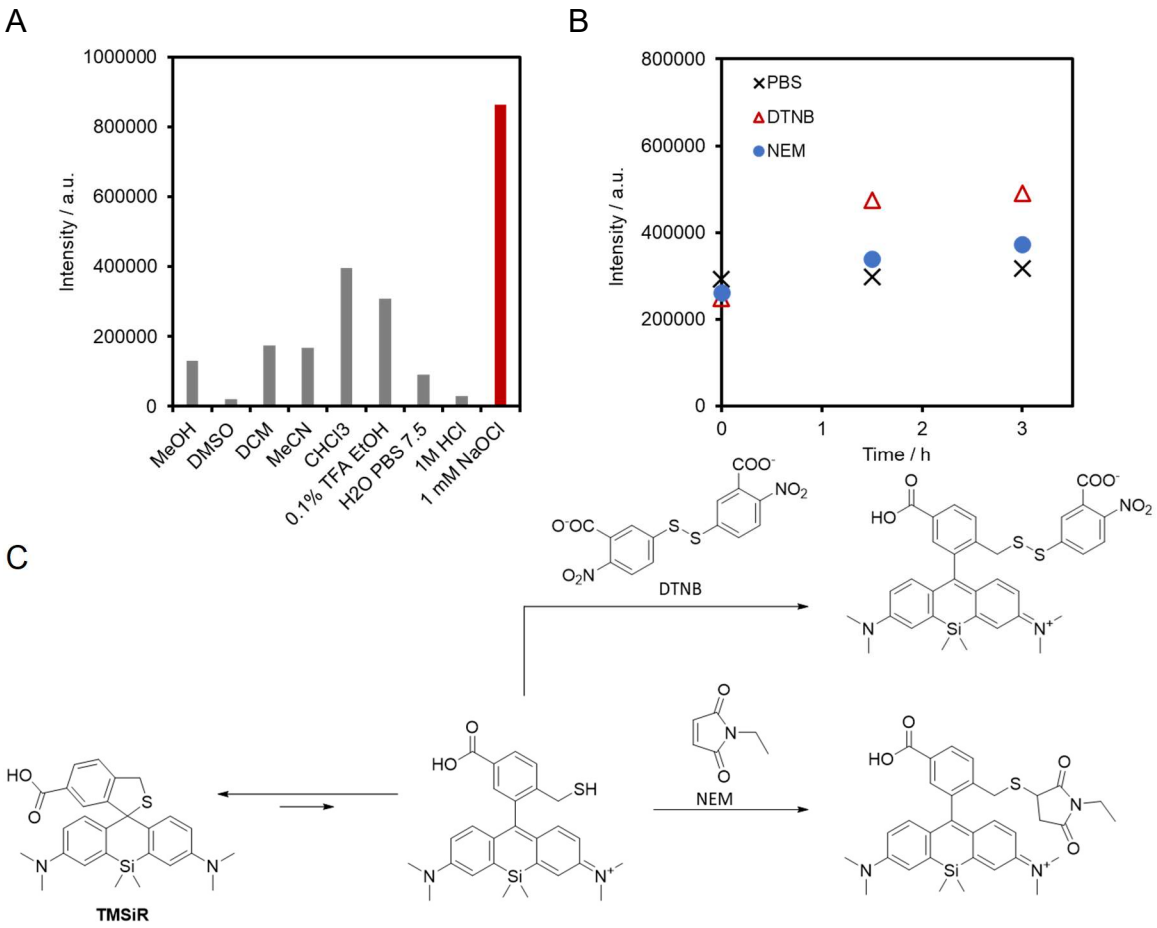

Figure 4-7. (A) Fluorescence emission of 0.42 μM **TMSiR** with 1% MeOH in different solvent conditions. (B) Fluorescence emission of 5 μM **TMSiR** at 680 nm with time in 1 mM DTNB (red), 1 mM NEM (blue), or PBS (black). (C) Reaction scheme of **TMSiR** with DTNB and NEM.

4.2.3. Dynamic thiol-thioester exchange systems for thiol-ene chemistry

4.2.3.1. Design and Synthesis

Aside from ring opening and closing mechanisms for modulating fluorescence and chemical reactivity as described above, we also explored schemes where fluorescence and reactivity could be controlled via fluorescence quenching and covalent thiol exchange. We designed a novel fluorophore-quencher system and paired it with a thiol-thioester exchange scheme (Scheme 4-3 B).[36] Similar to disulfide exchange, thioester exchanges consist of dynamic thioester bonds that can be interchanged between thiols and thioesters with fast kinetics and at low

concentrations in aqueous or organic media. Because of its favorable features, this exchange system has been utilized for studying protein folding, rapid combinatorial testing of ligands for enzymatic binding, and other biochemical applications.[37],[38] For the purpose of chemistry at a single molecular scale using thiol-ene photoclicking, we determined that this reaction could be used for spontaneous switching between a state that is reactive (thiol) and unreactive (thioester) towards an alkene substrate. We confirmed via NMR studies that only thiols, and not thioesters, can participate in thiol-ene photoclicking. Irradiation of n-octanethiol and styrene with blue light in the presence of eosin y photoinitiator led to formation of the sulfide photoclick product, however, the same reaction with acylated n-octanethiol, a thioester, led to no reaction occurring (Figure 4-8 A, B).

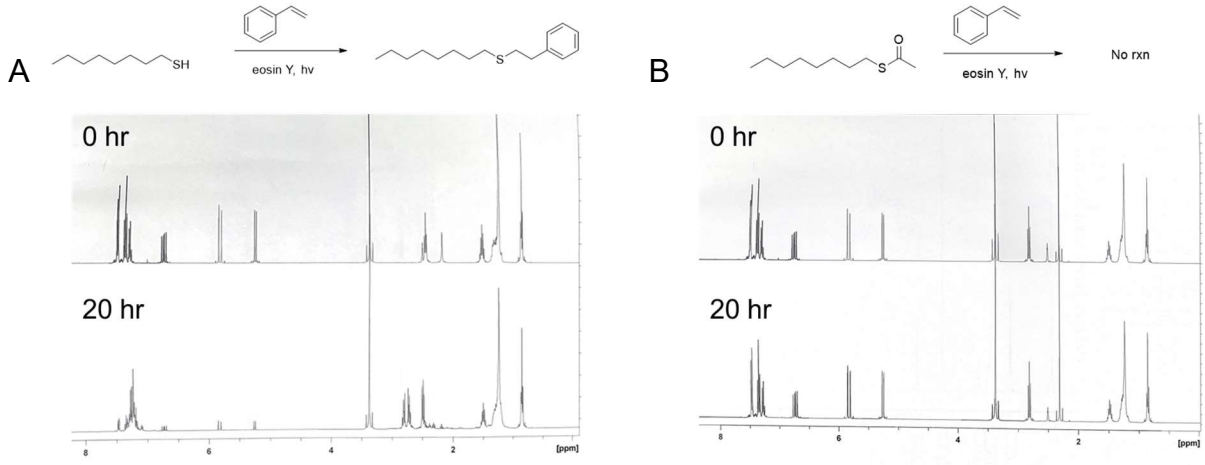

Figure 4-8. (A) ^{1}H NMR traces at 0 hours and 20 hours of light irradiation for n-octanethiol with styrene and eosin y. (B) ^{1}H NMR at 0 hours and 20 hours of light irradiation for acylated n-octanethiol with styrene and eosin y.

For the photoclicking to be targeted at an active molecule, a fluorescent indicator is required which can signal when a molecule exists as a thiol and not as a thioester. To accomplish this, we incorporated a fluorescence quenching strategy into a thioester exchange system to pair reactivity with fluorescence emission (Scheme 4-3 C). Forster resonance energy transfer (FRET)

is a process by which a donor molecule in its excited state (in this case, a fluorophore) non-radiatively transfers its energy to an acceptor molecule in close proximity and with spectral overlap (in this case, a quencher). The acceptor molecule is thus promoted to its excited state, and can relax radiatively if it is a fluorophore, or non-radiatively if it is a dark quencher (Scheme 4-3 A).

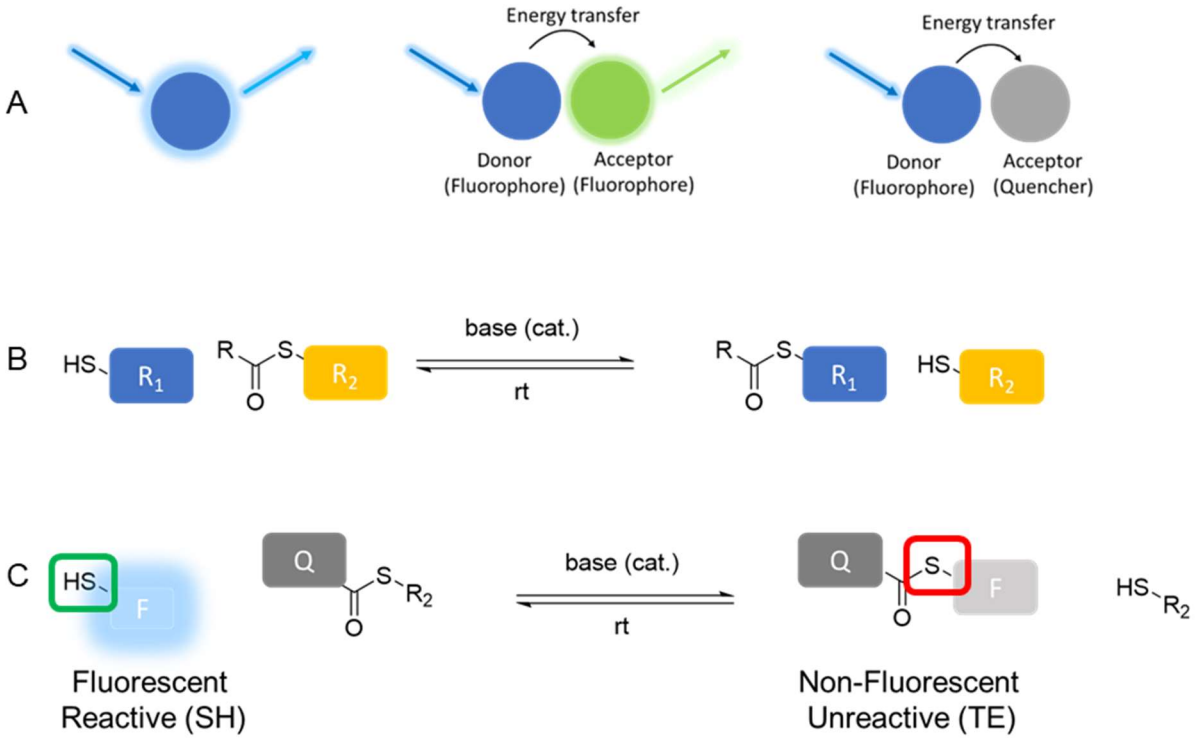

Scheme 4-3. (A) Energy transfer. Left: fluorophore absorbs and re-emits light. Middle: Donor fluorophore absorbs light, transfers energy non-radiatively to acceptor fluorophore, which emits light. Right: Donor fluorophore absorbs light, transfers energy to acceptor quencher, which relaxes without emitting light. (B) Reaction scheme for base promoted thiol-thioester exchange. (B) Spontaneous quenching of fluorescence and conversion of thiol (SH) functionality to thioester (TE) via thioester exchange between fluorophore (F) and quencher (Q) compounds.

First, we functionalized a fluorescent molecule with a thiol functionality so that it is reactive towards alkenes in a thiol-ene photoclick reaction. Next, we prepared a thioester which incorporates a fluorescence quencher. Upon thiol-thioester exchange between these two species, a new thioester is formed comprising of the fluorophore and the quencher. Because of the newly formed covalent linkage and close proximity between the fluorophore and quencher, quenching can occur, and because the compound exists as a thioester, it is no longer reactive towards alkenes.

Only when the dye exists as a thiol is it fluorescent. As a thioester, its fluorescence is quenched. Dynamic occurrence of this process results in spontaneous switching between the reactive, fluorescent state and the unreactive, non-fluorescent state.

4.2.3.2. Selection and synthetic modification of dye-quencher system

We began investigating fluorophore and quencher pairs by first synthesizing fluorescent dyes incorporating a thiol functionality. We chose three dyes with specific spectroscopic properties to cover a large range of emission wavelengths: coumarin 343 is a small water-soluble dye with an emission max of 470 nm (blue); rhodamine B is a xanthene-based dye with high quantum yields which emits at 565 nm (orange); and silicon rhodamine is a silicon incorporating xanthene based dye with a 680 nm emission (red). We appended thiols to the three dyes at their carboxylic acid reactive handles via condensation reactions with trityl protected cysteamine or mercaptoethanol. Cleavage of the trityl (Mmt or Trt) furnished the thiol functionalized dyes **coumarin-SH**, **RhB-SH** and **SiR-SH** (scheme 4-4).

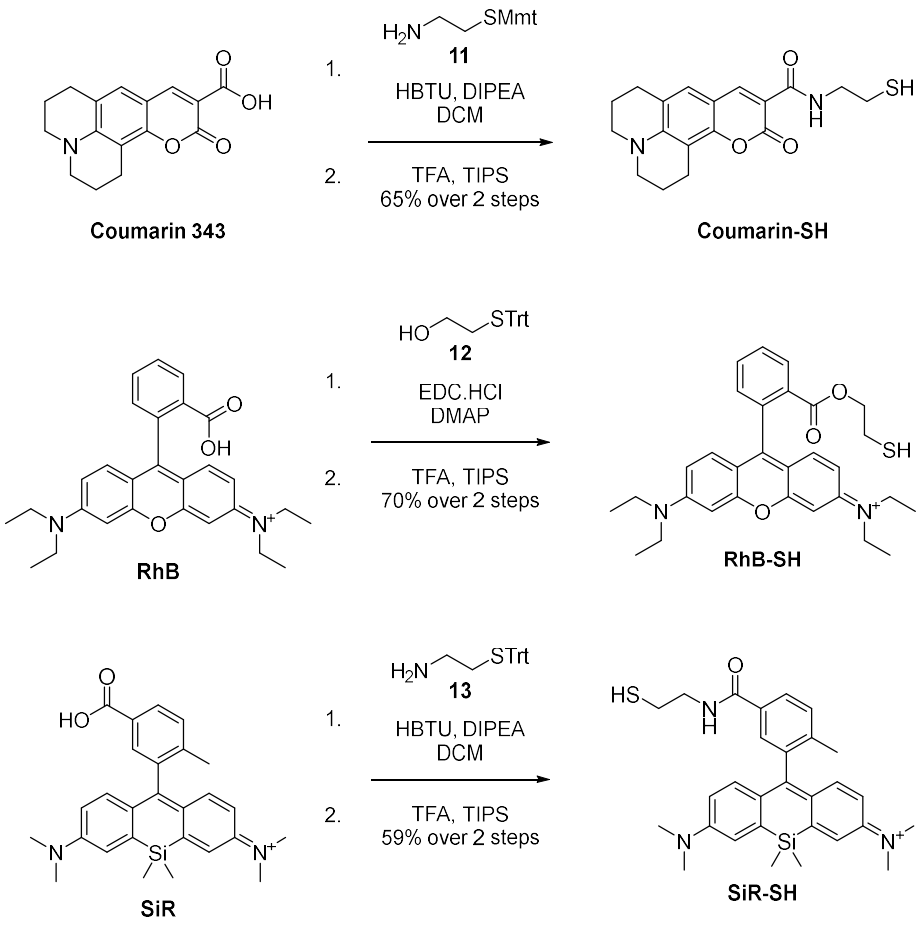

Scheme 4-4. Synthesis of **RhB-SH** and **SiR-SH**.

While quenchers such as the Blackhole Quencher series exist for longer wavelengths that could be paired with RhB and SiR (λ_{em} >550 nm), the low-cost and ease of availability of lower wavelength quenchers pushed us to investigate **coumarin-SH** quenching systems. DABCYL is a well-known, commercially available diazobenzene-based FRET quencher which is effective in quenching emission in the range of 350—550 nm. We paired DABCYL with **coumarin-SH** based on their spectral overlap and investigated the quenching efficiency in this fluorophore-quencher system using fluorescence quantum yield (Φ_{fl}) experiments (Eq. 4-1). Absolute fluorescence quantum yields were measured using an integrating sphere (Appendix A).

$$\Phi_{fl} = \frac{n\ photons\ emitted}{n\ photons\ absorbed} \qquad (Eq\ 4-1)$$

We measured the fluorescence quantum yield of mixtures of **coumarin-SH** and DABCYL in DMSO at different concentrations. Because FRET quenching efficiency is inversely proportional to the distance between the energy donor and the energy acceptor, we found that the quantum yield of the mixture increased with increasing dilution (i.e., decreasing concentration): the more concentrated the solution, the closer the proximity of the quencher and the fluorophore, the higher the quenching efficiency, and the lower the emission (Figure 4-9). In a sample of covalently linked fluorophore and quencher, fluorescence is quenched independent of concentration since the quencher is held in proximity to the fluorophore via covalent bonds. We synthesized **coumarin-DABCYL**, a thioester compound covalently linking **coumarin-SH** and DABCYL (Scheme 4-4). The fluorescence quantum yield of this quencher-linked compound was found to be 0.063 in DMSO, which is low as expected, compared to the 0.196 quantum yield of the **coumarin-SH** precursor which has no quencher attached (Figure 4-9).

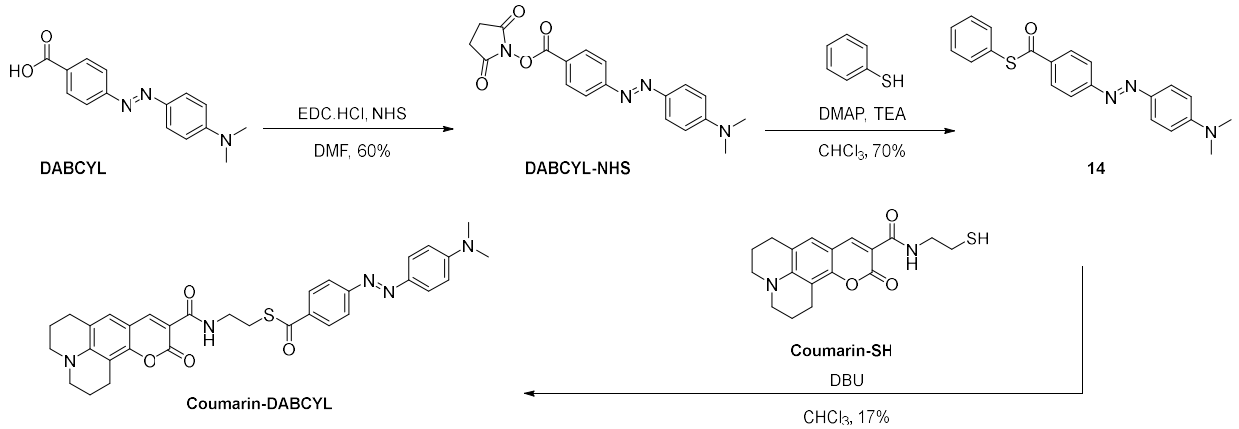

Scheme 4-5. Synthesis of **coumarin-DABCYL**.

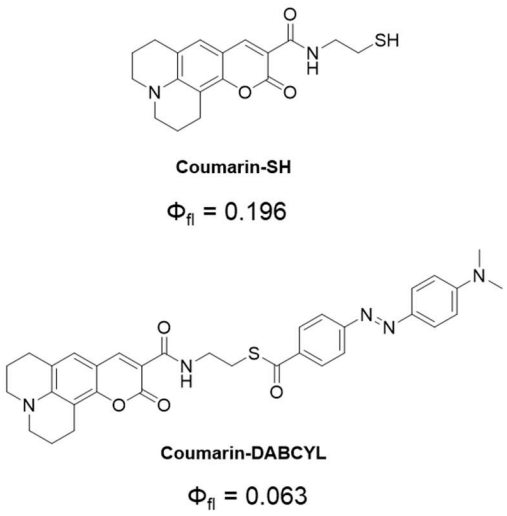

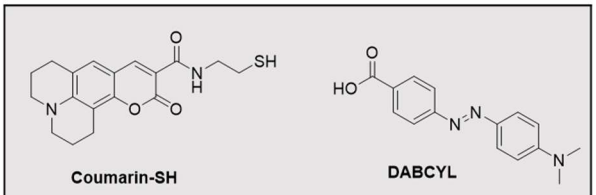

Concentration	Φ_{fl}
0.3 μM	0.148
3 μM	0.131
30 μM	0.072

Figure 4-9. Fluorescent quantum yields in DMSO of **coumarin-SH**, **coumarin-DABCYL**, and a 1:1 mixture of **coumarin-SH** with DABCYL at different concentrations.

4.2.3.3.Optimization of thiol-thioester exchange

Following confirmation that fluorescence quenching occurs between **coumarin-SH** and DABCYL, we next optimized the thiol-thioester exchange using model thiol and thioester compounds. According to earlier literature, thioesters made with thiols of low pK_a (such as thiophenol and 2-mercaptopyridine) have high acyl transferability and participate efficiently in thioester exchange.[36] Based on this we synthesized compound **14,** the DABCYL thioester of thiophenol as the reaction partner which would readily undergo thioester exchange (Scheme 4-5).

We investigated the kinetics of thioester exchange between compound **14** and several different thiols with varying pK_a via ^1H NMR experiments. The reaction was carried out in deuterated DMSO which promotes thioester exchange in the presence of catalytic triethylamine. NMR scans were acquired over time intervals of 0—24 hours, at which point the reaction reached equilibrium. The integrals at equilibrium for starting material and product peaks were used as a measure of their concentration to calculate the equilibrium constant K_{eq}. Figure 4-10 shows an

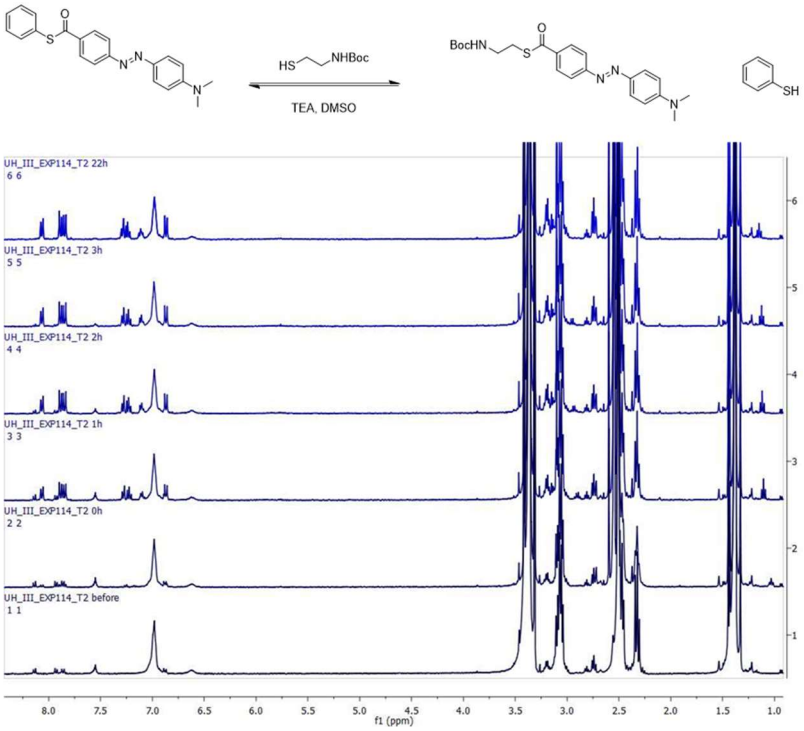

Figure 4-10. ^{1}H NMR spectra of the reaction between compound **14** and (boc-amino)ethanethiol in deuterated DMSO with 0.1 equiv. TEA at different time intervals after mixing.

example of NMR traces acquired at different time points for the reaction between compound **14** and (boc-amino)ethanethiol showing disappearance of starting material peaks and appearance of product peaks.

Table 4-1 summarizes the reactants, products and measured K_{eq} values for thioester exchange reactions explored between thioester **14** and various thiols. Product formation was favored in reaction with methyl 3-mercaptopropionate and (boc-amino)ethanethiol, while product formation was disfavored in reaction with n-octanethiol and 2- mercaptopyridine.

Starting Thioester	Starting Thiol	K_{eq}	Product Thioester	Product Thiol
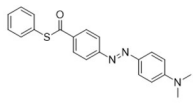	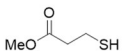	2.75 ± 0.32 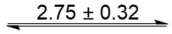 TEA, DMSO	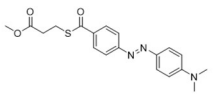	
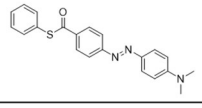	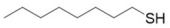	0.206 ± 0.078 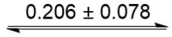 TEA, DMSO	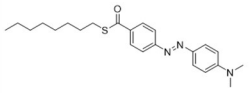	
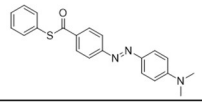		0.00120 ± 0.0009 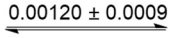 TEA, DMSO	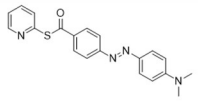	
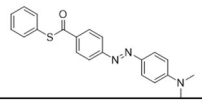	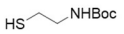	2.27 ± 1.30 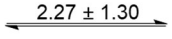 TEA, DMSO	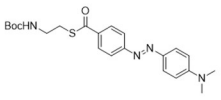	

Table 4-1. Summary data for ^{1}H NMR kinetics experiments to study thioester exchange reactions.

4.2.3.4. Thiol-thioester exchange for fluorescence and reactivity

With optimized reaction conditions and a suitable fluorophore quencher pair, we next investigated the thioester exchange reaction between the quencher-linked thioester **14** and the fluorophore linked thiol **coumarin-SH**. ^{1}H NMR data from 0 hours to 20 hours after mixing the reactants in DMSO-d6 with catalytic triethylamine showed no formation of product peaks. However, on addition of DBU (1,8-diazabicyclo[5.4.0]undec-7-ene) to the same reaction tube, new peaks appeared within 1 hour of addition. This is likely because DBU is a stronger base as compared to TEA and better able to deprotonate **coumarin-SH** and generate the thiolate which attacks the thioester. The exchange reaction with catalytic DBU was carried out and the equilibrium constant was calculated to be 1.01 ± 0.44, indicating product and reactant formation to be equally favorable (Figure 4-11).

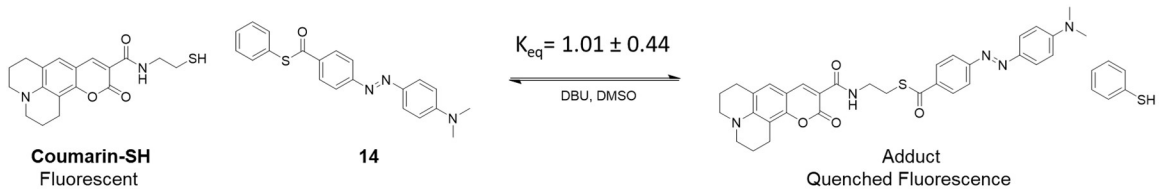

Figure 4-11. Thioester exchange reaction between compound **14** and **coumarin-SH**.

After characterizing the reaction via NMR, fluorescence spectroscopy experiments were carried out to determine if the exchange could be monitored spectroscopically. As a mixture of **coumarin-SH** and thioester **14,** the fluorescence quenching in dilute solutions is expected to be minimal and fluorescence emission should be high. After thioester exchange and formation of the adduct at equilibrium, the fluorescence emission is expected to be quenched due to formation of covalently linked dye-quencher adduct. In fluorescence emission experiments, only minimal differences were observed between the emission intensity of the reaction solution at 0 hours and at 20 hours after mixing the reagents despite NMR validation of adduct formation (Figure 4-12A). We instead carried out fluorescence quantum yield experiments to confirm the exchange spectroscopically. Since fluorescence quantum yield (Φ_{fl}) is a measure of how many photons are emitted by a sample as a proportion of how many photons are absorbed by the sample, Φ_{fl} measurements are not susceptible to variation due to errors in volumes from evaporation, unlike fluorescence emission which is concentration dependent. In Φ_{fl} studies we found the quantum yield of a 1 μM mixture of **coumarin-SH** and compound **14** at 0 hours after mixing with DBU catalyst to be 0.102 (Figure 4-12B). After 20 h of reaction, at equilibrium, the quantum yield was 0.049. This Φ_{fl} at equilibrium is roughly half of that at the start of the reaction, which agrees with the K_{eq} value of ~1: The fluorescent **coumarin-SH** and the non-fluorescent adduct are in roughly equal concentrations, and half the population of absorbing species are emissive.

A

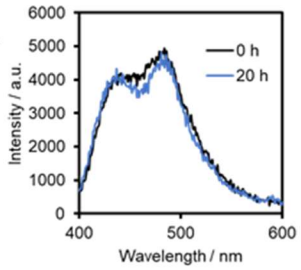

B

Time	Φ_{fl}
0 h	0.102
20 h	0.049

Figure 4-12. (A) Fluorescence emission of 1 µM mixture of **coumarin-SH** and compound **14** in DMSO with 0.1 equiv DBU at 0 hours (black) and 20 hours (blue) after mixing. (B) Fluorescence quantum yields of 1 µM mixture of **coumarin-SH** and compound **14** in DMSO with 0.1 equiv DBU at 0 hours and 20 hours after mixing.

These experiments together confirm that exchange of thiol and thioester functionality occurs in this system and leads to quenching and restoration of fluorescence. On a molecular scale, this translates to spontaneously blinking dyes with paired reactivity and fluorescence which forms the foundation for single molecule chemical lithography.

4.2.4. Ring opening systems for Wolf Rearrangement chemistry

4.2.4.1. Design, synthesis and characterization of **HMSiR** and **HMSiR-2.**

In chapter 2, we demonstrated that visible light mediated Wolff Rearrangement of diazoketones such as **RhBNN** can be used for surface functionalization.[32] **RhBNN**, when irradiated with visible light, forms a highly reactive carbene intermediate that reacts with surrounding nucleophiles.[39] Previously, we utilized this chemistry to carry out patterned labelling in polyvinylalcohol films, live cells, and polymer resin with resolutions of almost 2 µm. To build upon the technique and push the resolution into the super resolution regime, we aimed to develop a scheme for spontaneous fluorescence and reactivity with this system as well. For reaction with **RhBNN**, we envisioned a molecule that would uncage a nucleophilic functionality and fluoresce spontaneously via a ring opening mechanism. Hydroxymethyl silicon rhodamine (**HMSiR**)[40] is a

high performing single molecule imaging dye developed by Urano *et al.* which spontaneously switches between an alcohol and an ether at pH 7.4. In its open form, **HMSiR** exists as a nucleophilic alcohol with conjugated xanthene rings that make it fluorescent. In its closed form, **HMSiR** is an unreactive, non-fluorescent ether.

We synthesized **HMSiR** using a modified literature procedure (Scheme 4-6). 3-Iodo-4-methylbenzoic acid was first brominated in a radical bromination reaction, the product of which was hydrolyzed to aldehyde **16** and then reduced to benzylalcohol **17** using sodium borohydride at low temperature. *t*-Butyl protection of the carboxylic acid and alcohol functionalities afforded compound **18**, which then underwent lithium-halogen exchange with *n*-butyllithium and reacted with Si-anthrone (chapter 2 compound **1**) to form the *t*-butyl protected dye **19**. Deprotection with TFA yielded the final hydroxymethyl silicon rhodamine **HMSiR**.

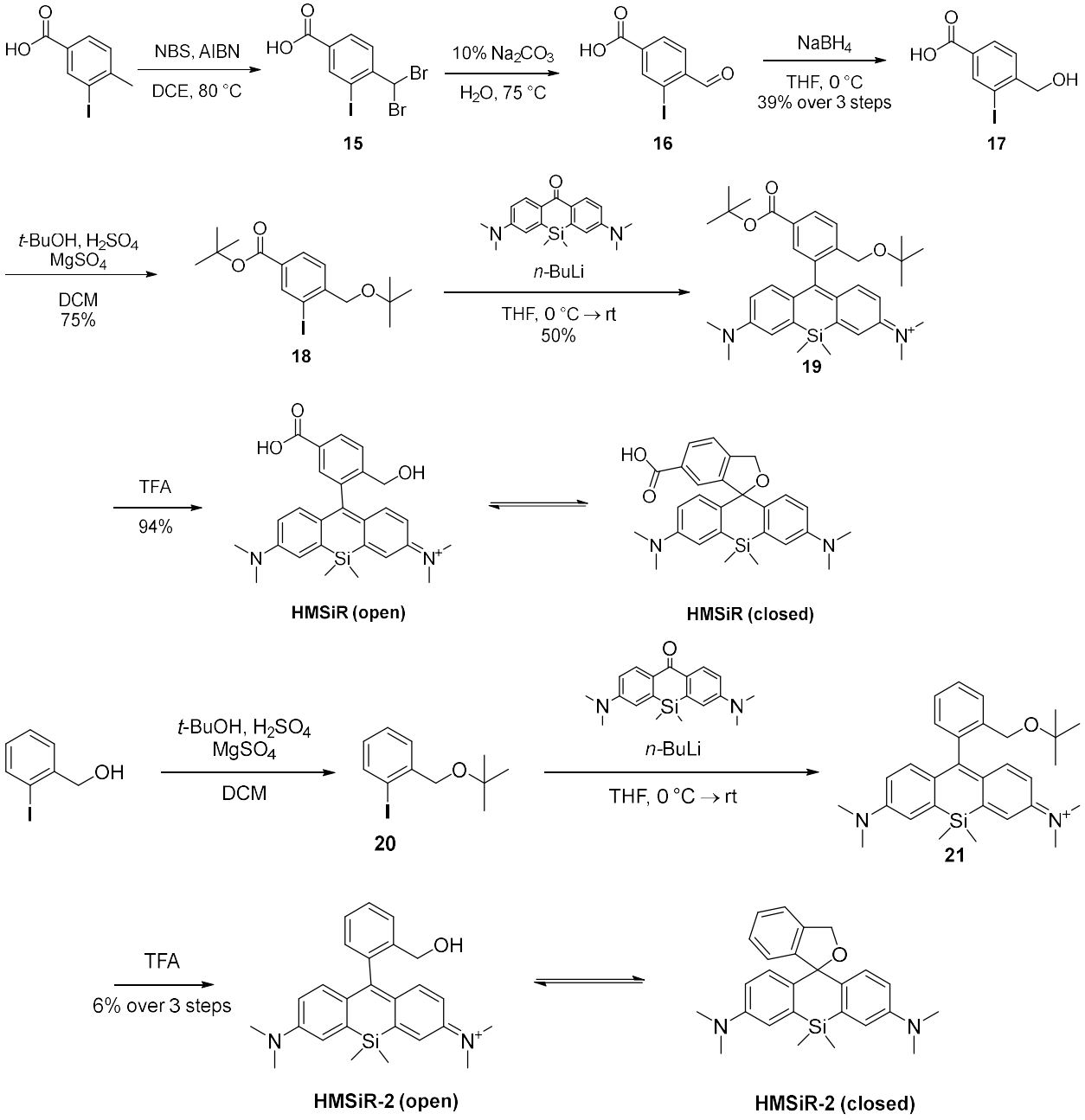

Scheme 4-6. Synthesis of **HMSiR** and **HMSiR-2.**

HMSiR exists primarily in its open and fluorescent form at low pH, and in its closed, non-fluorescent form at higher pH. We observed the difference in fluorescence instensity at these pH by linking **HMSiR** at its carboxylic acid functionality to amine-functionalized resin in an amide coupling, and imaging the resin beads on a fluorescence microscope in buffers of pH 5 and pH 7.4 (Figure 4-13). At pH 5, a majority of the **HMSiR** molecules are protonated, red fluorescence

emissive, and blue in color. At pH 7.4, only a small subset of the population is fluorescent at a given time before transitioning to their closed form. Because **RhBNN** is reactive towards nucleophiles when irradiated with light, it is reactive only towards the open form of **HMSiR**, which has a reactive hydroxyl group, and unreactive towards the closed, ether from of **HMSiR**.

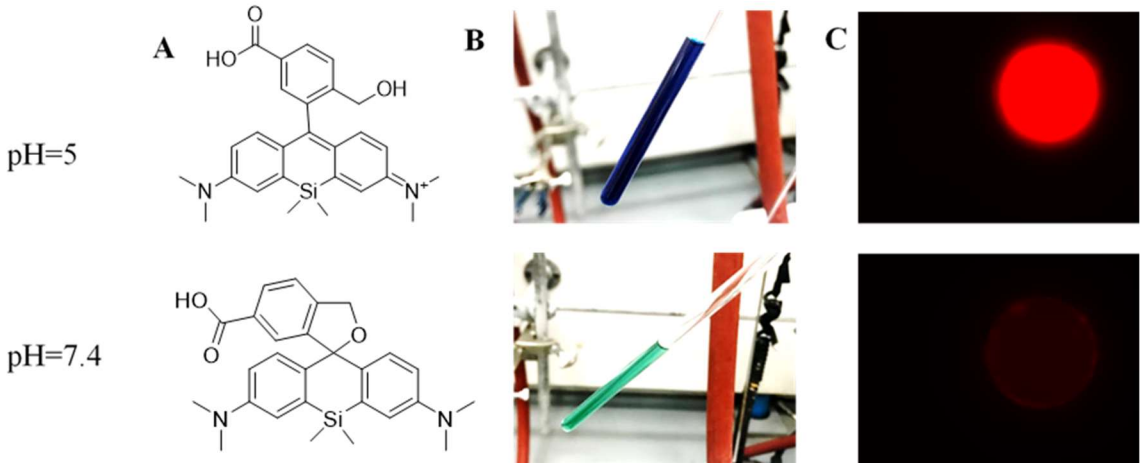

Figure 4-13. (A) structure of **HMSiR** in its open form at acidic pH and in its closed form at neutral pH (B) photograph of **HMSiR** with TFA in MeOD and with TEA in MeOD (C) polymer resin functionalized with **HMSiR** and imaged in buffers of pH=5 and pH=7.4 under EVOS fluorescence microscope

We also synthesized **HMSiR-2,** which does not contain the carboxylic acid pendant group and studied its pH dependent emission spectroscopically in aqueous systems (Scheme 4-6 B). The highest emission was found to be at pH 5 (Figure 4-14 A). At pH below and above pH 5, the emission was found to be lower. In organic solvents, **HMSiR-2** exhibited high emission intensities (Figure 4-14 B). In acetonitrile, acetone and chloroform, the emission intensities were comparable to those in aqueous systems at pH 5. In DMSO, methanol and ethyl acetate the intensities were lower, resembling those at pH 6—7, indicating a smaller subset of molecules in their open state. Interestingly, in methanol, the fluorescence emission intensity was found to decrease with time, which could suggest a shift in equilibrium towards the closed form in this solvent (Figure 4-14 B, C). A similar decrease was observed in ethyl acetate with time, but at a much slower rate.

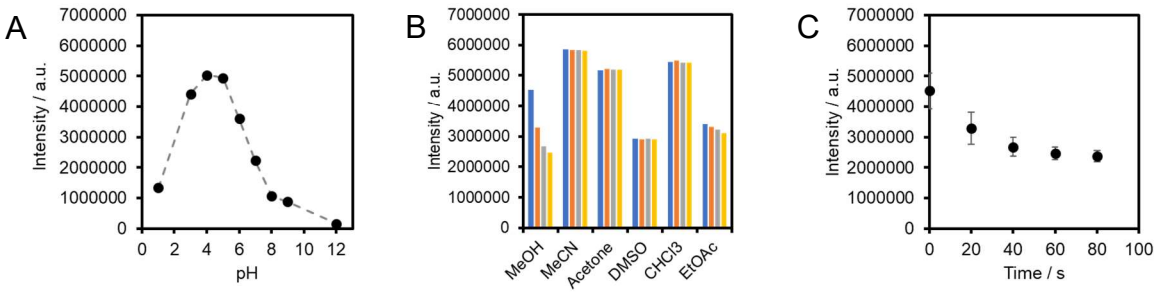

Figure 4-14. (A) pH dependent emission of **HMSiR-2** at 670 nm in 1% MeOH and aqueous systems with pH 1—12. (B) Solvent dependent emission of **HMSiR-2** in different solvents at 0 s (blue), 20 s (red), 40 s (gray) and 60 s (yellow) after mixing. (C) Emission intensity of **HMSiR-2** in methanol with time.

4.2.4.2. Wolff Rearrangement with paired fluorescence and reactivity

Based on the evidence that **HMSiR-2** interchanges between its open and closed form, we proceeded to test the reaction between **HMSiR-2** and **RhBNN.** We chose chloroform as the solvent for two reasons: to ensure **HMSiR-2** remains predominantly open and reactive, and so that **RhBNN** does not react with the non-nucleophilic solvent. A 1:1 mixture of **RhBNN** and **HMSiR-2** in chloroform with 1 wt% eosin y was irradiated with blue light (Figure 4-15 A). Over a period of 24 hours, the color of the reaction went from blue (characteristic of HMSiR in its open form) to purple, indicating uncaging of the colorless **RhBNN** to form pink Rhodamine B. While ^{1}H NMR data did not conclusivley indicate formation of the product (Figure 4-15-B), mass spectrometry showed formation of the RhB-HMSiR adduct, which was not present in the non-irradiated control reaction (Figure 4-15 C). A strong peak in the mass spectrum also indicated a side reaction between **RhBNN** and water, suggesting the need for anhydrous conditions in future experiments.

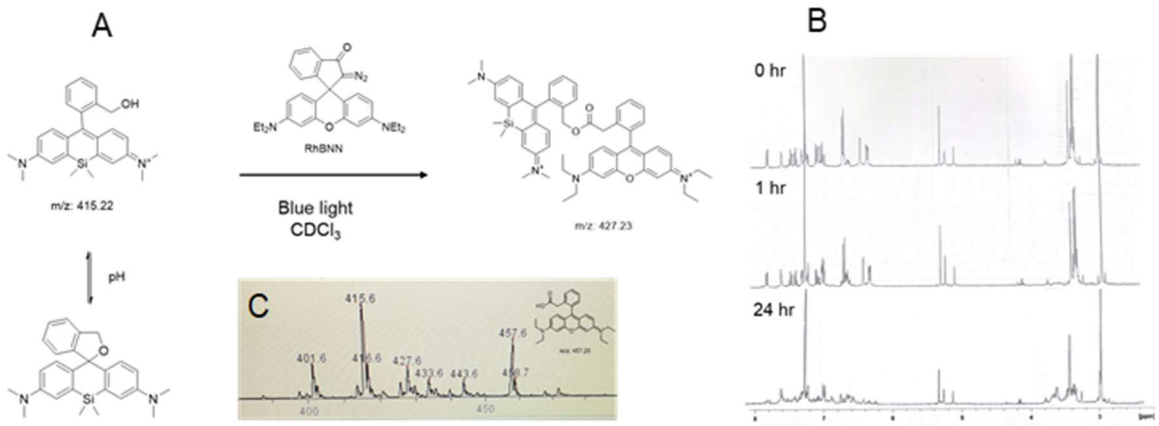

Figure 4-15. (A) Reaction scheme of light mediated Wolff rearrangment reaction between HMSiR-2 in its open form and RhBNN. (B) ^{1}H NMR spectra of reaction in A at 0 hr, 1 hr and 24 hr of blue light irradiation. (C) Mass spectrum of reaction in A 24 hr after irradiation.

4.3. Summary and Conclusions

Single molecule localization microscopy techniques have revolutionized the field of microscopy and opened an avenue for imaging beyond the diffraction limit of light. While other super resolution techniques such as STED microscopy, AFM microscopy and electron microscopy have been translated to super resolution lithography techniques, SMLM is yet to catch up. In this chapter we developed chemical systems which exhibit paired spontaneous fluorescence and reactivity which may enable lithography at a molecular scale. We explored ring opening and closing systems **TMSiR** and **TESiR**, and dynamic covalent thioester exchange chemistry between **coumarin-SH** and DABCYL thioesters to furnish systems for molecular thiol-ene chemistry. We also explored **HMSiR-2** and **RhBNN** as a reactive system for Wolff Rearrangement chemistry that may be used for single molecule lithography. Combined with super resolution imaging and light patterning systems and localization programs that are in development, the chemistry explored in this chapter forms the foundation for carrying out chemistry and lithography on a single molecular scale.

4.4. Experimental Procedures

4.4.1. General materials and methods

Silica gel P60 (SiliCycle) was used for column chromatography, and SiliCycle 60 F254 silica gel precoated sheets (0.25 mm thick) were used for analytical thin layer chromatography. Plates were visualized by fluorescence quenching under UV light or by staining with iodine. Reagents were purchased from Sigma-Aldrich (St. Louis, MO), Thermo Fisher Scientific (Waltham, MA), TCI America (Portland, OR), Alfa Aesar (Ward Hill, MA), EMD Millipore (Billerica, MA), Oakwood Chemical (West Columbia, SC), or Cayman Chemical (Ann Arbor, MI) and used without further purification. ^{1}H NMR and ^{13}C NMR were obtained on a JEOL 500 MHz or a Bruker 400 MHz spectrometer in the Department of Chemistry at Southern Methodist University. ^{1}H and ^{13}C NMR spectra for characterization of new compounds and monitoring reactions were collected in $CDCl_3$ or CD_3OD (Cambridge Isotope Laboratories, Cambridge, MA). All chemical shifts are reported in the standard notation of parts per million. Coupling constant units are in Hertz (Hz). Splitting patterns are indicated as follows: s, singlet; d, doublet; t, triplet; m, multiplet; dd, doublet of doublets. Low resolution mass spectroscopy was performed on a Advion LCMS (ESI source). Absorbance spectra were collected using either a DU 800 or a HORIBA QM-8075-11 spectrophotometer. Fluorescence spectra were acquired using either a Hitachi F-7000 fluorescence spectrophotometer or a HORIBA QM-8075-11 spectrophotometer.

4.4.2. Synthetic procedures

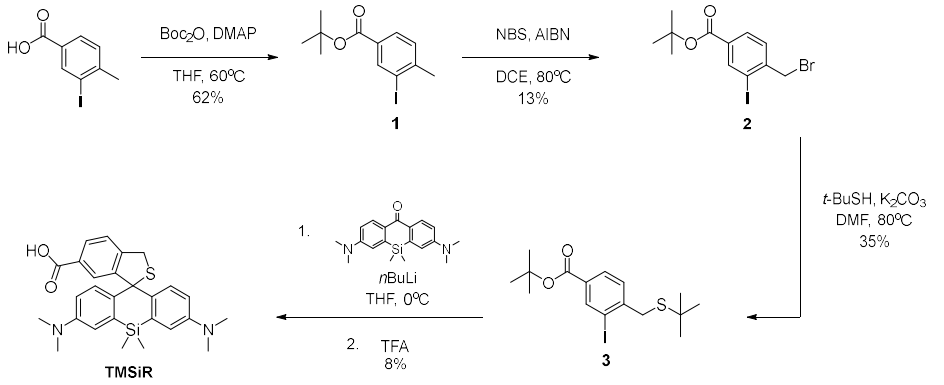

Scheme 4-7. Synthesis of **TMSiR**.

Tert-butyl 3-iodo-4-methylbenzoate (1).[41] 3-Iodo-4-methylbenzoic acid (4.31 g, 16.5 mmol, 1 equiv), boc anhydride (8.97 g, 41.1 mmol, 2.5 equiv), and DMAP (0.400 g, 3.29 mmol, 0.2 equiv) were combined in a round bottom flask with 40 mL THF. The reaction was heated at reflux for 20 h, after which the volatiles were evaporated and the residue was taken up in DCM. The reaction was washed with sat. aq. $NaHCO_3$ and brine, and dried over sodium sulfate. The organics were filtered, concentrated and purified via column chromatography (95:5 hexanes:ethyl acetate) to yield compound **1** as a golden oil with 62% yield. ^{1}H NMR (500 MHz, $CDCl_3$): δ 8.36 (d, J = 1.7 Hz, 1H), 7.81 (dd, J = 1.7, 8.0 Hz, 1H), 7.22 (d, J = 8.0 Hz, 1H), 2.42 (s, 3H), 1.55 (s, 9H); ^{13}C NMR (125 MHz, $CDCl_3$): δ 164.23, 146.18, 139.90, 131.25, 129.40, 129.23, 100.51, 81.41, 81.02, 28.40, 28.24, 27.97.

tert-butyl 4-(bromomethyl)-3-iodobenzoate (2). Compound **1** (2.11 g, 6.63 mmol, 1 equiv), NBS (1.39 g, 7.81 mmol, 1.2 equiv) and AIBN (0.22 g, 1.30 mmol, 0.2 equiv) were combined in a round bottom flask with 50 mL 1,2-dichloroethane and heated under reflux for 3 days, after which time the reaction was cooled and washed with sat. aq. sodium bicarbonate and sat. aq. ammonium chloride and extracted with DCM. The combined organics were dried over sodium sulfate, filtered, concentrated and purified via column chromatography with 20:1 hexanes:ethyl

acetate. A mixed fraction was obtained containing starting material **1** and product **2** in the ratio 2:1, giving an approximate product yield of 13%. ^{1}H NMR (400 MHz, $CDCl_3$): δ 8.45 (s, 1H), 7.94 (d, 1H), 7.29 (d, 1H), 4.61 (s, 2H), 1.60 (s, 9H).

tert-butyl 4-((tert-butylthio)methyl)-3-iodobenzoate (3). Mixed fraction containing compound **2** (1.03 g, ~2.60 mmol. 1 equiv) was combined with tert-butyl mercaptan (0.044 mL, 3.90 mmol, 1.5 equiv) and potassium carbonate (0.54 g, 3.90 mmol, 1.5 equiv) in 5 mL DMF and heated under reflux overnight. The reaction was then taken up in sat. aq. ammonium chloride and extracted with DCM. Combined organics were dried over sodium sulfate, filtered and concentrated. Column chromatography with 4:1 hexanes:DCM yielded the product **3** as a pale yellow oil in 35% yield. ^{1}H NMR (500 MHz, $CDCl_3$): δ 8.35 (d, J = 1.7 Hz, 1H), 7.85 (dd, J = 1.7, 8.0 Hz, 1H), 7.44 (d, J = 8.0 Hz, 1H), 3.83 (s, 2H), 1.54 (s, 9H), 1.33 (s, 9H); ^{13}C NMR (125 MHz, $CDCl_3$): δ 164.00, 145.82, 140.56, 132.15, 129.93, 129.37, 100.00, 99.95, 81.59, 43.56, 38.63, 31.02, 28.25.

3',7'-bis(dimethylamino)-5',5'-dimethyl-3H,5'H-spiro[benzo[c]thiophene-1,10'-dibenzo[b,e]siline]-6-carboxylic acid (TMSiR). Compound **3** (0.24 g, 0.59 mmol, 3.3 equiv) and silicon anthrone (chapter 2 compound **1**) (0.064 g, 0.20 mmol, 1 equiv) were added to a round bottom flask under nitrogen. Anhydrous THF (5 mL) was then added, and the reaction was cooled to 0 °C. n-BuLi (2.0 M in hexanes, 0.35 mL 0.72 mmol, 3.6 equiv) was added dropwise and the reaction stirred for 2 hours at room temperature. The reaction was quenched with aq. 1 M HCl, causing a color change to blue, and then basified with sat. aq. sodium bicarbonate. The reaction was extracted with DCM, and the combined organics were dried over sodium sulfate and filtered. The crude precursor was subjected to column chromatography with 0 – 100% MeOH in DCM. This blue precursor was then dissolved in trifluoroacetic acid (3 mL) and stirred overnight. Mass spectrometry indicated complete conversion of starting material. The TFA was evaporated off and

the residue was taken up in DCM and washed with aq. sat. sodium bicarbonate. The organics were dried over sodium sulfate and filtered, and concentrated then purified via column chromatography (1:1 ethyl acetate:hexanes). The product eluted as a white solid that gradually turned blue in solution or on TLC upon exposure to air. ^{1}H NMR (500 MHz, $CDCl_3$): δ 8.05 (dd, J = 1.7, 8.0 Hz, 1H), 7.77 (s, 1H), 7.46 (d, J = 8.0 Hz, 1H), 6.95 (d, J = 2.9 Hz, 2H), 6.64—6.58 (m, 4H), 4.37 (s, 2H), 2.94 (s, 12H), 0.63 (s, 3H), 0.52 (s, 3H); ^{13}C NMR (125 MHz, $CDCl_3$): δ 170.35, 149.89, 148.60, 148.03, 140.72, 135.23, 130.0, 129.27, 129.18, 129.00, 124.80, 116.73, 114.60, 69.74, 40.65, 37.85, 1.41, -2.46.

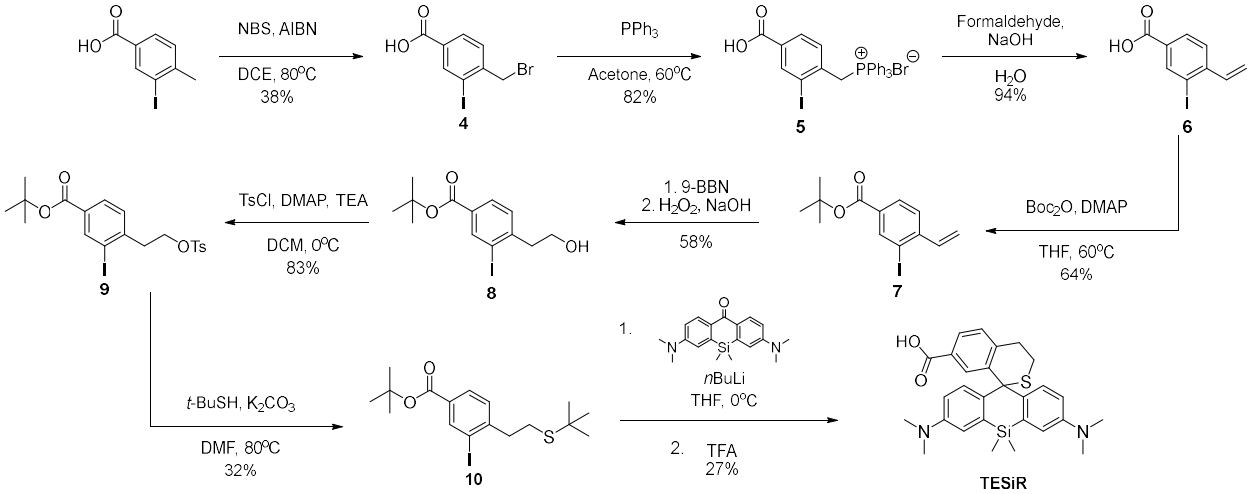

Scheme 4-8. Synthesis of **TESiR**.

4-(bromomethyl)-3-iodobenzoic acid (4). 3-iodo-4-methylbenzoic acid (4.29 g, 16.3 mmol, 1 equiv), NBS (2.90 g, 16.5 mmol, 1 equiv) and AIBN (0.20 g, 1.16 mmol, 0.07 equiv) were combined in a round bottom flask with 50 mL 1,2-dichloroethane. The reaction was heated under reflux for 3 days, after which it was cooled to room temperature and then cooled in an ice bath to 0 °C. The white crystals formed were isolated via vacuum filtration and washed with cold DCM to yield the product with 38% yield. ^{1}H NMR (400 MHz, acetone-d_6): δ 8.50 (s, 1H), 8.04 (d, 1H), 7.78 (d, 1H), 4.79 (s, 2H).

(4-carboxy-2-iodobenzyl)triphenylphosphonium bromide (5). Compound **4** (2.13 g, 6.25 mmol, 1 equiv) and triphenylphosphine (1.65 g, 6.29 mmol, 1 equiv) were dissolved in 25 mL acetone in a round bottom flask. The reaction was heated to 60 °C and stirred under reflux for 1 hr. A white precipitate was observed. After 1 hour of stirring, the reaction was cooled to 0 °C and the precipitate was allowed to settle. The solvent was pipeted off, and the residue was rinsed with cold hexanes thrice. In the final rinse, the hexanes were evaporated off from the reaction to yield **5** as a white powder with 82% yield. ^{1}H NMR (400 MHz, DMSO-d_6): δ 8.25 (s, 1H), 7.96 (m, 3H), 7.77 (m, 7H), 7.65 (m, 6H), 7.23 (d, 1H), 5.22 (d, 2H).

3-iodo-4-vinylbenzoic acid (6). Compound **5** (0.69 g, 1.14 mmol, 1 equiv) was combined with H_2O (2.4 mL) and 37% formaldehyde (4.7 mL) in a round bottom flask. While vigorously stirring, 5 M NaOH (1.8 mL) was added dropwise over 10 min, and the reaction was then stirred for an additional 1 hour. The white suspension formed was filtered to remove the precipitate and the filtrate was transferred to a separatory funnel and acidified with conc. HCl until a white suspension formed. This was extracted with a mixture of DCM:iPrOH (3:1) thrice. The combined organics were dried over sodium sulfate, filtered and concentrated to yield compound with 94% yield. ^{1}H NMR (400 MHz, acetone-d_6): δ 8.50 (s, 1H), 8.02 (d, 1H), 7.79 (d, 1H), 6.94 (m, 1H), 5.94 (d, 1H), 5.51 (d, 1H).

tert-butyl 3-iodo-4-vinylbenzoate (7). Compound **6** (0.30 g, 1.08 mmol, 1 equiv), boc anhydride (0.59 g, 2.7 mmol, 2.5 equiv), and DMAP (0.02 g, 0.22 mmol, 0.2 equiv) were combined in a round bottom flask under nitrogen. Anhydrous THF (5 mL) was added and the reaction was stirred under reflux overnight. The volatiles were evaporated off and the residue was taken up in diethyl ether and washed with sat. aq. sodium bicarbonate, water and brine. The organics were dried over sodium sulfate, filtered and concentrated, and isolated via column chromatography with 20:1

hexanes:ethyl acetate. Compound **7** was isolated as a colorless oil with 64% yield. ^{1}H NMR (500 MHz, $CDCl_3$): δ 8.39 (d, J = 1.7 Hz, 1H), 7.88 (d, J = 8.0 Hz, 1H), 7.78 (d, J = 8.0 Hz, 1H), 6.87 (dd, J = 14.3, 6.3 Hz, 1H), 5.68 (d, J = 17.1, 1H), 5.38 (d, J = 10.9, 1H), 1.57 (s, 9H); ^{13}C NMR (125 MHz, $CDCl_3$): δ 164.03, 144.44, 140.50, 140.11, 132.58, 129.35, 125.86, 118.81, 98.97, 81.65, 28.52, 28.26, 28.00.

tert-butyl 4-(2-hydroxyethyl)-3-iodobenzoate (8). Compound **7** (0.23 g, 0.70 mmol, 1 equiv) in a round bottom flask was flushed with nitrogen, dissolved in anhydrous THF (5 mL), and cooled to 0 °C. 9-BBN (0.5 M in hexanes, 3.0 mL, 1.5 mmol, 2.1 equiv) was added dropwise, after which the ice bath was removed. The reaction was allowed to stir overnight at room temperature, after which it was quenched by dropwise addition of methanol (2 mL) at 0 °C. Then 2 M NaOH (5 mL) was added, followed by 30% H_2O_2 (3 mL), resulting in cloudiness to develop. The ice bath was removed and the reaction was stirred for an additional 3.5 hours, after which it was quenched with 1 M HCl and extracted with DCM. The combined organics were dried over sodium sulfate, filtered, concentrated, and isolated via column chromatography (5:1 hexanes:ethyl acetate) with 58% yield. ^{1}H NMR (500 MHz, $CDCl_3$): δ 8.30 (s, 1H), 7.78 (d, J = 8.0 Hz, 1H), 7.21 (d, J = 8.0 Hz, 1H), 3.74 (t, J = 13.2, 2H), 2.94 (t, J = 12.6, 2H), 1.50 (s, 9H); ^{13}C NMR (125 MHz, $CDCl_3$): δ 164.30, 146.16, 140.38, 131.70, 129.97, 129.25, 100.26, 81.70, 61.62, 43.78, 28.22.

tert-butyl 3-iodo-4-(2-(tosyloxy)ethyl)benzoate (9). Tosyl chloride (0.08 g, 0.42 mmol, 1.1 equiv) and DMAP (0.005 g, 0.04 mmol, 0.1 equiv) were combined in an oven-dried flask under nitrogen. DCM (2 mL) and triethylamine (0.11 mL, 0.77 mmol, 2 equiv) were added and the reaction was cooled to 0 °C. Compound **8** (0.13 g, 0.39 mmol, 1 equiv), dissolved in 2 mL DCM was added to the reaction dropwise, which was then allowed to warm to room temperature and stir overnight. The reaction was washed with sat. aq. sodium bicarbonate, water, and brine, then dried

over sodium sulfate, filtered and concentrated. The product was isolated via column chromatography (30:7 hexanes: ethyl acetate) with 83% yield. ^{1}H NMR (500 MHz, $CDCl_3$): δ 8.18 (d, J = 1.2 Hz, 1H), 7.72 (dd, J = 1.7, 8.0 Hz, 1H), 7.52 (d, J = 8.6 Hz, 2H), 7.12 (d, J = 8.0 Hz, 2H), 7.08 (d, J = 8.0, 1H), 4.14 (d, J = 13.2, 2H), 2.98 (d, J = 13.2, 2H), 2.30 (s, 3H), 1.50 (s, 9H); ^{13}C NMR (125 MHz, $CDCl_3$): δ 163.78, 144.80, 143.46, 140.37, 132.51, 130.35, 129.85, 129.27, 127.80, 99.64, 81.66, 68.48, 39.84, 28.19, 21.68.

tert-butyl 4-(2-(tert-butylthio)ethyl)-3-iodobenzoate (10). Compound **9** (0.16 g, 0.32 mmol, 1 equiv), tert-butyl mercaptan (0.05 mL, 0.44 mmol, 1.4 equiv) and potassium carbonate (0.09 g, 0.63 mmol, 2 equiv) were combined in a round bottom flask with 5 mL DMF. The reaction was stirred under reflux overnight. The DMF was evaporated off and the residue was taken up in sat. aq. ammonium chlroided and extracted with DCM. The combined organic extracts were dried over sodium sulfate, filtered and concentrated and the product was isolated via column chromatography (7:1 hexanes:EtOAc) with 32% yield. ^{1}H NMR (500 MHz, $CDCl_3$): δ 8.35 (d, J = 1.7 Hz, 1H), 7.83 (dd, J = 1.7, 8.0 Hz, 1H), 7.23 (d, J = 8.0 Hz, 1H), 2.95 (t, J = 16.0 Hz, 2H), 2.70 (t, J = 15.5, 2H), 1.53 (s, 9H), 1.28 (s, 9H); ^{13}C NMR (125 MHz, $CDCl_3$): δ 164.01, 147.98, 140.47, 131.88, 129.46, 129.39, 99.69, 81.48, 42.52, 41.42, 31.12, 28.25, 28.21.

3,7-bis(dimethylamino)-5,5-dimethyl-5H-spiro[dibenzo[b,e]siline-10,1'-isothiochromane]-7'-carboxylic acid (TESiR). Compound **10** (0.18 g, 0.42 mmol, 3 equiv) and silicon anthrone (chapter 2 compound **1**) (0.042 g, 0.13 mmol, 1 equiv) were combined in an oven-dried flask under nitrogen. Anhydrous THF (3 mL) was added and the reaction was cooled to 0 °C. nBuLi (2.0 M in hexanes, 0.4 mL, 0.8 mmol, 6 equiv) was added dropwise until the reaction turned a permanent red color. The reaction was stirred for an additional 2 hr at room temperature. After this, 1 M HCl was used to quench the reaction, and then sat. aq. sodium bicarbonate was added to basify the

reaction to pH 8. The reaction was extracted with DCM, and the combined blue organic extracts were dried over sodium sulfate, filtered and concentrated. Column chromatography with (a) 100% ethyl acetate to elute the impurities and then (b) 1% to 7% MeOH in DCM with 0.5% TFA to elute the blue product afforded the TESiR precursor in 41% yield. This precursor was dissolved in 5 mL TFA and allowed to stir overnight. The TFA was evaporated off and column chromatography with (a) 100% ethyl acetate to elute the impurities and (b) 5% MeOH in DCM to elute the product afforded the **TESiR** as a pale blue solid with 27% yield over 2 steps. The product could be further purified via recrystallization from hot chloroform to yield white crystals or via trituration with hexanes to yield a white powder. ^{1}H NMR (500 MHz, $CDCl_3$): δ 7.86 (d, J = 8.0 Hz, 1H), 7.59 (s, 1H), 7.31 (d, J = 8.0 Hz, 1H), 7.12 (s, 2H), 6.68 (d, J = 8.6 Hz, 2H), 6.59 (d, J = 9.2 Hz, 2H), 3.32 (t, J = 10.9 Hz, 2H), 2.98 (s, 12H), 2.69 (t, J = 11.5, 2H), 0.63 (s, 3H), 0.54 (s, 3H); ^{13}C NMR (125 MHz, $CDCl_3$): δ 168.52, 147.09, 143.06, 142.35, 135.74, 133.90, 130.77, 130.10, 127.88, 127.26, 117.54, 113.84, 55.39, 49.15, 40.95, 32.81, 29.59, 25.12, 1.17, 0.90.

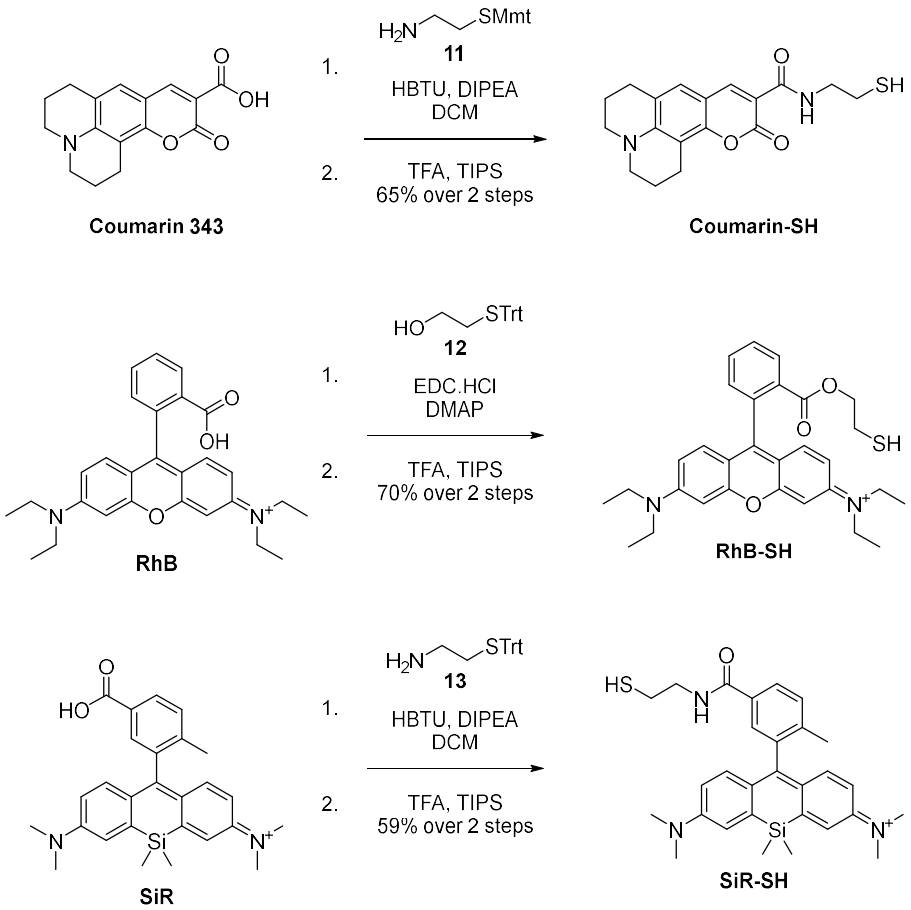

Scheme 4-9. Synthesis of thiol-functionalized fluorophores.

2-(((4-methoxyphenyl)diphenylmethyl)thio)ethan-1-amine (11).[42] Cysteamine (0.10 g, 1.3 mmol, 1 equiv) was dissolved in TFA (2 mL) and DCM (1 mL) in a round bottom flask. 4-methoxytrityl chloride (0.40 g, 1.3 mmol, 1 equiv) was then added. The reaction changed color to red. An additional 0.5 mL of DCM was added and the reaction was stirred at room temperature for 3 hours. The solvent was evaporated off and the residue was taken up in DCM and basified with 3 M NaOH, wherein the color changed from red to colorless. After extraction with additional DCM, the combined organic extracts were dried over sodium sulfate, filtered and concentrated. Column chromatography 0—7% MeOH in DCM yielded the **11** as a golden oil.

N-(2-mercaptoethyl)-11-oxo-2,3,6,7-tetrahydro-1H,5H,11H-pyrano[2,3-f]pyrido[3,2,1-ij]quinoline-10-carboxamide (Coumarin-SH). Coumarin 343 (0.05 g, 0.18 mmol, 1 equiv) was

suspended in DCM (3 mL) in a round bottom flask and cooled to 0 °C. DIPEA (93 µL, 0.53 mmol, 3 equiv) and HBTU (0.20 g, 0.53 mmol, 3 equiv) were then added and the reaction was allowed to stir for 10 min. Compound **11**, dissolved in 2 mL DCM was then added and the reaction was allowed to stir overnight at room temperature. The crude reaction was subjected to column chromatography with 0—2% MeOH in DCM to yield a yellow solid, which was further purified by recrystallization from hot ethyl acetate and hexanes to obtain brown crystals. These crystals (0.08 g, 0.12 mmol) were dissolved in 4 mL DCM in a round bottom flask. TFA (0.25 mL) and TES (0.25 mL) were added and the reaction stirred for 10 mins, at which point TLC showed complete conversion. The volatiles were evaporated and the residue was subjected to column chromatography with 0—3% MeOH in DCM to obtain **coumarin-SH** as a yellow solid with 65% yield. ^{1}H NMR (500 MHz, $CDCl_3$): δ 9.15 (s, 1H), 8.53 (s, 1H), 6.95 (s, 1H), 3.59 (q, J = 19.5 Hz, 2H), 3.29 (t, J = 17.2 Hz, 4H), 2.83 (q, J = 12.6 Hz, 2H), 2.74—2.71 (m, 4H), 1.93 (m, 4H), 1.44 (t, J = 17.2, 1H); ^{13}C NMR (125 MHz, $CDCl_3$): δ 163.99, 163.10, 152.75, 148.38, 148.24, 127.14, 119.8, 108.38, 108.25, 105.65, 50.31, 49.88, 42.90, 27.50, 24.59, 21.15, 20.20, 20.13.

2-(tritylthio)ethan-1-ol (12). Compound **12** was synthesized according to literature procedure.[43]

3',6'-bis(diethylamino)-2-(2-mercaptoethyl)spiro[isoindoline-1,9'-xanthen]-3-one (RhB-SH). Rhodamine B hydrochloride (0.48 g, 1.0 mmol, 1 equiv), EDC.HCl (0.21 g, 1.1 mmol, 1.1 equiv), DMAP (0.024 g, 0.2 mmol, 0.2 equiv), and compound **12** (0.35 g, 1.1 mmol, 1.1 equiv) were combined in a round bottom flask under nitrogen and DCM (5 mL) was added. The reaction was stirred at room temperature for 3 hours, after which it was diluted with DCM and washed with water. The aqueous wash was extracted with DCM, and the combined organic extracts were washed with 0.1 M HCl and dried over sodium sulfate. After filtering and concentrating, the residue (0.55 g) was dissolved in DCM (3 mL) and TFA (6 mL) with triisopropylsilane (0.2 mL)

and stirred for 1 hour, at which point mass spectrometry indicated complete conversion. The volatiles were evaporated and the residue subjected to column chromatography with 0—5% MeOH in DCM and 0.1% TFA. **RhB-SH** was isolated as a pink solid with 70% yield over 2 steps. ^{1}H NMR (500 MHz, $CDCl_3$): δ 8.29 (d, J = 6.9 Hz, 1H), 7.78—7.73 (m, 2H), 7.30 (d, J = 6.9 Hz, 1H), 7.06 (d, J = 9.2 Hz, 2H), 6.80—6.77 (m, 4H), 4.13 (t, J = 12.6 Hz, 2H), 3.57 (q, J = 21.8 Hz, 8H), 2.55 (q, J = 21.8 Hz, 2H), 1.29 (t, J = 14.3 Hz, 12H); ^{13}C NMR (125 MHz, $CDCl_3$): δ 165.05, 158.87, 157.91, 155.64, 132, 132, 131.49, 131.31, 130.56, 130.31, 129, 114.13, 113.59, 96.38, 66.89, 46.07, 22.94, 12.40.

2-(tritylthio)ethan-1-amine (13).[44] Trityl chloride (0.56 g, 2.0 mmol, 1 equiv) was dissolved in DCM (2 mL), and cysteamine (0.18 g, 2.3 mmol, 1.2 equiv) was added, TFA (0.9 mL) and an additional 1 mL of DCM were then added and the reaction was stirred for 3 hours. The reaction was quenched with 1 M NaOH until pH 12, and then extracted with ethyl acetate. The organics were dried over sodium sulfate, filtered and concentrated, and then purified via column chromatography using 0—7% MeOH in DCM with 1% TEA. The product was obtained in 98% yield as a yellow oil which solidified into a white solid over time.

N-(7-(dimethylamino)-10-(5-((2-mercaptoethyl)carbamoyl)-2-methylphenyl)-5,5-dimethyldibenzo[b,e]silin-3(5H)-ylidene)-N-methylmethanaminium (SiR-SH). Silicon rhodamine **SiR** (0.015 g, 0.034 mmol, 1 equiv) was suspended in DCM (2 mL) and cooled to 0 °C. DIPEA (20 μL, 0.13 mmol, 3 equiv) was added and stirred. After 10 mins, HBTU (0.046 g, 0.12 mmol, 3 equiv) was added and the reaction was stirred for another 10 mins. Compound **13** (0.025 g, 0.078 mmol, 2 equiv) dissolved in 1 mL DCM was then added to the reaction which was allowed to stir overnight at room temperature. The reaction was diluted with DCM and washed with sat. aq. ammonium chloride, sat. aq. sodium bicarbonate, brine, and dried over sodium sulfate.

The crude mixture was subjected to column chromatography with 0—50% MeOH in DCM to obtain the trityl-protected product. This was then dissolved in DCM (1 mL) with TFA (0.6 mL) and TIPS (0.03 mL) and stirred for 40 mins. The volatiles were dried and then purified via trituration: the residue was dissolved in a minimal volume of DCM (~0.2 mL) and hexanes were added pipetwise until a precipitate formed. The suspension was filtered, and the residue was washed with hexanes, then collected by dissolving the residue in methanol and concentrating to obtain **SiR-SH** with 59% yield. ^{1}H NMR (500 MHz, methanol-d_4): δ 7.94 (d, 1H), 7.60 (s, 1H), 7.51 (d, 1H), 7.35 (d, 2H), 7.01 (d, 2H), 6.74 (d, 2H), 3.50 (t, 2H), 3.32 (s, 12H), 2.67 (t, 2H), 2.08 (s, 3H), 0.59 (s, 6H). ^{13}C NMR (125 MHz, $CDCl_3$): δ 167.81, 154.47, 148.19, 140.77, 139.86, 139.10, 131.67, 130.34, 127.68, 127.46, 127.00, 120.98, 114.05, 23.05, 18.14, -2.53.

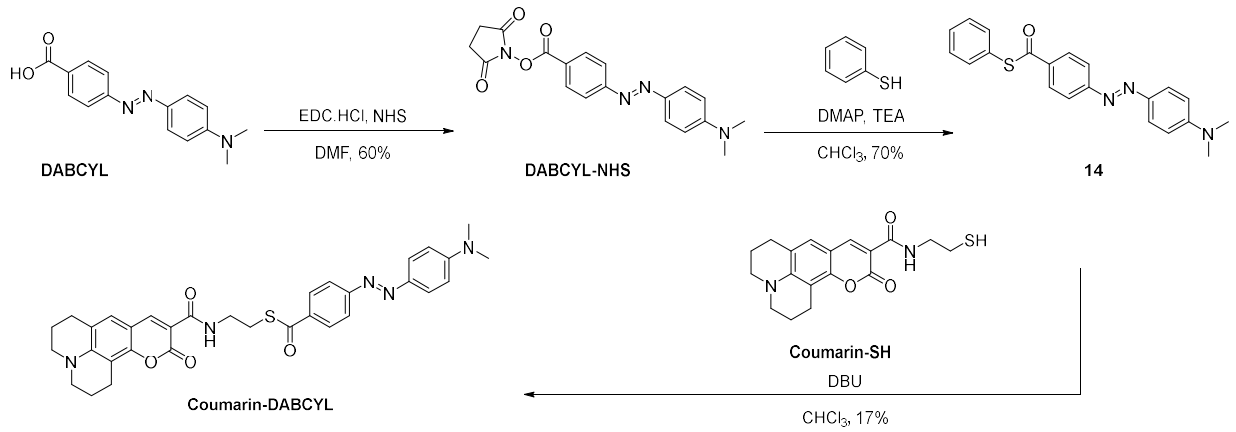

Scheme 4-10. Synthesis of **coumarin-DABCYL**.

2,5-dioxopyrrolidin-1-yl-4-((4-(dimethylamino)phenyl)diazenyl)benzoate (DABCYL-NHS).[45] In a round bottom flask, DABCYL (0.50 g, 1.85 mmol, 1 equiv) was dissolved in DMF (15 mL). EDC.HCl (0.71 g, 3.7 mmol, 2 equiv) and N-hydroxysuccinimide (0.28 g, 2.41 mmol, 1.3 equiv) were added and the reaction was allowed to stir at room temperature overnight. The volatiles were evaporated, and the residue was purified via column chromatography using 0—3% MeOH in DCM. The product was obtained as an orange-red solid with 59% yield.

S-phenyl-4-((4-(dimethylamino)phenyl)diazenyl)benzothioate (14). DABCYL-NHS (0.12 g, 0.33 mmol, 1 equiv) was dissolved in chloroform (15 mL) in a round bottom flask. DMAP (0.02 g, 0.14 mmol, 0.4 equiv), triethylamine (0.95 mL, 6.8 mmol, 20 equiv) and thiophenol (0.35 mL, 3.4 mmol, 10 equiv) were then added. The reaction was warmed to 35 °C and stirred overnight, after which the reaction was concentrated and purified via column chromatography with 1:1 hexanes:DCM and then 1:2 hexanes:DCM. Compound **14** was collected as an orange solid with 82% yield. ^{1}H NMR (400 MHz, $CDCl_3$): δ 8.13 (d, *J* = 8.6 Hz, 2H), 7.91 (m, 4H), 7.53–7.46 (m, 5H), 6.76 (d, *J* = 9.2 Hz, 2H), 3.12 (s, 6H).

S-(2-(11-oxo-2,3,6,7-tetrahydro-1H,5H,11H-pyrano[2,3-f]pyrido[3,2,1-ij]quinoline-10-carboxamido)ethyl)-4-((4-(dimethylamino)phenyl)diazenyl)benzothioate (Coumarin-DABCYL). Compound **14** (0.02 g, 0.06 mmol, 1 equiv), **coumarin-SH** (0.02 g, 0.06 mmol, 1 equiv) and DBU (1 μL, 0.006, 0.1 equiv) were dissolved in chloroform and stirred at 35 °C overnight. The crude mixture was subjected to column chromatography with 0—2% MeOH in DCM. The fractions containing product as determined by TLC were further purified using preparatory TLC with DCM as the solvent system and running the plate twice to separate the product from the coumarin starting material. **Coumarin-DABCYL** was obtained as an orange solid with 17% yield. ^{1}H NMR (400 MHz, $CDCl_3$): δ 9.17 (t, 1H), 8.63 (s, 1H), 8.10 (d, 2H), 7.90 (m, 4H), 7.03 (s, 1H), 6.79 (d, 2H), 3.76 (q, 2H), 3.36 (m, 6H), 3.14 (s, 6H), 2.91 (t, 2H), 2.79 (t, 2H), 2.00 (m, 4H).

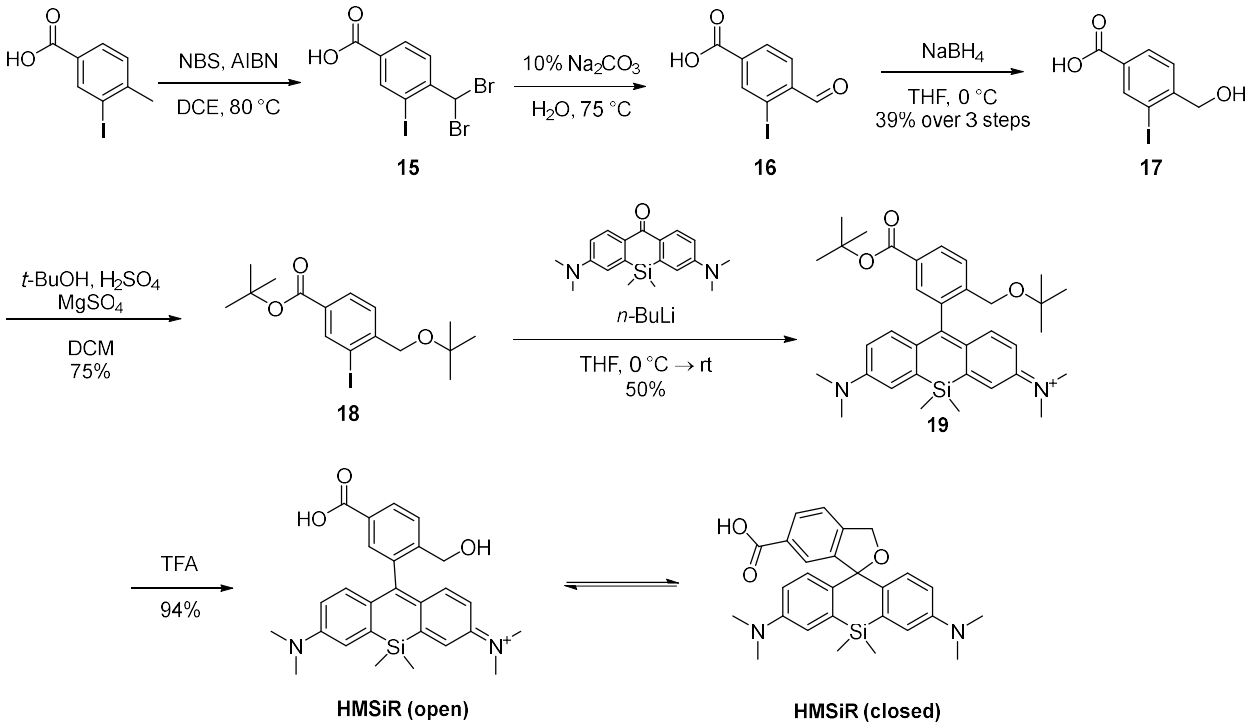

Scheme 4-11. Synthesis of **HMSiR**.

4-(dibromomethyl)-3-iodobenzoic acid (15). 3-iodo-4-methyl-benzoic acid (2.05 g, 7.8 mmol, 1 equiv), N-bromosuccinimide (4.04 g, 23 mmol, 3 equiv) and AIBN (0.024 g, 0.15 mmol, 0.02 equiv) were added to a round-bottom flask with 1,2-dichloroethane (60 mL). The reaction was heated to 80 °C and stirred under reflux for 16 hours. After allowing the reaction to cool, it was basified with 1M K_2CO_3 and extracted with DCM. The aqueous layer was then acidified with 1M HCl and extracted with 2% iPrOH in DCM. The combined organics were washed with H_2O and brine, then dried over Na_2SO_4 and concentrated. Mass spec showed presence of peak at 418 with splitting pattern for 2Br. The crude product was used for the next step as is.

4-formyl-3-iodobenzoic acid (16). Crude product **15** (2.15 g) from the previous step was dissolved in 10% Na_2CO_3 (50 mL) and stirred at 75 °C for 16 hours. After filtering off the precipitate, the filtrate was acidified with 1M HCl and extracted with EtOAc. The combined organics were washed with brine and concentrated to obtain an off-white solid. The mass spectra

and ^{1}H NMR in MeOD indicated presence of the alcohol and aldehyde products. The crude product was carried forward to the next step as is.

4-(hydroxymethyl)-3-iodobenzoic acid (17). Crude aldehyde **16** from the previous step (1.10 g, 1 equiv) was added to a round-bottom flask and dissolved in dry THF (12 mL). The reaction was cooled to 0 °C and $NaBH_4$ (0.21 g, 5.6 mmol, 1.4 equiv) was added. The reaction was stirred at 0 °C for 3.5 hours, at which time mass spectrum of an aliquot showed only presence of the alcohol peak at 276 and no aldehyde peak at 274. The reaction was carefully quenched with 1M HCl and the THF was evaporated under reduced pressure. The reaction mixture was diluted with 1M HCl and then extracted with 2% iPrOH in DCM. The organics were combined and concentrated to obtain the crude product, which was purified via column chromatography with 2:3 EtOAc:Hexanes as the solvent system. The product was further purified by dissolving in minimal EtOAc and precipitating into cold hexanes and filtering. A white solid was obtained (0.87 g, 39% over 3 steps). ^{1}H NMR (500 MHz, MeOD): δ 8.37 (d, *J*= 1.7 Hz, 1H), 7.99 (dd, *J* = 1.7, 8.0 Hz, 1H), 7.57 (d, *J* = 8.0 Hz, 4.56 (s, 2H); ^{13}C NMR (125 MHz, MeOD): δ 166.82, 148.41, 139.91, 130.95, 129.24, 126.92, 95.04, 67.95.

tert-butyl 4-(tert-butoxymethyl)-3-iodobenzoate (18). To a stirred suspension of DCM (30 mL) and $MgSO_4$ (2.19 g, 18 mmol, 10 equiv) was added 18 M H_2SO_4 (0.20 mL, 3.6 mmol, 2 equiv). After 15 mins of stirring, *t*-BuOH (2.60 mL, 27 mmol, 15 equiv) was added followed by compound **17** (0.500 g, 1.8 mmol, 1 equiv). The flask was capped and parafilmed and allowed to stir for 1–4 days, as indicated by TLC. The reaction was quenched with sat. $NaHCO_3$ and extracted with EtOAc. The organics were washed with brine, dried over Na_2SO_4 and concentrated. The product was purified via column chromatography with 10:1 hexanes:EtOAc to yield a colorless oil (0.528 g, 75%). ^{1}H NMR (500 MHz, $CDCl_3$): δ 8.29 (d, *J* = 1.2 Hz, 1H), 7.87 (dd, *J* = 1.7, 8.0 Hz, 1H),

7.48 (d, J = 8.0 Hz, 1H), 4.40 (s, 2H), 1.57 (s, 9H), 1.30 (s, 9H); ^{13}C NMR (125 MHz, $CDCl_3$): δ 164.38, 146.69, 139.67, 132.23, 129.21, 128.43, 127.88, 96.12, 81.45, 74.16, 68.25, 28.26, 27.75.

N-(10-(5-(tert-butoxycarbonyl)-2-(tert-butoxymethyl)phenyl)-7-(dimethylamino)-5,5-dimethyldibenzo[b,e]silin-3(5H)-ylidene)-N-methylmethanaminium (19). In an oven-dried flask was added iodide **18** (0.378 g, 0.97 mmol, 3.2 equiv) and Si-anthrone (chapter 2 compound **1)** (0.0980 mg, 0.30 mmol, 1 equiv). The flask was evacuated and backfilled with N_2 thrice, after which anhydrous THF (5 mL) was added. The reaction was stirred at rt for 5 mins until the starting materials dissolved, and then was cooled to 0 °C. 2.0 M *n*-BuLi in hexanes (0.45 mL, 0.90 mmol, 3 equiv) was added, half of which was added over 5 mins (a yellow to red color change was observed with every drop), and the remaining volume was added after 1 hour of stirring. The reaction was quenched with 1M HCl, and then neutralized with sat. $NaHCO_3$, after which it was extracted with DCM. The combined organics were washed with brine and dried over Na_2SO_4 and concentrated to obtain the crude product, which was purified via column chromatography with 1:1 EtOAc:Hexanes, followed by MeOH in DCM, increasing from 1% to 5%. Compound **19** was isolated as a blue solid (0.087 g, 50%). ^{1}H NMR (500 MHz, $CDCl_3$): δ 8.05 (dd, J = 1.7, 8.0 Hz, 1H), 7.61 (m, 2H), 7.16 (d, J = 2.9 Hz, 2H), 6.97 (d, J = 9.7, 2H), 6.55 (dd, J = 2.9, 9.2 Hz, 2H), 4.09 (s, 2H), 3.35 (s, 12H), 1.53 (s, 9H), 0.87 (s, 9H), 0.61 (s, 3H), 0.58 (s, 3H); ^{13}C NMR (125 MHz, $CDCl_3$): δ 167.75, 165.04, 154.16, 148.35, 142.00, 137.95, 131.14, 130.04, 129.87, 129.04, 127.76, 121.07, 113.91, 81.88, 73.84, 61.88, 41.54, 28.25, 27.22, –0.51.

N-(10-(5-carboxy-2-(hydroxymethyl)phenyl)-7-(dimethylamino)-5,5-dimethyldibenzo[b,e]silin-3(5H)-ylidene)-N-methylmethanaminium (HMSiR). Compound **19** (0.06 g, 0.1 mmol) was dissolved in TFA (15 mL) and allowed to stir at rt overnight, after which mass spectrometry indicated complete conversion of starting material. The volatiles were

evaporated off to yield **HMSiR** as a blue solid (0.04 g, 94%). ^{1}H NMR and ^{13}C NMR spectra indicated the dye was present in open and closed forms. Triethylamine (0.1 mL) was added and ^{1}H and ^{13}C NMR spectra were obtained for the closed form of the dye. ^{1}H NMR (500 MHz, MeOD): δ 7.85 (d, *J*= 6.9 Hz, 1H), 7.49 (s, 1H), 7.35 (d, *J* = 6.9 Hz, 1H), 7.09 (d, *J*=8.6, 2H), 6.94 (d, *J* = 2.3 Hz, 2H), 6.63 (d, *J* = 6.9 Hz, 2H), 5.44 (s, 2H), 2.83 (s, 12H), 0.64 (s, 3H), 0.49 (s, 3H); ^{13}C NMR (125 MHz, MeOD): δ 165.83, 149.14, 142.73, 140.78, 138.75, 133.91, 128.53, 128.20, 124.76, 121.19, 121.00, 116.48, 114.53, 72.85, 39.53, –1.10, –1.41.

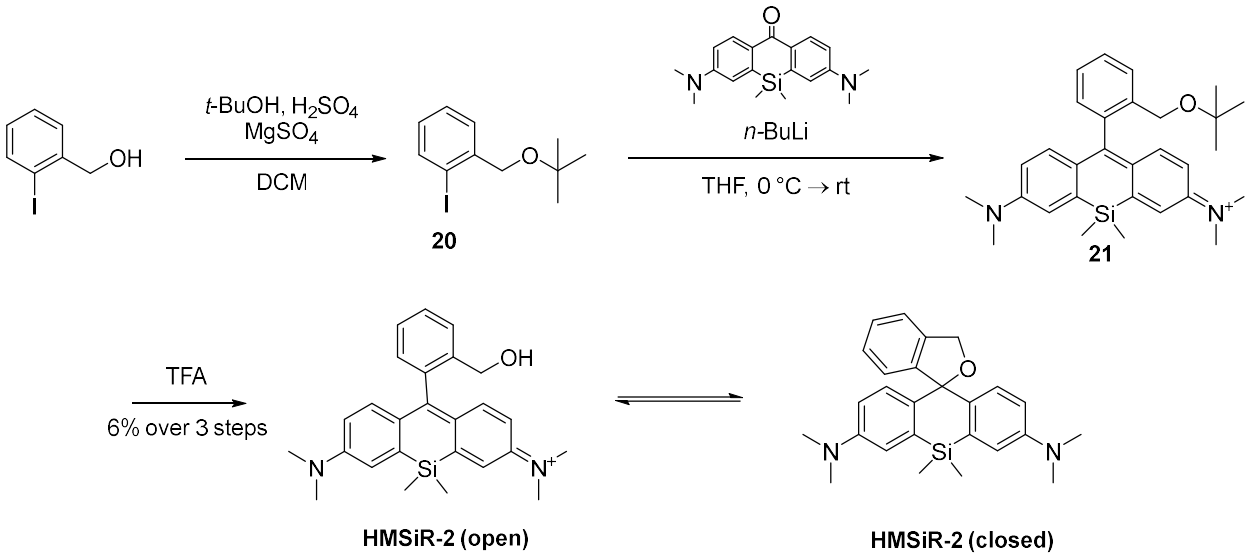

Scheme 4-12. Synthesis of **HMSiR-2**.

1-(tert-butoxymethyl)-2-iodobenzene (20). To a vigorously stirred suspension of $MgSO_4$ (2.0 g, 17.2 mmol, 10 equiv) in DCM (5 mL) in a round bottom flask, was added H_2SO_4 (18 M, 0.10 mL, 1.7 mmol, 1 equiv). After 15 min of stirring, a mixture of 4-iodobenzyl alcohol (0.40 g, 1.7 mmol, 1 equiv) and tert-butylalcohol (2.5 mL, 26.1 mmol, 15 equiv) in DCM (5 mL) was added to the reaction flask, which was then tightly capped and allowed to stir at room temperature for 3 days while monitoring via TLC. The reaction was quenched with sat. aq. sodium bicarbonate and extracted with DCM. The combined organics were dried over sodium sulfate, filtered and

concentrated. Column chromatography using CombiFlash with 0-10% EtOAc in hexanes afforded the pure product as a colorless oil. ^{1}H NMR (400 MHz, $CDCl_3$): δ 7.83 (d, 1H), 7.56 (d, 1H), 7.37 (m, 1H), 6.98 (m, 1H), 4.44 (s, 2H), 1.35 (s, 9H).

N-(10-(2-(tert-butoxymethyl)phenyl)-7-(dimethylamino)-5,5-dimethyldibenzo[b,e]silin-3(5H)-ylidene)-N-methylmethanaminium (21). Compound **20** (0.08 g, 0.28 mmol, 3 equiv) and Si-anthrone (chapter 2 compound **1**) (0.03 g, 0.092 mmol, 1 equiv) were dissolved in 2.5 mL anhydrous THF in an oven dried round bottom flask under nitrogen. The reaction was cooled to zero °C and n-BuLi (2.6 M in hexanes, 0.11 mL, 0.28 mmol 3 equiv) was added dropwise. After an additional 1 hour of stirring, the reaction was quenched with 1 M HCl, basified with sat. aq. sodium bicarbonate and extracted with DCM. The organic extracts were dried over sodium sulfate, filtered, concentrated and purified via column chromatography using (a) 100% ethyl acetate to elute impurities and then (b) 0-3% MeOH in DCM to elute the product as a blue solid. ^{1}H NMR (400 MHz, $CDCl_3$): δ 7.55 (d, 1H), 7.49 (t, 1H), 7.40 (t, 1H), 7.16 (s, 2H), 7.07 (d, 3H), 6.59 (d, 2H), 4.08 (s, 2H), 3.39 (s, 12H), 0.89 (s, 9H), 0.64 (s, 3H), 0.64 (s, 3H).

N-(7-(dimethylamino)-10-(2-(hydroxymethyl)phenyl)-5,5-dimethyldibenzo[b,e]silin-3(5H)-ylidene)-N-methylmethanaminium (HMSiR-2). Compound **21** was dissolved in TFA (3 mL) and DCM (2 mL) and allowed to stir overnight. The volatiles were then evaporated and the residue was taken up in DCM and washed with 1 M NaOH. The organic layer was dried over sodium sulfate, filtered and concentrated, and then purified via column chromatography with (a) 100% ethyl acetate as the solvent system to elute impurities and then (b) 2-8% MeOH in DCM to elute **HMSiR-2** as a blue solid in a 1:1 mixture of open and closed forms with 6% yield over 3 steps. Proton NMR is tabulated as a 1:1 mix of open and closed isomers. ^{1}H NMR (400 MHz, $CDCl_3$): δ

7.63 (s, 3H), 7.28 (d, 2H), 7.24 (d, 3H), 7.02 (d, 6H), 6.67 (m, 4H), 5.25 (s, 2H), 5.11 (s, 2H), 3.43 (s, 12H), 2.97 (s, 12H), 0.70 (s, 3H), 0.64 (s, 6H), 0.57 (s, 3H).

4.4.3. Spectroscopic Methods

4.4.3.1. **TMSiR** and **TESiR** characterization

pH dependence. A solution of 0.4 μM **TMSiR** in 1% MeOH and pH 3 buffer (100 mM sodium citrate, pH = 2.98) was prepared in a cuvette, which was gently shaken to ensure mixing. Emission was then collected from 660–800 nm while exciting at 650 nm. The process was repeated with solutions of pH 1 (0.1 M HCl), pH 4 (100 mM sodium citrate, pH = 4.00), pH 5 (100 mM sodium citrate, pH = 4.97), pH 6 (100 mM PBS , pH = 5.85), pH 7.4 (100 mM PBS, pH = 7.45), pH 8 (50 mM Tris and10 mM NaCl, pH = 7.93), pH 9 (100 mM Tris, pH = 8.98), and pH 10. A similar procedure was used for 0.5 μM **TESiR**.

NaOCl response. A solution of 0.4 μM **TMSiR** in 900 μL DI H_2O with 1% MeOH was prepared in a cuvette. 100 μL of a 10 mM NaOCl stock solution was added for a final concentration of 1 mM NaOCl. Emission from 660-800 nm was acquired immediately after addition with excitation at 650 nm. The process was repeated without NaOCl. A similar procedure was used for 0.5 μM **TESiR**.

Solvent dependence. A 0.4 μM solution of **TMSiR** with 1% MeOH was prepared in DCM in a cuvette. Fluorescence emission at 665 nm was recorded while exciting at 650 nm. The process was repeated with DMSO, MeCN, chloroform, MeOH, PBS (pH = 7.4), and 0.1% TFA in EtOH.

Thiol trapping. A 5 μM solution of **TMSiR** in PBS (pH = 7.4) and 1—2% MeOH was prepared in a cuvette and emission was acquired at 670 nm while exciting at 650 nm at 0 h, 1.5 and 3 h after

preparing. The process was repeated for solutions of 5 μM **TMSiR** in PBS with 1 mM DTNB and with 1 mM NEM.

4.4.3.2. Thioester exchange

Thiol-ene with n-octanethiol and acylated n-octanethiol. n-octanethiol (16.5 μL, 0.1 mmol, 1 equiv), styrene (11 μL, 0.1 mmol, 1 equiv) and eosin y (0.001 g, 0.002 mmol, 0.02 equiv) dissolved in 600 μL DMSO-d6 and added to an NMR tube. The NMR tube was irradiated with blue light from an LED lamp for 20 h and ^{1}H NMR were acquired at 0 h and 20 h of irradiation. A similar procedure was carried out using acylated n-octanethiol, which was synthesized according to previous procedure.[36]

Fluorescence quantum yields of coumarin and DABCYL compounds. Absolute fluorescent quantum yields were acquired using an integrating sphere from HORIBA in a quartz cuvette with real time excitation and emission corrections enabled. For **Coumarin-SH** a 3.7 x 10^{-8} M sample in DMSO was prepared. Emission was collected from 300—600 nm, with excitation at 350 nm. Slits were kept at 2 nm to ensure that the excitation pulse did not saturate the detector. Quantum yield was calculated using emission counts from 400 to 580 nm and excitation counts from 340 to 360 nm for a blank trace (100% DMSO) and the sample trace using the in-built quantum yield calculator accessory in Felix GX. For coumarin-DABCYL 2.9 x 10^{-8} M sample in DMSO was used. For DABCYL a 3.7 x 10^{-8} M sample was used. For a 1:1 mix of DABCYL and **coumarin-SH**, 30 μM, 3 μM, and 0.3 μM solutions were used.

NMR kinetics of model reactions. Compound **14** (0.001 g, 0.0028 mmol, 1 equiv) was suspended in 600 μL of DMSO-d6 and a ^{1}H NMR was acquired. From a stock solution of methyl mercaptopropionate and TEA (60 μL and 8 μL respectively) in 1000 μL DMSO, 5 μL was added

to the reaction NMR tube for a final concentration of 14.6 mM **14** and thiol (1 equiv), and 1.46 mM TEA (0.1 equiv). ^{1}H NMR spectra were acquired at 0 h, 1 h, 2 h, 3 h, 4 h and 24 h after mixing. The equilibrium constant was calculated by integrating peaks at t = 24 h corresponding to the reactant thiol and thioester and the product thiol and thioester and dividing by the number of protons corresponding to each peak as a measure of each species' concentration at equilibrium. The procedure was carried out in triplicate. The same procedure was repeated for exchange reactions of compound **14** with 2-mercaptopyridine, n-octanethiol, and boc-aminoethanethiol.

NMR kinetics of coumarin-SH and thioester 14 exchange. Compound **14** (0.0008 g, 0.002 mmol, 1 equiv) and **coumarin-SH** (0.0006 g, 0.002 mmol, 1 equiv) were dissolved in DMSO-d6 (400 µL) and an ^{1}H NMR spectrum was acquired. DBU (0.03 µL, 0.0002 mmol, 0.1 equiv) in 100 µL DMSO-d6 (via serial dilutions of DBU) was then added and ^{1}H NMR spectra were collected at 3.5, and 22 h after mixing. K eq was calculated as described above. The procedure was carried out in triplicate.

Fluorescence emission and quantum yields of coumarin-SH and thioester 14 exchange. Compound **14** (0.0001 g, 0.0004 mmol, 1 equiv) and **coumarin-SH** (0.0001 g, 0.0003 mmol, 1 equiv) were dissolved in 100 µL DMSO and DBU (0.03 µL, 0.1 equiv) was added for a final concentration of 3 mM **14** and **Coumarin-SH**. The exchange reaction was allowed to occur at this concentration for 24 hours. At t = 0 and 24 hours after mixing, an aliquot of the solution was serially diluted to 0.3 µM and an emission scan from 400 to 600 nm was acquired while exciting at 350 nm. For fluorescence quantum yields a similar procedure with the integrating sphere as above was used.

4.4.3.3. HMSiR

HMSiR functionalized resin synthesis and imaging. Amine resin (Rink amide) (0.020 g, 0.005 mmol, 1 equiv) was swollen in DMF. **HMSiR** (0.003 g, 0.006 mmol, 1.2 equiv) was activated with HBTU (0.006 g, 0.015 mmol, 3 equiv) and DIPEA (2.6 μL, 0.015 mmol, 3 equiv) in DMF (0.2 mL) for 10 mins, after which it was pulled into a fritted syringe containing the swollen resin with an additional 0.2 mL DMF. The reaction was allowed to proceed overnight while rocking gently. The resin was washed with DMF several times then DCM. Pale brown colored **HMSiR** functionalized resin was obtained. A small quantity of these **HMSiR** functionalized beads was transferred onto glass coverslips and 0.02 mL of PBS buffer (pH = 7.4) or citric acid buffer (pH = 5.0) was added. After allowing the resin beads to soak in the buffers for 5 mins, the resin beads were imaged on the EVOS fluorescence microscope using a Cy5 filter cube.

pH dependence. A solution of **HMSiR-2** with 1% MeOH in pH 3 buffer (100 mM sodium citrate, pH = 2.98) was prepared in a cuvette, which was gently shaken to ensure mixing. Emission was then collected from 665–720 nm while exciting at 650 nm. The process was repeated with **HMSiR-2** with 1% MeOH in solutions of of pH 1 (1 M HCl), pH 4 (100 mM sodium citrate, pH = 4.00), pH 5 (100 mM sodium citrate, pH = 4.97), pH 6 (100 mM PBS , pH = 5.85), pH 7.4 (100 mM PBS, pH = 7.45), pH 8 (50 mM Tris and10 mM NaCl, pH = 7.93), pH 9 (100 mM Tris, pH = 8.98), and pH 13 (1 M NaOH).

Solvent dependence. A solution of **HMSiR-2** with 1% MeOH was prepared in acetone in a cuvette. Fluorescence emission at 670 nm was recorded while exciting at 650 nm at 0 s, 20 s, 40 s, and 60 s after preparing the solution. The process was repeated with **HMSiR-2** with 1% MeOH in solutions of DMSO, MeCN, chloroform, MeOH, and ethyl acetate. For DMSO, the emission was recorded at 685 nm. For ethyl acetate, the fluorescence at an additional timepoint of 5 min

was also recorded. For MeOH the procedure was carried out in triplicate with an additional timepoint at 80 s.

RhBNN Wolff rearrangement and HMSiR-2 trapping. A 1 mM solution of **HMSiR-2** in $CDCl_3$ was mixed with a 2 mM solution of RhBNN in $CDCl_3$ and 0.6 mL was added to an NMR tube. The tube was irradiated with blue light from and LED lamp for 24 hours. ^{1}H NMR spectra and ESI mass spectra were collected at 0 h, 0.25 h, 1.25 h, 2.5 h, and 24 h of irradiation. A control experiment was prepared similarly but kept in the dark throughout the 24 hours.

4.5. References

1. Persons T. M.; Droitcour J. A.; Larson E. M.; Armes M. W.; Ettaro L. R.; Farah P. G.; Howard K. L.; Johnson D. R.; Martinez S.; Ryen T. S.; Offutt S. E.; Petersen C. D.; Stevens A. O.; Vance W. K.; Wallestad K. J. Nanomanufacturing: Emergence and Implications for U.S. Competitiveness, the Environment, and Human Health. U. S. G. A. Office, Ed.; **2014**.
2. Liddle, J. A.; Gallatin, G. M. Nanomanufacturing: A Perspective. *ACS Nano* **2016**, *10* (3), 2995–3014.
3. Liu, C.; Gillette, E. I.; Chen, X.; Pearse, A. J.; Kozen, A. C.; Schroeder, M. A.; Gregorczyk, K. E.; Lee, S. B.; Rubloff, G. W. An All-in-One Nanopore Battery Array. *Nature Nanotechnology* **2014**, *9* (12), 1031–1039
4. Misra, R.; Acharya, S.; Sahoo, S. K. Cancer Nanotechnology: Application of Nanotechnology in Cancer Therapy. *Drug Discovery Today* **2010**, *15* (19-20), 842–850.
5. Hill, C.; Amodeo, A.; Joseph, J. V.; Patel, H. R. Nano- and Microrobotics: How Far Is the Reality? *Expert Review of Anticancer Therapy* **2008**, *8* (12), 1891–1897.
6. Balasubramanian, S.; Kagan, D.; Jack Hu, C.-M.; Campuzano, S.; Lobo-Castañon, M. J.; Lim, N.; Kang, D. Y.; Zimmerman, M.; Zhang, L.; Wang, J. Micromachine-Enabled Capture and Isolation of Cancer Cells in Complex Media. *Angewandte Chemie International Edition* **2011**, *50* (18), 4161–4164
7. Cancer Nanotechnology Plan 2015; Hartshorn, C., Ed.; National Cancer Institute: Rockville, MD, **2016**, https://www.cancer.gov/sites/ocnr/research/plan.

8. Leary, S. P.; Liu, C. Y.; Apuzzo, M. L. Toward the Emergence of Nanoneurosurgery: Part III—Nanomedicine: Targeted Nanotherapy, Nanosurgery, and Progress Toward the Realization of Nanoneurosurgery. *Neurosurgery* **2006**, *58* (6), 1009–1026.

9. Dickherber, A.; Morris, S. A.; Grodzinski, P. NCI Investment in Nanotechnology: Achievements and Challenges for the Future. *Wiley Interdisciplinary Reviews: Nanomedicine and Nanobiotechnology* **2014**, *7* (3), 251–265.

10. Tian, B.; Zheng, X.; Kempa, T. J.; Fang, Y.; Yu, N.; Yu, G.; Huang, J.; Lieber, C. M. Coaxial Silicon Nanowires as Solar Cells and Nanoelectronic Power Sources. *Nature* **2007**, *449* (7164), 885–889.

11. Yin, X.; Zang, Y.; Zhu, L.; Low, J. Z.; Liu, Z.-F.; Cui, J.; Neaton, J. B.; Venkataraman, L.; Campos, L. M. A Reversible Single-Molecule Switch Based on Activated Antiaromaticity. *Science Advances* **2017**, *3* (10).

12. Flood, A. H.; Stoddart, J. F.; Steuerman, D. W.; Heath, J. R. Whence Molecular Electronics? *Science* **2004**, *306* (5704), 2055–2056

13. Yang, Y.; Ruan, G.; Xiang, C.; Wang, G.; Tour, J. M. Flexible Three-Dimensional Nanoporous Metal-Based Energy Devices. *Journal of the American Chemical Society* **2014**, *136* (17), 6187–6190.

14. Fang, F.; Zhang, X.; Gao, W.; Guo, Y.; Byrne, G.; Hansen, H. Nanomanufacturing—Perspective and Applications. *CIRP Annals* **2017**, *66* (2), 683–705.

15. Ishikawa, S.; Iijima K.; Otsuka H. Nanofabrication Technologies to Control Cell and Tissue Function for Biomedical Applications in Nanobiomaterials: Nanostructured Materials for Biomedical Applications; Narayan R., Ed.; Woodhead Publishing, **2018**; pp 385-409

16. Altissimo, M. E-Beam Lithography for Micro-/Nanofabrication. *Biomicrofluidics* **2010**, *4* (2), 26503.

17. Piner, R. D.; Zhu, J.; Xu, F.; Hong, S.; Mirkin, C. A. "Dip-Pen" Nanolithography. *Science* **1999**, *283* (5402), 661.

18. Hell, S. W.; Wichmann, J. Breaking the Diffraction Resolution Limit by Stimulated Emission: Stimulated-Emission-Depletion Fluorescence Microscopy. *Optics Letters* **1994**, *19* (11), 780.

19. Scott, T. F.; Kowalski, B. A.; Sullivan, A. C.; Bowman, C. N.; Mcleod, R. R. Two-Color Single-Photon Photoinitiation and Photoinhibition for Subdiffraction Photolithography. *Science* **2009**, *324* (5929), 913–917.

20. Klar, T. A.; Wollhofen, R.; Jacak, J. Sub-Abbe Resolution: from STED Microscopy to STED Lithography. *Physica Scripta* **2014**, *T162*, 014049.

21. Li, H.; Vaughan, J. C. Switchable Fluorophores for Single-Molecule Localization Microscopy. *Chemical Reviews* **2018**, *118* (18), 9412–9454

22. Zhuang, X. Nano-Imaging with STORM. *Nature Photonics* **2009**, *3* (7), 365–367.

23. Patterson, G.; Davidson, M.; Manley, S.; Lippincott-Schwartz, J. Superresolution Imaging Using Single-Molecule Localization. *Annual Review of Physical Chemistry* **2010**, *61* (1), 345–367.

24. Bates, M.; Huang, B.; Dempsey, G. T.; Zhuang, X. Multicolor Super-Resolution Imaging with Photo-Switchable Fluorescent Probes. *Science* **2007**, *317* (5845), 1749–1753.

25. Heilemann, M.; van de Linde, S.; Schüttpelz, M.; Kasper, R.; Seefeldt, B.; Mukherjee, A.; Tinnefeld, P.; Sauer, M. Subdiffraction-Resolution Fluorescence Imaging with Conventional Fluorescent Probes. *Angewandte Chemie International Edition* **2008**, *47* (33), 6172–6176.

26. Lukyanov, K. A.; Chudakov, D. M.; Lukyanov, S.; Verkhusha, V. V. Photoactivatable Fluorescent Proteins. *Nature Reviews Molecular Cell Biology* **2005**, *6* (11), 885–890.

27. Hell, S. W.; Kroug, M. Ground-State-Depletion Fluorscence Microscopy: A Concept for Breaking the Diffraction Resolution Limit. *Applied Physics B Lasers and Optics* **1995**, *60* (5), 495–497.

28. Fölling, J.; Bossi, M.; Bock, H.; Medda, R.; Wurm, C. A.; Hein, B.; Jakobs, S.; Eggeling, C.; Hell, S. W. Fluorescence Nanoscopy by Ground-State Depletion and Single-Molecule Return. *Nature Methods* **2008**, *5* (11), 943–945.

29. Bretschneider, S.; Eggeling, C.; Hell, S. W. Breaking the Diffraction Barrier in Fluorescence Microscopy by Optical Shelving. *Physical Review Letters* **2007**, *98* (21).

30. Morozumi, A.; Kamiya, M.; Uno, S.-nosuke; Umezawa, K.; Kojima, R.; Yoshihara, T.; Tobita, S.; Urano, Y. Spontaneously Blinking Fluorophores Based on Nucleophilic Addition/Dissociation of Intracellular Glutathione for Live-Cell Super-Resolution Imaging. *Journal of the American Chemical Society* **2020**.

31. Heilemann, M.; van de Linde, S.; Mukherjee, A.; Sauer, M. Super-Resolution Imaging with Small Organic Fluorophores. *Angewandte Chemie International Edition* **2009**, *48* (37), 6903–6908.

32. Haris, U.; Plank, J. T.; Li, B.; Page, Z. A.; Lippert, A. R. Visible Light Chemical Micropatterning Using a Digital Light Processing Fluorescence Microscope. *ACS Cent. Sci.* **2021**, *8*, 67-76.

33. Koide, Y.; Urano, Y.; Hanaoka, K.; Terai, T.; Nagano, T. Development of an Si-Rhodamine-Based Far-Red to near-Infrared Fluorescence Probe Selective for

Hypochlorous Acid and Its Applications for Biological Imaging. *Journal of the American Chemical Society* **2011**, *133* (15), 5680–5682.

34. Uno, S.-nosuke; Kamiya, M.; Morozumi, A.; Urano, Y. A Green-Light-Emitting, Spontaneously Blinking Fluorophore Based on Intramolecular Spirocyclization for Dual-Colour Super-Resolution Imaging. *Chemical Communications* **2018**, *54* (1), 102–105.
35. Huang, J.; Zhu, J.; Snyder, S. A.; Morris, A. J.; Turner, S. R. Nanoporous Highly Crosslinked Polymer Networks with Covalently Bonded Amines for CO2 Capture. *Polymer* **2018**, *154*, 55–61.
36. Worrell, B. T.; Mavila, S.; Wang, C.; Kontour, T. M.; Lim, C.-H.; McBride, M. K.; Musgrave, C. B.; Shoemaker, R.; Bowman, C. N. A User's Guide to the Thiol-Thioester Exchange in Organic Media: Scope, Limitations, and Applications in Material Science. *Polymer Chemistry* **2018**, *9* (36), 4523–4534.
37. Woll, M. G.; Gellman, S. H. Backbone Thioester Exchange: a New Approach to Evaluating Higher Order Structural Stability in Polypeptides. *Journal of the American Chemical Society* **2004**, *126* (36), 11172–11174.
38. Larsson, R.; Pei, Z.; Ramström, O. Catalytic Self-Screening of Cholinesterase Substrates from a Dynamic Combinatorial Thioester Library. *Angewandte Chemie International Edition* **2004**, *43* (28), 3716–3718.
39. Belov, V. N.; Wurm, C. A.; Boyarskiy, V. P.; Jakobs, S.; Hell, S. W. Rhodamines NN: A Novel Class of Caged Fluorescent Dyes. *Angewandte Chemie International Edition* **2010**, *49* (20), 3520–3523.
40. Uno, S.-nosuke; Kamiya, M.; Yoshihara, T.; Sugawara, K.; Okabe, K.; Tarhan, M. C.; Fujita, H.; Funatsu, T.; Okada, Y.; Tobita, S.; Urano, Y. A Spontaneously Blinking Fluorophore Based on Intramolecular Spirocyclization for Live-Cell Super-Resolution Imaging. *Nature Chemistry* **2014**, *6* (8), 681–689.
41. Ryan, L. S.; Gerberich, J.; Haris, U.; Nguyen, D.; Mason, R. P.; Lippert, A. R. Ratiometric pH Imaging Using a 1,2-Dioxetane Chemiluminescence Resonance Energy Transfer Sensor in Live Animals. *ACS Sens.* **2020**, 5, 2925-2932.
42. Mahon, A. B.; Arora, P. S. Design, Synthesis and Protein-Targeting Properties of Thioether-Linked Hydrogen Bond Surrogate Helices. *Chem. Commun.* **2012**, *48* (10), 1416–1418.
43. Yeo, W.-S.; Min, D.-H.; Hsieh, R. W.; Greene, G. L.; Mrksich, M. Label-Free Detection of Protein-Protein Interactions on Biochips. *Angewandte Chemie International Edition* **2005**, *44* (34), 5480–5483.

44. Qu, Y.; Wang, X.; Pei, Z.; Pei, Y. Cancer-Mitochondria Dual-Targeting Glycol/Ferrocenium-Based Polydopamine Nanoparticles for Synergistic Photothermal and Photodynamic Therapy. *ChemMedChem* **2021**, *17* (2).

45. Hu, M.; Li, L.; Wu, H.; Su, Y.; Yang, P.-Y.; Uttamchandani, M.; Xu, Q.-H.; Yao, S. Q. Multicolor, One- and Two-Photon Imaging of Enzymatic Activities in Live Cells with Fluorescently Quenched Activity-Based Probes (QABPs). *J. Am. Chem. Soc.* **2011**, *133* (31), 12009–12020.

Chapter 5

SILICON RHODAMINE BASED CHEMILUMINOPHORE FOR NEAR INFRARED CHEMILUMINESCENCE IMAGING IN VIVO

5.1. Introduction

Chemiluminescence is a photochemical phenomenon evolved in nature with growing scientific and technological applications, wherein light is generated via a chemical reaction. The decomposition of 1,2-dioxetanes following a chemically initiated electron exchange luminescence (CIEEL) mechanism is one such chemical reaction that generates light, and forms the basis of chemiluminescent molecular bioimaging.[1] CIEEL is proposed to proceed via an electron transfer from the phenolate to the 1,2-dioxetane, followed by bond cleavage, and then another back electron transfer to form the singlet excited state of the phenolate, which emits a photon of light (Scheme 5-1). The mechanism can be triggered by masking the phenolate with a protecting group (PG) that is exclusively deprotected by an analyte of interest, resulting in spontaneous light generation.

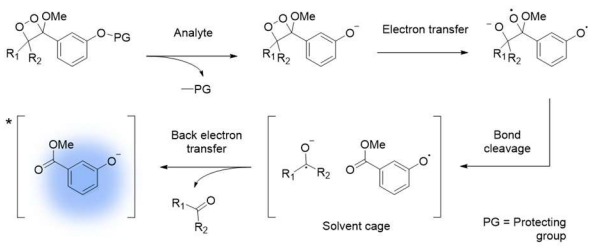

Scheme 5-1. CIEEL Mechanism. Reprinted with permission from ref 18. Copyright 2023 American Chemical Society.

Unlike fluorescence imaging, chemiluminescence imaging features response independent of light excitation, thus bypassing background signal from autofluorescence, and enabling

higher imaging sensitivity. In recent years, the repository of these triggerable 1,2-dioxetane probes which exhibit chemiluminescence emission in response to specific bioanalytes has rapidly grown following demonstration of their in-vivo use[2,3] and aqueous compatibility.[4,5] Indeed, chemiluminescent imaging now spans analytes including but not limited to enzymes,[3] reactive nitrogen, oxygen, and sulfur species,[6] metal ions, protein interactions,[7] pH,[8,9] and hypoxia.[10,11] In order to further the *in-vivo* applicability of these imaging agents, efforts are underway to shift their chemiluminescence emission from the conventional blue and green emission to the near infrared (NIR), which allows higher signal penetration through tissue and higher imaging depth.[12,13,14] Extension of π-conjugation and introduction of push-pull systems have been explored as strategies to red-shift the emission of the benzoate decomposition product directly.[13,15] Another strategy to achieve red-shifted emission is the use of non-radiative energy transfer schemes, where the excited state benzoate generated during the CIEEL process transfers energy to an appended red-emitting fluorophore based on spectral overlap of the luminophores (Figure 5-1 A). Previously, energy transfer based NIR chemiluminescence has been reported for detection of hypoxia,[11] pH,[10] H_2O_2, hydrazine, and enzymes like ß-galactosidase[16] and alkaline phosphatase.[17] A technique for obtaining *quantitative* chemiluminescent measurements of analytes from such unimolecular energy transfer schemes is conjunction of chemiluminescence with analyte responsive fluorescence for resultant ratiometric response. The ratio of analyte- dependent response from the acceptor and analyte- independent response from the chemiluminophore donor enables quantification of cellular parameters and analytes, as has been demonstrated by pH and hypoxia probes **Ratio-pHCL-1** and **IrCL1-3** (Figure 5-1 B).[11,9,18]

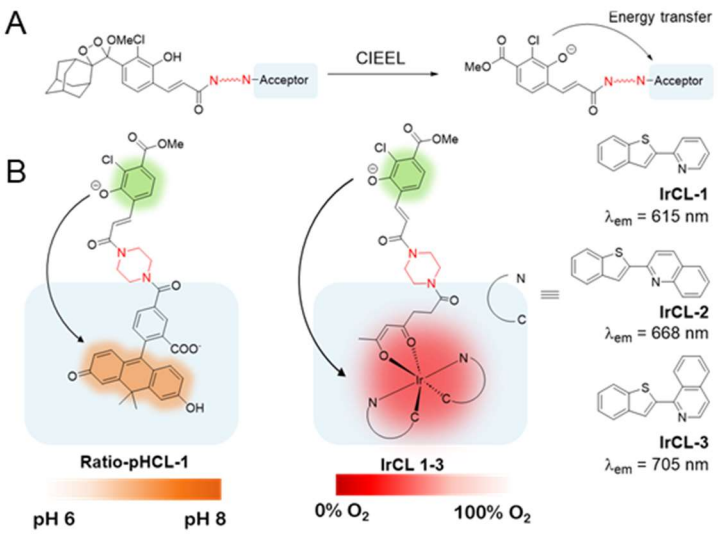

Figure 5-1. (A) 1,2-dioxetane donor and fluorophore acceptor adducts for energy transfer chemiluminescence. (B) A carbofluorescein fluorophore and an iridium phosphore appended to spiroadamantane 1,2-dioxetanes for ratiometric pH and oxygen probes. Adapted with permission from ref 18. Copyright 2023 American Chemical Society.

While combinations of 1,2-dioxetanes have been explored with several NIR-emitting luminophores including quinone-cyanine,[16] and iridium complexes,[11] limitations of these systems including poor aqueous solubility, low quantum yields, and challenging syntheses leave room for exploration of synthetically accessible and high performing chemiluminescence energy transfer acceptors. Of NIR emitting fluorophores, silicon rhodamines (SiR)[19] in particular have been used extensively for development of triggerable fluorescent probes, owing to their aqueous solubility, high quantum yield, and photostability.[20] Turn-on fluorescent probes for *in vivo* bioimaging of enzymes,[21,22] endogenous peroxynitrite[23,] lysosomal pH,[24] retinal hypoxia,[25] nitric oxide,[26,27] hypochlorous acid,[28,29] neuronal calcium ions,[30] and zinc ions[20] based on silicon rhodamine dyes have been reported. In comparison, chemiluminescent probes incorporating this fluorescent emitter are non-existent.

Aside from silicon-based scaffolds, dyes with large Stokes shifts can also be explored as acceptors for energy transfer luminescence.[31,32,33] Traditionally, fluorophore Stokes shifts, such as those of Rhodamine B, Rhodamine 6G and Rhodamine 101, are less than 30 nm and emission

wavelengths are lower than 600 nm. However, modification of these structures with groups that result in a narrowed HOMO-LUMO gap allow for Stokes shifts in ranges of 100 nm. Washington Red (WR) dyes are a class of rhodol based fluorophores that incorporate fused tetrahydroxyquinoxaline rings in the core of the scaffold in order to widen their Stokes shift and red shift emission.[33] Fluorescent sensors for H_2S[33] and pH,[31] among others, have been developed using such molecules owing to their NIR emission, high quantum yield, and photostability. Like SiR, these fluorophores as well are yet to be investigated as acceptors for chemiluminescence resonance energy transfer. Translation of these SiR and WR fluorogenic probes to chemiluminescent counterparts will provide access to NIR imaging of a wide variety of analytes through tissue, thus furthering the applicability of chemiluminescence in biosensing and analyte quantification.

Herein, we report NIR silicon rhodamine based chemiluminophores, **SiRCL-OAc** and **SiRCL-OH**, and NIR tetrahydroxyquinoxaline-modified rhodol based chemiluminophores, **WRCL-OAc** and **WRCL-OH**, which exhibit energy transfer from an excited state 1,2-dioxetane to the appended SiR or WR emitter in aqueous systems. We explore design and synthesis, pH dependent response and chemiluminescence decay kinetic of these agents, and for **SiRCL-OH**, we report chemiluminescence quantum yield, as well as demonstration of *in vivo* imaging.

5.2. Results and Discussion

5.2.1. Design and synthesis of **SiRCL-OAc** and **SiRCL-OH**

We designed **SiRCL-OH** to consist of a chemiluminescent spiroadamantane 1,2-dioxtetane scaffold with an unprotected phenol attached to a silicon rhodamine fluorophore. We used a piperazine linker at the acrylate moiety of the 1,2-dioxetane to link to the silicon rhodamine

fluorophore **SiR** based on previous success with this linker.[9] For synthesis of **SiR**, formaldehyde was first used in acidic conditions to homodimerize N,N-dimethyl-3-bromoaniline to afford compound **1** (Scheme 5-2). Silicon was incorporated into the scaffold by trapping the product of a lithium-halogen exchange at −78 °C with dichlorodimethylsilane resulting in compound **2**, which was then oxidized to form the silicon anthrone **3** using $KMnO_4$. Anthrone **3** was reacted with tert-butyl protected iodobenzoate **4** via a lithium-halogen exchange and nucleophilic addition to the ketone. Upon acidification of the reaction mixture, the intensely blue colored dye **5** was formed. Deprotection of the carboxylic acid led to the final product **SiR**, a dark blue colored dye with 685 nm red fluorescence emission. This fluorophore was reacted with 1-boc-piperazine, and the resulting compound was deprotected in TFA in order to achieve the reactive piperazine handle. The enol ether scaffold **8** with an acrylate functionality, prepared according to literature procedures was appended to the silicon rhodamine to furnish the dioxetane precursor **9** after cleavage of the phenol's acetate protecting group with ammonium acetate. Reaction with singlet oxygen afforded **SiRCL-OH** as the chemiluminescent dioxetane with a free phenol. **SiRCL-OAc** was synthesized as the acetate protected phenol by bypassing the ammonium acetate deprotection step before dioxetane formation (Scheme 5-2).

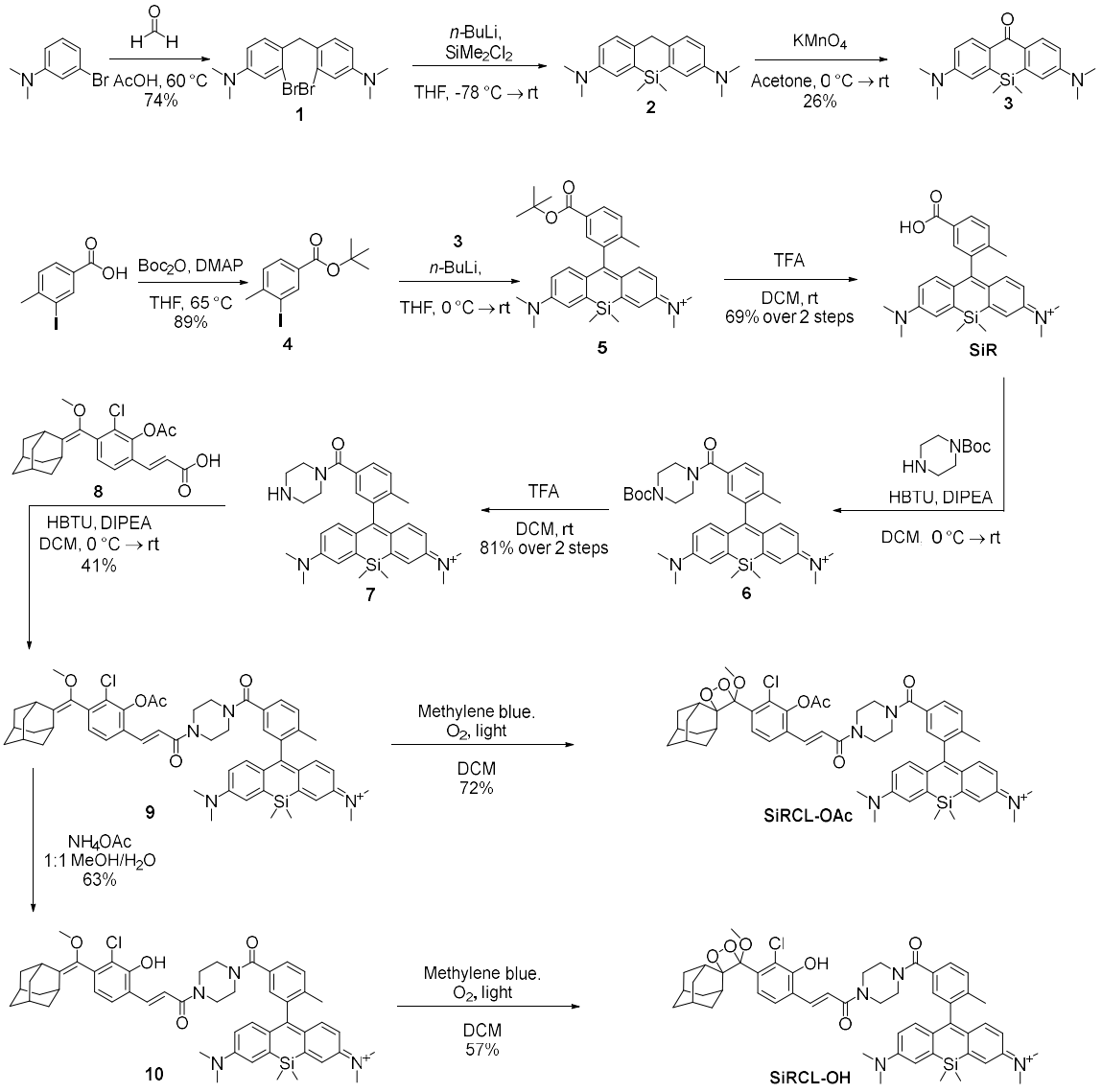

Scheme 5-2. Synthesis of **SiRCL-OAc** and **SiRCL-OH.**

5.2.2. Characterization and Chemiluminescence Response of **SiRCL-OH**

Following synthesis, we moved to characterizing spectroscopic properties of the chemiluminescent molecules. We found that the **SiRCL** dyes exhibited an absorbance maximum at 655 nm, and we verified that this spectrum overlaps with the emission of the energy donor, methyl acrylate dioxetane,[4] which is a requisite for resonance energy transfer (Figure 5-2 A). We studied the chemiluminescent response of **SiRCL-OAc**. Addition of 0.1 M NaOH, which cleaves the acetate protecting group and generates the emissive phenolate led to chemiluminescence

(Figure 5-2 B). Under these basic conditions, the 540 nm peak corresponding to direct emission from the benzoate was significantly larger than the 680 nm peak corresponding to NIR emission due to energy transfer, even at high DMSO concentrations during DMSO dependence studies (Figure 5-2 C, D). This may be due to base mediated hydrolysis of the linkage between the benzoate and the silicon rhodamine: chemiluminescence resonance energy transfer efficiency is dependent on the distance between donor and acceptor, so severance of the covalent bond between the donor and acceptor leads to poor energy transfer and only direct emission from the donor molecule.

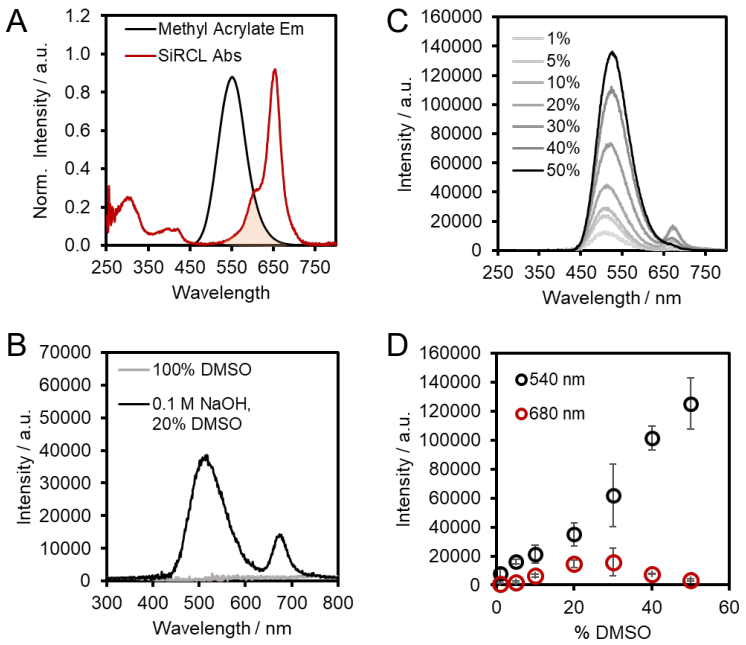

Figure 5-2. (A) Spectral overlap between methyl acrylate dioxetane emission and **SiRCL** absorbance. (B) Chemiluminscence emission spectra of 20 µM **SiRCL-OAc** in the absence of NaOH and in the presence of 0.1 M NaOH in 20% DMSO. (C) Chemiluminescence emission traces of 20 µM **SiRCL-OAc** in varying DMSO concentration in 0.1 M NaOH. (D) Emission intensity at 540 nm and 680 nm with varying DMSO concentration in 0.1 M NaOH. Error bars are ± S.D. with n = 3 replicates.

We next tested **SiRCL-OH,** which has a free phenol and does not require strong base for triggering chemiluminescence. In acidic buffer, when the compound exists as a phenol, no chemiluminescence emission was observed. In buffers with pH higher than the pKa of the phenol, chemiluminescence emission peaks at 540 nm and 680 nm were observed, corresponding to direct emission from the excited state benzoate and emission from the silicon rhodamine due to energy transfer, respectively (Figure 5-3 A). Luminescence response to varying pH was studied. **SiRCL-OH** showed no emission signal at pH below 5. A significant response was observed at pH 7.4, and maximum emission was reached at pH 9 (Figure 5-3 B). At pH 13, in 0.1 M NaOH the 540 nm peak rose drastically, and the 680 nm peak reduced in intensity, which again suggests hydrolysis and cleavage of the **SiR** from the compound in strongly basic conditions. We also studied the DMSO dependence of the emission. Emission intensity generally increased with DMSO concentration in PBS at both emission wavelengths, with emission at 680 nm increasing significantly between 10% and 35% DMSO and then dropping at higher DMSO concentrations than this (Figure 5-3 C, D).

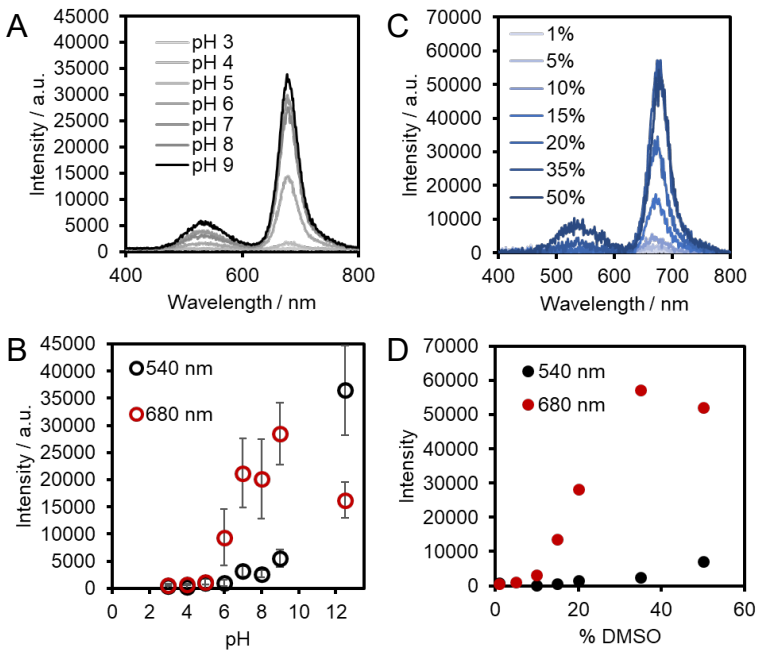

Figure 5-3. (A) Chemiluminescence emission traces of 20 µM **SiRCL-OH** in 30% DMSO and pH buffers between pH 3 and 9. (B) Emission intensity at 540 nm and 680 nm with varying pH between 3 and 13 in 30% DMSO. Error bars are ± S.D. with n = 3–5 replicates. (C) Chemiluminescence emission traces of 20 µM **SiRCL-OH** in varying DMSO concentration at pH 7.4. (D) Emission intensity at 540 nm and 680 nm with varying DMSO concentration and pH 7.4.

Previously, polymeric enhancers such as Emerald II Enhancer and Sapphire II Enhancer have been used to enhance and red-shift chemiluminescent signal of 1,2-dioxetanes. The polymer encapsulates the luminophore, creating a hydrophobic microenvironment and reducing aqueous quenching. The enhancer also contains dyes that act as an energy acceptor for energy transfer and red-shifted emission.[34] We investigated whether an enhancer could be used to improve the signal of **SiRCL-OH.** Chemiluminescence emission traces with and without addition of Emerald II revealed that only the 540 nm peak was enhanced, while the 680 nm peak was attenuated in the presence of enhancer, perhaps indicating energy transfer to the enhancer fluorophore instead of to the silicon rhodamine (Figure 5-4 A). We next monitored the decay of chemiluminescence emission for **SiRCL-OH** from 0 to 60 min (Figure 5-4 B) and determined the rate constant *k* by mathematically fitting the experimental data to a model for exponential decay (Table 5-1, equation

1). We found the half-life of the emission at 680 nm to be 1.96 ± 0.24 min and the half-life of the emission at 540 nm to be 1.79 ± 0.29 min in 30% DMSO and pH 7.4 (Figure 5-4 C, Table 5-1, equation 2).

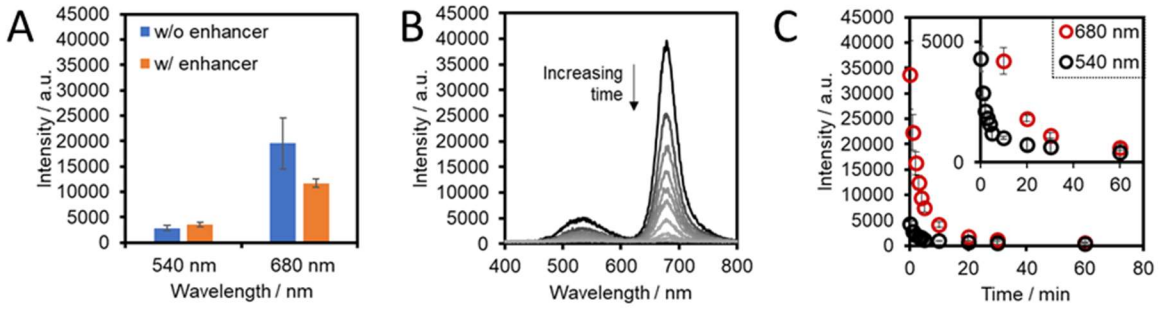

Figure 5-4. (A) Chemiluminescence emission of **SiRCL-OH** at 540 nm and 680 nm without and with the addition of 5% Emerald II enhancer in 30% DMSO and PBS 7.4. (B) Chemiluminescence time course scans from 0 to 60 mins after addition of PBS 7.4 to **SiRCL-OH** with 30% DMSO. (C) Emission decay between 0 to 60 mins at 540 nm and 680 nm. Inset: Intensity axis scaled down to 5000 a.u. for detailed view of 540 nm emission decay. Experiments conducted with Rokia Osman, SMU.

Table 5-1. Exponential decay parameters and determination of half-life of **SiRCL-OH** emission.

$I_t = I_0\, e^{-kt} + B$ (Equation $5-1$) $\qquad t_{1/2} = \ln(2)/k$ (Equation $5-2$)

	I_0	k (min^{-1})	B	$t_{1/2}$ (min)
540 nm	3480 ± 254	0.394 ± 0.068	694 ± 239	1.79 ± 0.29
680 nm	31100 ± 6360	0.357 ± 0.042	1740 ± 234	1.96 ± 0.24

5.2.3. Chemiluminescence quantum yield

Chemiluminescence quantum yield (Φ_{CL}) is a measure of the efficiency of light emission from a chemical reaction. It is defined as the number of photons emitted by a chemiluminescent

reaction as a fraction of the number of reactive intermediates formed in the reaction. Φ_{CL} is a quantifiable measure of how much energy released in a chemical reaction is converted into light. The higher the quantum yield, the more efficient the reaction is at producing light. Chemiluminescence quantum yields range from 0 to 1, with 1 indicating that all reactive intermediates produce light and 0 indicating that no light is produced.

We calculated the chemiluminescence quantum yield of **SiRCL-OH** using a method based on previously reported procedures.[35,36,11] Equation 5-3 summarizes calculation of Φ_{SiRCL}, the chemiluminescent quantum yield of **SiRCL-OH** (Equation 5-3). Q_{SiRCL} is the total light emission from **SiRCL-OH**, obtained by integrating the kinetic profile of 20 μM **SiRCL-OH** chemiluminescent decay in PBS (pH = 7.4) with 30% DMSO over 3600 s at 680 nm (Figure 5-5 A). n_{SiRCL} is the number of moles of **SiRCL-OH**. F_{lum} is the calibration factor to convert the total light emission of the sample from arbitrary units to Einstein units, calculated using the chemiluminescent standard luminol and Equation 5-4, where Φ_{lum} is the reference chemiluminescence quantum yield of luminol (0.0114 ± 0.0006 E mol^{-1}), Q_{lum} is the integrated emission intensity under a kinetic emission profile of luminol in PBS at pH 11.6 with consecutive additions of hemin (Figure 5-5 B), and n_{lum} is the number of moles of luminol used. F_{spect} is the spectral correction factor, calculated as the light that passes through the wavelength selective monochromator at a particular wavelength (integrated intensity from [λ – ½ slits] to [λ + ½ slits]) as a fraction of the total light emission of the sample across all wavelengths (integrated intensity from 400 to 800 nm) (Equation 5-5). This accounts for the differences in spectral shape between luminol emission and **SiRCL-OH** emission. $F_{spect(lum)}$ was calculated using luminol emission spectrum, and $F_{spect(SiRCL)}$ with **SiRCL-OH** emission spectrum (Figure 5-5 C, D). With incorporation of F_{spect}, only the chemiluminescence emission decay at a single wavelength needs

to be considered for quantum yield calculation despite there being dual emission peaks in the spectrum of **SiRCL-OH**. To account for the sensitivity of the photomultiplier tube detector at different wavelengths, we enabled real-time corrections on the instrument which automatically correct the raw data based on the manufacturer provided correction factors at each wavelength. These corrected traces were used in all calculations.

$$\mathrm{F_{SiRCL}} = \frac{Q_{SiRCL} f_{lum} F_{spect(lum)}}{n_{SiRCL} F_{spect(SiRCL)}} \qquad \text{Equation } 5-3$$

$$f_{lum} = \frac{\phi_{lum} n_{lum}}{Q_{lum}} \qquad \text{Equation } 5-4$$

$$F_{spe} = \frac{\int_{\lambda - slit/2}^{\lambda + slit/2} S(\lambda) d\lambda}{\int_{\lambda_i}^{\lambda_f} S(\lambda) d\lambda} \qquad \text{Equation } 5-5$$

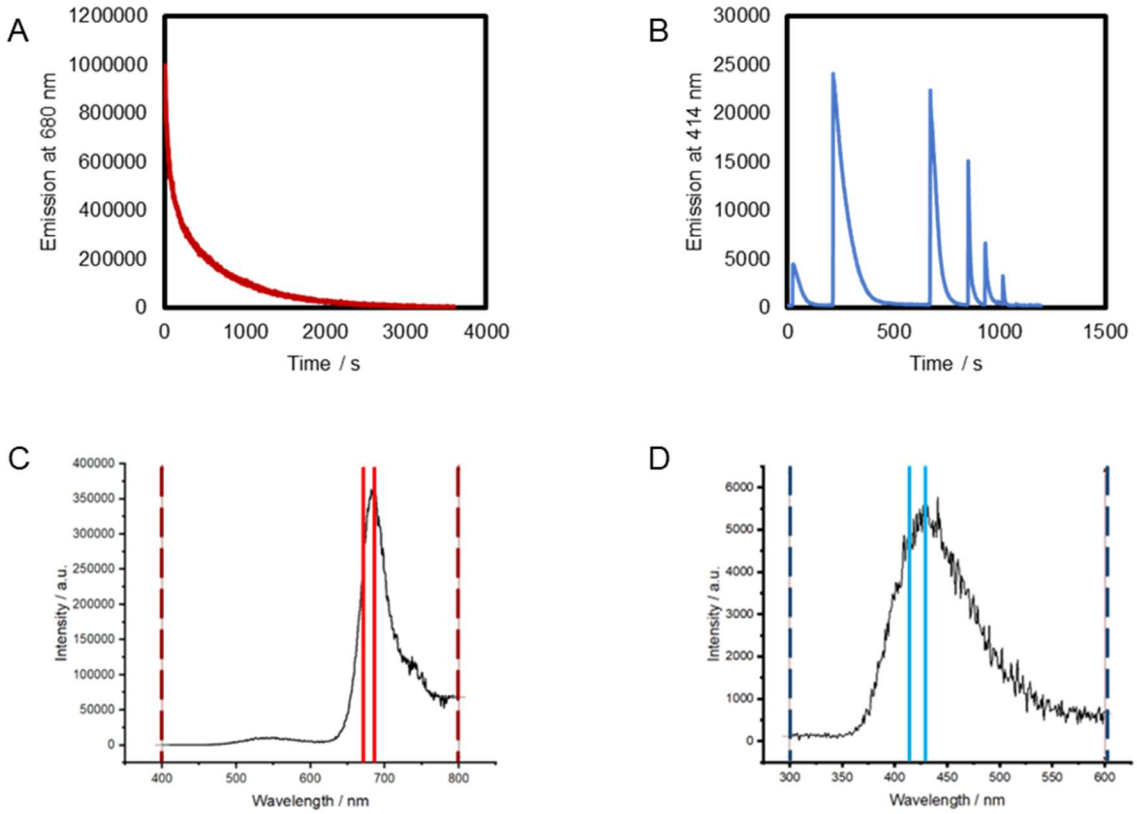

Figure 5-5. (A) Kinetic profile of 20 μM **SiRCL-OH** chemiluminescent decay in PBS (pH = 7.4) with 30% DMSO over 3600 s at 680 nm for determination of Q_{SiRCL}. (B) Kinetic profile of 0.1 mM luminol emission in PBS solvent with consecutive additions of hemin for determination of Q_{lum}. (C) Chemiluminescence emission spectrum of **SiRCL-OH** in PBS (pH = 7.4) with 30% DMSO. $F_{spect(SiRCL)}$ is calculated as the ratio of integrated emission intensity at 673 – 687 nm (solid red lines) and integrated emission intensity at 400 – 800 nm (dashed red lines). (D) Chemiluminescence emission spectrum of luminol in PBS (pH = 11.6) with 30% DMSO. $F_{spect(lum)}$ is calculated as the ratio of integrated emission intensity at 407 – 421 nm (solid blue lines) and integrated emission intensity at 300 – 600 nm (dashed blue lines).

Chemiluminescence quantum yield of **SiRCL-OH** using emission decay and $F_{spect(SiRCL)}$ at 680 nm was calculated to be 0.0037 ± 0.0004. A summary of quantum yield data calculated using different calculation parameters is included in Table 5-2. We calculated quantum yield with **SiRCL-OH** decay and $F_{spect(SiRCL)}$ at 540 nm, as well as by disregarding F_{spect} altogether and summing the total emission data at 540 nm and 680 nm. Lastly, we determined Φ_{SiRCL} with using uncorrected data and a correction factor (f_{photo}), which is another method to account for detector

sensitivity used in referenced literature.[35] Importantly, all variations produce Φ_{SiRCL} figures that are in close agreement with each other, in the range of 0.4%.

Table 5-2. Chemiluminescent quantum yield of **SiRCL-OH** with varying calculation procedures. Calculation carried out my Maidelyevis Castro, SMU.

	Auto corrected data			F_{spect} (680 nm)	
	F_{spect} (680 nm)	F_{spect} (540 nm)	$\Phi_{540} + \Phi_{680}$	f_{photo}	Auto corrections
Φ_{SiRCL}	0.0037 ± 0.0004	0.0040 ± 0.0012	0.0045 ± 0.0004	0.0042 ± 0.0006	0.0037 ± 0.0004

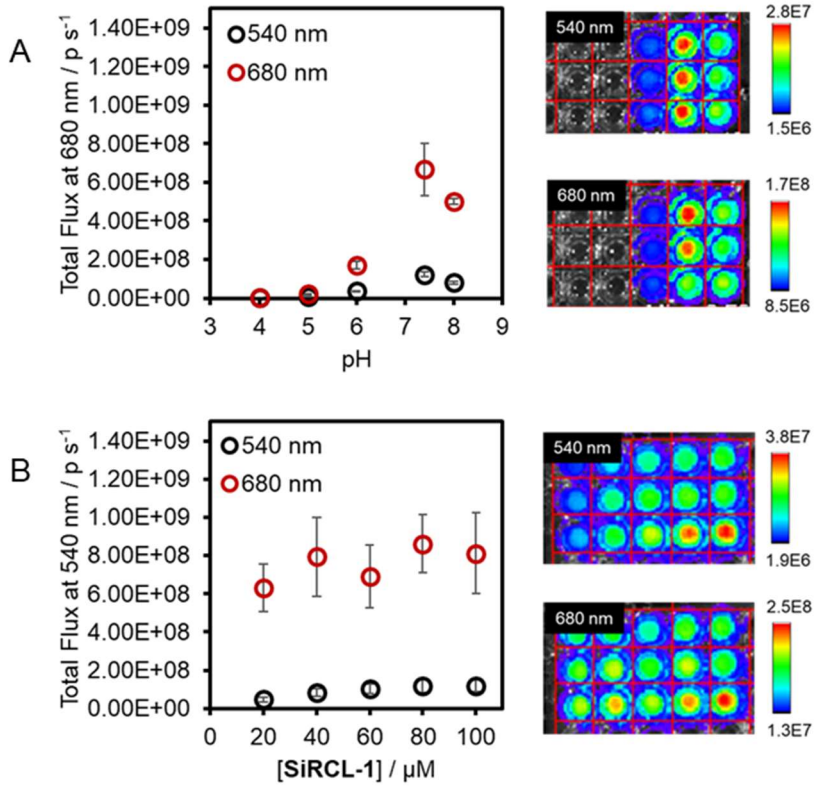

Figure 5-6. (A) IVIS imaging of chemiluminescence pH dependence of 20 µM **SiRCL-OH** in 30% DMSO and pH 4-8. (B) IVIS imaging of chemiluminescence concentration dependence of 20-100 µM **SiRCL-OH** in 30% DMSO and pH 7.4. Experiment conducted by Rokia Osman and Maidelyevis Castro, SMU.

5.2.4. Tissue surrogates and *In Vivo* studies

We observed chemiluminescence response of **SiRCL-OH** in tissues surrogates using an IVIS spectrum instrument, which is a highly sensitive camera to detect and image chemiluminescence. First, we conducted in vitro pH and concentration dependence studies in 94-well plates. pH dependence data was found to agree with data obtained using the HORIBA fluorimeter. Concentration dependence studies revealed that emission intensity generally increased with **SiRCL-OH** concentration at both wavelengths, nearing a plateau at higher concentrations. Interestingly, a decrease from the trend at 60 µM **SiRCL-OH** was observed at 680 nm, with no corresponding change at 540 nm.

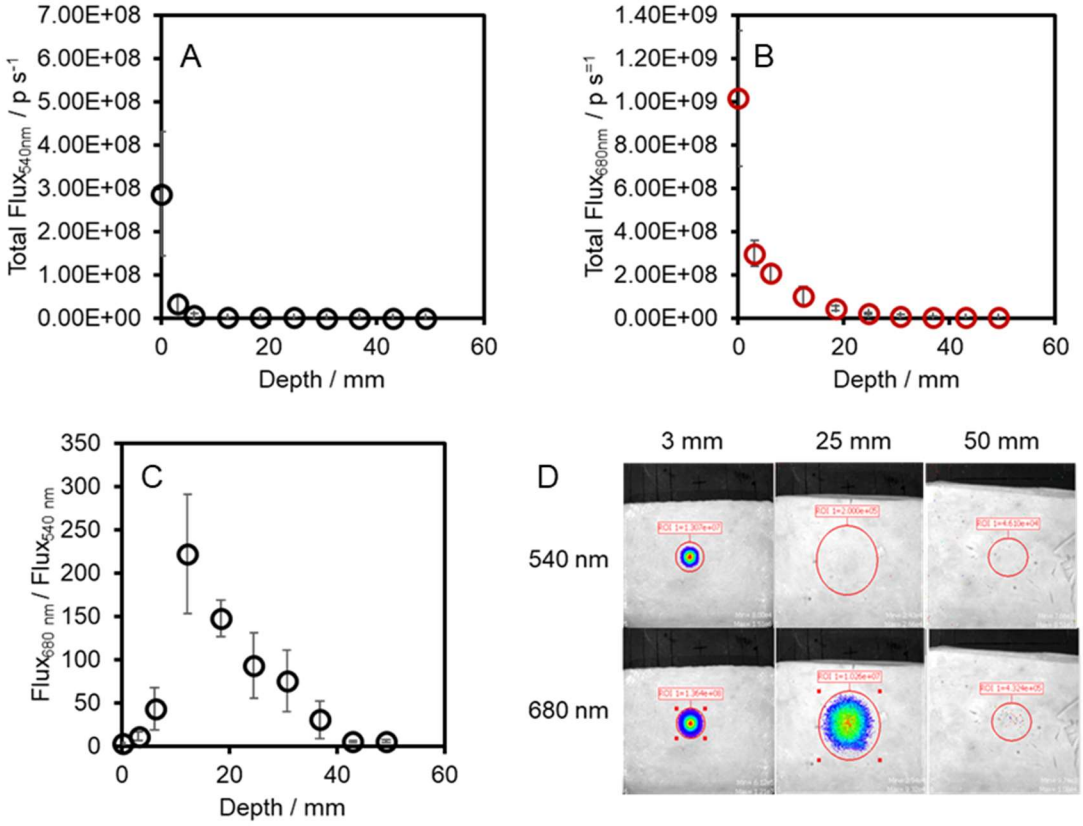

Figure 5-7. Chemiluminescence signal at (A) 540 nm and (B) 680 nm from 100 µM solution of **SiRCL-OH** in 30% DMSO and PBS (pH 7.4) through turkey deli slices with increasing tissue depth (C) Ratio of flux at 680 nm and 540 nm with tissue depth. (D) Luminescence heat map images of chemiluminescence signal at 540 nm and 680 nm through tissue of varying depths. Experiment conducted by Rokia Osman and Maidelyevis Castro, SMU.

Next, we investigated the depth penetration of **SiRCL-OH** emission through tissue (Figure 5-7). Turkey deli slices were used to model tissue. A 100 µM solution of **SiRCL-OH** in 30% DMSO and PBS (pH 7.4) was prepared in a well plate and increasing number of turkey deli slices were added on top, before imaging luminescence at 540 nm and 680 nm. We found that the depth penetration of the emission signal at 540 nm was about 25 mm (Figure 5-7 A), while the penetration of the NIR emission signal at 680 nm was much higher, showing total flux greater than the background even at 50 mm of tissue (Figure 5-7 B). The ratio of response at 680 nm and 540 nm with increasing depth indicates the better tissue penetration of the NIR signal, nearly 225 times higher than the signal at 540 nm at a depth of 12 mm (Figure 5-7 C). Injections of **SiRCL-OH** into chicken breast tissue revealed that signal could be observed through this model as well at both wavelengths, up to at least 20 mm (Figure 5-8 A).

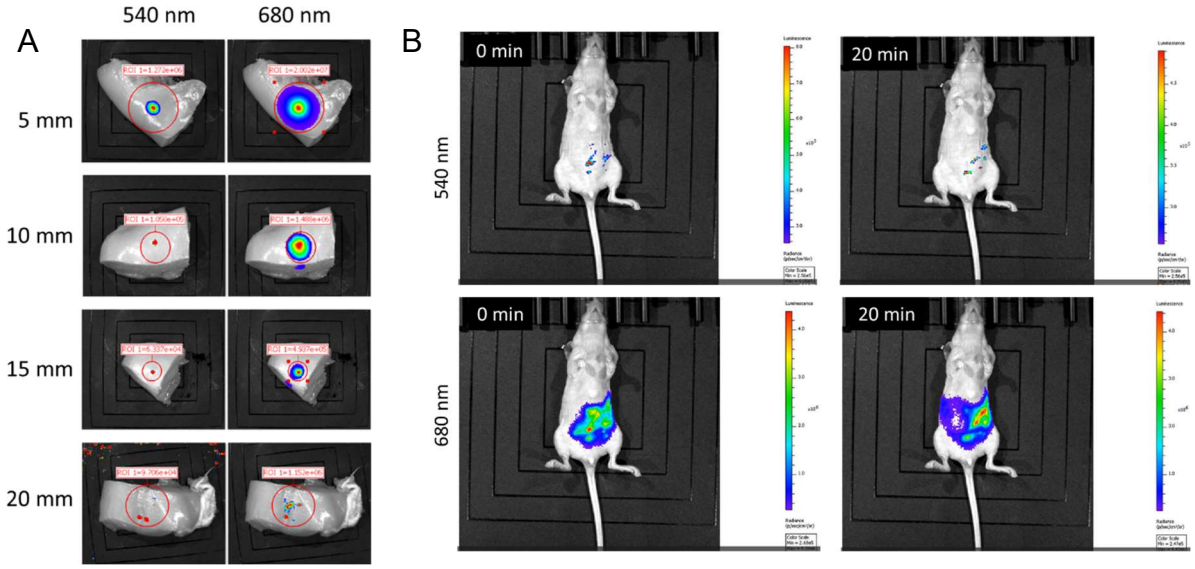

Figure 5-8. (A) Signal penetration through chicken breast tissue at 540 and 680 nm with increasing injection depth of 30 µL of 100 µM **SiRCL-OH** in 30% DMSO and PBS (pH = 7.4). (B) Chemiluminescence signal at 680 nm in live mice injected with 20 µL of 100 µM **SiRCL-OH** in PBS (pH = 7.4) in IP cavity at 0 min and 20 min after injection. Experiments conducted by Rokia Osman and Maidelyevis Castro, SMU and Hashini Wanniarachchi, UTSW.

Following successful studies in tissue models, we studied the performance of **SiRCL-OH** in living mice (Figure 5-8 B). 20 μL of 100 μM **SiRCL-OH** in PBS (pH = 7.4) was injected into the intraperitoneal cavity of live athymic nude mice at UT Southwestern medical center, and chemiluminescence signal was measured at 540 nm and 680 nm over a period of 20 min. We found that the signal was strong even after 20 min of injection, indicating stability and long half-life *in vivo*. The signal was observed to perfuse throughout the IP cavity with time, and high emission was imaged at certain "hot spots" where the compound seemed to aggregate, perhaps near the liver. In these *in vivo* experiments as well, the flux at 680 nm was stronger than at 540 nm as expected.

5.2.5. Synthesis and Characterization of **WRCL-OAc** and **WRCL-OH**

We synthesized **WRCL-OAc** and **WRCL-OH** using a similar strategy as that for **SiRCL-OH**. Washington Red dye WR4 was synthesized according to literature procedure,[33] and then appended to the acrylate enol ether **8** *via* a piperazine linker (Scheme 5-3). **WRCL-OAc** was synthesized as the 1,2-dioxetane with an acetate protected phenol, and **WRCL-OH** was synthesized as the free phenol by cleaving the acetate using ammonium acetate before reaction with singlet oxygen for dioxetane formation.

Following synthesis, spectroscopic characterization revealed significant, almost complete, spectral overlap of **WRCL** dyes' absorbance and emission of the methyl acrylate dioxetane (Figure 5-9 A). While the excitation maximum of the compounds was 565 nm, the emission maximum was 665 nm, which equates to a large Stokes shift of 100 nm. We tested the chemiluminescence response of **WRCL-OAc** by reacting in 0.1 M NaOH, which served to cleave the acetate group, resulting in production of the phenolate which undergoes CIEEL and generates light. We observed

that the 540 nm in this strongly basic medium was large, but the NIR emission intensity at 665 nm was very low (Figure 5-9 B).

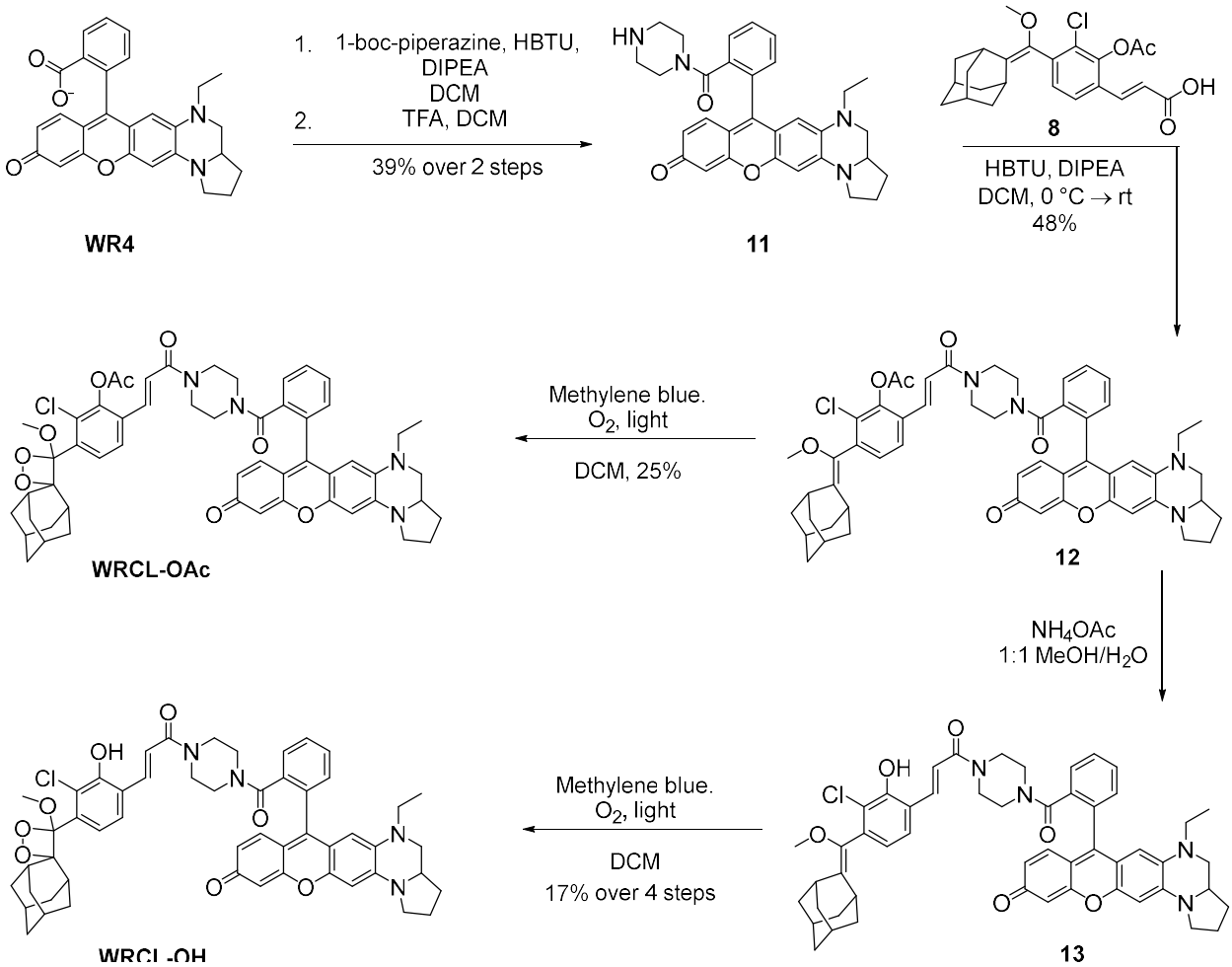

Scheme 5-3. Synthesis of **WRCL-OAc** and **WRCL-OH**.

This is similar to the behavior of **SiRCL** in sodium hydroxide, and suggests that strong base causes cleavage of the dye from the benzoate. To generate chemiluminescence without exposure to strong base, we synthesized the free phenol derivative, **WRCL-OH**. Isolation of the compound proved challenging due to polar solvent systems required for column chromatography and generation of the product in different configurations due to its asymmetric and bulky nature. Chemiluminescence studies of semi-pure substance revealed that although response to change in pH was observed, the emission intensity and energy transfer for **WRCL-OH** were poor as

compared to **SiRCL-OH** (Figure 5-9 C, D). Further investigation with a higher purity sample is likely to generate improved results.

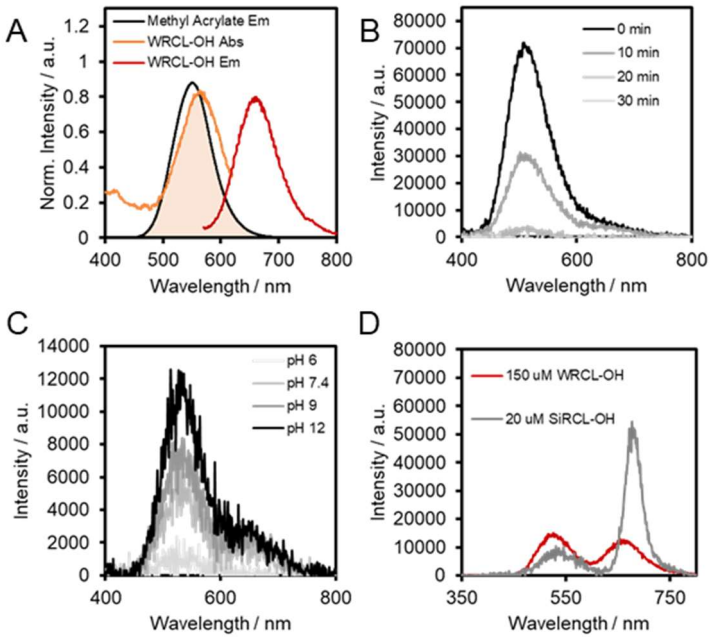

Figure 5-9 (A) Spectral overlap between methyl acrylate dioxetane emission and **WRCL** absorbance. (B) Chemiluminescence response and signal decay of 40 µM **WRCL-OAc** in 0.1 M NaOH and 80% DMSO. (C) pH dependence of 20 µM **WRCL-OH** in 20% DMSO in pH 6–12. (D) Comparison of response for 150 µM **WRCL-OH** and 20 µM **SiRCL-OH** in 50% DMSO at pH 7.4.

5.3. Summary and Conclusions

To summarize, we reported near-infrared emitting chemiluminophores, **SiRCL-OAc**, **SiRCL-OH**, **WRCL-OAc** and **WRCL-OH**, which exhibit energy transfer from an excited state 1,2-dioxetane to the appended SiR or WR emitter in aqueous systems. We explore design and synthesis, pH dependent response and chemiluminescence decay kinetic of these agents, and for **SiRCL-OH**, we calculated chemiluminescence quantum yield, as well as demonstrated imaging through tissue. While these chemiluminophores are not specific for imaging particular bioanalytes, their demonstration of efficient energy transfer, impressive performance in tissue, and relatively high aqueous quantum yield is foundational work for NIR imaging of a wide variety of analytes

through tissue using agents similar to these, thus furthering the applicability of chemiluminescence in biosensing and analyte quantification.

5.4. Experimental Methods

5.4.1. General Materials and Methods

Silica gel P60 (SiliCycle) was used for column chromatography, and SiliCycle 60 F254 silica gel precoated sheets (0.25 mm thick) were used for analytical thin layer chromatography. Plates were visualized by fluorescence quenching under UV light or by staining with iodine. Reagents were purchased from Sigma-Aldrich (St. Louis, MO), Thermo Fisher Scientific (Waltham, MA), TCI America (Portland, OR), Alfa Aesar (Ward Hill, MA), EMD Millipore (Billerica, MA), Oakwood Chemical (West Columbia, SC), or Cayman Chemical (Ann Arbor, MI) and used without further purification. ^{1}H NMR and ^{13}C NMR were obtained on a JEOL 500 MHz spectrometer in the Department of Chemistry at Southern Methodist University. ^{1}H and ^{13}C NMR spectra for characterization of new compounds and monitoring reactions were collected in $CDCl_3$ or CD_3OD (Cambridge Isotope Laboratories, Cambridge, MA). All chemical shifts are reported in the standard notation of parts per million. Coupling constant units are in Hertz (Hz). Splitting patterns are indicated as follows: s, singlet; d, doublet; t, triplet; q, quartet; m, multiplet; dd, doublet of doublets; dt, doublet of triplets. Low resolution mass spectroscopy was performed on a Advion LCMS (ESI source). Absorbance spectra were collected using either a DU 800 or a HORIBA QM-8075-11 spectrophotometer. Fluorescence spectra were acquired using either a Hitachi F-7000 fluorescence spectrophotometer or a HORIBA QM-8075-11 spectrophotometer.

5.4.2. Synthesis of **SiRCL-OAc** and **SiRCL-OH**

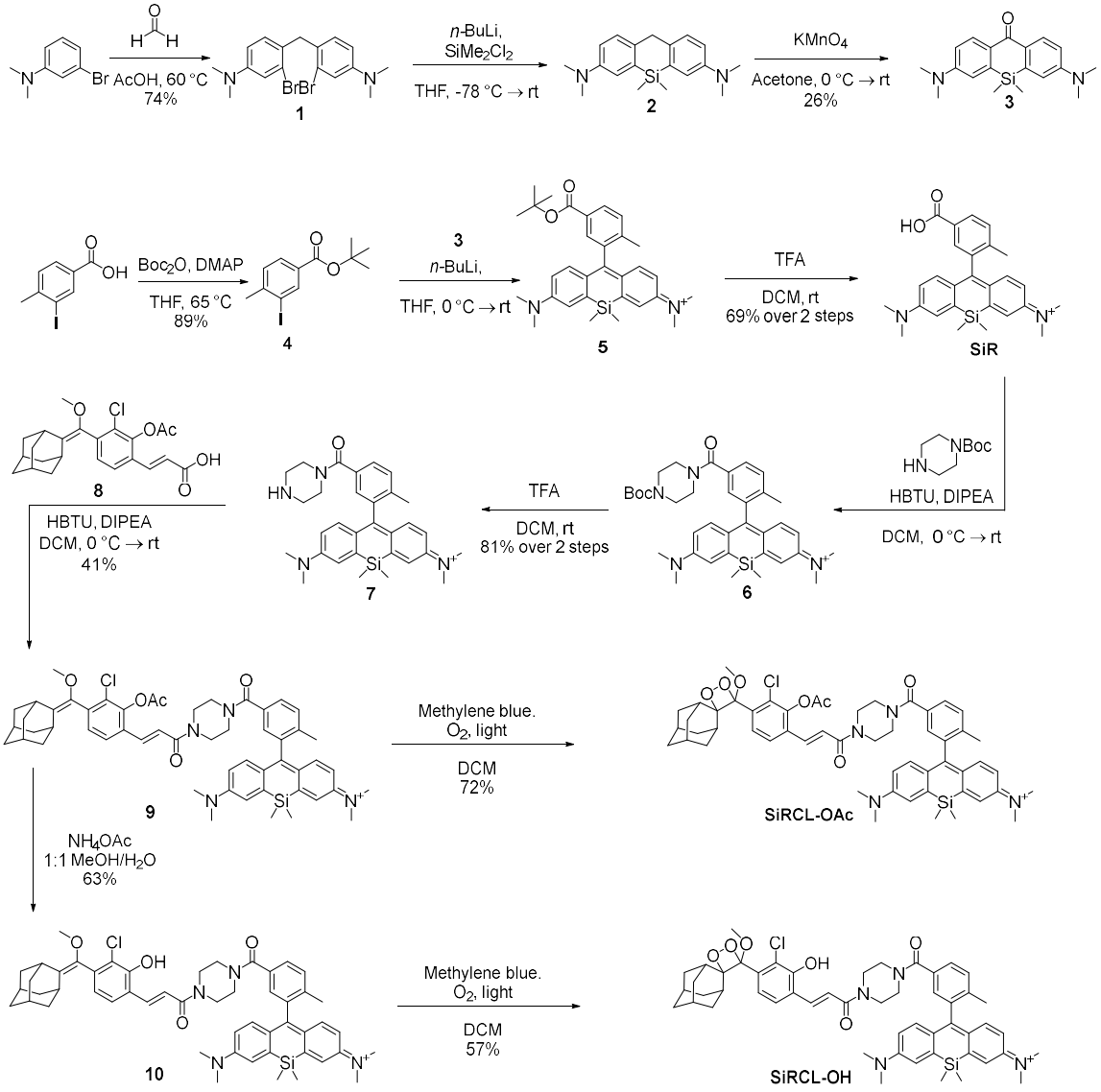

Scheme 5-4. Synthesis of **SiRCL-OAc** and **SiRCL-OH.**

4,4'-methylenebis(3-bromo-N,N-dimethylaniline) (1). 3-bromo-N,N-dimethylaniline (2.10 mL, 14.7 mmol, 2 equiv) was combined with 3 mL of 37% formaldehyde and dissolved in 24 mL acetic acid. The reaction was heated to 60 °C and stirred for 1.5h, after which TLC showed that the starting material was used up. The volatiles were rotavapped off and Saturated $NaHCO_3$ was added carefully to the reaction until pH = 8. A white precipitate formed, which was extracted with EtOAc several times. The combined organic layers were washed with H_2O and brine, dried over Na_2SO_4

and concentrated to obtain the crude product as a pink solid, which was then purified using column chromatography with 20:1 hexanes:EtOAc as the solvent system. The off-white solid could be further recrystallized using hot hexanes (2.27 g, 74%). ^{1}H NMR (500 MHz, $CDCl_3$): δ 6.96 (d, J = 2.9 Hz, 2H), 6.87 (d, J = 8.6, 2H), 6.59 (dd, J = 2.9, 8.6 Hz, 2H), 4.02 (s, 2H), 2.92 (s, 12H); ^{13}C NMR (125 MHz, $CDCl_3$) δ 150.14, 130.89, 127.17, 125.73, 116.35, 111.97, 40.65, 40.00.

N3,N3,N7,N7,5,5-hexamethyl-5,10-dihydrodibenzo[b,e]siline-3,7-diamine (2). Compound **1** (1.97 g, 4.78 mmol, 1 equiv) was added into an oven-dried 3-neck flask fitted with an additional funnel and flushed with N_2. Anhydrous THF (30 mL) was added to dissolve the starting material. The reaction was cooled to –78 °C, and 1.6M *n*-BuLi in hexanes (8.00 mL, 12.8 mmol, 2.7 equiv) was added to the flask dropwise over 30 mins via addition funnel while stirring. The reaction changed from colorless to yellow. The reaction was allowed to stir at –78 °C for an additional 20 mins, at which point, the TLC indicated no more staring material present and the appearance of a new spot that turned blue on exposure to air. Dichlorodimethylsilane (0.80 mL, 6.63 mmol, 1.4 equiv) was then added to the flask dropwise. The reaction was allowed to stir for 28 hours, with the temperature rising from –78 °C to rt. The reaction was then quenched with 8 mL of 1M HCl to give a blue solution and was then basified to pH 8 with sat. $NaHCO_3$. The whole was extracted with DCM thrice, and the combined organic layers were concentrated to obtain a gray oil, which was used crude immediately for the next step.

3,7-bis(dimethylamino)-5,5-dimethyldibenzo[b,e]silin-10(5H)-one (3). Crude compound **2** was dissolved in 70 mL acetone and cooled to 0 °C. $KMnO_4$ (2.30 g, 14.6 mmol, 3 equiv) was added portionwise every 15 mins over the next 2 hours, and then stirred at rt for17 hours, while monitoring disappearance of starting material via TLC. The product appeared as a yellow fluorescent spot on TLC. The reaction was filtered over Celite to afford a clear green solution,

which was concentrated to obtain the crude product as a green solid. Purification via column chromatography with 5:1:1 hexanes: EtOAc: $CHCl_3$ solvent system and then recrystallization with hot 5:2:1 hexanes: EtOAc: $CHCl_3$ solvent afforded the product as yellow crystals (399 mg, 26%). ^{1}H NMR (500 MHz, $CDCl_3$): δ 8.40 (d, J = 9.2 Hz, 2H), 6.83 (dd, J = 2.9, 9.2 Hz, 2H), 6.79 (d, J = 2.9 Hz, 2H), 3.09 (s, 12H), 0.47 (s, 6H); ^{13}C NMR (125 MHz, $CDCl_3$) δ 185.36, 151.25, 140.57, 131.70, 129.72, 114.32, 113.22, 40.13, –0.89.

tert-butyl 3-iodo-4-methylbenzoate (4). 3-iodo-4-methylbenzoic acid (2.00 g, 7.63 mmol, 1 equiv), boc anhydride (4.10 g, 19.0 mmol, 2.5 equiv), and DMAP (0.19 g, 1.53 mmol, 0.2 equiv) were combined in a flask and dissolved in 20 mL anhydrous THF. The reaction was heated to 60 °C and stirred under reflux for 20 hours. After cooling the reaction to rt, the THF was rotavaped off and the residue was dissolved in Et_2O, which was then washed with sat. aq. $NaHCO_3$ (x3), H_2O, and brine. The organic layer was dried over Na_2SO_4 and concentrated to a golden oil. Purification via column chromatography with 9:1 hexanes:EtOAc yielded the product as a golden oil (2.17 g, 89%). ^{1}H NMR (500 MHz, $CDCl_3$): δ 8.36 (d, J = 1.7 Hz, 1H), 7.81 (dd, J = 1.7, 8.0 Hz, 1H), 7.22 (d, J = 8.0 Hz, 1H), 2.42 (s, 3H), 1.55 (s, 9H); ^{13}C NMR (125 MHz, $CDCl_3$): δ 164.23, 146.18, 139.90, 131.25, 129.40, 129.23, 100.51, 81.41, 81.02, 28.40, 28.24, 27.97.

N-(10-(5-carboxy-2-methylphenyl)-7-(dimethylamino)-5,5-dimethyldibenzo[b,e]silin-3(5H)-ylidene)-N-methylmethanaminium (SiR). Compound **4** (1.57 g, 4.93 mmol, 4 equiv) and silicon anthrone **3** (0.400 g, 1.23 mmol, 1 equiv) were added to an oven dried flask, which was evacuated and flushed with N_2 (x3). Dry THF (25 mL) was added and the reaction was stirred until starting materials dissolved. The reaction was then cooled to 0 °C, and 1.5M *n*-BuLi in hexanes (3.5 mL, 5.25 mmol, 4.2 equiv) was added dropwise. The reaction was stirred for an additional 3 hours at rt. 1M HCl was added to quench the reaction, resulting is an intense blue solution of pH = 1.

Saturated $NaHCO_3$ was added to neutralize the reaction, which was then extracted with DCM several times. The blue organic layer was washed with brine and dried over Na_2SO_4 and concentrated to a blue solid. This crude *t*-butyl ester product **5** was dissolved in DCM (15 mL) and trifluoroacetic acid (3 mL) was added. The reaction was stirred at rt for 3.5h, while monitoring product formation via mass spectroscopy. The volatiles were then evaporated off. The reaction was purified using column chromatography with 10% MeOH in DCM to obtain **SiR** as a blue solid (0.377 g, 69%). ^{1}H NMR (500 MHz, CD_3OD): δ 8.10 (dd, J = 2.3, 8.0 Hz, 1H), 7.72 (d, J = 1.7 Hz, 1H), 7.53 (d, J = 8.0 Hz, 1H), 7.37 (d, J = 2.3 Hz, 2H), 7.02 (d, J = 9.7 Hz, 2H), 6.77 (dd, J = 2.9, 9.7 Hz, 2H), 3.34 (s, 12H), 2.10 (s, 3H), 0.62 (s, 3H), 0.60 (s, 3H); ^{13}C NMR (125 MHz, CD_3OD): δ 169.05, 168.86, 155.78, 149.51, 142.60, 141.93, 140.34, 131.72, 131.23, 131.14, 129.78, 128.28, 122.35, 115.41, 40.94, 19.65, –1.10, –1.31.

N-(10-(5-(4-(tert-butoxycarbonyl)piperazine-1-carbonyl)-2-methylphenyl)-7-(dimethylamino)-5,5-dimethyldibenzo[b,e]silin-3(5H)-ylidene)-N-methylmethanaminium (6). In a round bottom flask, **SiR** (0.050 g, 0.13 mmol, 1 equiv) was dissolved in 6 mL DCM and cooled to 0 °C. DIPEA (0.070 mL, 0.40 mmol, 3.5 equiv) was then added dropwise, after which HBTU (0.062 g, 0.16 mmol, 1.4 equiv) was added. The reaction was stirred for 10 mins. 1-boc-piperazine (0.055 g, 0.26 mmol, 2.6 equiv) was added to the flask and allowed to rise to room temperature and stir overnight, after which TLC in 20:1 DCM:MeOH indicated reaction completion. The reaction was diluted with DCM and washed with saturated aqueous ammonium chloride, saturated aqueous sodium bicarbonate, water and brine, then dried over sodium sulfate. The crude was dry loaded onto a silica gel column and eluted with a 20:1 DCM:MeOH solvent system to afford the product 6 as a blue solid. ^{1}H NMR (500 MHz, MeOD): δ 7.50 (d, 2H, J = 2.3 Hz), 7.35 (d, 2H, J = 2.9 Hz), 7.33 (d, 1H, J = 2.9 Hz), 7.07 (d, 2H, J = 9.2 Hz), 6.79 (d, 2H, J =

9.7 Hz), 3.35-3.56 (bs, 8H), 3.32 (s, 12H), 2.06 (s, 3H), 1.43 (s, 9H), 0.59 (s, 3H), 0.58 (s, 3H); ^{13}C NMR (125 MHz, $CDCl_3$): δ 169.7, 167.9, 165.7, 163.8, 154.9, 154.2, 148.4, 141.1, 138.9, 138.0, 130.7, 127.8, 127.5, 127.1, 121.0, 114.3, 80.1, 46.6, 42.8, 40.2, 38.6, 28.4, 28.3, 19.4.

N-(7-(dimethylamino)-5,5-dimethyl-10-(2-methyl-5-(piperazine-1-carbonyl)phenyl)dibenzo[b,e]silin-3(5H)-ylidene)-N-methylmethanaminium (7). Crude compound **6** was dissolved in 6 mL of DCM and 2 mL of trifluoroacetic acid was then added. The reaction went from blue to yellow and was allowed to stir at room temperature for 2.5 hours. After this time, TLC and mass spectroscopy indicated complete conversion of the starting material to the product. The volatiles were evaporated off, and the residue was taken up in DCM and washed with saturated sodium bicarbonate and brine, then dried over sodium sulfate and filtered to obtain the product with 81% yield over 2 steps. ^{1}H NMR (500 MHz, MeOD): δ 7.53 (d, 2H, J = 2.9 Hz), 7.36 (d, 2H, J = 2.9 Hz), 7.27 (d, 1H, J = 1.8 Hz), 7.07 (d, 2H, J = 9.7 Hz), 6.77 (d, 2H, J = 9.7 Hz), 3.60-3.88 (bs, 8H), 3.34 (s, 12H), 2.08 (s, 3H), 0.59 (s, 3H), 0.58 (s, 3H); ^{13}C NMR (125 MHz, MeOD): δ 171.6, 149.5, 142.0, 140.5, 140.0, 132.0, 131.9, 128.9, 128.3, 122.3, 115.40, 44.2, 44.1, 40.1,38.9, 18.7.

N-(10-(5-(4-((E)-3-(2-acetoxy-4-(((1r,3r,5R,7S)-adamantan-2-ylidene)(methoxy)methyl)-3-chlorophenyl)acryloyl)piperazine-1-carbonyl)-2-methylphenyl)-7-(dimethylamino)-5,5-dimethyldibenzo[b,e]silin-3(5H)-ylidene)-N-methylmethanaminium (9). In a 25 mL round bottom flask equipped with a stir bar under N_2 atmosphere, Compound **8**10 (83 mg, 0.200 mmol, 1.0 equiv) was dissolved in 2 mL DCM. The reaction was cooled to 0 ºC. DIPEA (110 µL, 0.600 mmol, 3.0 equiv) and HBTU (230 mg, 0.600 mmol, 3.0 equiv) were then added and stirred for 10 min, at which time the HBTU activated ester was visible by TLC. Compound **7** (100 mg, 0.200 mmol, 1.0 equiv) was then added, and the reaction was allowed to stir overnight. Upon completion,

the reaction was washed with sat. aq. NH_4Cl and sat. aq. $NaHCO_3$, extracted with DCM, dried with Na_2SO_4, filtered, and concentrated under reduced pressure. Column chromatography (15% iPrOH/DCM) yielded compound **9** (84 mg, 0.092 mmol, 41%) as a blue solid. ^{1}H NMR (500 MHz, $CDCl_3$): δ 7.53 (d, 1H, *J* = 8.0 Hz), d 7.42 (dd, 2H, *J* = 6.4 Hz, *J* = 32.0 Hz), 7.17 (d, 1H, *J* = 8.0 Hz), 7.08 (s, 6H), 7.02 (d, 1H, *J* = 9.8 Hz), 6.75 (m, 2H), 3.50-3.74 (m, 8H), 3.28 (s, 12H), 3.24 (s, 3H), 2.35 (s, 3H), 2.06 (s, 3H), 1.88-1.64 (m, 14H), 0.53 (s, 6H); ^{13}C NMR (125 MHz, $CDCl_3$): δ 170.0, 165.8, 154.3, 148.3, 145.9, 141.3, 139.3, 138.9, 131.1, 129.5, 127.8, 127.1, 120.8, 120.1, 114.5, 57.3, 55.6, 43.6, 40.9, 39.2, 38.7, 37.1, 32.9, 29.9, 28.4, 20.6, 19.4, 18.6, 17.0, 12.9.

N-(10-(5-(4-((E)-3-(2-acetoxy-3-chloro-4-((1r,3r,5r,7r)-spiro[adamantane-2,3'-[1,2]dioxetan]-4'-yl)phenyl)acryloyl)piperazine-1-carbonyl)-2-methylphenyl)-7-(dimethylamino)-5,5-dimethyldibenzo[b,e]silin-3(5H)-ylidene)-N-methylmethanaminium (SiRCL-OAc). Compound **9** (0.016 g, 0.017 mmol) was dissolved in 3 mL DCM in a 2 neck flask and cooled to 0 °C. Methylene blue hydrate (0.1 mg, 0.1 equiv) was added to the reaction, after which oxygen gas was bubbled into the reaction mixture while irradiating with light. After 3 hours, upon completion of the reaction as observed by TLC and mass spectrometry, the reaction was purified using column chromatography with 10% MeOD in DCM. The product was obtained with 72% yield. ^{1}H NMR (400 MHz, methanol-d_4): δ 8.01 (s, 2H), 6.67-7.59 (m, 3H), 7.40 (d, 2H), 7.12 (d, 2H), 6.84 (d, 2H), 3.95-3.83 (m, 8H), 3.38 (s, 12H), 3.19 (s, 3H), 2.97 (s, 1H), 2.43 (s, 3H), 2.12 (s, 3H), 1.83-1.31 (m, 14H), 0.64 (s, 3H), 0.63 (s, 3H).

N-(10-(5-(4-((E)-3-(4-(((1r,3r,5R,7S)-adamantan-2-ylidene)(methoxy)methyl)-3-chloro-2-hydroxyphenyl)acryloyl)piperazine-1-carbonyl)-2-methylphenyl)-7-(dimethylamino)-5,5-dimethyldibenzo[b,e]silin-3(5H)-ylidene)-N-methylmethanaminium (10). Compound **9** (84 mg, 0.092 mmol) was dissolved in 1 mL MeOH in a 20 mL vial. NH_4OAc (150 mg, 2.00 mmol,

20 equiv) was dissolved in 1 mL water, then added and allowed to stir under N_2 atmosphere at RT for 3 days. Upon completion as determined by TLC and mass spectrometry, the reaction was washed with water and extracted with DCM, dried with Na_2SO_4, and concentrated under reduced pressure. Column chromatography (5-10% MeOH/DCM) yielded Compound **10** (50 mg, 58 mmol, 63%) as a blue solid. ^{1}H NMR (400 MHz, $CDCl_3$): δ 7.77 (m, 1H), 7.55 (d, 1H), 7.49 (d, 1H), 7.36 (d, 1H), 7.14 (m, 4H), 7.04 (m, 1H), 7.03 (m, 1H), 6.96 (m, 1H), 6.82 (s, 1H) 3.79-3.57 (m, 8H), 3.39 (s, 12H), 3.27 (s, 3H), 2.06 (s, 3H), 1.96-1.72 (m, 14H), 0.61 (s, 6H).

N-(10-(5-(4-((E)-3-(3-chloro-2-hydroxy-4-((1r,3r,5r,7r)-4'-methoxyspiro[adamantane-2,3'-[1,2]dioxetan]-4'-yl)phenyl)acryloyl)piperazine-1-carbonyl)-2-methylphenyl)-7-(dimethylamino)-5,5-dimethyldibenzo[b,e]silin-3(5H)-ylidene)-N-methylmethanaminium (SiRCL-OH). In a round bottom flask, compound **10** (30 mg, 0.035 mmol), was dissolved in 2 mL DCM at 0 ºC. 1 mg of methylene blue was added. The reaction was irradiated under yellow light for 3 hr while stirring and monitored by ESI-MS. Upon completion, the crude was evaporated onto silica gel and loaded for column chromatography in 5-10% MeOH/DCM, yielding **SiRCL-OH** (18 mg, 57%) as a blue solid. ^{1}H NMR (400 MHz, $CDCl_3$): δ 7.74 (m, 2H), 7.56 (m, 2H), 7.49 (m, 2H), 7.13, (m, 5H), 7.03 (m, 3H), 3.80-3.58 (m, 8H), 3.40 (s, 14H), 3.22 (s, 3H), 3.01 (s,1H), 2.10 (s, 3H), 1.72-1.54 (m, 12H), 0.61 (s, 6H).

5.4.3. Synthesis of **WRCL-OAc** and **WRCL-OH**

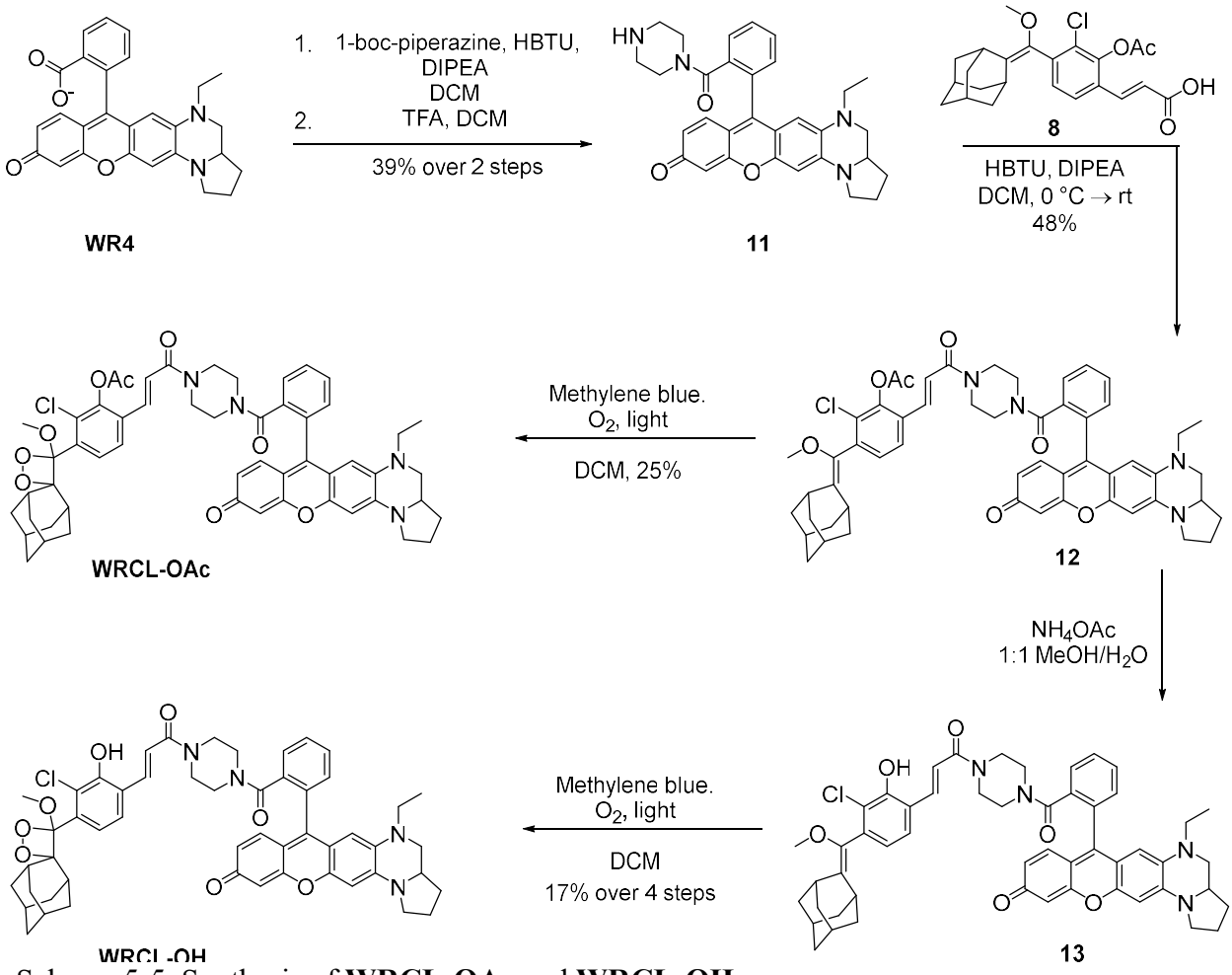

Scheme 5-5. Synthesis of **WRCL-OAc** and **WRCL-OH.**

5-ethyl-7-(2-(piperazine-1-carbonyl)phenyl)-1,2,3,3a,4,5-hexahydro-10H-chromeno[3,2-g]pyrrolo[1,2-a]quinoxalin-10-one (11). In a round bottom flask, **WR4** (0.030 g, 0.068 mmol, 1 equiv),[33] synthesized as previously published, was dissolved in 2 mL DCM and cooled to 0 °C, after which DIPEA (0.070 mL, 0.4 mmol, 6 equiv) and HBTU (0.033 g, 0.088 mmol, 1 equiv) were added. The reaction was allowed to stir for 10 min and then 1-boc-piperazine (0.036 g, 0.19 mmol, 3 equiv) was added. After stirring at room temperature overnight, the reaction turned from pink to a purple color and TLC showed starting material to be almost used up. The reaction was diluted in DCM and washed with water multiple times to remove the starting material while

monitoring via TLC. Mass spectrometry showed presence of product peak. After washing the organic layer with brine and drying over sodium sulfate, the volatiles evaporated. The residue was dissolved in 6 mL DCM and TFA (2 mL) was added. The reaction was stirred for 2 hours, at which time mass spectrometry indicated reaction completion. The volatiles were evaporated, and the residue was taken up in DCM and washed with sat. aq. sodium bicarbonate and brine. After drying over sodium sulfate and evaporating, the product was obtained as a purple solid without further purification with 80% crude yield over 2 steps. Crude ^{1}H NMR (400 MHz, methanol-d_4): δ 7.76 (d, 2H), 7.67 (d, 1H), 7.50 (m, 1H), 7.13 (m, 1H), 6.72 (d, 1H), 6.66 (m, 2H), 6.13 (d, 1H), 3.81 (m, 1H), 3.72 (m, 1H), 3.59 (m, 2H), 3.33 (m, 3H), 3.19 (m 2H), 2.86 (m, 2H), 2.62 (m, 4H) 2.24 – 2.12 (m, 3H), 1.62 (m, 1H), 1.04 (q, 3H).

3-(((1r,3r)-adamantan-2-ylidene)(methoxy)methyl)-2-chloro-6-((E)-3-(4-(2-(5-ethyl-10-oxo-1,2,3,3a,4,5-hexahydro-10H-chromeno[3,2-g]pyrrolo[1,2-a]quinoxalin-7-yl)benzoyl)piperazin-1-yl)-3-oxoprop-1-en-1-yl)phenyl acetate (12). Acrylate **8** (0.025 g, 0.060 mmol, 1 equiv) was dissolved in 1 mL DCM and cooled to 0 °C. DIPEA (0.067 mL, 0.38 mmol, 7 equiv) and HBTU (0.032 g, 0.084 mmol, 1.5 equiv) were added and stirred for 10 min. Compound **11** (0.028 g, 0.055 mmol, 1 equiv) was then dissolved in a mixture of 6 mL DCM and 10 µL DIPEA and added to the reaction flask and allowed to stir overnight at room temperature, after which TLC and MS indicated conversion to product. The reaction was diluted with DCM and washed with sat. aq. ammonium chloride, sat. aq. sodium bicarbonate, brine and dried over sodium sulfate and filtered. Column chromatography in 10% MeOH to 50% iPrOH in DCM yielded the product with 48% yield. ^{1}H NMR (400 MHz, methanol-d_4) scan in appendix B.

2-chloro-6-((E)-3-(4-(2-(5-ethyl-10-oxo-1,2,3,3a,4,5-hexahydro-10H-chromeno[3,2-g]pyrrolo[1,2-a]quinoxalin-7-yl)benzoyl)piperazin-1-yl)-3-oxoprop-1-en-1-yl)-3-((1r,3r)-

spiro[adamantane-2,3'-[1,2]dioxetan]-4'-yl)phenyl acetate (WRCL-OAc). Compound **12** (0.024 g, 0.026 mmol) was dissolved in 3 mL DCM was dissolved in 2 mL DCM at 0 ºC. Methylene blue hydrate (0.2 mg, 0.1 wt%) was added. The reaction was irradiated under yellow light for 7 hr while stirring and monitoring by ESI-MS. Upon completion, the crude was washed with water and sat. aq. ammonium chloride and the purified twice via column chromatography in a 10% MeOH/DCM system to get rid of impurities. Product fraction was collected with some decomposition product and other impurities present, as indicated by MS and NMR. ^{1}H NMR (400 MHz, methanol-d_4) scan in appendix B.

7-(2-(4-((E)-3-(4-(((1r,3r)-adamantan-2-ylidene)(methoxy)methyl)-3-chloro-2-hydroxyphenyl)acryloyl)piperazine-1-carbonyl)phenyl)-5-ethyl-1,2,3,3a,4,5-hexahydro-10H-chromeno[3,2-g]pyrrolo[1,2-a]quinoxalin-10-one (13). Crude compound **12** was dissolved in a mixture of 1 mL water, 3 mL MeOH and 2 mL THF. Ammonium acetate (0.140 g) in 1 mL water was added and the reaction was stirred for 3 days, after which MS indicated complete conversion. The reaction was diluted in water and extracted with DCM. Combined organics were dried over sodium sulfate, filtered, concentrated and subjected column chromatography in 1-10% MeOH in DCM. Proton NMR of fractions containing product showed presence of impurities as well. ^{1}H NMR (400 MHz, methanol-d_4) scan in appendix B.

7-(2-(4-((E)-3-(3-chloro-2-hydroxy-4-((1r,3r)-spiro[adamantane-2,3'-[1,2]dioxetan]-4'-yl)phenyl)acryloyl)piperazine-1-carbonyl)phenyl)-5-ethyl-1,2,3,3a,4,5-hexahydro-10H-chromeno[3,2-g]pyrrolo[1,2-a]quinoxalin-10-one (WRCL-OH). Compound **13** was dissolved in 3 mL DCM and cooled to 0 °C. Methylene blue hydrate (1 mg) was added and then oxygen was bubbled through the reaction while irradiating with light from a yellow lamp. After 2.5 hours, MS indicated conversion of starting material. The reaction was subjected to column chromatography

using 20:1 DCM:iPROH to 10:1 DCM:MeOH to obtain the product with 17% yield over 4 steps. ^{1}H NMR (400 MHz, methanol-d_4) scan in appendix B.

5.4.4. *In vitro* spectroscopic measurements

General Spectroscopic Methods. Fluorescence, chemiluminescence, and absorbance spectra were acquired on a HORIBA QM-8075-11 spectrophotometer in a 1.6 mL quartz cuvette (Starna Cells, Atascadero, CA). Each experiment was conducted at ambient temperature. Background readings were acquired and subtracted from sample spectra. Acquisition of spectra was started approximately 5–10 sec after mixing of reagents.

pH dependence. A solution of 20 μM **SiRCL-OH** in 30% DMSO and pH 3 buffer (100 mM sodium citrate, pH = 2.98) was prepared in a cuvette, which was gently shaken to ensure mixing. Emission was then collected from 400–800 nm with excitation slits at 0 nm, emission slits at 15 nm, and integration time of 0.1 s. The process was repeated with buffers at pH 4 (100 mM sodium citrate, pH = 4.00), pH 5 (100 mM sodium citrate, pH = 4.97), pH 6 (100 mM PBS , pH = 5.85), pH 7.4 (100 mM PBS, pH = 7.45), pH 8 (50 mM Tris and10 mM NaCl, pH = 7.93), pH 9 (100 mM Tris, pH = 8.98), and pH 13 (100 mM NaOH, pH = 12.6). A similar procedure was used for 20 μM **WRCL-OH** in 20% DMSO in pH 6–13 solutions.

DMSO dependence. A solution of 20 μM **SiRCL-OAc** in varying DMSO concentrations from 1% to 50% in 0.1 M NaOH were prepared in a cuvette and gently shaken. Chemiluminescence emission was collected with excitation slits closed and emission slits of 15 nm. Emission intensities at 540 nm and 680 nm were plotted against % DMSO. Similar methods were used for **SiRCL-OH** DMSO dependence, in PBS buffer (pH = 7.45) and varying % DMSO.

Kinetic decay and half-life determination. A solution of 20 μM **SiRCL-OH** in 30% DMSO and pH 7.4 buffer (100 mM PBS, pH = 7.45) was prepared in a cuvette, which was gently shaken to ensure mixing. Emission from 400–800 nm was then collected at time points of 0, 1, 2, 3, 4, 5, 10, 20 and 30 min after mixing with excitation slits at 0 nm, emission slits at 15 nm, and integration time of 0.1 s. The intensities at 540 nm and 680 nm were plotted against time to generate decay curves and the decay constant k was determined by mathematically fitting the experimental data to a model for exponential decay (Eq 5-1). Half-life was calculated using Eq 5-2. Experiments were repeated in triplicate and average values calculated.

$$I_t = I_0\, e^{-kt} + B \quad (\text{eq } 5-1)$$

$$t_{1/2} = \ln(2)/k \quad (\text{eq } 5-2)$$

Enhancer studies. A solution of 20 μM **SiRCL-OH** in PBS buffer (pH 7.4), 30% DMSO and 5% Emerald II Enhancer was prepared and chemiluminescence emission was recorded. Control experiment in the absence of enhancer was similarly conducted, and the measurements were repeated in triplicate.

Chemiluminescence quantum yield. Φ_{CL} were determined as detailed in section 5.3.

5.4.5. IVIS spectrum experiments

pH dependence. In an opaque 96 well-plate, solutions of 60 μM **SiRCL-OH** were prepared with 30% DMSO in buffers of pH 4 (100 mM sodium citrate, pH = 4.00), pH 5 (100 mM sodium citrate, pH = 4.97), pH 6 (100 mM PBS , pH = 5.85), pH 7.4 (100 mM PBS, pH = 7.45), and pH 8 (50 mM Tris and10 mM NaCl, pH = 7.93) in triplicate. Chemiluminescence images were acquired using the IVIS spectrum with exposure time of 1, 3, 5, and 10 seconds, binning medium, F/stop of 1, excitation blocked, and images acquired using a 540 nm bandpass filter, then a 680 nm bandpass

filter. Image analysis was carried out in the Living Image software by using grid ROIs for the well plate, which were then measured to give a total flux (p/s) for each ROI at each wavelength.

Concentration dependence. A similar procedure was used as for pH dependence. Solutions of **SiRCL-OH** in 30% DMSO and PBS (pH = 7.4) were prepared at concentrations of 20, 40, 60, 80, and 100 μM. Acquisition and analysis was carried out as above.

Tissue depth penetration. Turkey deli slices (Walmart, Dallas TX) were used as tissue model for measuring signal depth penetration. A 100 μM solution of **SiRCL-OH** in 30% DMSO and PBS (pH = 7.4) was prepared in a single well in the center of a white opaque 96-well plate and luminescence was imaged using exposure time of 1, 3 and 10 seconds, binning medium, F/stop 1, FOV C (12.9 cm), and excitation blocked. The process was then repeated (with a freshly prepared solution for every data point) with 2, 4, 8, 12, 16, 20, 24, 28, and 32 slices of turkey on top of the sample, such that the entire plate was covered for every experiment and luminescence was measured through the tissue. Images were acquired first using a 540 nm bandpass filter, then a 680 nm bandpass filter and images were analyzed using Living Image software by selecting and measuring individual ROIs for the test area. The procedure was carried out in triplicate.

Tissue injection. A 100 μM solution of **SiRCL-OH** was prepared with 30% DMSO and PBS (pH = 7.4). 30 μL of this solution was then immediately injected into boneless chicken breast tissue (Walmart, Dallas, TX) at a depth of 0.5 cm (using a pre-marked needle) and luminescence was acquired using exposure times of 1, 3 and 10 seconds with binning X, FOV C, F/stop 1 and excitation blocked. Images were acquired first through 540 nm filter and then 680 nm filter.

***In vivo* imaging.** Animal imaging experiments were carried out at UT Southwestern Medical Center using an IVIS Spectrum (Perkin Elmer, Waltham, MA) and approved by the UT

Southwestern Institutional Animal Care and Use Committee. Athymic nude mice under anesthesia were injected with a 20 μL of 100 μM **SiRCL-OH** in PBS buffer with 10% DMSO into the intraperitoneal (IP) cavity, immediately after which acquisition was started with exposure time of 1 s, binning X, FOV C, F/stop 1 and excitation blocked. Images were acquired through 540 nm filter and 680 nm filter every 30 s for 20 min.

5.5. References

1. Haris, U.; Kagalwala, H. N.; Kim, Y. L.; Lippert, A. R. Seeking Illumination: The Path to Chemiluminescent 1,2-Dioxetanes for Quantitative Measurements and *in Vivo* Imaging. *Accounts of Chemical Research* **2021**, *54* (13), 2844–2857.
2. Cao, J.; Lopez, R.; Thacker, J. M.; Moon, J. Y.; Jiang, C.; Morris, S. N.; Bauer, J. H.; Tao, P.; Mason, R. P.; Lippert, A. R. Chemiluminescent Probes for Imaging H2S in Living Animals. *Chemical Science* **2015**, *6* (3), 1979–1985.
3. Liu, L.; Mason, R. P. Imaging β-Galactosidase Activity in Human Tumor Xenografts and Transgenic Mice Using a Chemiluminescent Substrate. *PLoS ONE* **2010**, *5* (8).
4. Green, O.; Eilon, T.; Hananya, N.; Gutkin, S.; Bauer, C. R.; Shabat, D. Opening a Gateway for Chemiluminescence Cell Imaging: Distinctive Methodology for Design of Bright Chemiluminescent Dioxetane Probes. *ACS Central Science* **2017**, *3* (4), 349–358.
5. Lippert, A. R. Unlocking the Potential of Chemiluminescence Imaging. *ACS Central Science* **2017**, *3* (4), 269–271.
6. Bezner, B. J.; Ryan, L. S.; Lippert, A. R. Reaction-Based Luminescent Probes for Reactive Sulfur, Oxygen, and Nitrogen Species: Analytical Techniques and Recent Progress. *Analytical Chemistry* **2019**, *92* (1), 309–326.
7. Jones, K. A.; Kentala, K.; Beck, M. W.; An, W.; Lippert, A. R.; Lewis, J. C.; Dickinson, B. C. Development of a Split Esterase for Protein–Protein Interaction-Dependent Small-Molecule Activation. *ACS Central Science* **2019**, *5* (11), 1768–1776.
8. An, W.; Mason, R. P.; Lippert, A. R. Energy Transfer Chemiluminescence for Ratiometric Ph Imaging. *Organic & Biomolecular Chemistry* **2018**, *16* (22), 4176–4182.
9. Ryan, L. S.; Gerberich, J.; Haris, U.; Nguyen, D.; Mason, R. P.; Lippert, A. R. Ratiometric pH Imaging Using a 1,2-Dioxetane Chemiluminescence Resonance Energy Transfer Sensor in Live Animals. *ACS Sensors* **2020**, *5* (9), 2925–2932.

10. Ryan, L. S.; Gerberich, J.; Cao, J.; An, W.; Jenkins, B. A.; Mason, R. P.; Lippert, A. R. Kinetics-Based Measurement of Hypoxia in Living Cells and Animals Using an Acetoxymethyl Ester Chemiluminescent Probe. *ACS Sensors* **2019**, *4* (5), 1391–1398.

11. Kagalwala, H. N.; Gerberich, J.; Smith, C. J.; Mason, R. P.; Lippert, A. R. Chemiluminescent 1,2-Dioxetane Iridium Complexes for near-Infrared Oxygen Sensing. *Angewandte Chemie International Edition* **2022**, *61* (12).

12. Mason, E. A.; Lopez, R.; Mason, R. P. Wavelength Shifting of Chemiluminescence Using Quantum Dots to Enhance Tissue Light Penetration. *Optical Materials Express* **2016**, *6* (4), 1384.

13. Green, O.; Gnaim, S.; Blau, R.; Eldar-Boock, A.; Satchi-Fainaro, R.; Shabat, D. Near-Infrared Dioxetane Luminophores with Direct Chemiluminescence Emission Mode. *Journal of the American Chemical Society* **2017**, *139* (37), 13243–13248.

14. East, A. K.; Lucero, M. Y.; Chan, J. New Directions of Activity-Based Sensing for *in Vivo* Nir Imaging. *Chemical Science* **2021**, *12* (10), 3393–3405.

15. Huang, J.; Jiang, Y.; Li, J.; Huang, J.; Pu, K. Molecular Chemiluminescent Probes with a Very Long near-Infrared Emission Wavelength for in Vivo Imaging. *Angewandte Chemie* **2020**, *133* (8), 4045–4049.

16. Hananya, N.; Eldar Boock, A.; Bauer, C. R.; Satchi-Fainaro, R.; Shabat, D. Remarkable Enhancement of Chemiluminescent Signal by Dioxetane–Fluorophore Conjugates: Turn-on Chemiluminescence Probes with Color Modulation for Sensing and Imaging. *Journal of the American Chemical Society* **2016**, *138* (40), 13438–13446.

17. Kagalwala, H. N.; Lippert, A. R. Energy Transfer Chemiluminescent Spiroadamantane 1,2-Dioxetane Probes for Bioanalyte Detection and Imaging. *Angewandte Chemie International Edition* **2022**, *61* (42).

18. Haris, U.; Lippert, A. R. Exploring the Structural Space of Chemiluminescent 1,2-Dioxetanes. *ACS Sensors* **2022**, *8* (1), 3–11.

19. Fu, M.; Xiao, Y.; Qian, X.; Zhao, D.; Xu, Y. A Design Concept of Long-Wavelength Fluorescent Analogs of Rhodamine Dyes: Replacement of Oxygen with Silicon Atom. *Chemical Communications* **2008**, No. 15, 1780.

20. Koide, Y.; Urano, Y.; Hanaoka, K.; Terai, T.; Nagano, T. Evolution of Group 14 Rhodamines as Platforms for near-Infrared Fluorescence Probes Utilizing Photoinduced Electron Transfer. *ACS Chemical Biology* **2011**, *6* (6), 600–608.

21. Iwatate, R. J.; Kamiya, M.; Umezawa, K.; Kashima, H.; Nakadate, M.; Kojima, R.; Urano, Y. Silicon Rhodamine-Based near-Infrared Fluorescent Probe for γ-Glutamyltransferase. *Bioconjugate Chemistry* **2018**, *29* (2), 241–244.

22. Li, M.; Wang, C.; Wang, T.; Fan, M.; Wang, N.; Ma, D.; Hu, T.; Cui, X. Asymmetric Si-Rhodamine Scaffolds: Rational Design of Ph-Durable Protease-Activated NIR Probes *in Vivo*. *Chemical Communications* **2020**, *56* (16), 2455–2458.

23. Miao, J.; Huo, Y.; Shi, H.; Fang, J.; Wang, J.; Guo, W. A Si-Rhodamine-Based near-Infrared Fluorescent Probe for Visualizing Endogenous Peroxynitrite in Living Cells, Tissues, and Animals. *Journal of Materials Chemistry B* **2018**, *6* (27), 4466–4473.

24. Mao, G.-J.; Liang, Z.-Z.; Gao, G.-Q.; Wang, Y.-Y.; Guo, X.-Y.; Su, L.; Zhang, H.; Ma, Q.-J.; Zhang, G. A Photostable Si-Rhodamine-Based near-Infrared Fluorescent Probe for Monitoring Lysosomal Ph during Heat Stroke. *Analytica Chimica Acta* **2019**, *1092*, 117–125.

25. Piao, W.; Tsuda, S.; Tanaka, Y.; Maeda, S.; Liu, F.; Takahashi, S.; Kushida, Y.; Komatsu, T.; Ueno, T.; Terai, T.; Nakazawa, T.; Uchiyama, M.; Morokuma, K.; Nagano, T.; Hanaoka, K. Development of AZO-Based Fluorescent Probes to Detect Different Levels of Hypoxia. *Angewandte Chemie International Edition* **2013**, *52* (49), 13028–13032.

26. Huo, Y.; Miao, J.; Han, L.; Li, Y.; Li, Z.; Shi, Y.; Guo, W. Selective and Sensitive Visualization of Endogenous Nitric Oxide in Living Cells and Animals by a Si-Rhodamine Deoxylactam-Based near-Infrared Fluorescent Probe. *Chemical Science* **2017**, *8* (10), 6857–6864.

27. Mao, Z.; Jiang, H.; Song, X.; Hu, W.; Liu, Z. Development of a Silicon-Rhodamine Based near-Infrared Emissive Two-Photon Fluorescent Probe for Nitric Oxide. *Analytical Chemistry* **2017**, *89* (18), 9620–9624.

28. Mao, G.-J.; Liang, Z.-Z.; Bi, J.; Zhang, H.; Meng, H.-M.; Su, L.; Gong, Y.-J.; Feng, S.; Zhang, G. A Near-Infrared Fluorescent Probe Based on Photostable Si-Rhodamine for Imaging Hypochlorous Acid during Lysosome-Involved Inflammatory Response. *Analytica Chimica Acta* **2019**, *1048*, 143–153.

29. Koide, Y.; Urano, Y.; Hanaoka, K.; Terai, T.; Nagano, T. Development of an Si-Rhodamine-Based Far-Red to near-Infrared Fluorescence Probe Selective for Hypochlorous Acid and Its Applications for Biological Imaging. *Journal of the American Chemical Society* **2011**, *133* (15), 5680–5682.

30. Egawa, T.; Hanaoka, K.; Koide, Y.; Ujita, S.; Takahashi, N.; Ikegaya, Y.; Matsuki, N.; Terai, T.; Ueno, T.; Komatsu, T.; Nagano, T. Development of a Far-Red to near-Infrared Fluorescence Probe for Calcium Ion and Its Application to Multicolor Neuronal Imaging. *Journal of the American Chemical Society* **2011**, *133* (36), 14157–14159.

31. Zhang, Y.; Xia, S.; Fang, M.; Mazi, W.; Zeng, Y.; Johnston, T.; Pap, A.; Luck, R. L.; Liu, H. New near-Infrared Rhodamine Dyes with Large Stokes Shifts for Sensitive Sensing of Intracellular Ph Changes and Fluctuations. *Chemical Communications* **2018**, *54* (55), 7625–7628.

32. Ren, T.-B.; Xu, W.; Zhang, W.; Zhang, X.-X.; Wang, Z.-Y.; Xiang, Z.; Yuan, L.; Zhang, X.-B. A General Method to Increase Stokes Shift by Introducing Alternating Vibronic Structures. *Journal of the American Chemical Society* **2018**, *140* (24), 7716–7722.

33. Chen, W.; Xu, S.; Day, J. J.; Wang, D.; Xian, M. A General Strategy for Development of near-Infrared Fluorescent Probes for Bioimaging. *Angewandte Chemie International Edition* **2017**, *56* (52), 16611–16615.

34. Beck, S.; Koster, H. Applications of Dioxetane Chemiluminescent Probes to Molecular Biology. *Analytical Chemistry* **1990**, *62* (21), 2258–2270.

35. Stevani, C. V.; Silva, S. M.; Baader, W. J. Studies on the Mechanism of the Excitation Step in Peroxyoxalate Chemiluminescence. *Eur. J. Org. Chem.* **2000**. 4037–4046.

36. Augusto, F. A.; De Souza, G. A.; De Souza, S. P.; Khalid, M.; Baader, W. J. Efficiency of electron transfer initiated chemiluminescence. *Photochem. Photobiol*. **2013, *89,*** 1299–1317.

Chapter 6

CONCLUSION

The ability to study and precisely manipulate chemicals with light has rapidly driven the evolution of photochemistry from a curiosity to an essential field of study with crucial applications in wide-ranging fields over the last few centuries. With advanced understanding of light-matter interactions, scientists have uncovered innovative solutions to address some of the world's most pressing needs in energy generation, biotechnology, and nanomanufacturing. Photons of light impart energy to photoactive chemical systems, driving processes and transformations that are difficult, if not impossible, without light. Optogenetics, phototherapeutics, photopharmacology, high resolution imaging, additive manufacturing, and photolithography are among the numerous breakthrough advancements founded on the behavior of tailored molecules in response to light. In this thesis, we developed techniques to further the resolution, scope, and versatility of light-mediated microscale fabrication and microscale imaging using such photoactive molecules, and demonstrated applications of these techniques.

Our custom-built DLP fluorescence microscope is a key pillar of the patterning capabilities presented in this thesis. With this microscope, at a fraction of the cost of commercially available systems, we achieved high resolution microscale projection and imaging of patterned, multicolor light, as well as additional capabilities that are not yet available on commercial fluorescence imaging systems such as microscale 3D printing. The resulting versatile 'one-stop-shop' was used

for patterning in living cells, on polymer films, on polymer beads, and for photocuring polymer resin in 2D and 3D. Notably, imaging and patterned-light activation are both possible within the same system, key for future experiments where light activation is triggered in response to real time imaging data. Additional advancements in a newer generation of this microscope are underway to enable super resolution imaging and high intensity irradiation for innovative applications in lithography and molecular targeting.

In conjunction with microscopy, tailored chemistry is another major component of this work and its future applications. Chemical reactions such as photoclick reactions, photorearrangements, and radical polymerizations are powerful tools when tailored for specific applications. By tagging reagents with customized fluorophores or uncaging fluorescence, we achieved real time monitoring of these reactions as they occurred, and by designing compatible polymer substrates, we demonstrated patterned surface functionalization with these varied chemistries. Not only do these results tease exciting applications in lithography, nanorobotics, and metamaterials, but compatibility with living cells also offers an attractive route to target molecules to specific cells and subcellular structures for proteomics and elucidation of cellular pathways. Additionally, we demonstrated mediation of multiple chemistries orthogonally in the same system at targeted sites by exploiting their unique photoinitiation conditions, and we envision creative applications of this scheme in photopharmacology and light-controlled biotechnology. Finally, through microfabrication of structures with embedded catalysts, we generated self-propelled micromotors with intriguing behaviors that we continue to investigate.

The work in this thesis has limitless potential for continued exploration towards revolutionary technologies; molecular agents for non-invasive imaging and treatment of disease, electronics and nanomaterials crafted with molecular specificity and unprecedented resolutions,

catalytic microbots programmed with stimuli-specific responses, trackable microcapsules for cargo delivery at sites of interest... The possibilities are endless, and the reward is sure to be sweet for eager investigators!

APPENDIX A: SCANNED NMR SPECTRA

1. CHAPTER 2 COMPOUNDS – NMR SPECTRA

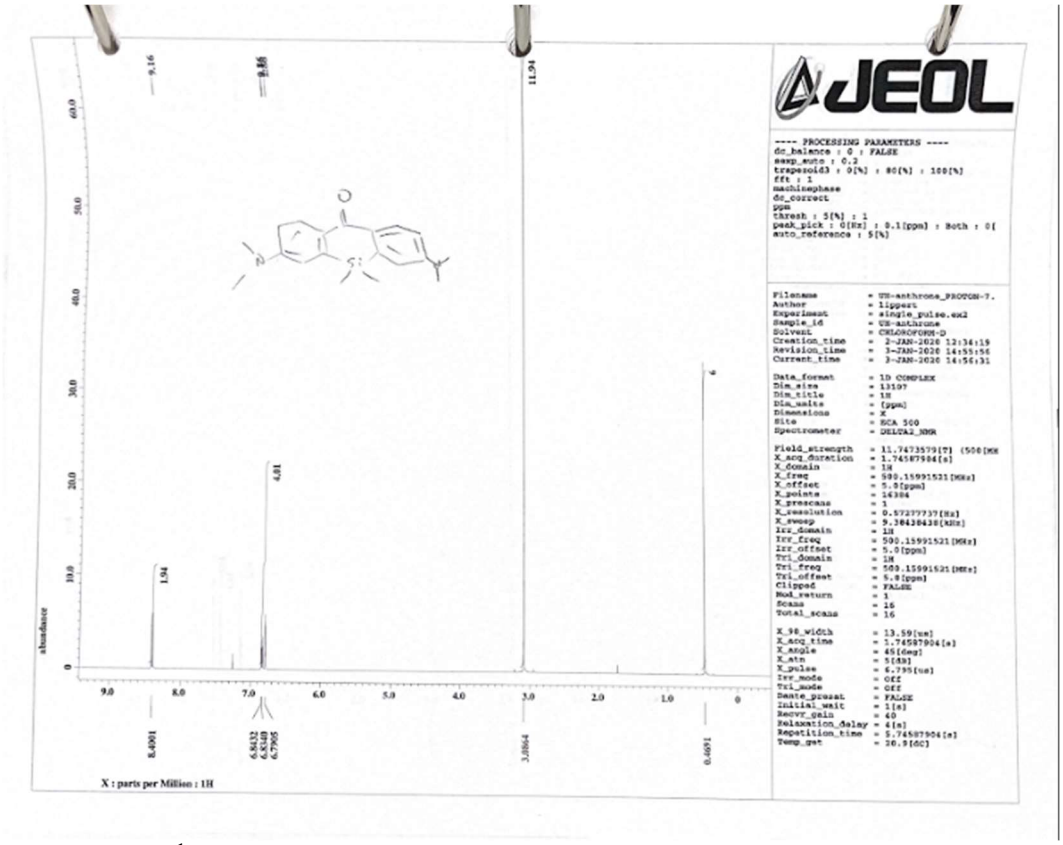

Compound **1** ^{1}H NMR

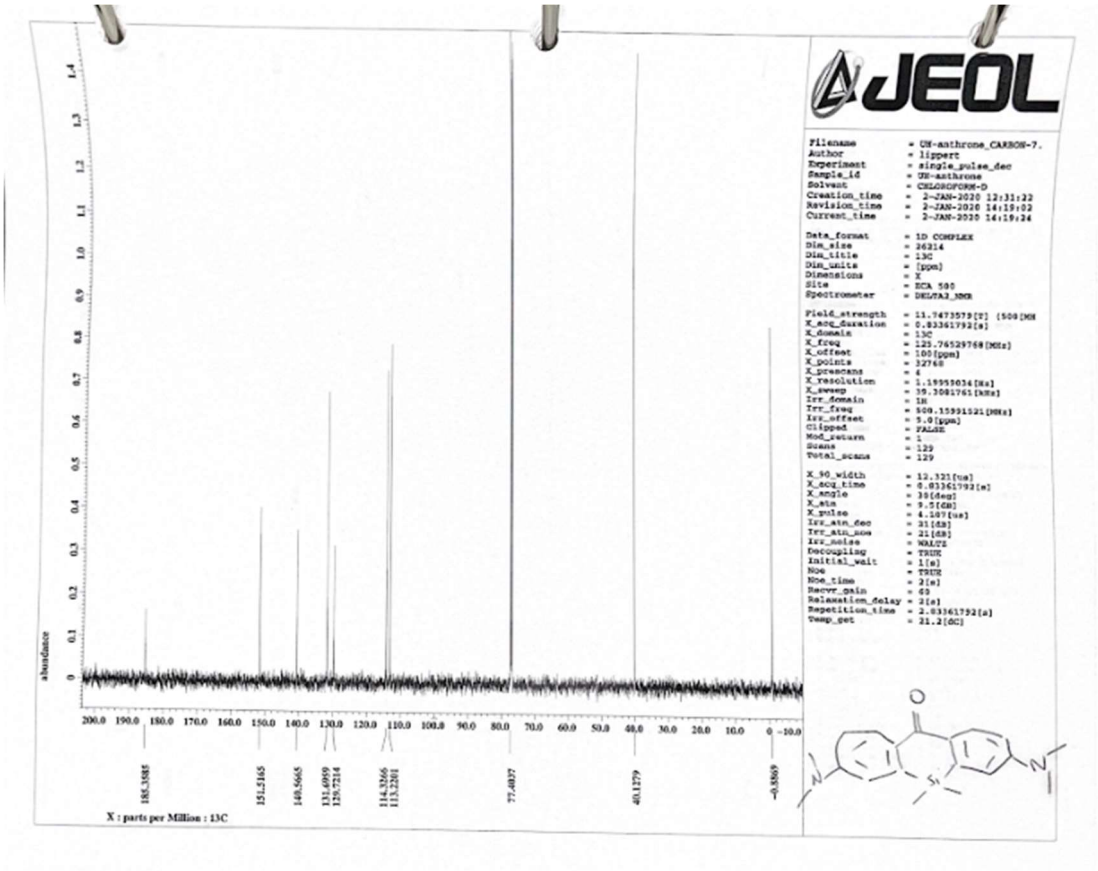

Compound **1** ^{13}C NMR

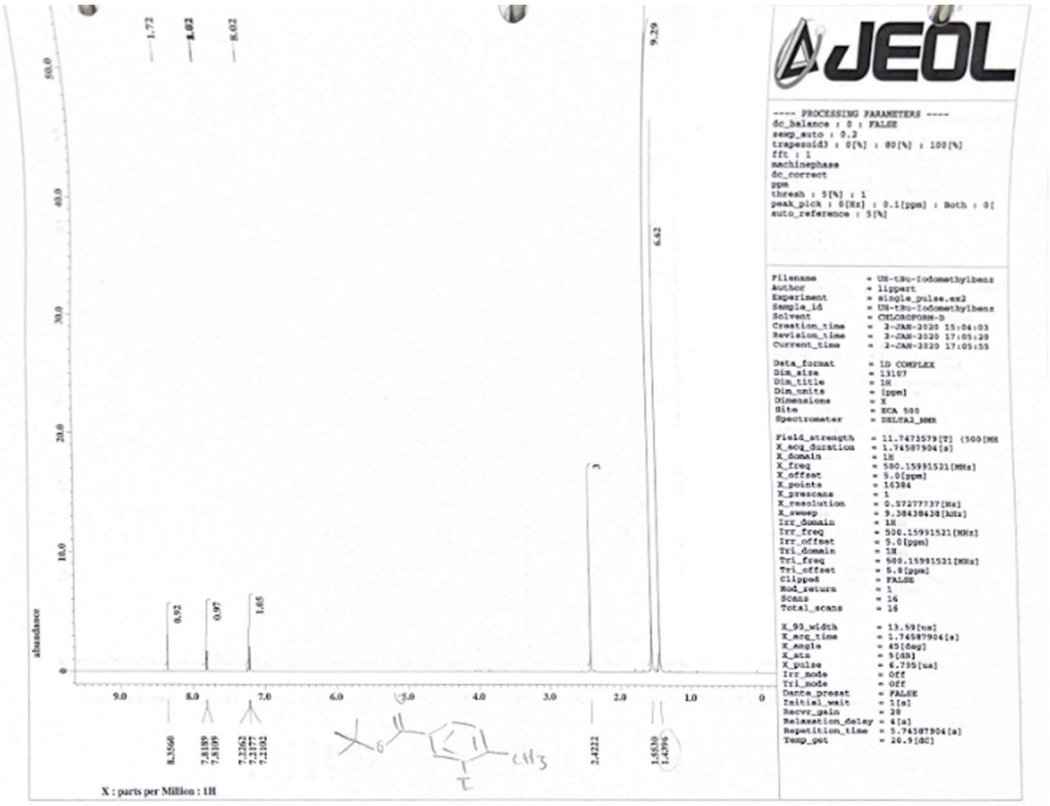

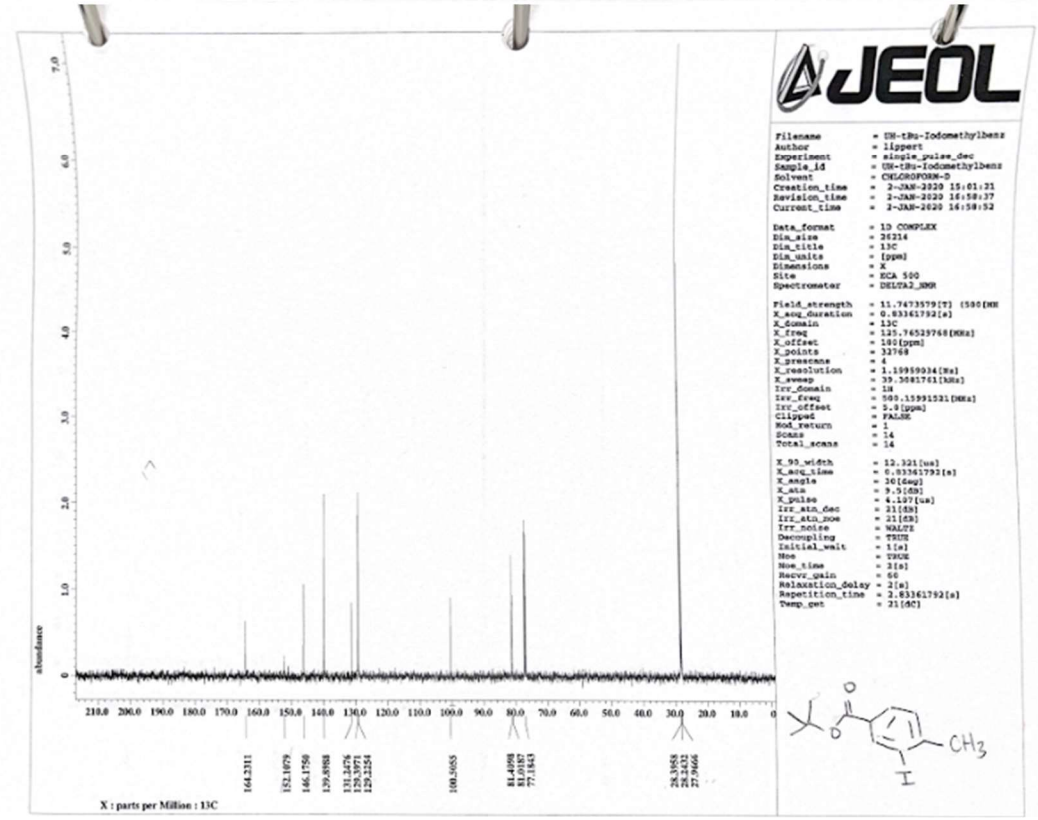

Compound **2** ^{1}H NMR and ^{13}C NMR

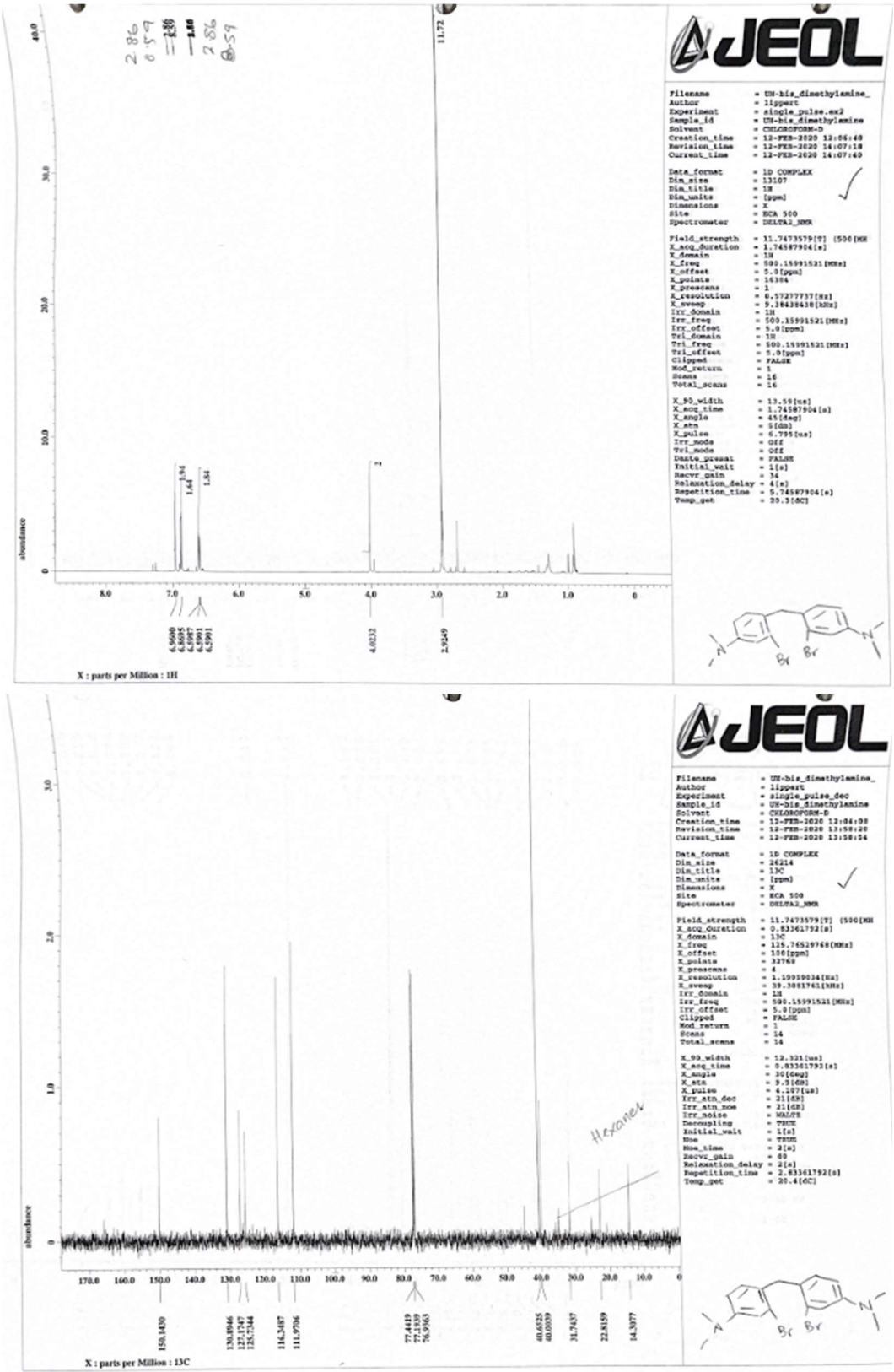

Compound **3** ^{1}H NMR and ^{13}C NMR bis bromo

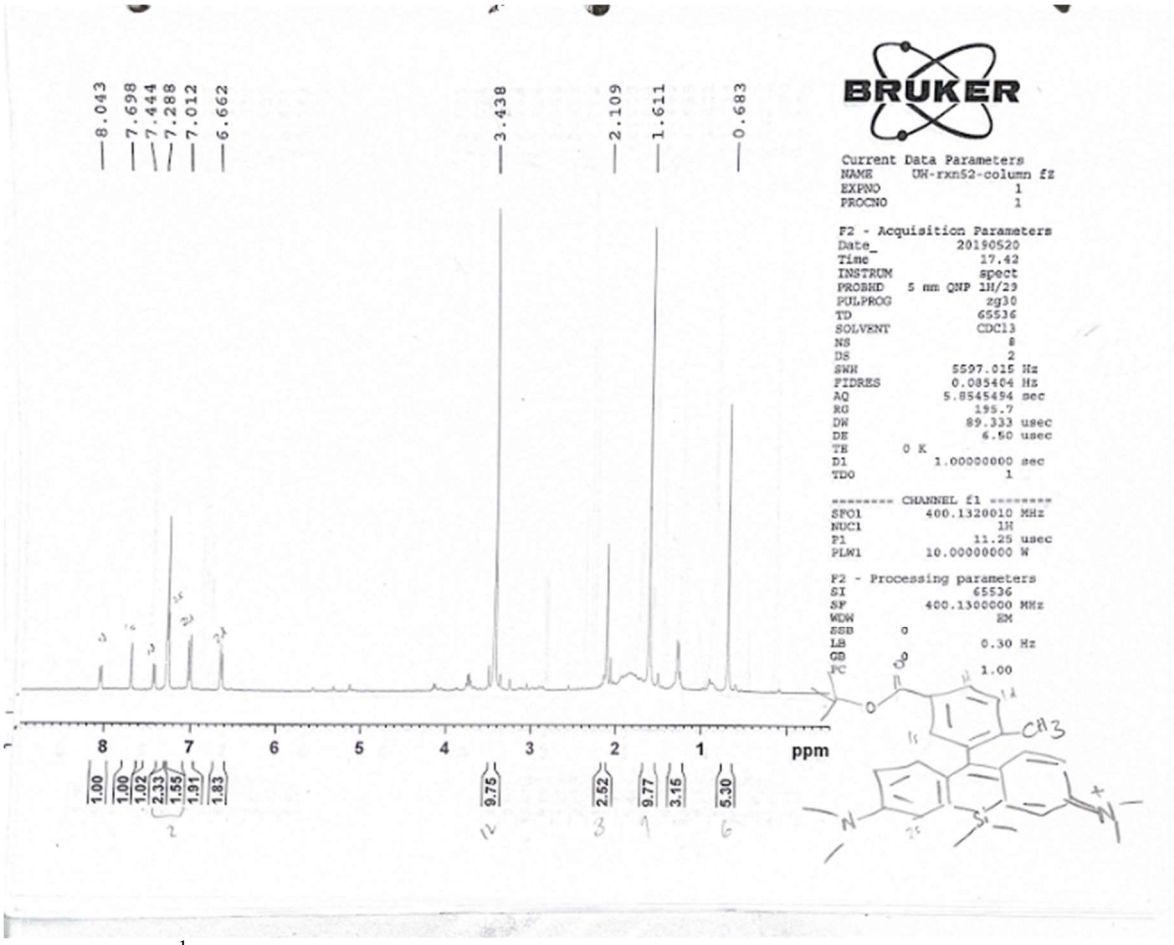

Compound **5** ^{1}H NMR

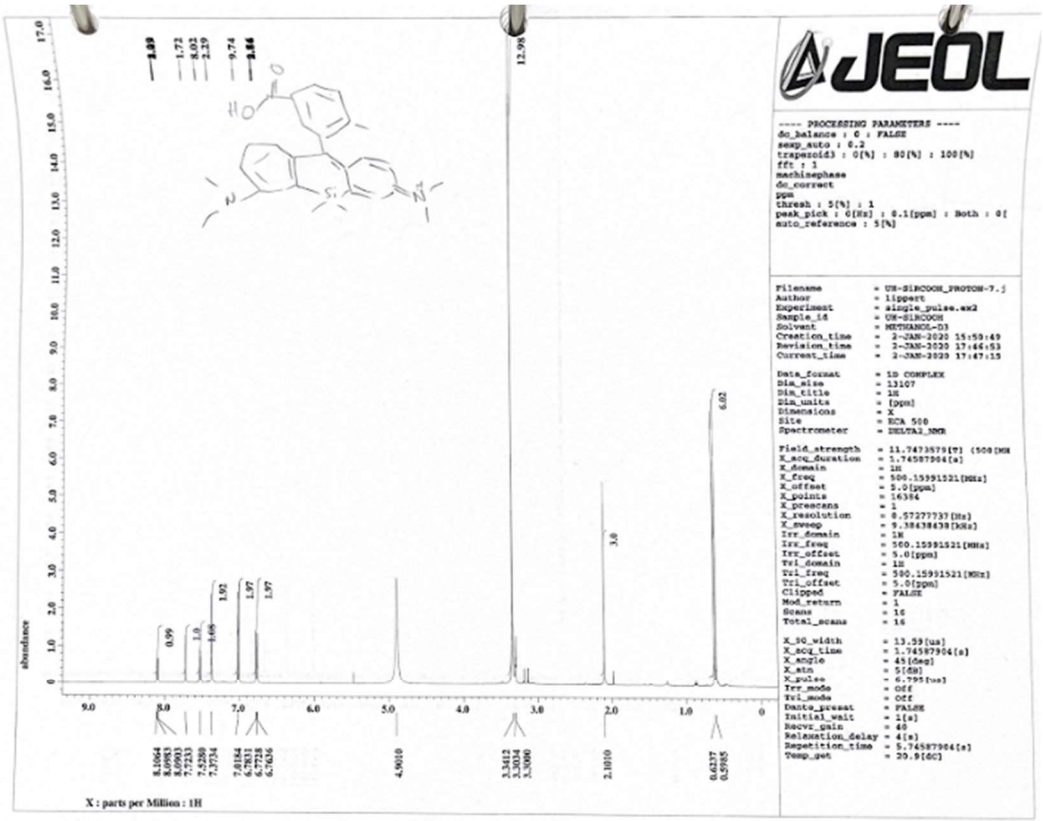

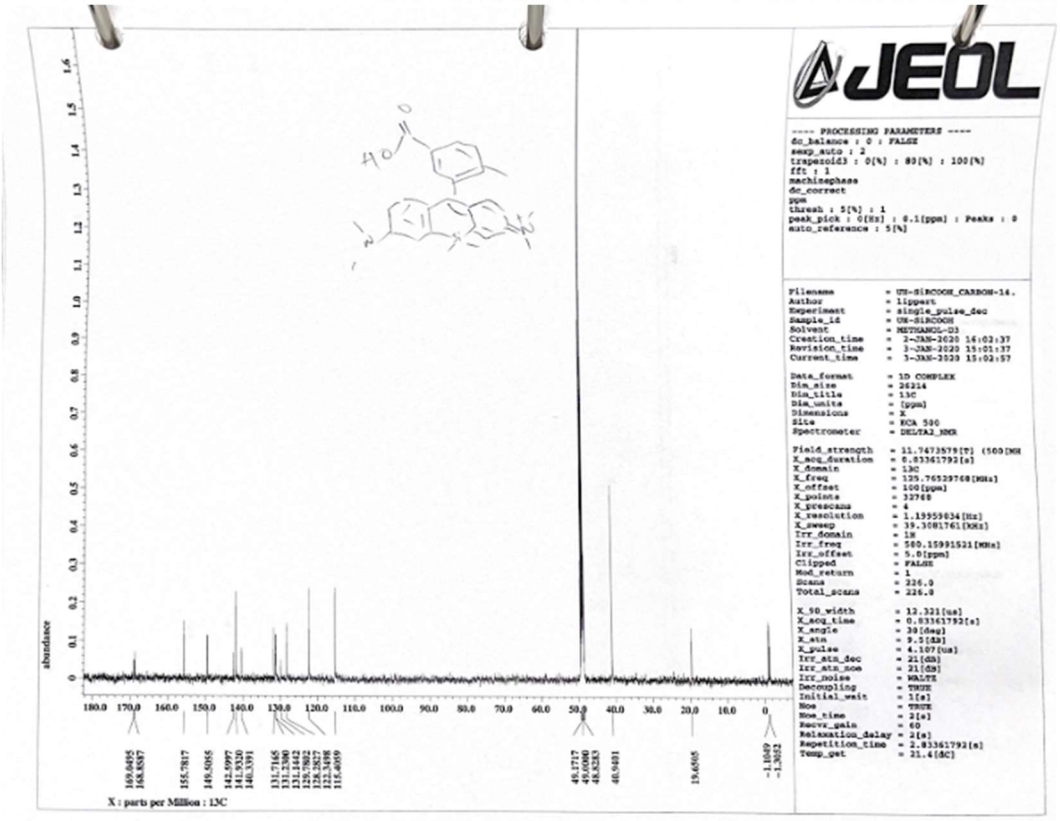

SiR ^{1}H NMR and ^{13}C NMR

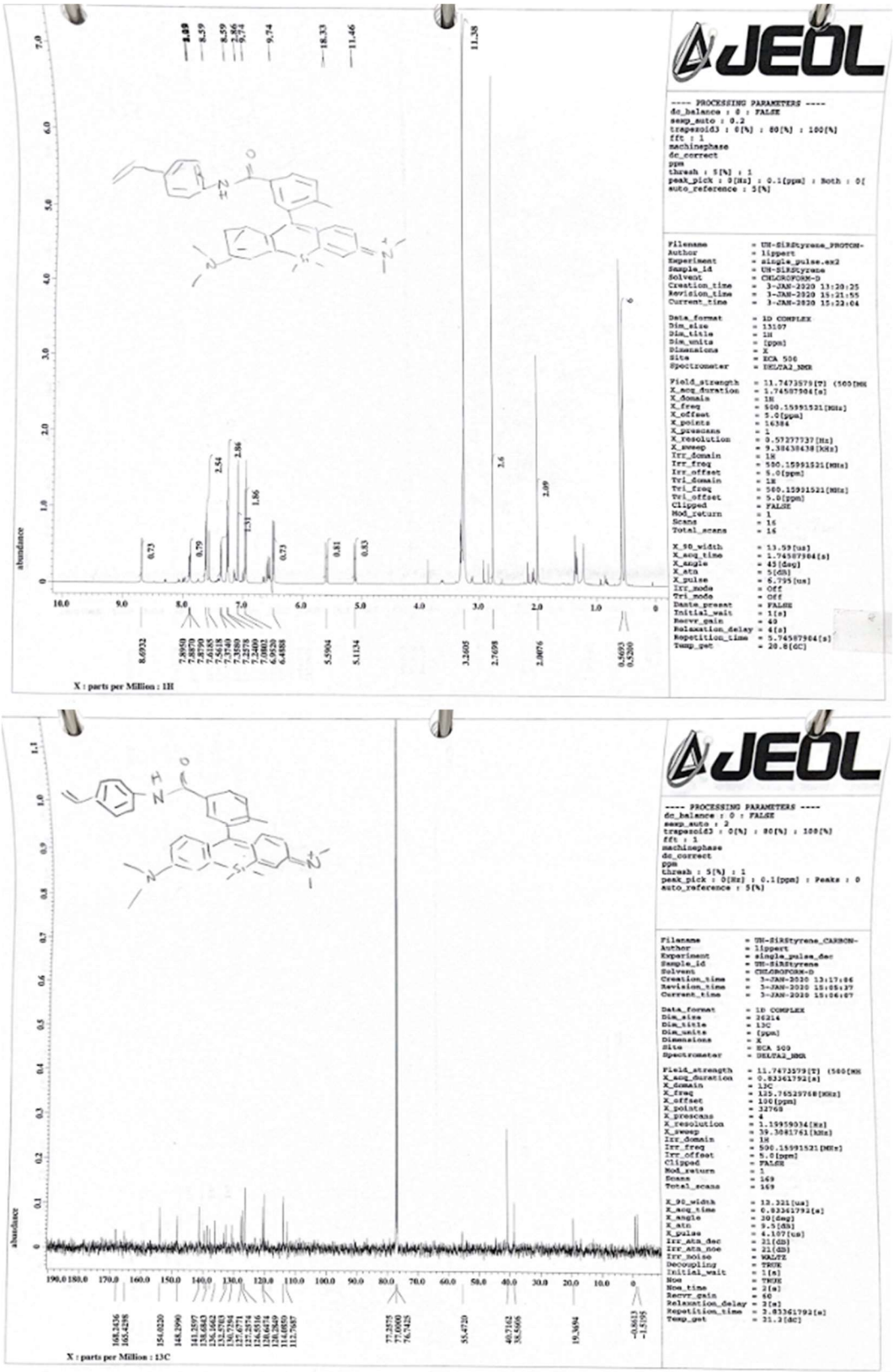

SiR-styrene ^{1}H NMR and ^{13}C NMR

2. CHAPTER 4 COMPOUNDS – NMR SPECTRA

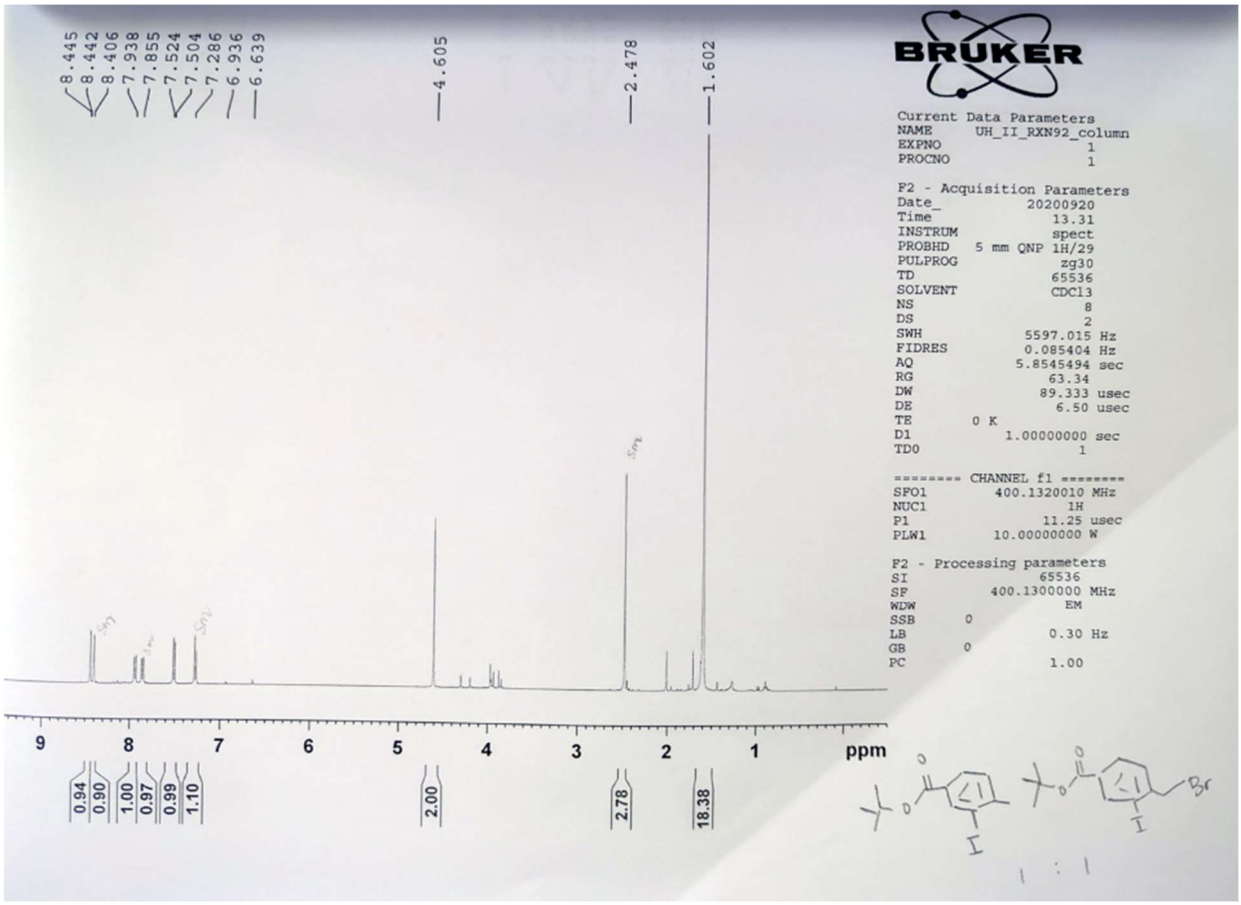

Compound **2** HNMR

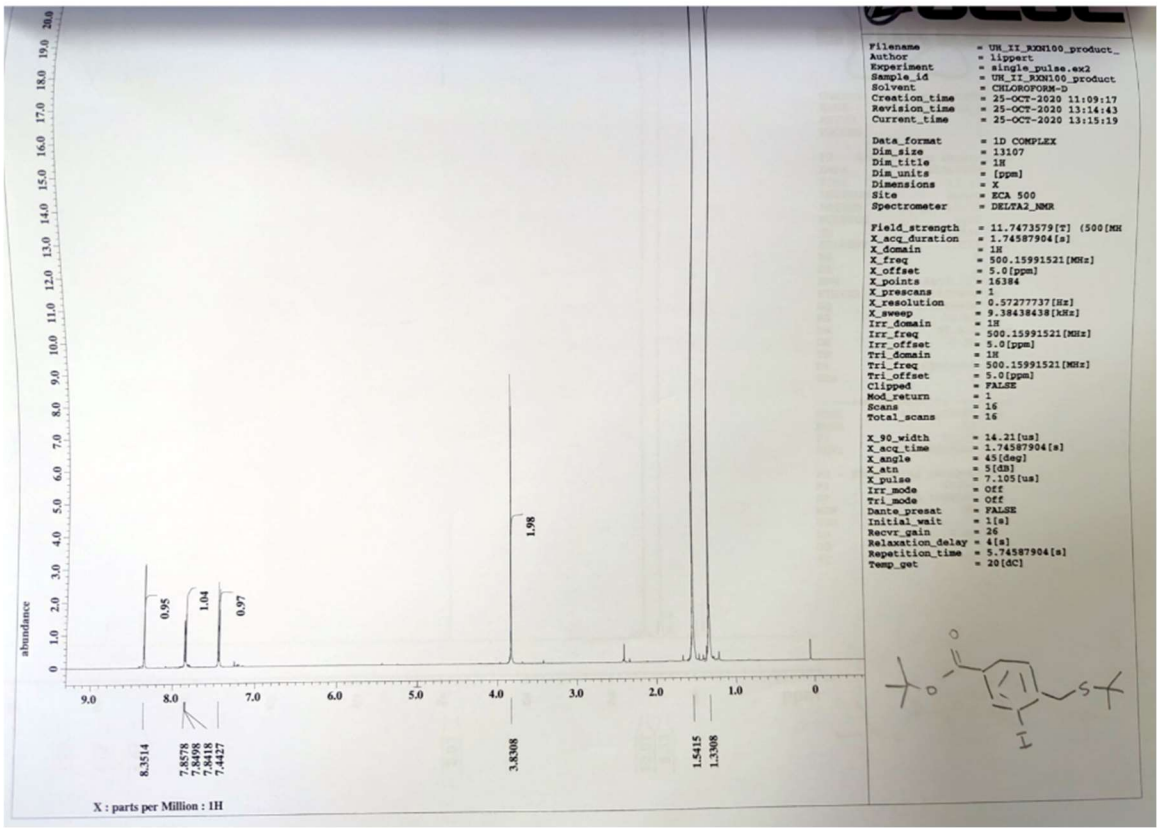

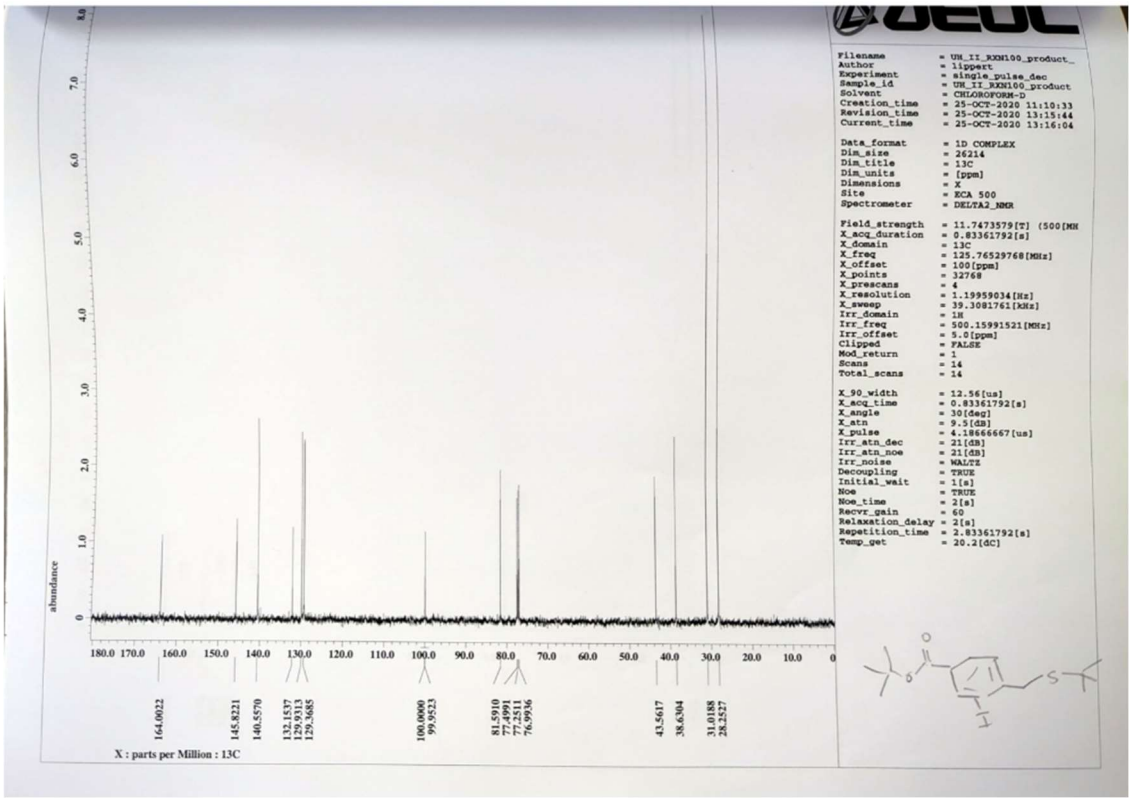

Compound **3** ^{1}HNMR and ^{13}C NMR

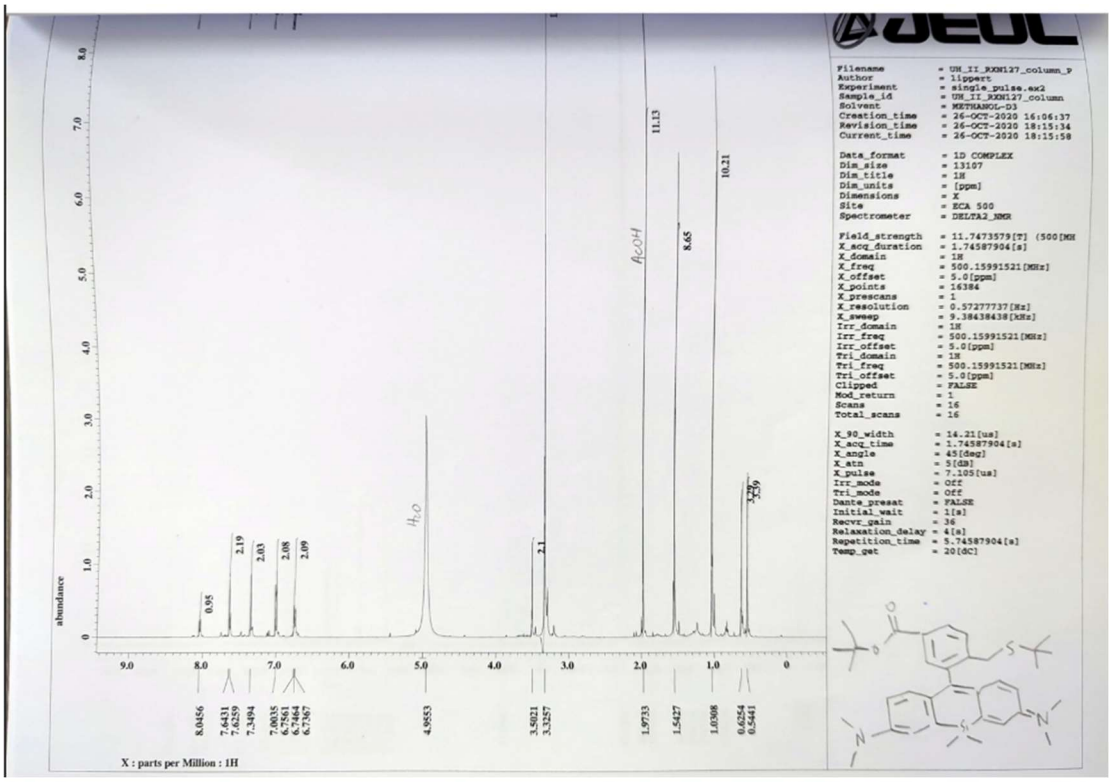

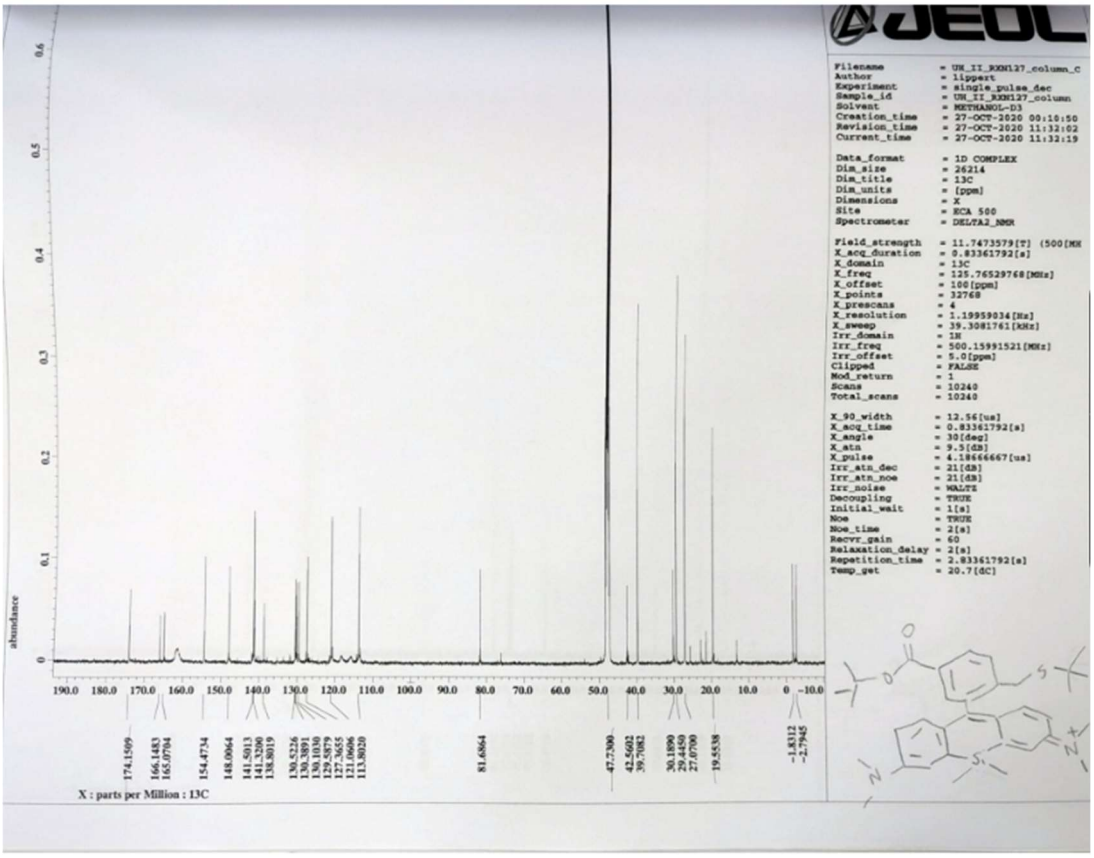

TMSiR ^{1}HNMR and ^{13}C NMR

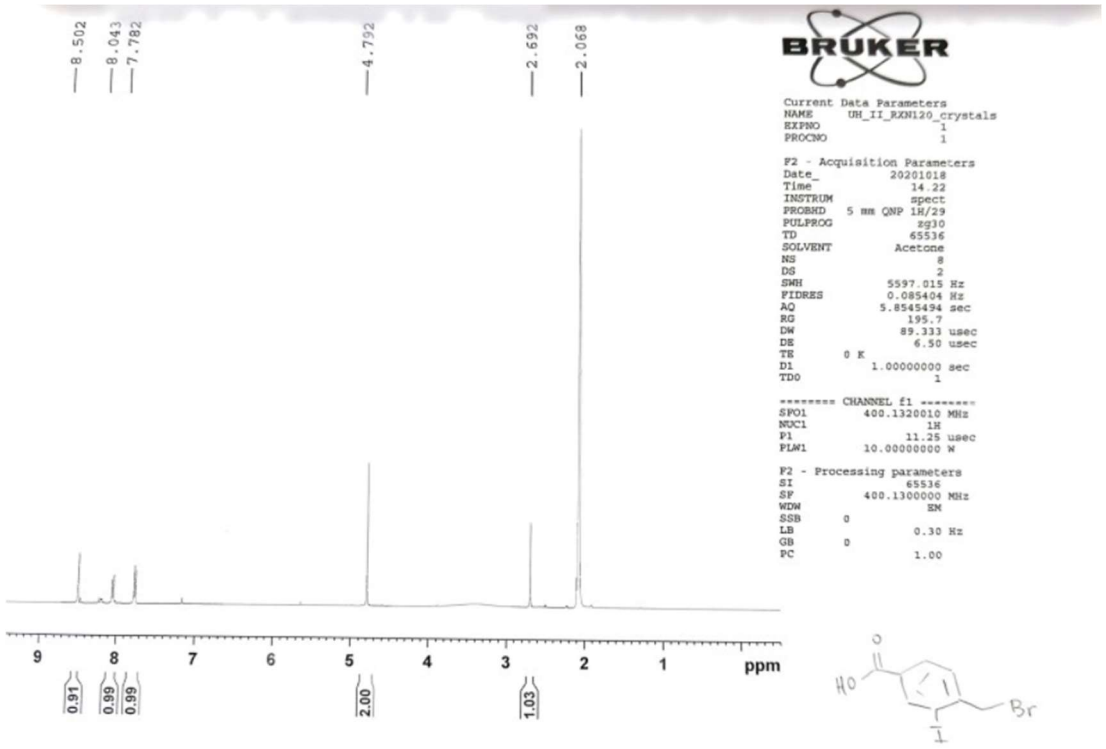

Compound **4** ^{1}H NMR

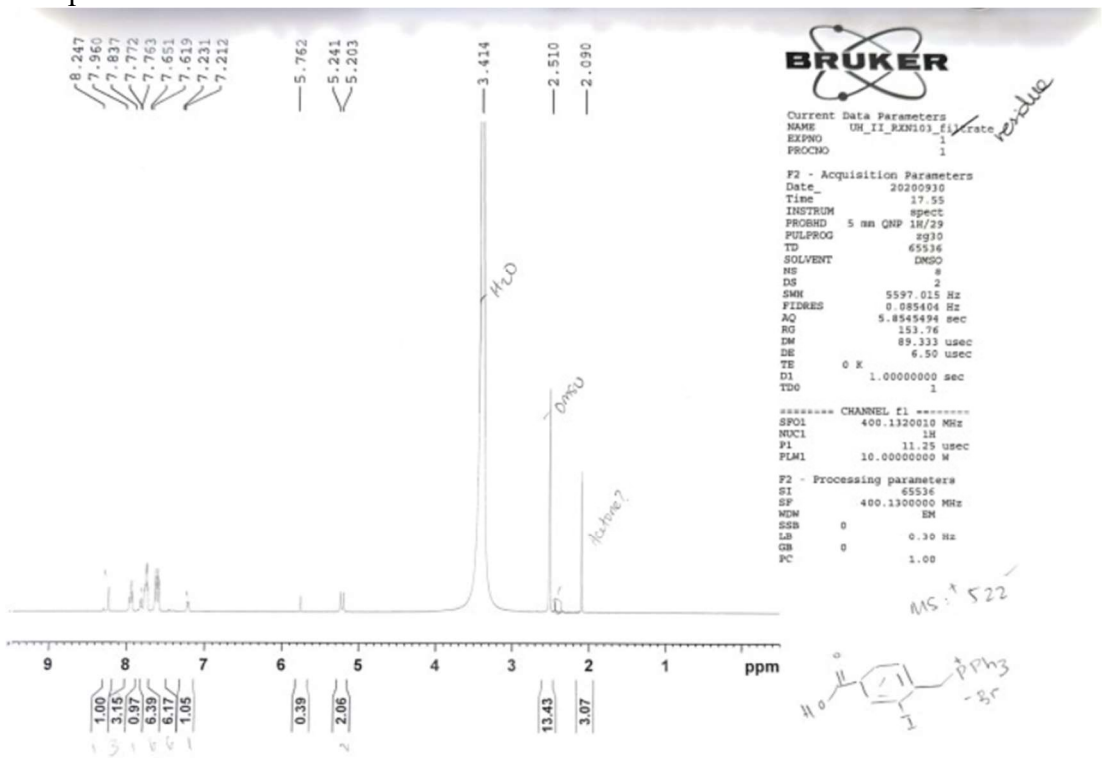

Compound **5** ^{1}H NMR

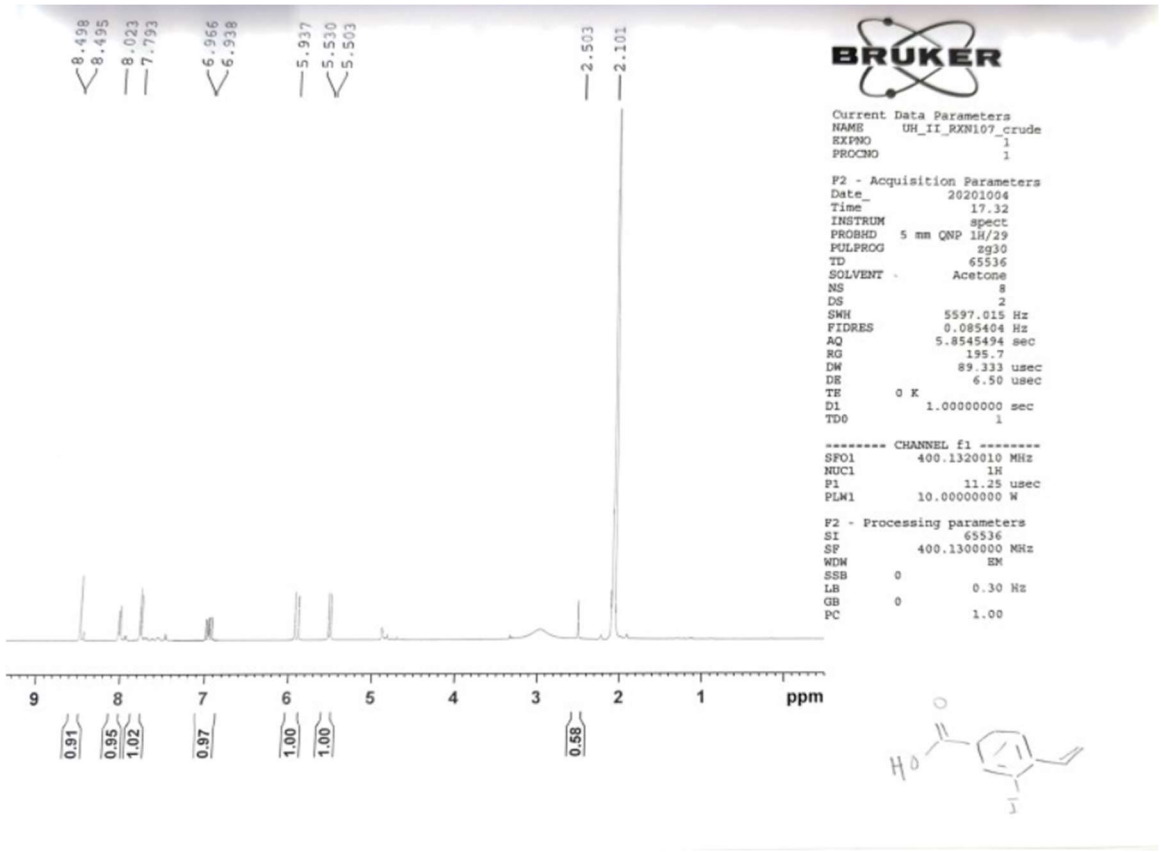

Compound **6** ^{1}H NMR

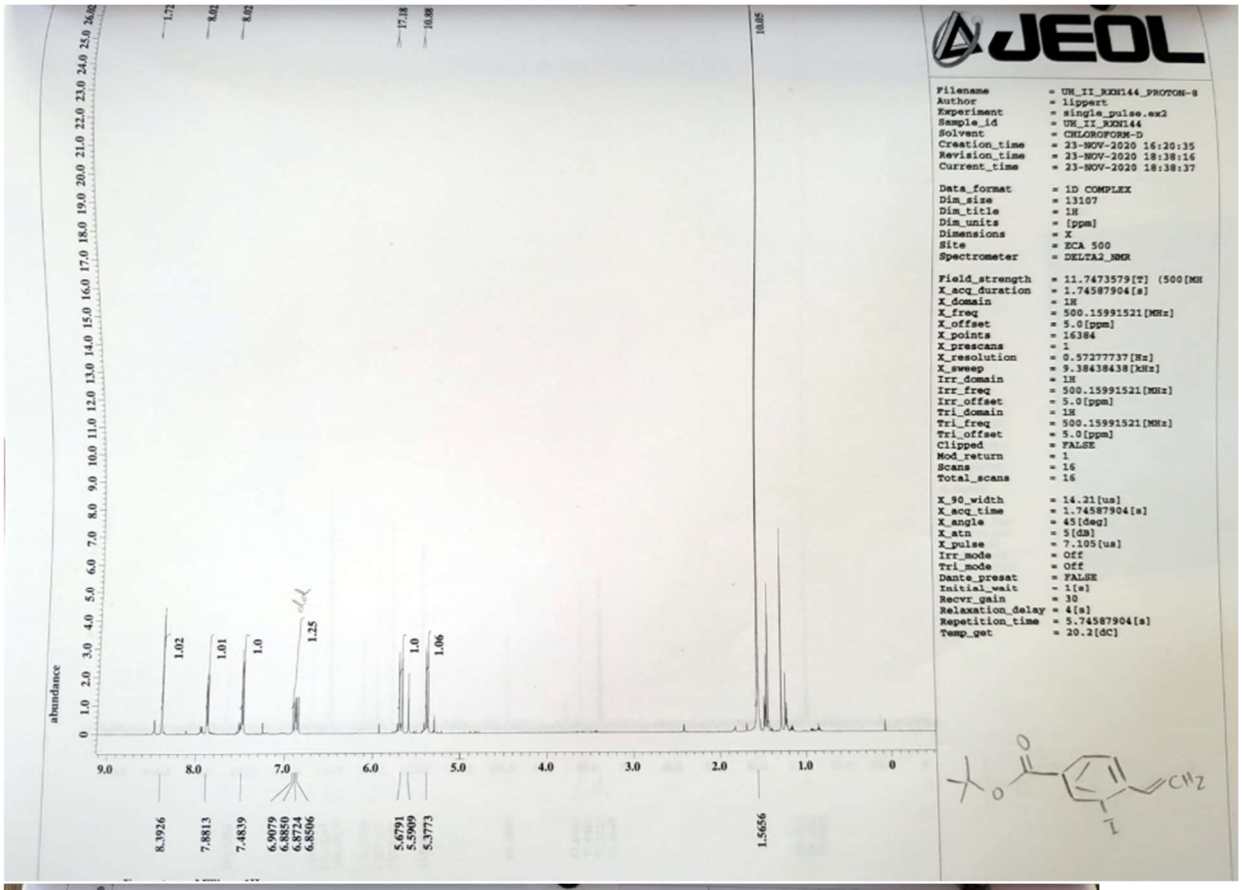

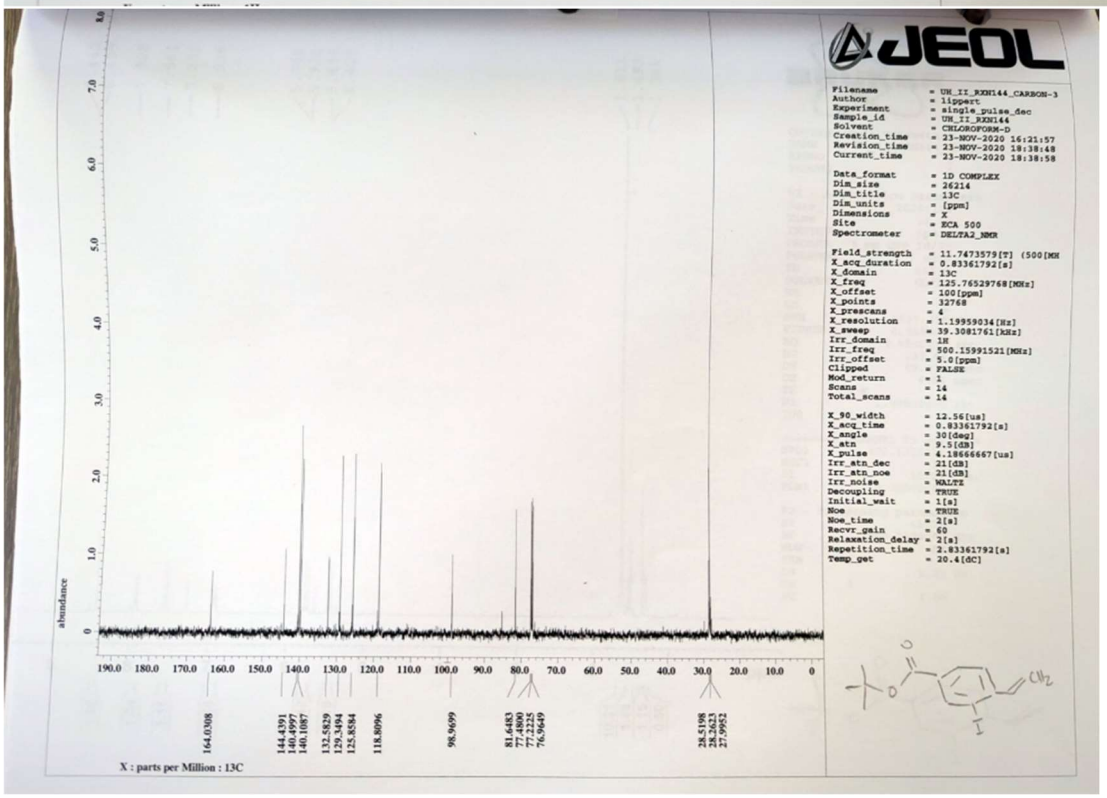

Compound **7** ^{1}H NMR and ^{13}C NMR

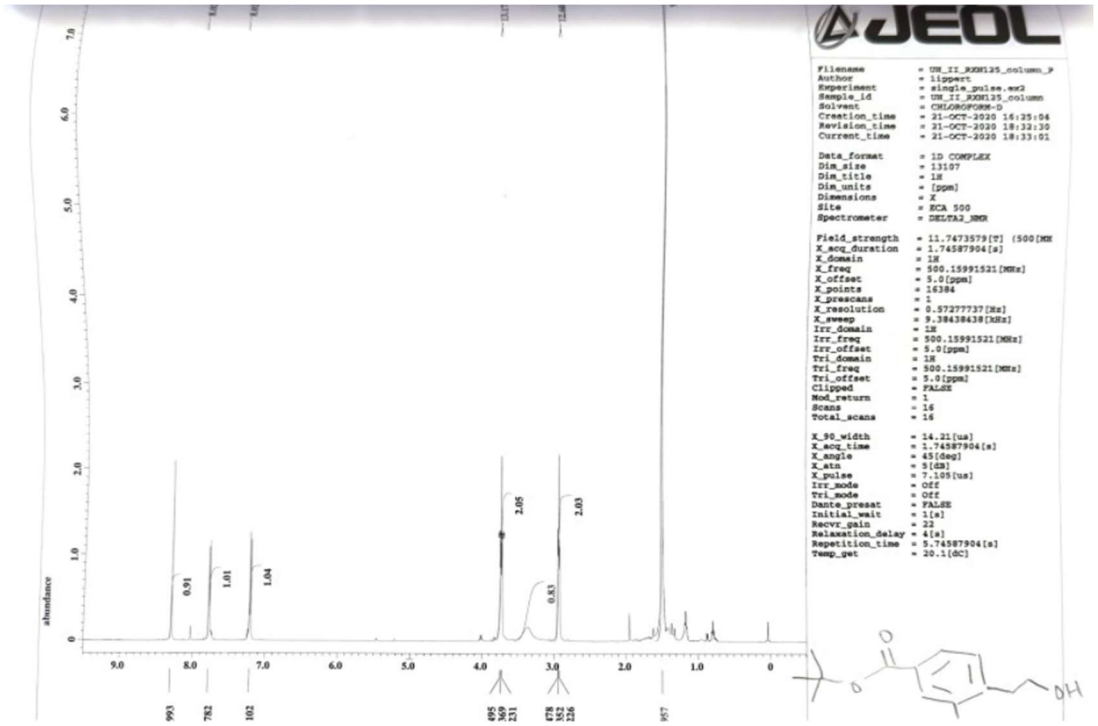

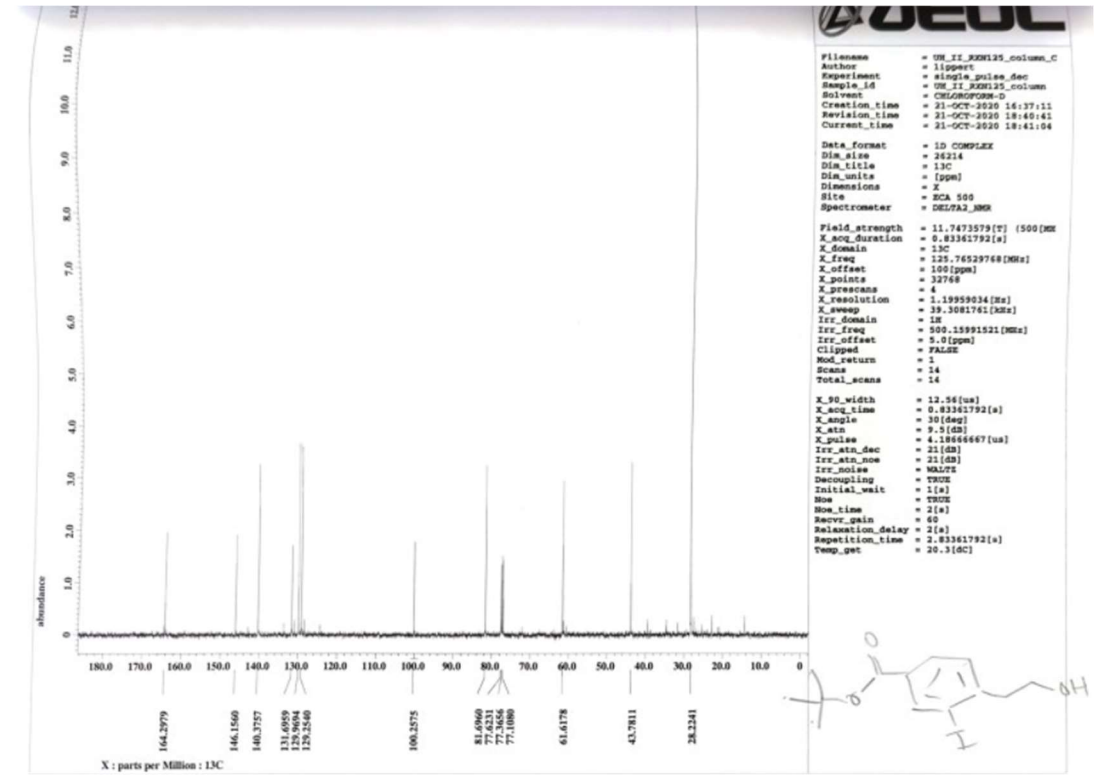

Compound **8** ^{1}H NMR and ^{13}C NMR

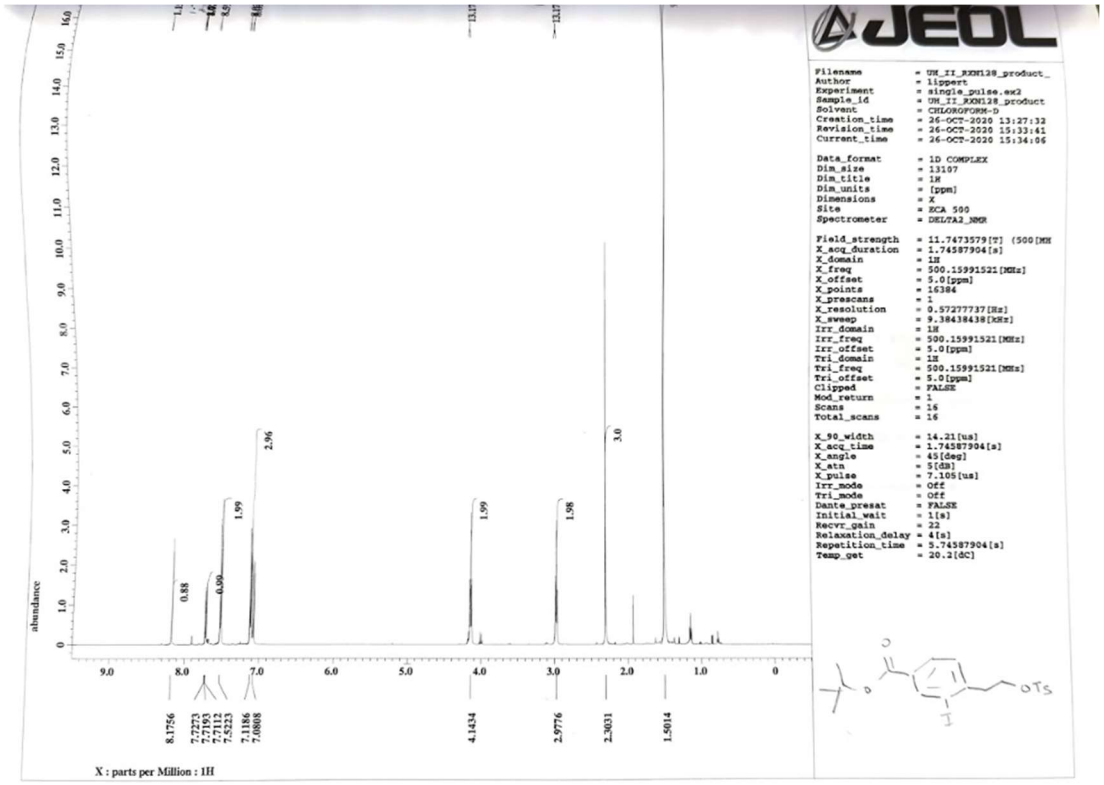

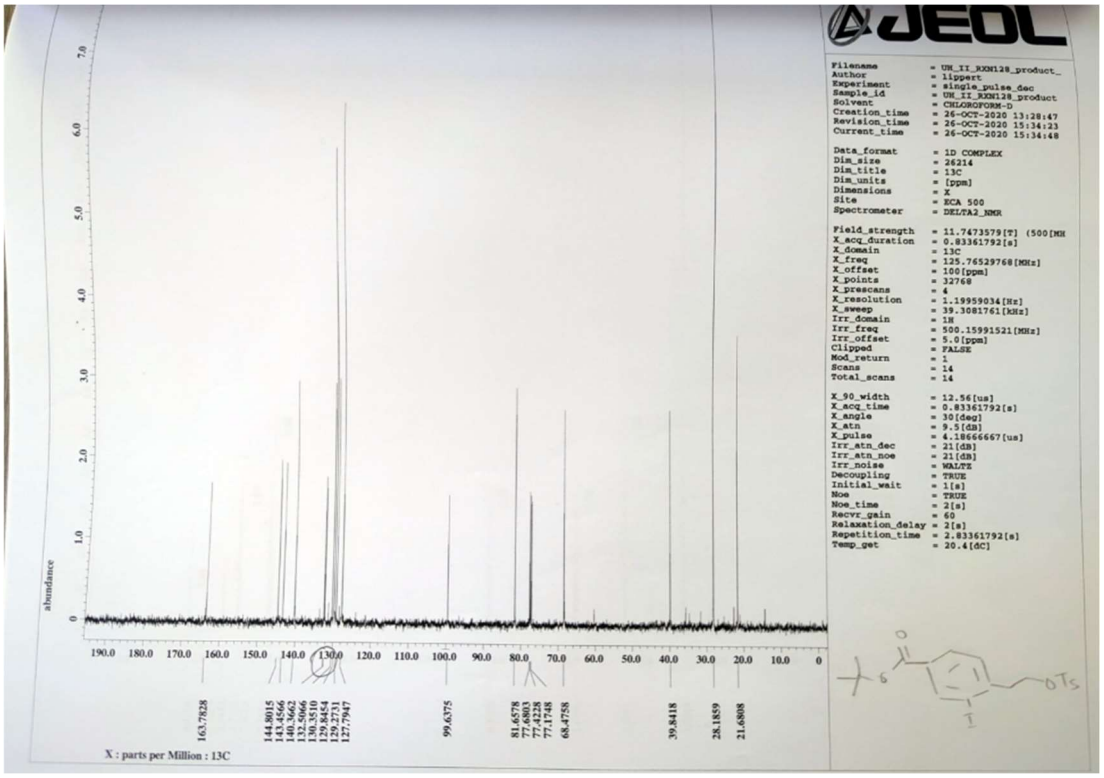

Compound **9** ^{1}H NMR and ^{13}C NMR

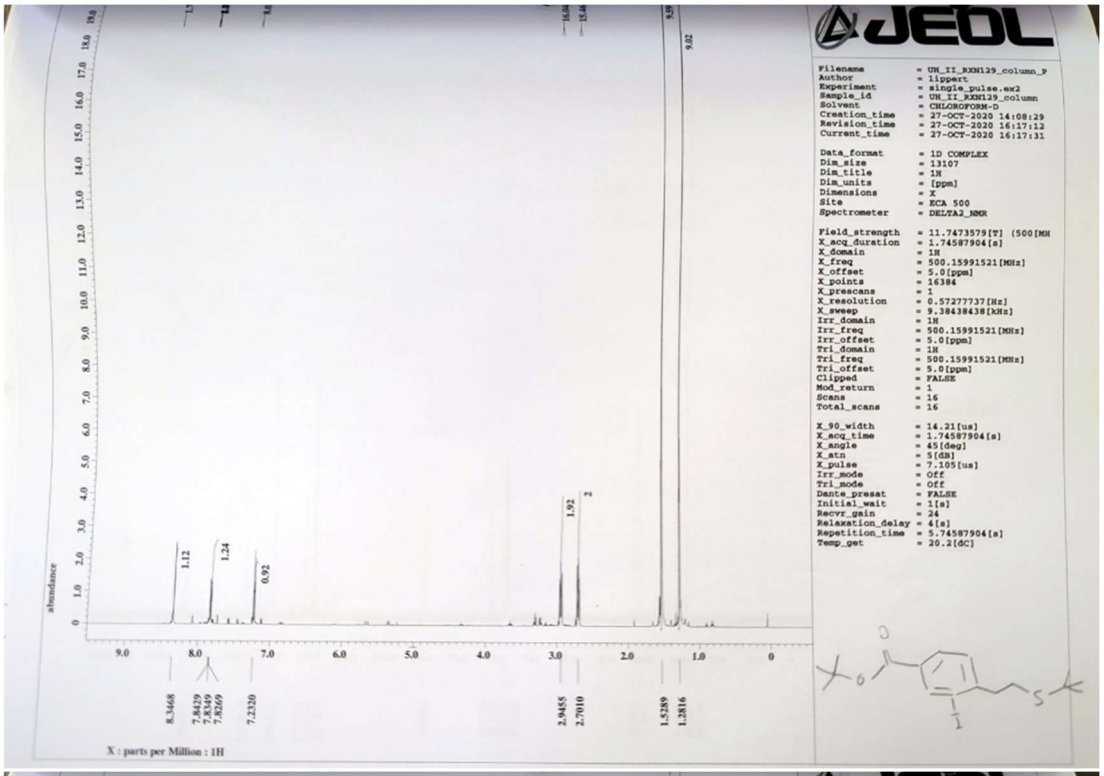

Compound **10** ^{1}H NMR and ^{13}C NMR

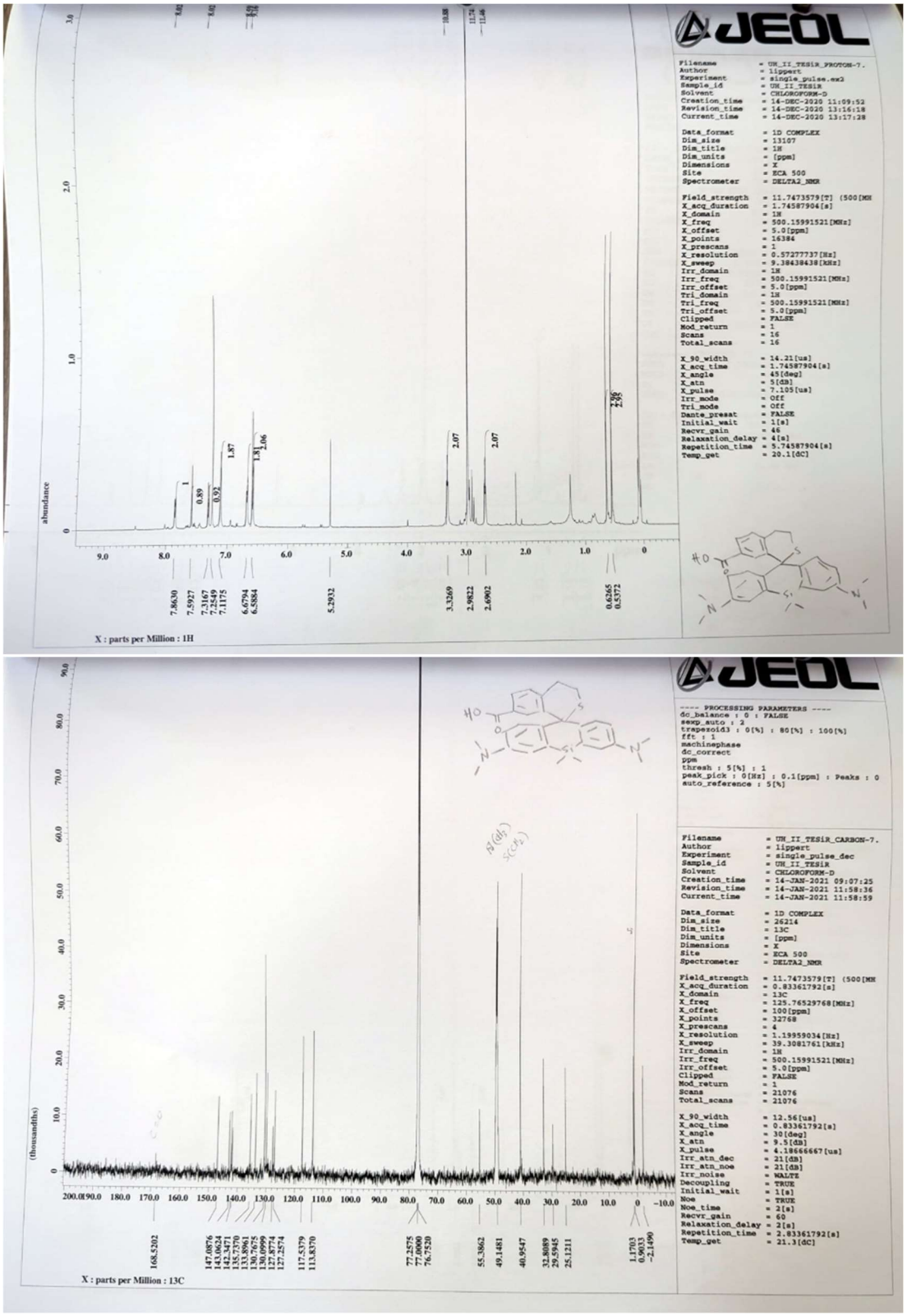

TESiR ^{1}H NMR and ^{13}C NMR

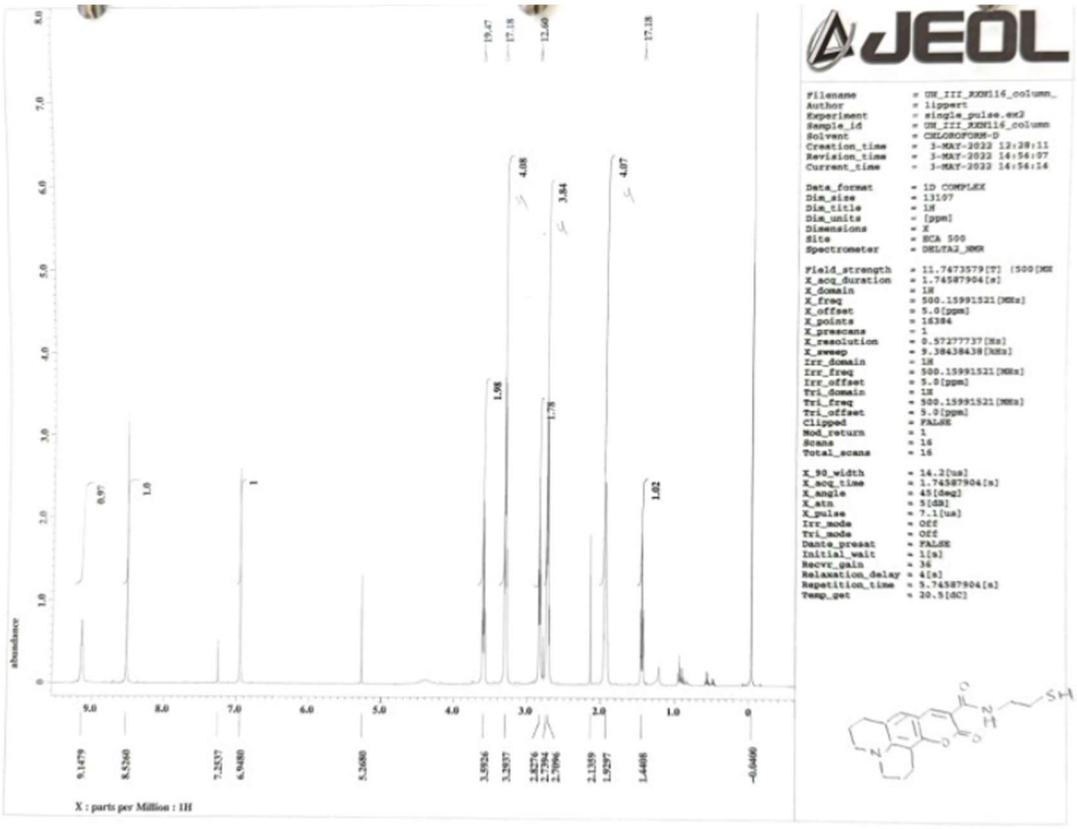

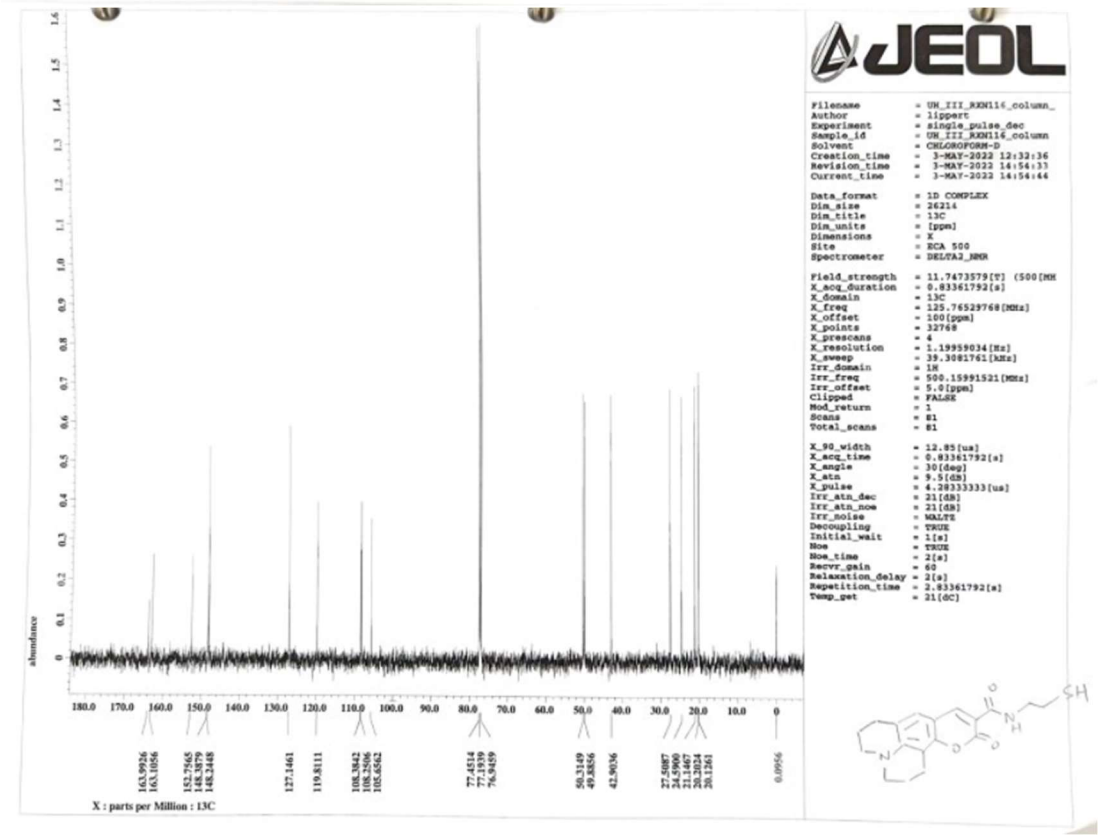

Coumarin-SH ^{1}H NMR and ^{13}C NMR

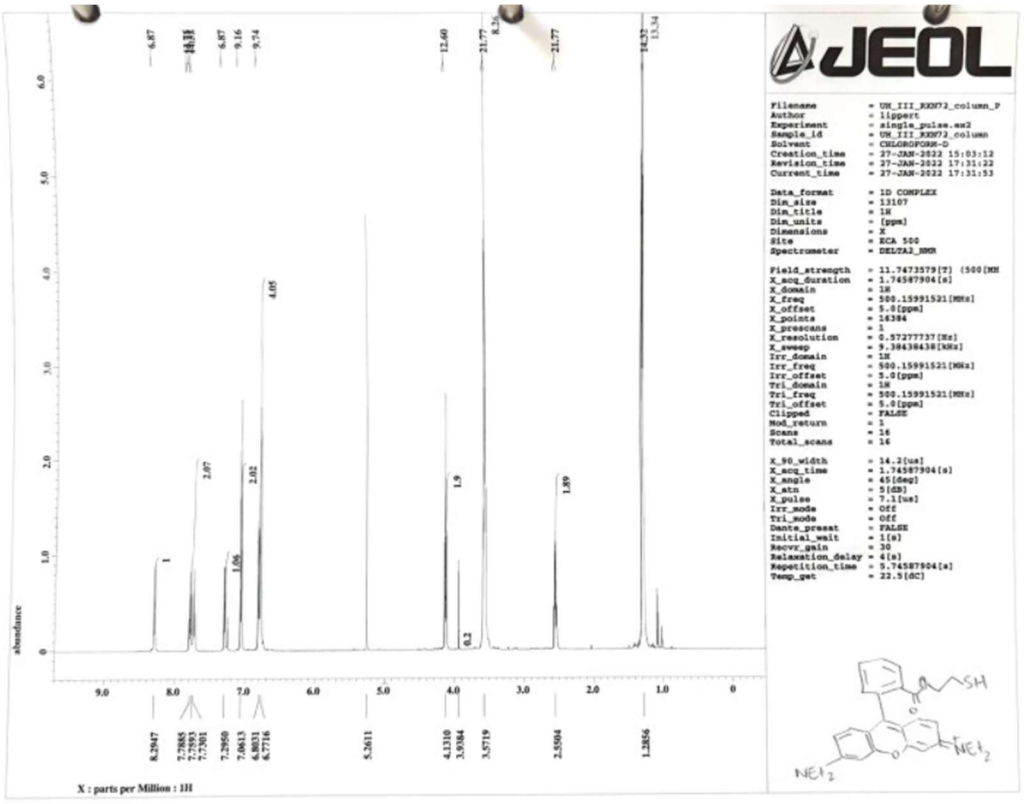

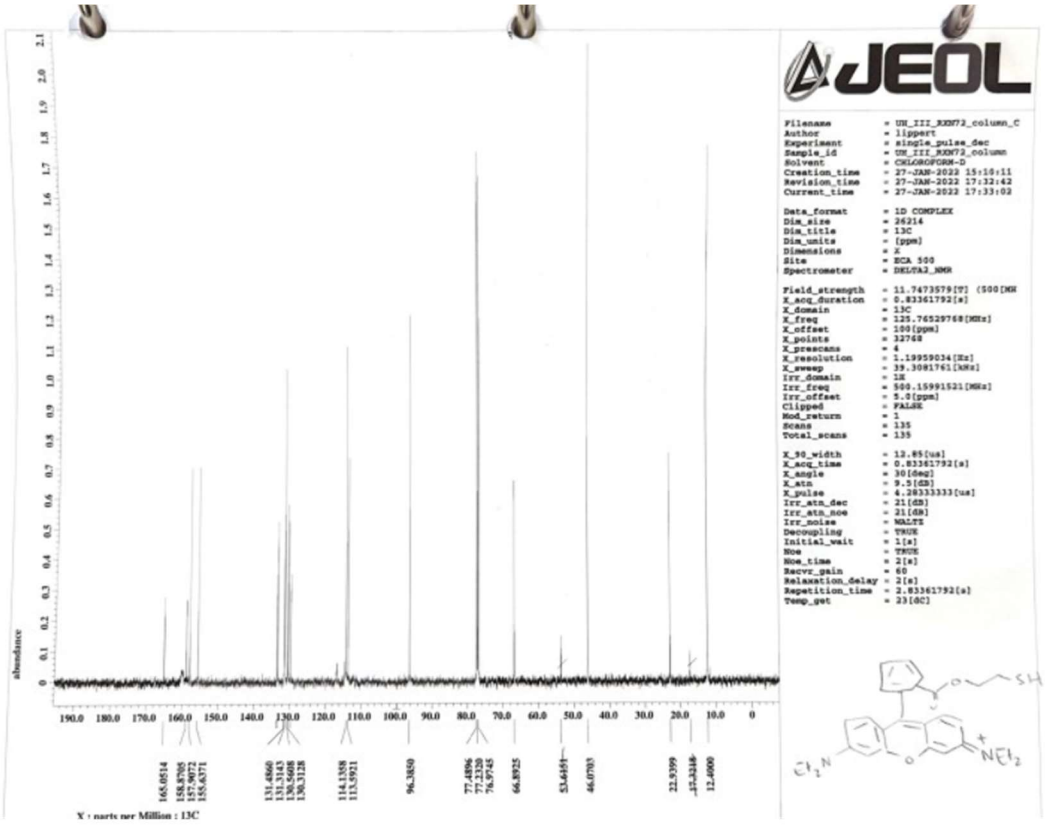

RhB-SH ^{1}H NMR and ^{13}C NMR

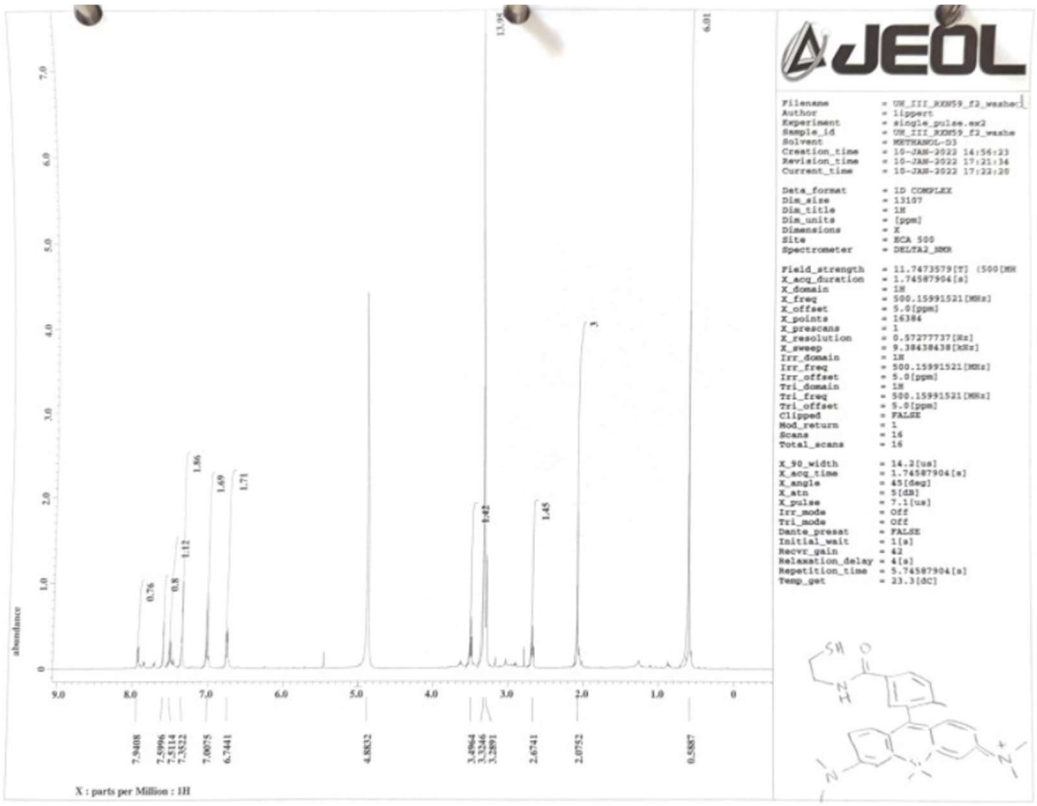

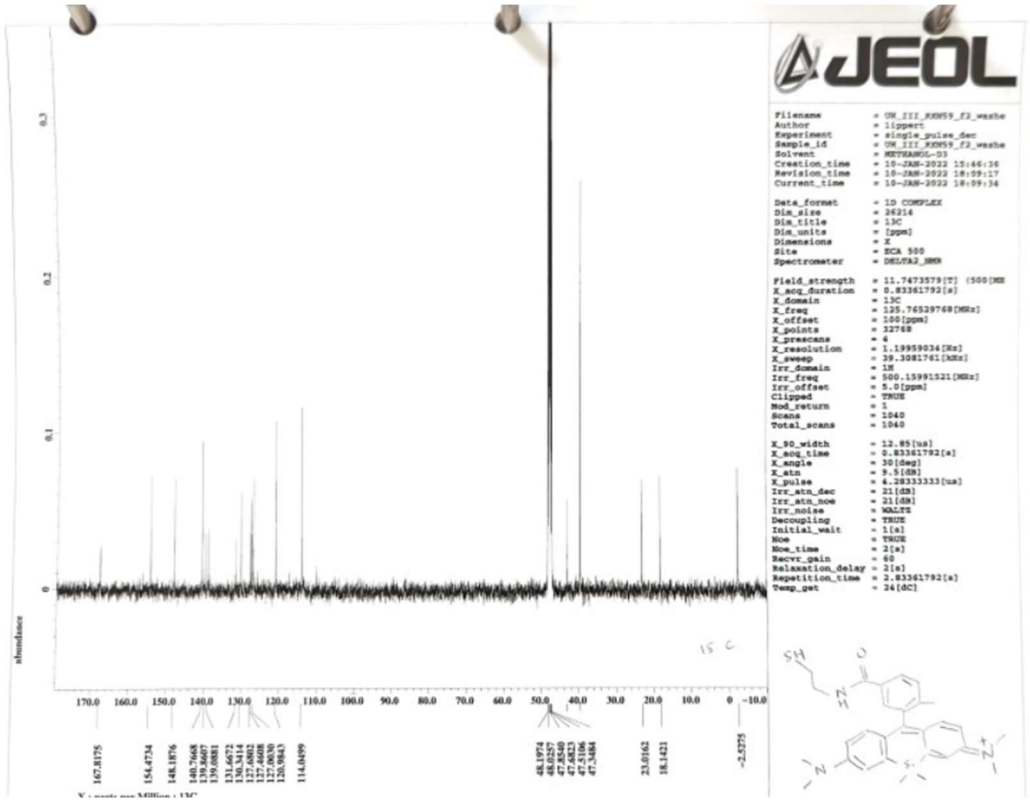

SiR-SH ^{1}H NMR and ^{13}C NMR

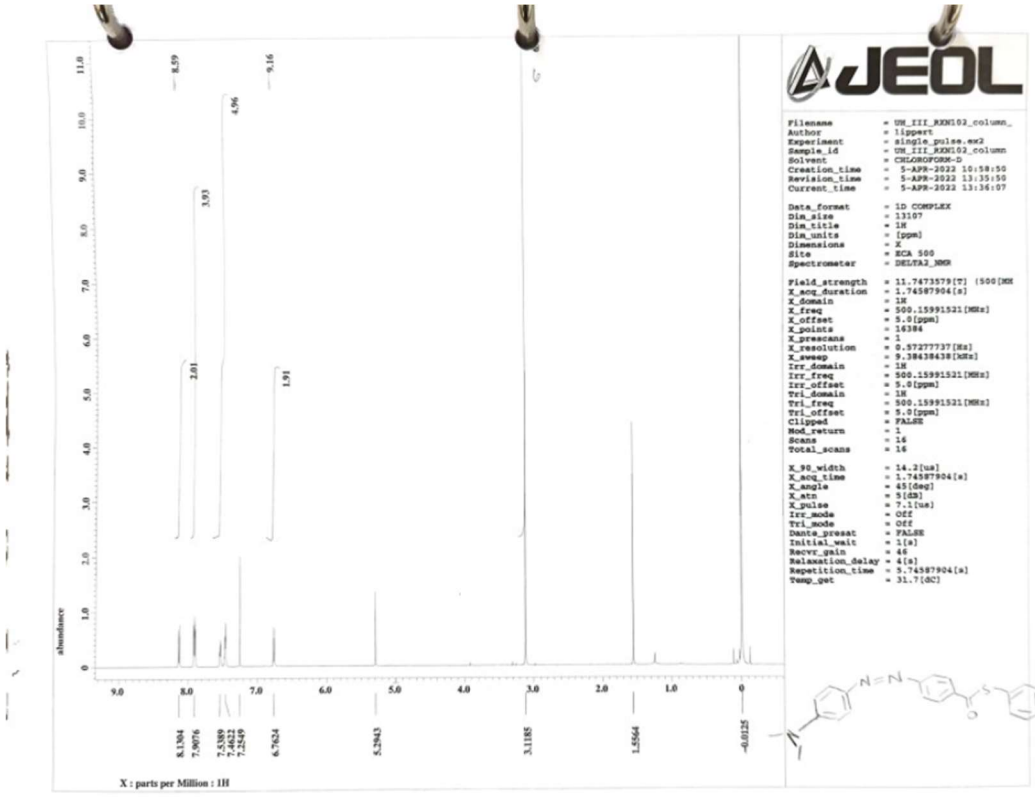

Compound **14** ^{1}H NMR

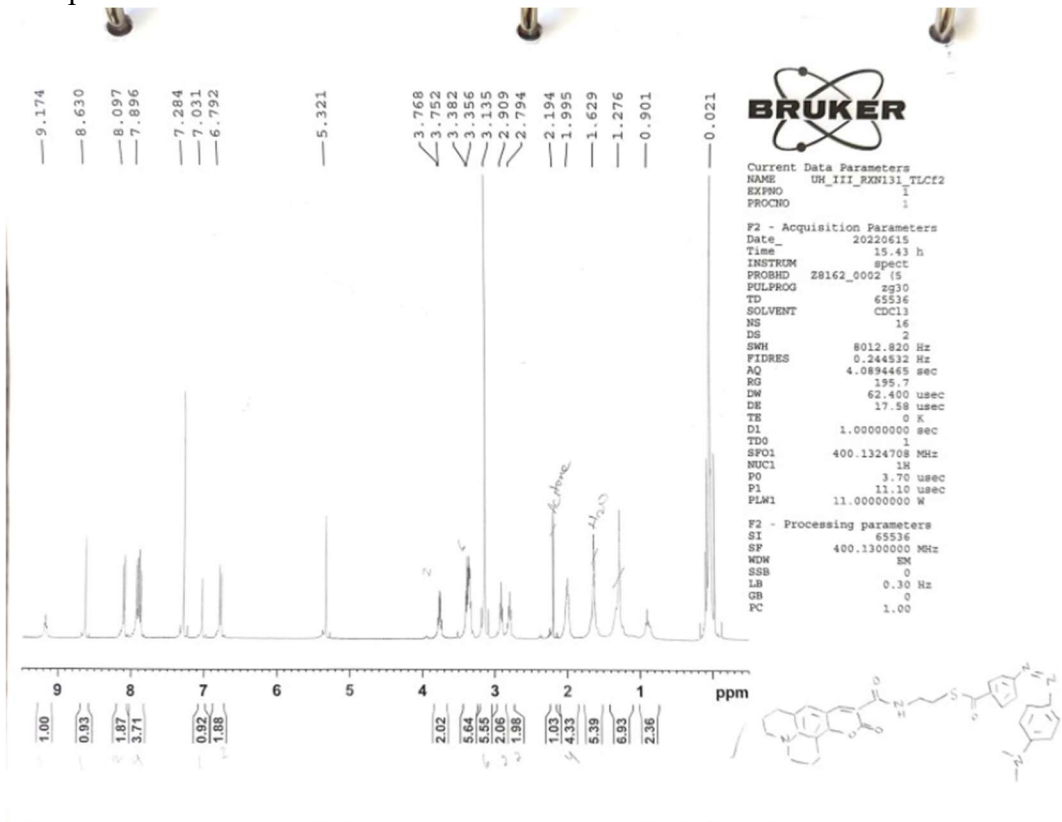

Coumarin-DABCYL ^{1}H NMR

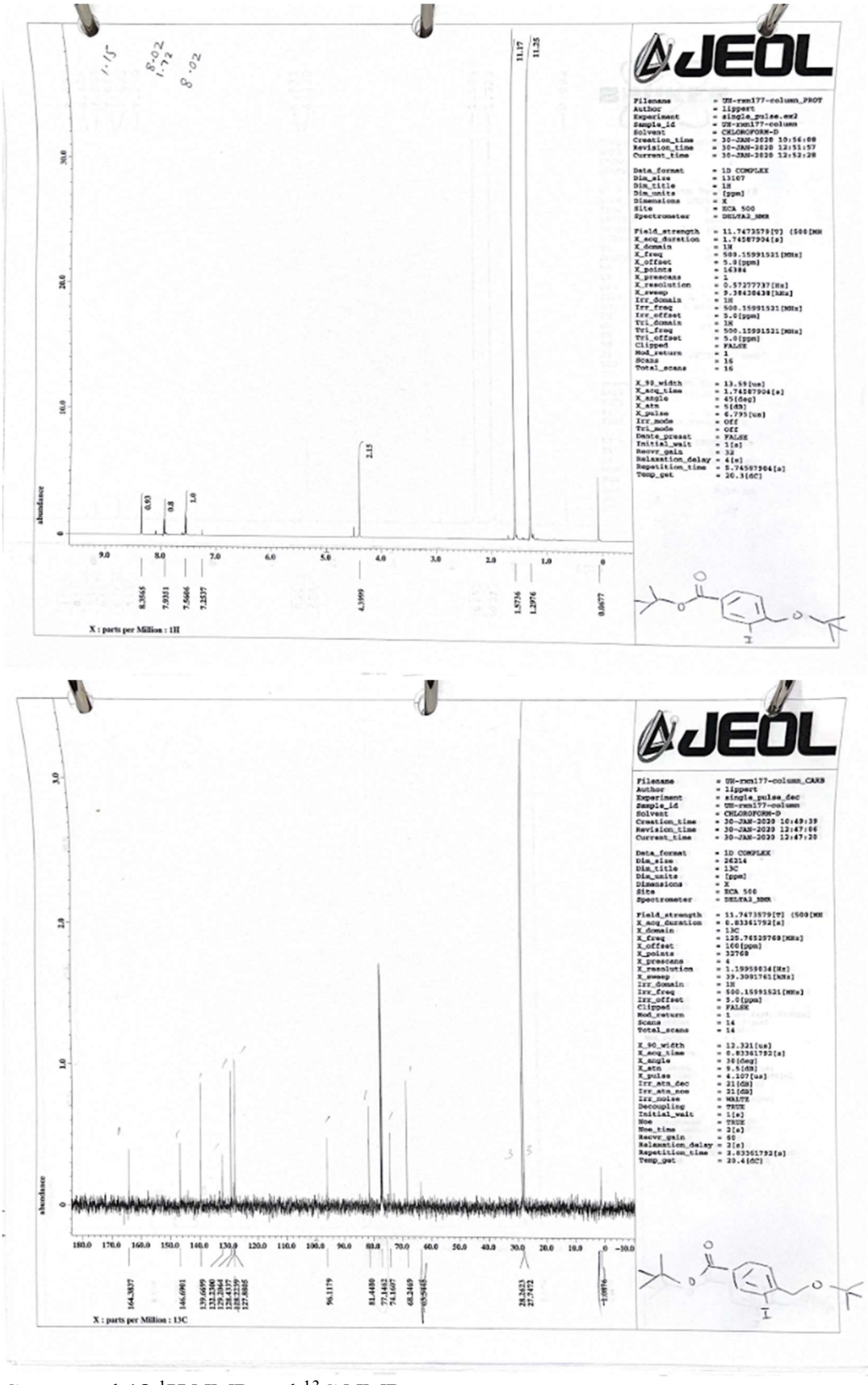

Compound **18** ^{1}H NMR and ^{13}C NMR

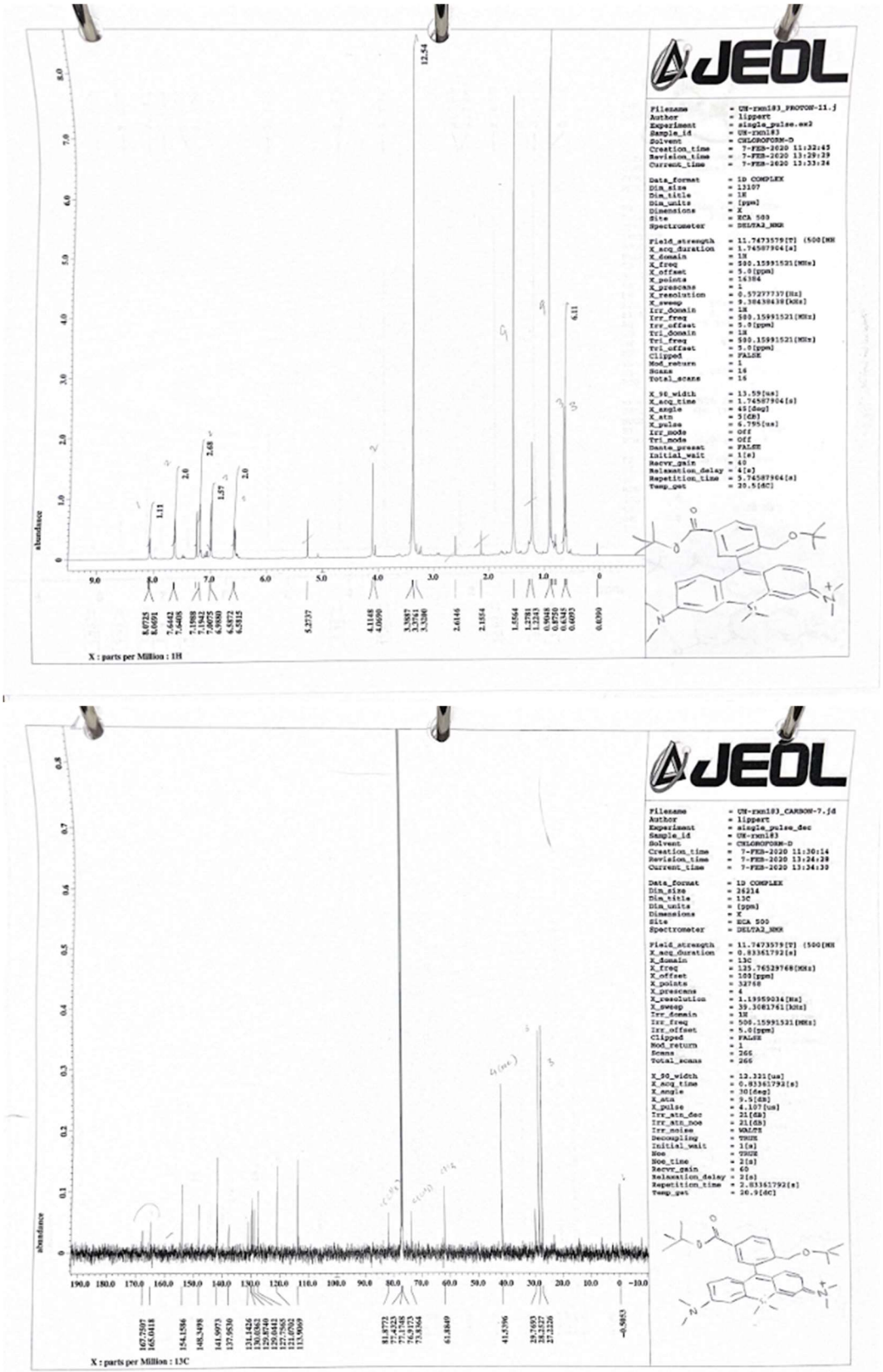

Compound **19** ^{1}H NMR and ^{13}C NMR

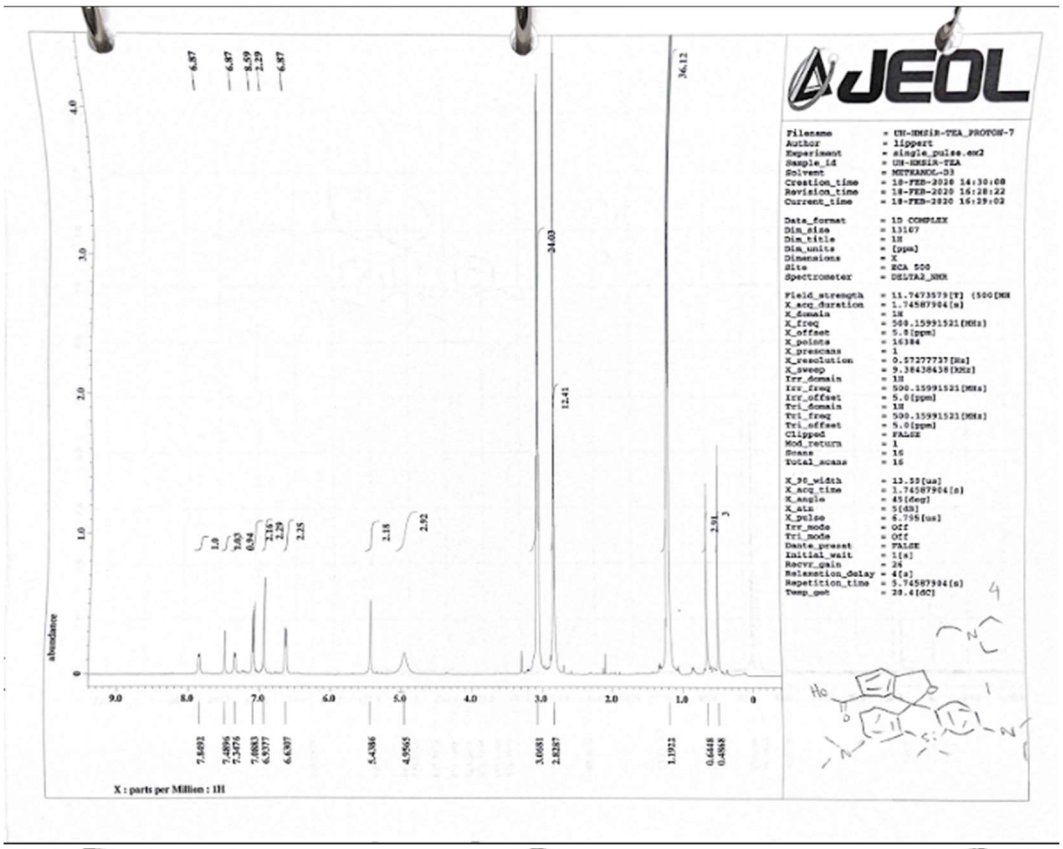

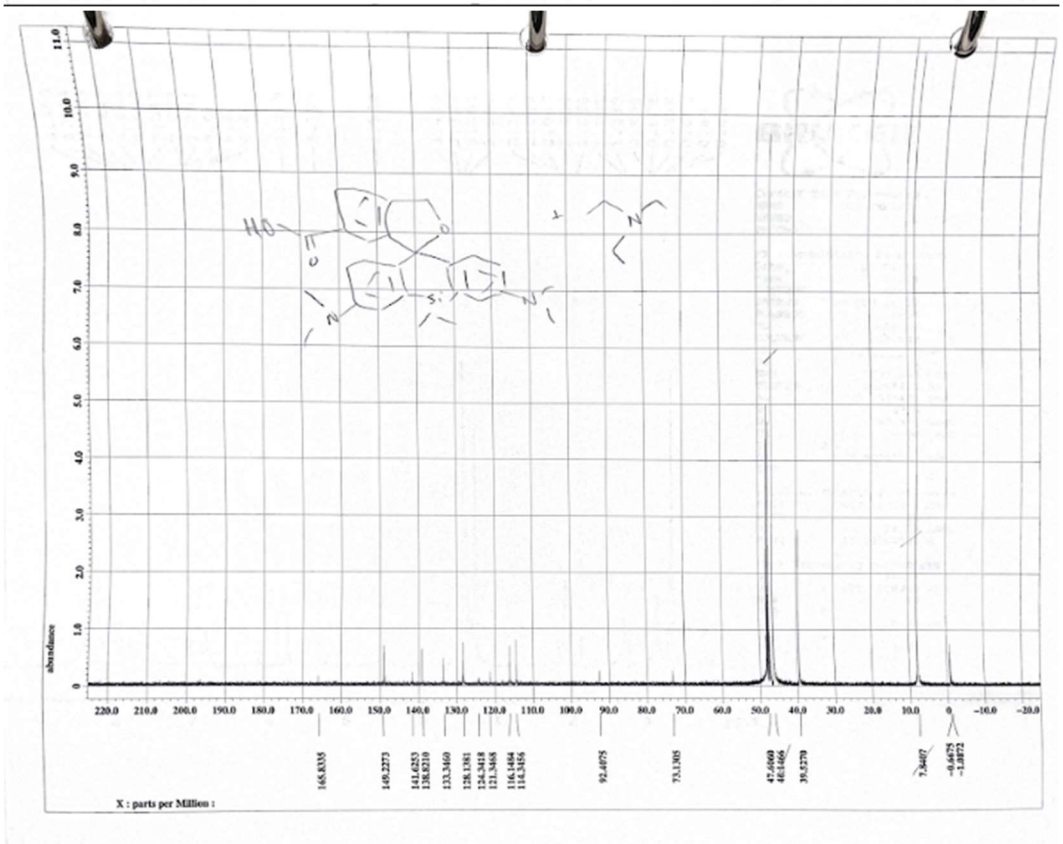

HMSiR ^{1}H NMR and ^{13}C NMR

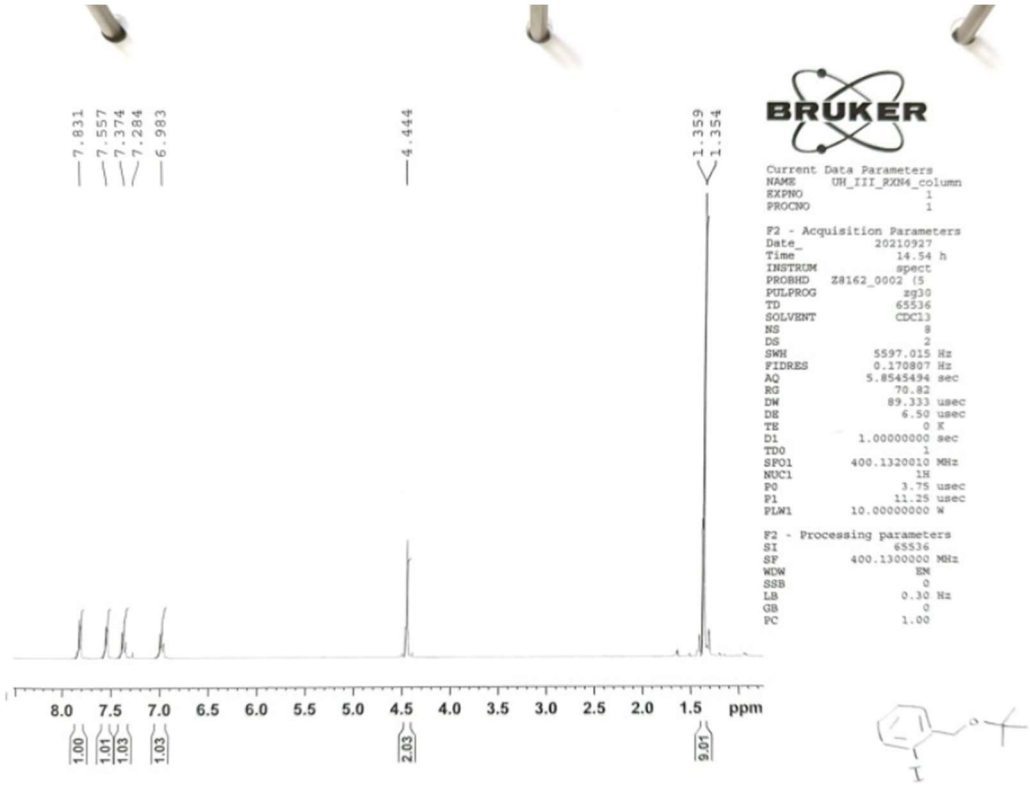

Compound **20** ^{1}H NMR

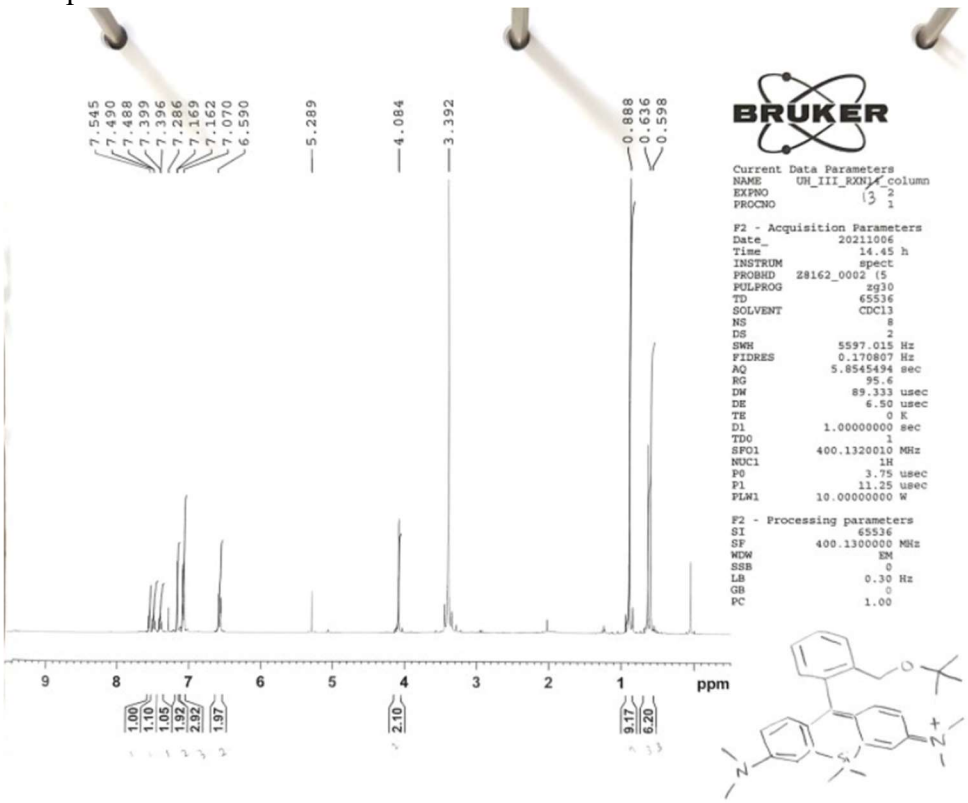

Compound **21** ^{1}H NMR

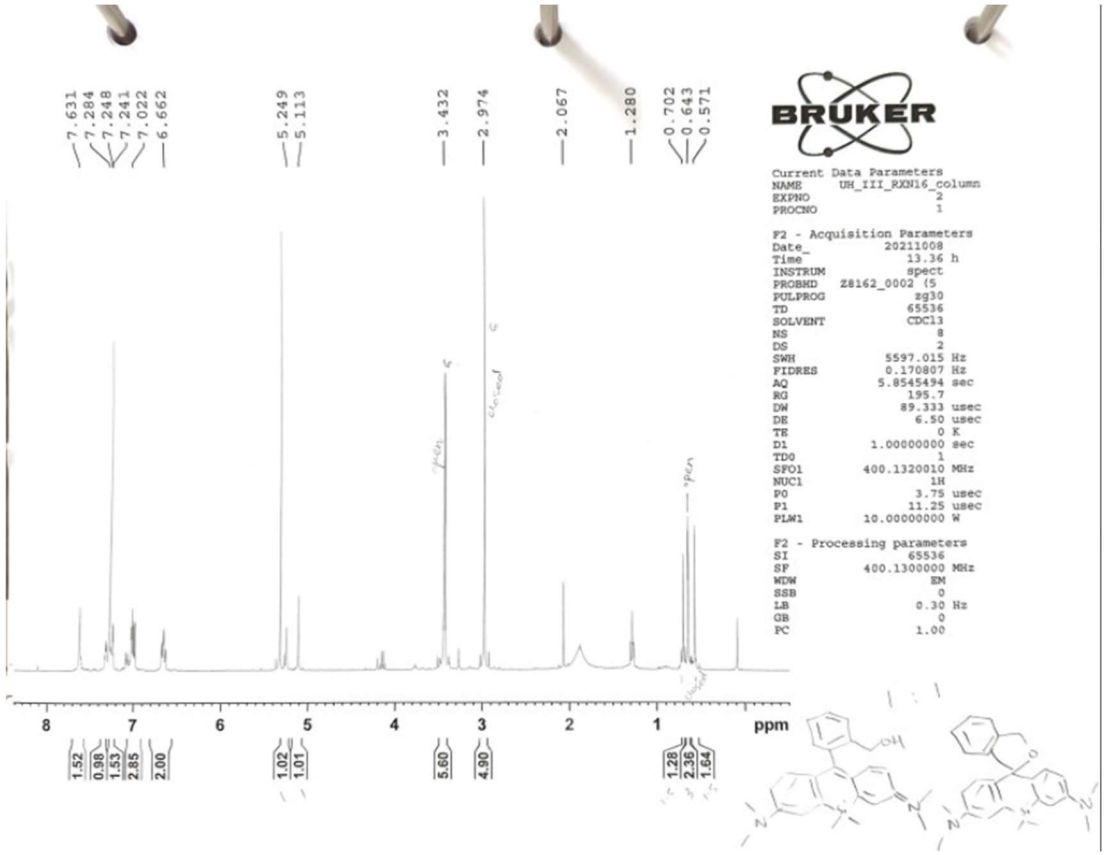

HMSiR-2 ^{1}H NMR

3. CHAPTER 5 COMPOUNDS – NMR SPECTRA

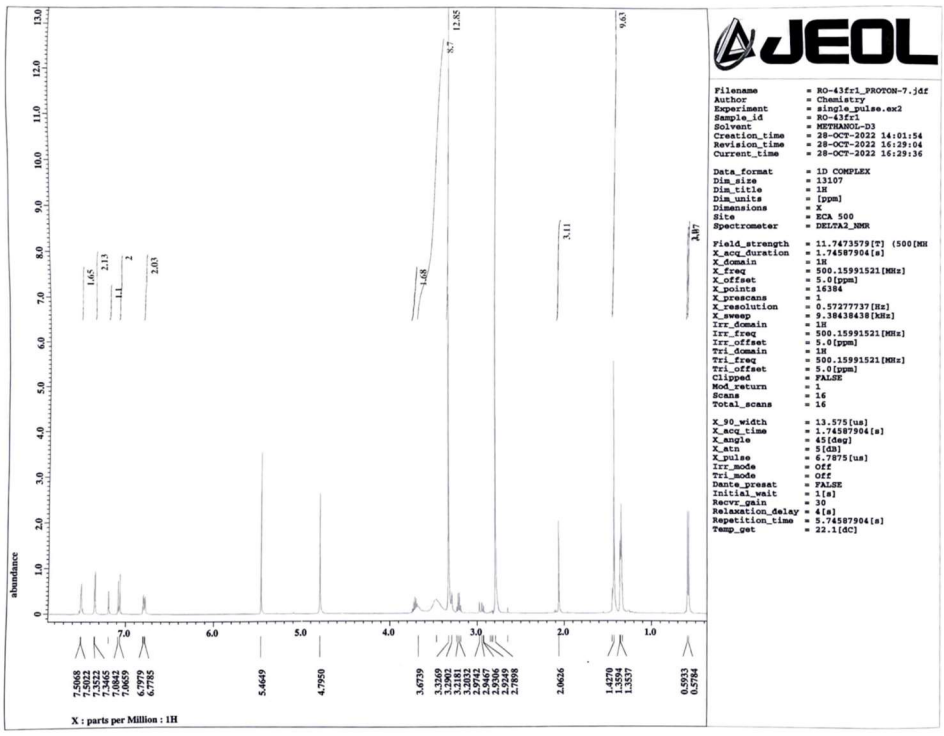

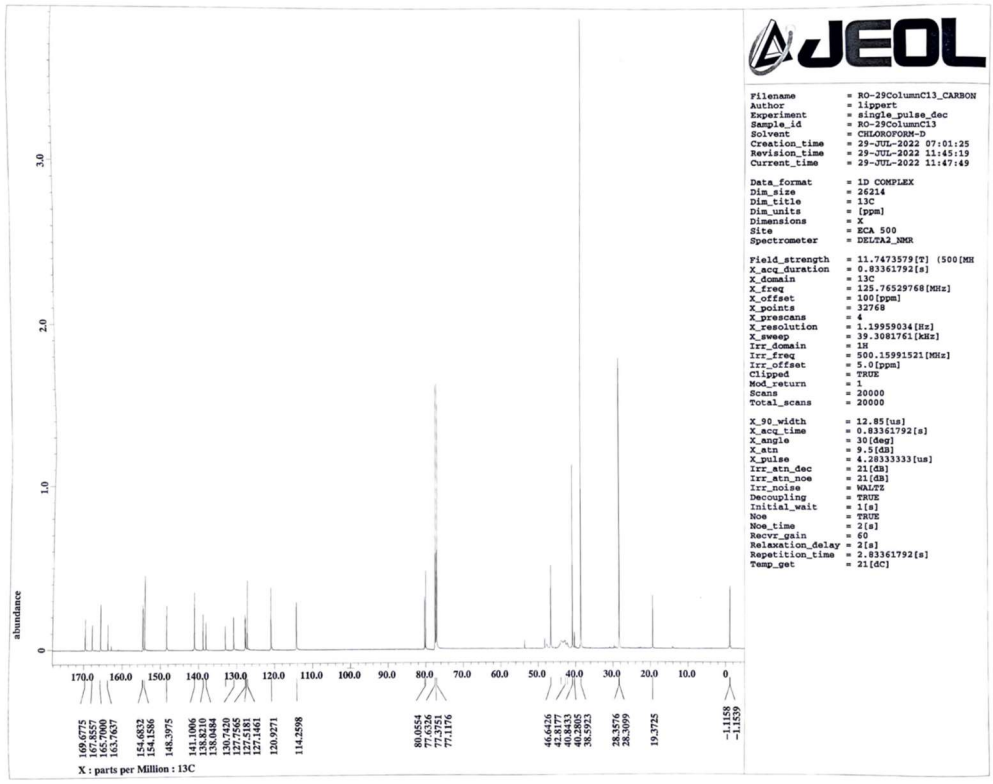

Compound **6** ^{1}H NMR and ^{13}C NMR. Experiment by Rokia Osman, SMU.

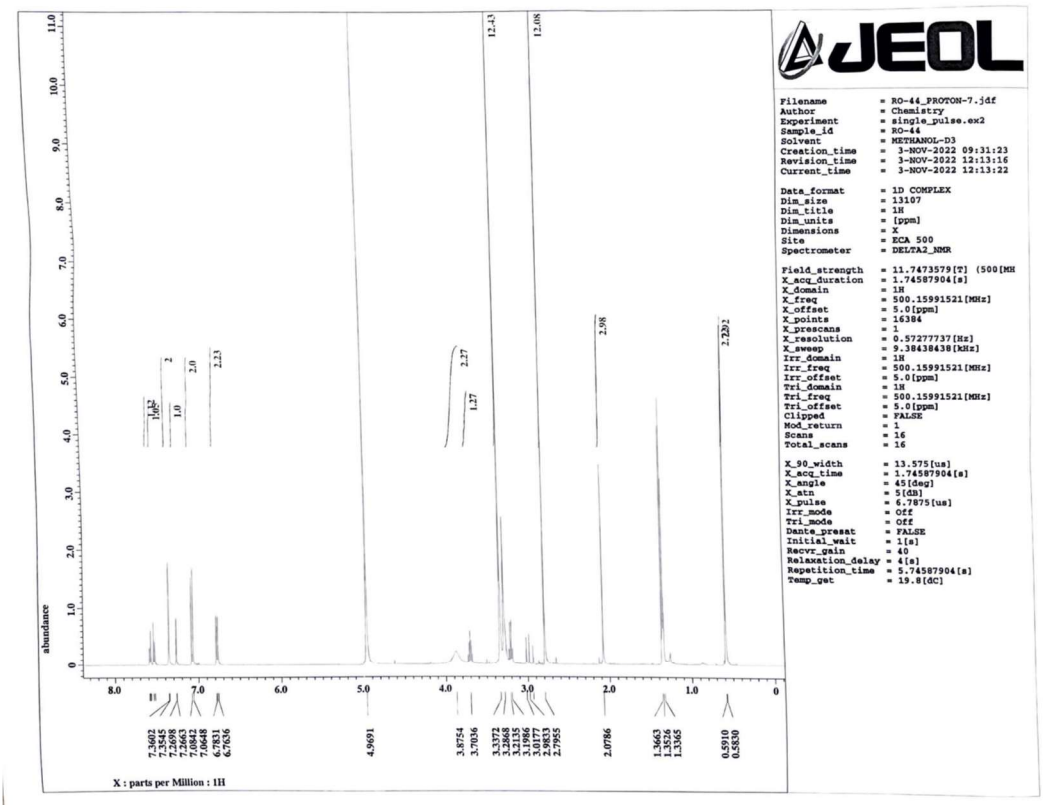

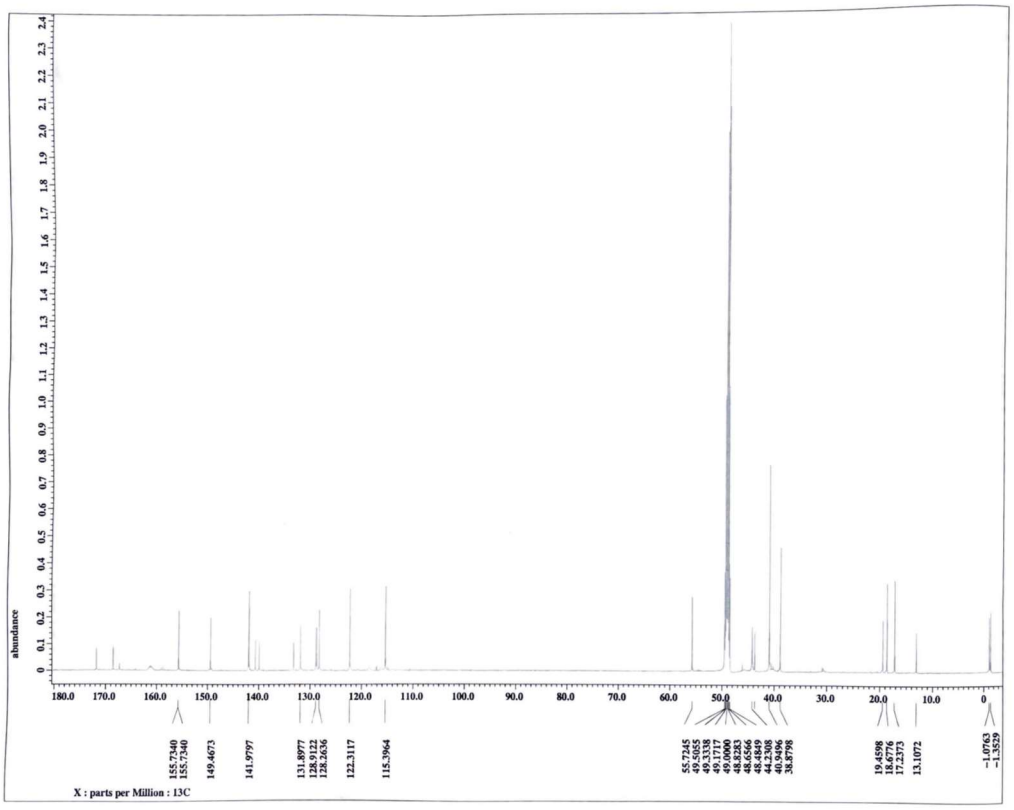

Compound **7** ^{1}H NMR and ^{13}C NMR. Experiment by Rokia Osman, SMU

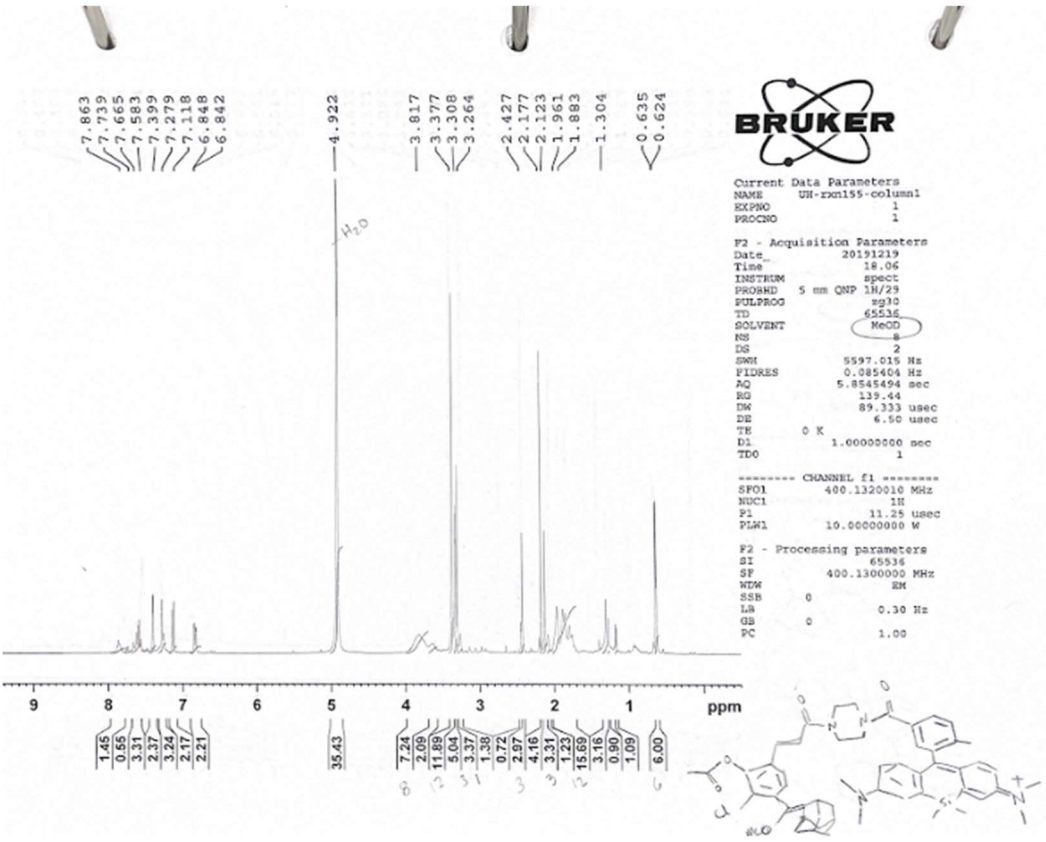

Compound **9** ^{1}H NMR and ^{13}C NMR

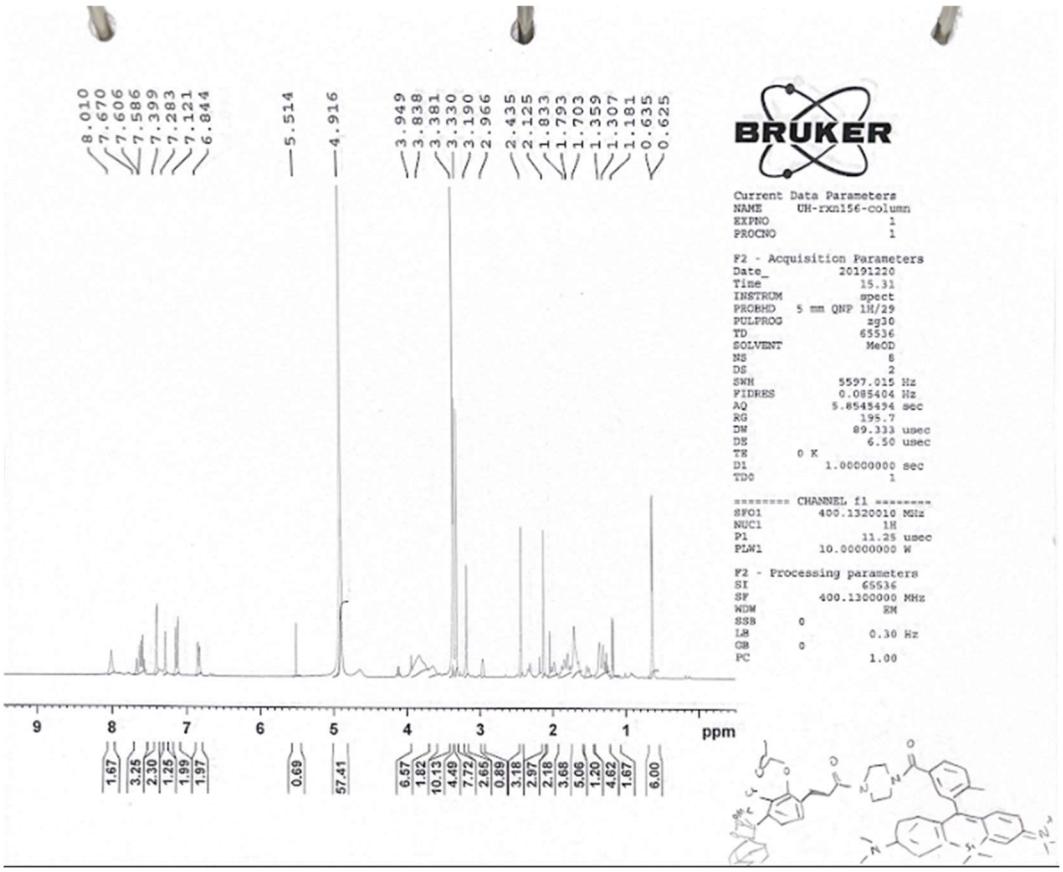

SiRCL-OAc ^{1}H NMR

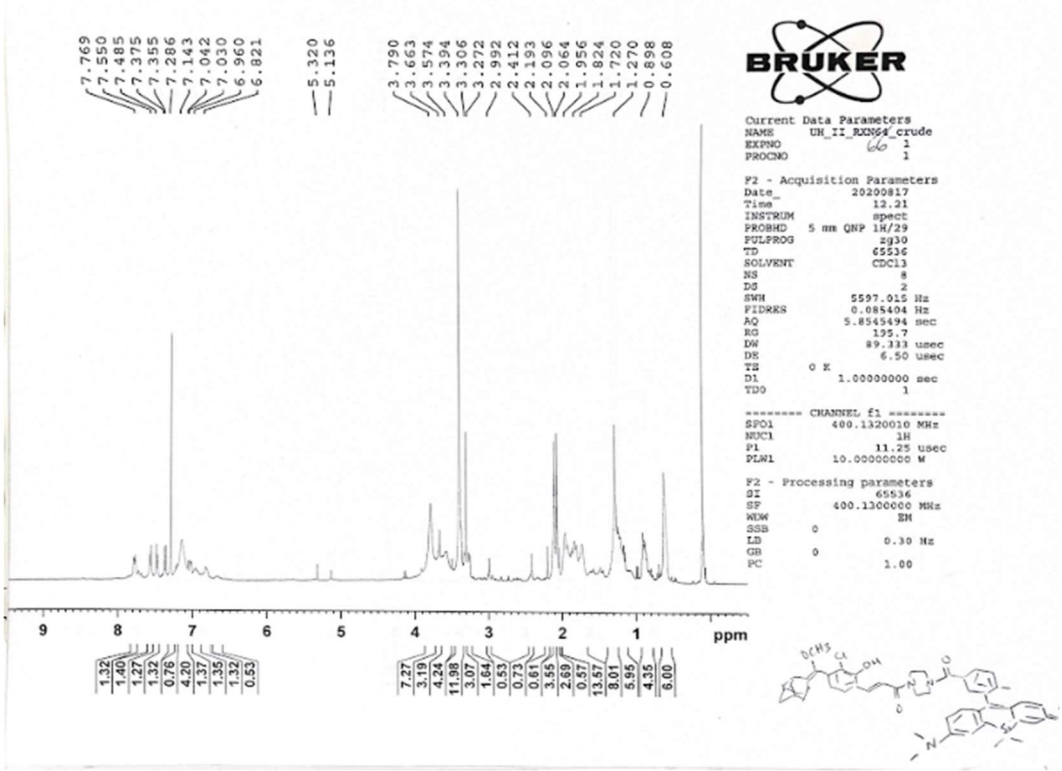

Compound **10** ^{1}H NMR

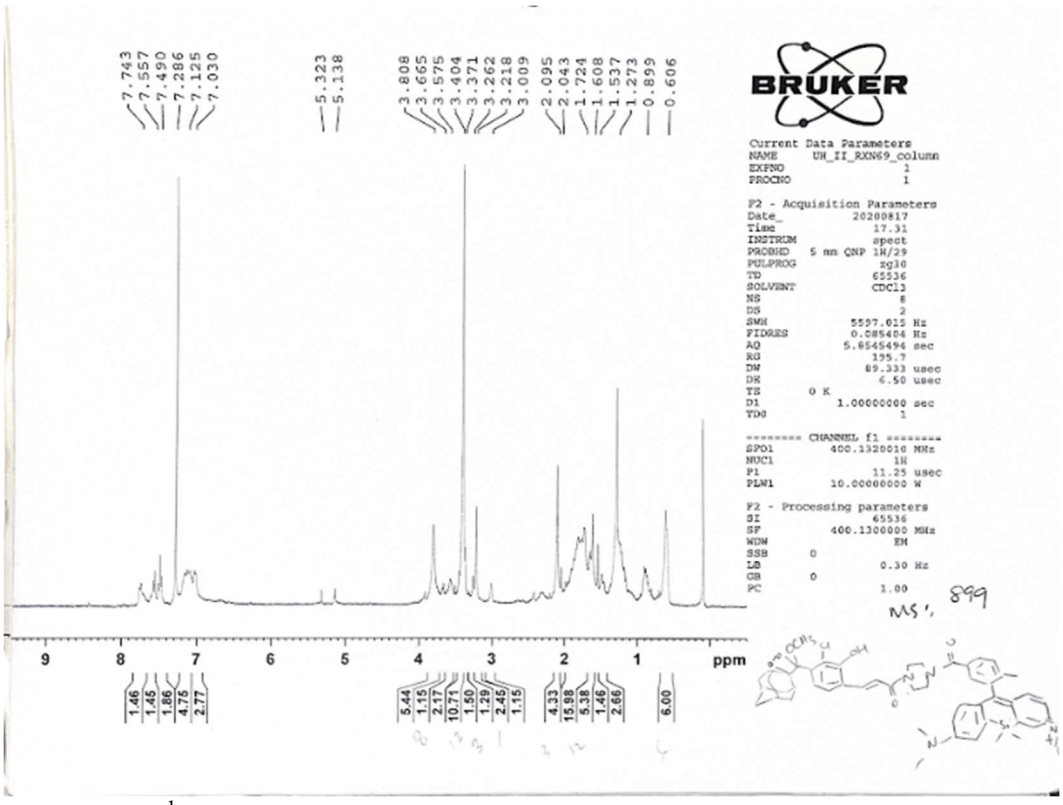

SiRCL-OH ^{1}H NMR

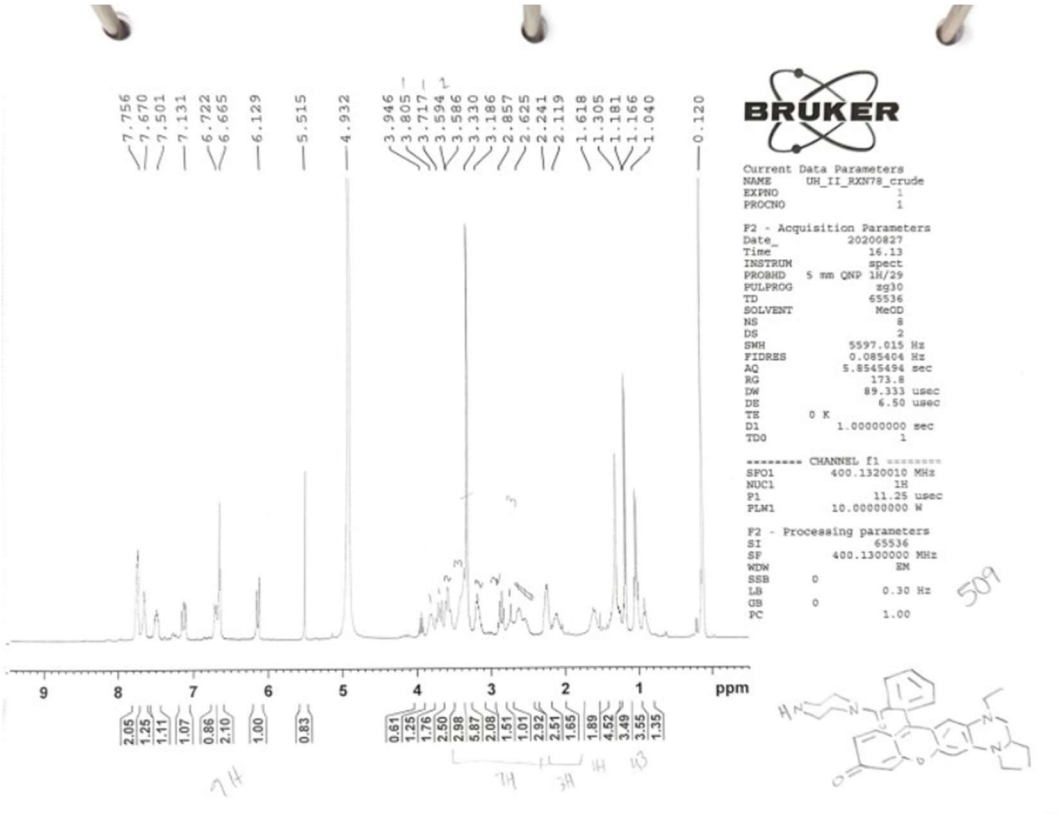

Compound **11** ^{1}H NMR

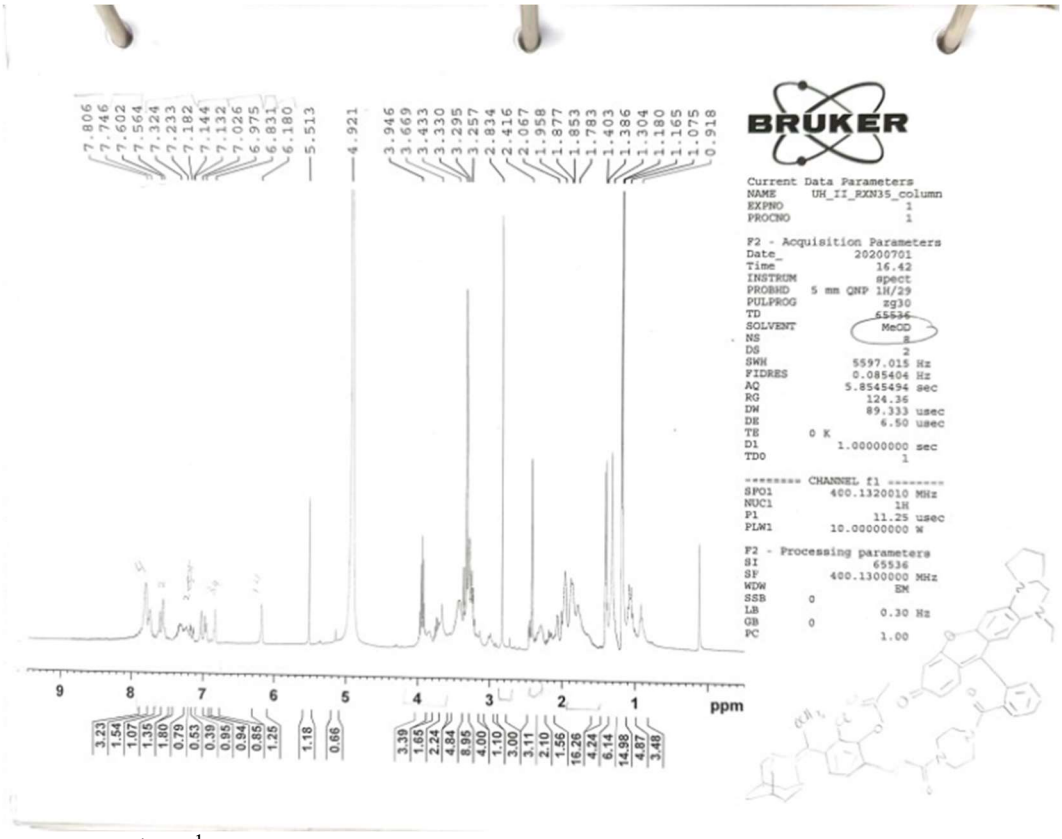

Compound **12** ^{1}H NMR

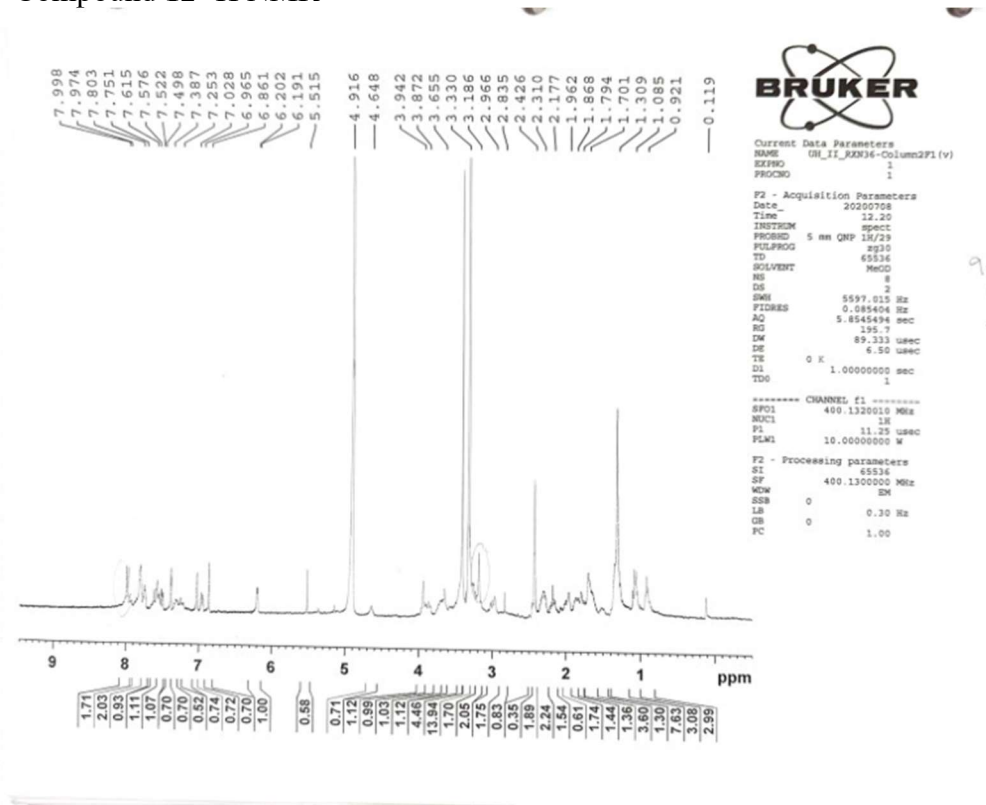

WRCL-OAc ^{1}H NMR

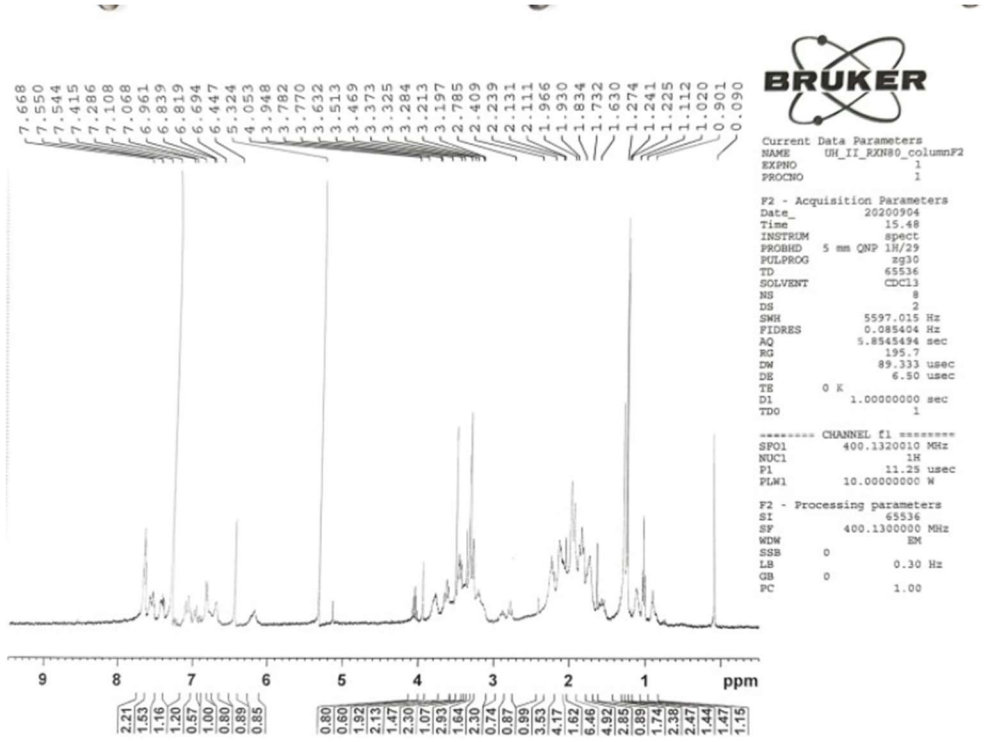

Compound **13** ^{1}H NMR

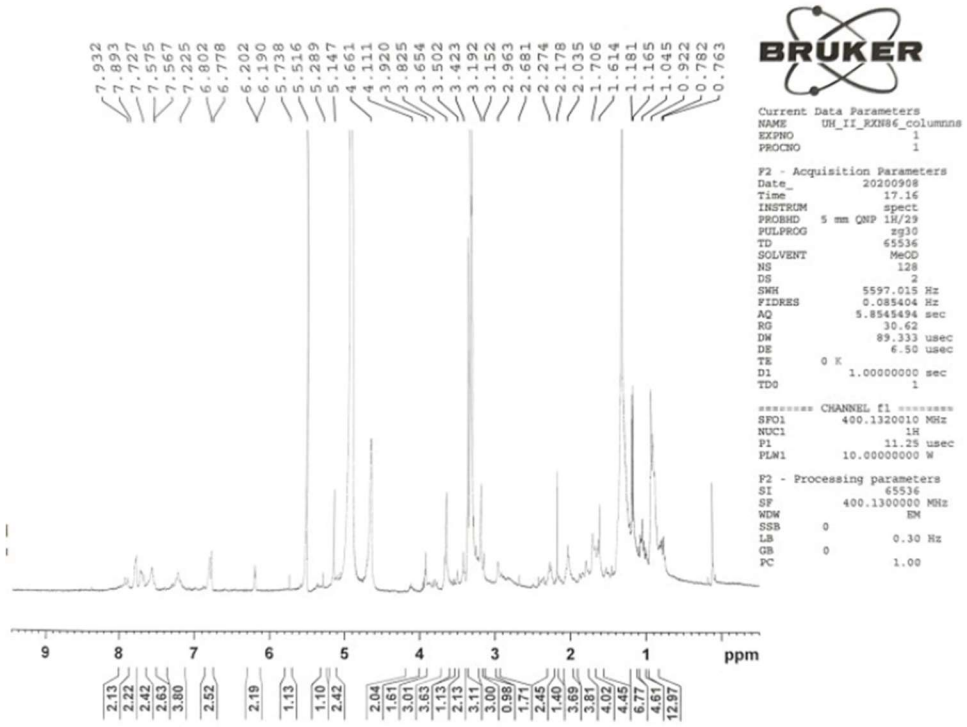

WRCL-OH ^{1}H NMR

APPENDIX B: FLUORESCENCE QUANTUM YIELD

Measuring absolute fluorescence quantum yield using the integrating sphere.

This procedure is for determining absolute fluorescence quantum yield of a sample using the HORIBA QM8075-11-C spectrophotometer.

1. Unscrew the PTI cuvette holder from the instrument and install the cuvette holder for use with the integrating sphere. The PTI holder needs to be carefully tucked into the top right corner inside the instrument without tugging on the wires, scratching the optics, or obstructing the light path.
2. In this example, the sample is a 3 μM solution of a coumarin derivative in 100% DMSO. Samples for fluorescence quantum yields need to be prepared in cuvettes designated for integrating sphere measurements. These cuvettes have a stopper instead of a screw cap. The standard cuvettes with screw caps used in the lab are too tall for measurements in the integrating sphere and may damage the coating inside the sphere.
3. To set up acquisition, select the hardware configuration for fluorescence measurements (Ex 300 Em 400 Temp) and enter the setup for acquiring emission spectra. Set excitation wavelength as the excitation wavelength of the sample (for the coumarin derivative, the excitation wavelength is 350 nm). Set the range of emission collection from before the excitation wavelength and after the wavelength of complete emission. It is helpful to refer to

an emission trace of the sample (eg, if exciting at 350 nm and sample emission is from 400-580 nm, set the emission range to be collected from 300 - 600 nm).

4. Enable real time excitation corrections. In the real time corrections tab in acquisition setup, enable the excitation correction and choose Excorr_300_quanta. Input the excitation wavelength (350 nm in this case) and press “go to”. Then click “open shutter”. The voltage in the signal bar will increase (unless it is already maxed out). Close the shutter. Reduce the bias using the scale and observe the signal bar with the shutters open and closed until the difference in the voltage when the shutter is open and the shutter is closed is ~1 V. Once this is done, click apply.
5. Enable real time emission corrections Enable emission correction and select the option for emcorr_sphere_914_cuvette/slide_quanta.
6. Place the sample in the sample holder and gently and very carefully place the integrating sphere over it. The round edge of the sphere should face the front to align with the round edge of the sample holder. Close the lid of the instrument and acquire the spectrum. Two traces will be generated, one is the uncorrected spectrum and the other is corrected. The corrected spectrum [COR] will be used for quantum yield experiments. This is I(λ). The trace should have a sharp excitation scattering pulse (at 350 nm in this example) and a much smaller, broader emission peak corresponding to the emission of the sample (400-580 nm in this case). Zoom in the y axis may be necessary to see the emission peak. If the peak for the excitation scattering is not sharp and looks cut off at the top, the detector is saturated. Make the ex and em slits smaller (1-2 nm for all slits is usually a good range) and repeat acquisition.

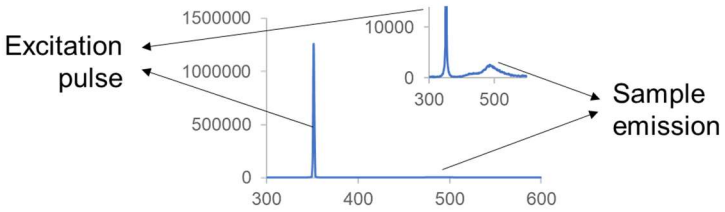

7. Repeat the same acquisition for a blank reference sample (in this case 100% DMSO). The blank trace will show only the sharp excitation scattering pulse and no other emission peak. This is I_{ref}.

8. To calculate the quantum yield, go to Math in the toolbar and launch the Quantum Yield Calculator for Int. Sphere. In the emission section, select the corrected sample trace for the I(λ) and the corrected blank trace for I_{ref} from the dropdown. In the trace pair adjustment section, select the option for emission and then drag the cursor to adjust the area on the spectra to highlight the complete region of sample emission (400 to 580 nm in this case). Click "execute 1". Repeat the same process in the excitation section. Select the I(λ) trace and the I_{ref} traces from the dropdown, change the trace pair adjustment to excitation, and then drag to highlight the area of the spectra comprising the excitation pulse (in this case 340 – 360 nm). Click "execute 2". The quantum yield will be calculated and displayed at the bottom.

9. For instances where different slit sizes are required for emission and excitation (when the sample has very low emission and the excitation pulse saturates the detector when slits that allow any emission to be observed are used), emission and excitation traces need to be collected separately with different slit sizes. Eg: excite at 350 nm and collect from 320 to 480 nm with 1 nm slits for attenuated excitation scattering. Then excite at 350 nm and collect from 400 to 600 nm with 10 nm slits to obtain high emission signal. In this case, the blank trace needs to be acquired with both slit sizes and a scaling factor needs to be calculated which can be input in the calculator.

APPENDIX C: DRY-LOADING COLUMN

Dry-loading sample onto column for chromatography

When a column chromatography purification requires very non-polar solvent systems (e.g. more than 90% hexanes in ethyl acetate, or hexanes with DCM), or when dissolving the sample to load onto the column requires a very polar solvent (such as methanol or acetone), or when a large volume of solvent is required to dissolve the sample, wet-loading the sample onto column may lead to poor separation due to the polar wet-load solvent interfering with the chromatography solvent system. Dry-loading is a technique for loading a sample without any solvent onto a silica gel column.

1. In a flask, dissolve the sample in a volatile solvent such as DCM. If insoluble in DCM, methanol or acetone can be used.
2. Add silica gel to the solution. Generally, add about as much silica gel as would be needed to form a 1–3 cm thick layer in the column. The larger the column and mass of the sample, the more silica should be added.
3. Rotavap the mixture to complete dryness. Keep a balled up Kimwipe in the bump trap during evaporation (the mixture *will* bump!) At the end, the sample should resemble a loose powder which flows smoothly like silica gel. If this is not the case, rotavap for a longer time. If still sticky, it is possible that the ratio of silica to sample is too low. Add additional silica gel and some solvent to the flask and repeat.

4. Remove sample from rotavap. Scrape the sides of flask with a spatula if needed.
5. Pack silica gel chromatography column as normal with clean silica gel and the required solvent system, without adding the final layer of sand. Next, use red tubing to gently blow air into the column (without a ground glass adapter) to evaporate solvent from the sides of the column. This will prevent the sample from sticking to the sides.
6. Pour sample into the column through a funnel. Add a few pipets of the solvent system to wet the newly added silica sample. This will prevent cracks from developing in the column due to dry silica.
7. Add final layer of sand, followed by the solvent system and begin flash chromatography.

APPENDIX D: SOLID PHASE PEPTIDE SYNTHESIS

General methods and techniques for solid phase peptide synthesis.

1. Fritted syringes (2.5 mL, VWR #MSPP-SF-0250) are used for SPPS.
2. Magnetic stir bars should be avoided as these can damage resin beads. Tape the syringe to an orbital shaker or votexer or rotavap for agitation.
3. Resin should be swollen in DMF (before experiments) or DCM (for washing) and shrunk with isopropanol (for washing).
4. For peptide coupling, standard procedure is 1 eq resin, 3 eq HBTU, 3 eq DIPEA, and 3 eq carboxylic acid. The carboxylic acid should be preactivated in with DIPEA and HBTU in DMF for 10 min before this solution is pulled up into the reaction syringe containing the swollen resin. React overnight.
5. For wash steps, wash with the reaction solvent (typically DMF), followed by several washes of DCM and then cycles of DCM and iPrOH.
6. To dry beads, especially when they need to be weighed, you can insert front end of the syringe (2.5 mL size) into red tubing and connect it to house vacuum. Pull vacuum overnight. Make sure the plunger of the syringe is pulled up and secured so it doesn't crush the beads. For the large syringes (10 mL), remove the plunger and insert red tubing into the syringe then connect to air. Make sure the syringe is secure. Dry under a gentle stream for about 10 mins.

APPENDIX E: NIR FLUORESCENCE DETECTOR

Some notes about using the InGaAs NIR emission detector for HORIBA QM-8075-11.

1. The NIR detector should be on and used ONLY WHEN AT CRYOGENIC TEMPERATURE.
2. Fill the dewar attached to the detector with liquid nitrogen using the provided funnel. Fill slowly as the liquid will spurt. Check the level of the liquid nitrogen using notches on the funnel. Keep topping up if carrying out long experiments.
3. After adding the liquid nitrogen, allow 10 mins for the detector to cool BEFORE turning the detector on using the power switch on the device. Remember to turn this off once experiments are done (while the detector is still cold).
4. The hardware configuration setting for using the NIR detector in fluorescence mode is the "Ex 750 Em 400 NIRactive".
5. Gain for the detector can be toggled between high and low using a switch on the detector.
6. Spectrum acquisition is similar to how a non-NIR sample is set up. The only difference is that the y axis units will be in volts instead of counts of photons.
7. Lippert Lab has the dye IR-1061 in inventory which can be used to check that the detector is working (ex: 950 nm, em: ~1110 nm in DCM).
8. For real time corrections, choose the options in the lookup table corresponding to the InGaAs emission detector and 750 grating.